Aristotle University of Thessaloniki

Master Thesis

Galaxy Cluster Rotation

Author:
Maria Manolopoulou

Supervisor:
Manolis Plionis

May 20, 2014

Abstract

In this thesis we study the possible rotation of galaxy-members in clusters, developing, testing and applying a novel algorithm. Finding rotational modes in galaxy clusters would lead to the necessity of correcting the dynamical cluster mass calculation. Such a correction is important in cosmological research, which use cluster masses as cosmological probes. To validate our algorithms we construct realistic Monte-Carlo clusters in order to confirm whether our method provides robust indications of rotation. We also compare our method to that of other studies found in the literature. We then apply our methodology on a sample of Abell clusters, selected such that the different Bautz-Morgan types, corresponding to distinct evolutionary phases of the clusters, are represented equally. We select galaxy cluster members using the SDSS spectroscopic database. We apply several tests indicating possible rotation on each cluster and we derive conclusions regarding its rotation or not, its rotational centre, rotation axis orientation, rotational velocity amplitude and, finally, the clockwise or counterclockwise direction of rotation on the plane of the sky. We find 23 rotating (or possibly rotating) clusters (ie., $\sim 50\%$) either within 1.5 Mpc or within 2.5 Mpc distance from the cluster centre out of the total 45 clusters in our sample. We also find that out of the 23 rotating clusters five have strong indications of substructures, which implies that the rotation signal could well be due to coherent motions of the substructures themselves. Therefore, a secure fraction of rotating clusters (at least in our sample) is $\sim$40%. In an attempt to identify the causes of cluster rotation we correlate our rotation indicators with the cluster dynamical state provided either by their Bautz-Morgan type or by their X-ray isophotal shape. We find no correlation for the sample within a 1.5 Mpc radius from the cluster centre. However, for the case of an outer radius of 2.5 Mpc we do find an anti-correlation between X-ray isophotal sphericity and our rotational indicators, showing that rotation correlates with clusters that are dynamically unrelaxed. If this interpretation was correct, we should have found similar correlations also for the 1.5 Mpc radius case. The fact that we have not, suggests that the apparent rotation at the outer radius is produced by coherent motions of substructures, infalling in the dynamically young clusters.

Contents

1 Theoretical and observational prerequisites

In this chapter we will present the basic Cosmological background on which structure, and thus cluster, formation takes place.

1.1 The Standard Cosmological Model

Today, theoretical and observational cosmologists have established the current cosmological model for the Universe. It describes the evolution of the Universe from the Big Bang until today, as it passes trough several epochs, as we summarize below.

1.1.1 From the Big Bang until today

Lemaitre has stated that the universal expansion of space implies that it had smaller dimensions at earlier stages (cf. [50]). If the expansion is adiabatic, as is believed today, the Universe should have been denser and hotter in the past.

After the Big Bang ($\sim 10^{10}$ years ago), high temperatures prevail in the Universe and matter is ionised. The stage that lasts until 10^{-44} sec is the Planck epoch, when the particles are in a state of quantum uncertainty. A quantum cosmology theory is needed to specify the procedures that take place at that time.

The Planck epoch is followed by the inflationary epoch, when the expansion of the Universe passes through an exponential accelerated phase (cf. [63]). Its dimensions grow rapidly, until the age of 10^{-34} sec. The inflationary phase succeeds in solving many problems of the Standard Cosmological model, such as the monopole problem, the horizon problem, the initial fluctuations problem and the flatness problem. During the inflation, the Universe is in a false vacuum state and its inertial mass approaches zero. The total potential energy and the pressure is negative, which leads to the exponential expansion of the Universe.

The inflation epoch is followed by another brief stage, the reheating epoch. The expansion occurring is not adiabatic and the Universe is not at thermodynamic equilibrium. The accelerated expansion energy is converted in thermal energy that simultaneously fills the Universe with matter particles, including photons.

The following epoch is the radiation epoch, which lasts for thousands of years after the inflation epoch. During this epoch, relativistic particles with high energies dominate. At the early stages, matter is fully ionised, due to high temperatures that occur. Three individual stages are distinguished in chronological order: the quark epoch, the hadron epoch and the lepton epoch. During the quark epoch, quarks dominate; during the hadron epoch, nuclear particles (protons, neutrons) dominate, and during the lepton epoch, electrons, positrons, neutrinos and other leptons dominate the Universe. At the early lepton stage, protons and neutrons are equal in numbers, but this equilibrium is broken as the temperature falls. When this stage ends (at the age of Universe $\sim$1 sec), the ratio of protons to neutrons is $\sim$4:1, a fact that designates the final proportion of the light elements. Light nuclei can now start synthesize, such as nuclei of Deuterium, Helium and Lithium. By the time of a few seconds of the Universe age, 25% of the total baryonic matter is in the form of Helium-4 nuclei. The synthesis is completed 10^2 sec after the Big Bang (cf. [60] and [90]).

At the end of the radiation epoch occurs the equivalence phase between radiation and matter. This designates the beginning of the matter epoch, where non-relativistic particles with low energies dominate the Universe. Atoms are fully ionised as the temperature is higher than $4 \cdot 10^3$ K approximately. Collisions between photons and ions take place and the Universe is opaque to radiation; photons and ions are in thermal equilibrium. When the temperature drops lower than $4 \cdot 10^3$ K, at 10^5 years approximately, recombination occurs. Electrons are now binding to ions, the collisions with photons are much fewer and the Universe becomes transparent to radiation. The photons' energy is very low, due to the expansion, and corresponds to an almost perfect black body radiation spectrum with a temperature of 2.7 K. Therefore, the CMB radiation is relic radiation; a photograph of the Universe at the moment of recombination. For that reason, the CMB radiation is highly isotropic; only a bipolar anisotropy has been observed, which originates from the peculiar motion of our Local Group with respect to the cosmological rest frame (cf. [84] and [67]).

At $8 \cdot 10^9$ years after the Big Bang, the Universe enters an accelerated expansion epoch. This accelerated expansion is confirmed through the use as standard candles of supernovae type Ia observations. The relation between luminosity distance and redshift of the supernovae led to a negative value of the deceleration parameter q (cf. [66] and [87]). Cosmologists in order to provide a cause for the accelerated expansion have introduced the ″dark energy‶, a repulsive sort of matter with negative gravitational energy (cf. [65]). Nowadays, it is believed that the Universe is flat ($k = 0$) and dark energy constitutes about ∼70% of the matter in Universe ($\Omega_\Lambda \sim 0.7$), while the rest ∼30% ($\Omega_m \sim 0.3$) is cold dark matter (∼ 25%) and baryonic matter (∼ 5%) (cf. [2]).

1.1.2 Dynamical Cosmology

The Universe is homogeneous and isotropic on the large scales. This means that there is not a privileged position or a preferred direction in the Universe. This theory is called ″The Cosmological Principle‶ (cf. [100], [20] and [62]). Many observational evidence confirm the Cosmological Principal and the Big Bang theory we previously presented; the most important of these are:

1. The Universe expands and the redshifts[1] of the galaxies are proportional to their apparent magnitudes and, consequently, to their distances. Edwin Hubble observed this relation (cf. [41]), which can be expressed as

$$\vec{x} = R(t)\vec{r} \tag{1}$$

   where $\vec{x}$ is the physical coordinate, $\vec{r}$ is the co-moving coordinate (moving together with the expansion) and $R(t)$ is the expansion factor. This relation results to the ″Hubble law‶,

$$\vec{v} = H(t)\vec{x}$$

   where $H(t)$ is the Hubble function, and for the present time $H(t_0) = H_\circ$ is the Hubble constant

$$H_\circ = 100h\frac{km}{sec \cdot Mpc}$$

   where $h \sim 0.7$ (cf. [2]),

2. The highly isotropic cosmic microwave background radiation (CMB), whose spectrum corresponds to the spectrum of a black body with temperature ∼2.73 K, which is considered the temperature of the Universe (cf. [89]).

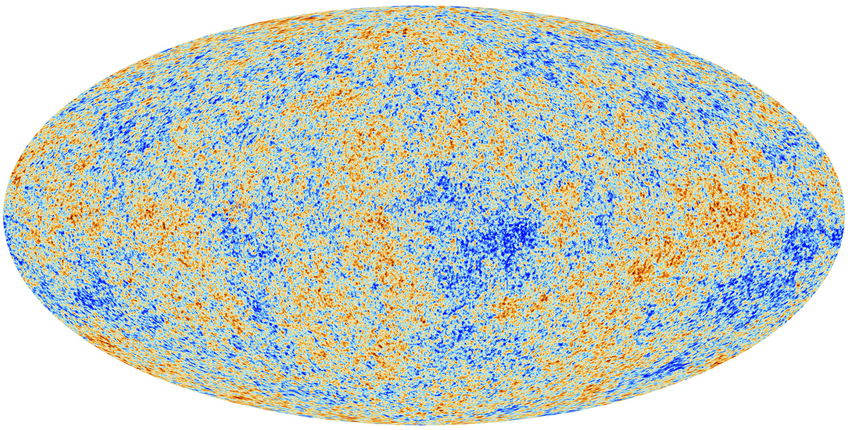

Figure 1: The CMB radiation taken from Planck satellite. The temperature deviations from 2.73 K is about 10^{-5} K.

3. The observed light element abundances (Hydrogen, Helium, Deuterium) correspond to the predicted from the theory ones (cf. [45]).

[1]Redshift, z, is the fractional shift of the light spectrum of a source.

Within the context of this homogeneous and isotropic model, we can derive the cosmological evolution using either Newtonian gravity or Einstein's field equations. We will use the former theory of gravity in this section. The cosmological parameters that are used below are:

- the total density of the Universe fluid, whatever its constituents

$$\rho_{tot} = \frac{3H_\circ^2}{8\pi G} = 1.88 \cdot 10^{-29} h^2 gr \cdot cm^{-3} \tag{2}$$

- the cosmological density parameter; the fractional density of the Universe,

$$\Omega = \frac{\rho}{\rho_{cr}}$$

- the deceleration parameter q; the rate at which the material content of the Universe is slowing down its expansion.

The homogeneity assumption is expressed as $\nabla\rho = 0$, where ρ is the density of the homogeneous and isotropic fluid, while the isotropy assumption is expressed as $\nabla \cdot \vec{v} = 3H(t) = 3\dot{R}/R$. Using the mass continuity equation,

$$\frac{\partial \rho}{\partial t} + \nabla \cdot (\rho \vec{v}) = -\frac{p}{c^2} \nabla \cdot \vec{v}$$

with p the pressure of the homogeneous and isotropic fluid and c the speed of light in vacuum, which is formed under the homogeneity and isotropy assumptions,

$$\dot{\rho} + 3\left(\rho + \frac{p}{c^2}\right)\frac{\dot{R}}{R} = 0 \tag{3}$$

and the Newton's equation of motion,

$$\ddot{R} = \frac{GM}{R^2}$$

with G the gravitational constant, we can derive the Friedmann equation

$$\frac{\dot{R}^2}{R^2} + \frac{kc^2}{R^2} = \frac{8\pi G\rho}{3} + \frac{\Lambda c^2}{3} \tag{4}$$

where k is the curvature of space and Λ is the cosmological constant. For a flat Universe with zero curvature, the Friedmann equation can be formed to

$$\frac{\ddot{R}}{R} = -\frac{4\pi G}{3}\left(\rho + \frac{3p}{c^2}\right) + \frac{\Lambda c^2}{3}$$

The different species of particles that dominated through different epochs of the Universe are described by distinct equations of state, which can all be parametrized to

$$p = w\langle v^2\rangle\rho$$

where $\langle v^2\rangle$ is the velocity dispersion of the fluid elements. For dominant contribution from relativistic particles, $w = 1/3$, whereas for contribution from non-relativistic, $w = 0$. For a given equation of state $p = p(\rho)$, the Friedmann equation can be solved to give the time evolution of $R(t)$. If we use this equation of state into the mass continuity equation (3), we get

$$\rho \propto R^{-3(1+w)}$$

and the Friedmann equation for the dust epoch (neglecting the radiation contribution) can be formed as

$$\frac{\dot{R}}{R} = H_\circ\left[\Omega_m (1+z)^3 + \Omega_k (1+z)^2 + \Omega_\Lambda\right]^{1/2} \Rightarrow H(z) = H_\circ E(z) \tag{5}$$

where the contribution of the curvature k and Λ to the total density parameter are respectively,

$$\Omega_k = -\frac{kc^2}{H_\circ^2 R_\circ^2}, \quad \Omega_\Lambda = \frac{\Lambda c^2}{3H_\circ^2}$$

From equation (5) for the present epoch we can obtain

$$\Omega_m + \Omega_k + \Omega_\Lambda = 1$$

We can prove that this equation is valid for every epoch, using equation (4). From the definition of the cosmological redshift, as the ratio of the detected wavelength to the emitted one, which is

$$1 + z = \frac{\lambda_\circ}{\lambda_1} = \frac{R(t_\circ)}{R(t_1)} \Rightarrow \frac{dR}{R_\circ} = -\frac{dz}{(1+z)^2}$$

and the Friedmann equation (5), we can deduce the age of the Universe for each cosmological model, from the equation

$$t_\circ = \frac{1}{H_\circ} \int_0^\infty \frac{dz}{(1+z)E(z)}$$

In the ΛCDM model, where $k \simeq 0$, the Hubble function in (5) is written

$$H(z) = H_\circ \left[\Omega_m (1+z)^3 + \Omega_\Lambda \right]^{1/2} \tag{6}$$

1.1.3 Structure formation

The structure we observe today in the Universe has been formed by the gravitational instability of density fluctuations that must have existed in the early stages of the Universe. A region of size r, with density $\rho(r)$, has a density contrast δ,

$$\delta = \frac{\delta\rho}{\rho} = \frac{\rho(r) - \bar{\rho}}{\bar{\rho}} \tag{7}$$

where $\bar{\rho}$ is the mean density. These fluctuations are amplified due to the gravitational instability and, if they detach from the Hubble expansion, they condense to galaxies, clusters, etc. The crucial length scale that determines the evolution of the irregularities in the expanding Universe is the Jeans length; it is the critical length where the two opposing forces balance.

In the case of a general collisional fluid, we should take into account its pressure and also the expanding background. We use the continuity equation, the Euler equation and the Poisson equation, which are respectively

$$\frac{\partial \rho(\vec{x},t)}{\partial t} + \nabla \cdot [\rho \vec{v}(\vec{x},t)] = 0$$
$$\frac{\partial \vec{v}(\vec{x},t)}{\partial t} + \vec{v} \cdot \nabla_x \vec{v} = -\nabla_x \Phi - \frac{\nabla_x P}{\rho(\vec{x},t)}$$
$$\nabla_x \Phi = 4\pi G \rho(\vec{x},t)$$

where $\rho(\vec{x},t)$ is the density, $p(\vec{x},t)$ is the pressure and $\vec{v}(\vec{x},t)$ is the velocity of the fluid which moves in a gravitational potential Φ. In an expanding Universe, the proper x and co-moving coordinate r are related with equation (1), which by differentiation gives the velocity

$$\vec{v}(\vec{x},t) = H\vec{x} + \mathbf{v}(\vec{x},t)$$

where $\mathbf{v}$ is the peculiar velocity due to local gravitational potentials. The density can now be written using equation (7) as

$$\rho(\vec{x},t) = \bar{\rho}(1 + \delta(\vec{x},t))$$

Changing coordinates to co-moving ones, using the perturbed velocity and density, we obtain after linearise the following equations of motion

$$\left(\frac{\partial \delta}{\partial t}\right)_r + \frac{1}{R}\nabla_r \mathbf{v} = 0$$
$$\left(\frac{\partial \mathbf{v}}{\partial t}\right)_r + H\mathbf{v} = -\frac{\nabla_r \delta\Phi}{R} - \frac{v_s^2}{\bar{\rho}R}\nabla_r \delta$$
$$\nabla_r^2 \delta\Phi = 4\pi G \bar{\rho} \delta$$

where $v_s = \sqrt{dp/d\rho}$ is the sound velocity, from which we derive the general differential equation of perturbation growth

$$\ddot{\delta} + 2\frac{\dot{R}}{R}\dot{\delta} = 4\pi G\bar{\rho}\delta + \frac{v_s^2}{R^2}\nabla^2\delta \tag{8}$$

In the matter-dominated Universe, for the collisionless component (dark matter) with $p = 0, v_s = 0$, this equation reduces to

$$\ddot{\delta} + 2\frac{\dot{R}}{R}\dot{\delta} = 4\pi G\rho\delta$$

whose solution is

$$\delta(\mathbf{x}, t) = A(\mathbf{x})t^{2/3} + B(\mathbf{x})t^{-1}$$

The first term is the growing mode and the second is the decaying mode which dominates only for a short time. Also $\delta \propto R$, since in the Eds model $R \propto t^{2/3}$. We appreciate that the second term of the general equation (8) in the right side is the Hubble drag, a pressure term which acts against the gravitational growth of the perturbations. For the case of baryonic matter, for when equation (8) is valid, we use the Fourier tranformation of equation (8), which is

$$\ddot{\delta_k} + 2\frac{\dot{R}}{R}\dot{\delta_k} = 4\pi G\rho\delta_k\left[1 - \frac{\pi v_s^2}{\lambda^2 G\bar{\rho}}\right]$$

Now, growth occurs when

$$\lambda > \lambda_J = v_s\left(\frac{\pi}{G\bar{\rho}}\right)^{1/2}$$

while in the opposite case, the perturbation will oscillate. The Jeans length λ_J corresponds to mass

$$M > M_J = \frac{4\pi}{3}\rho_m\left(\frac{\lambda}{2}\right)^3 = \frac{1}{6}\pi\rho_m\left[v_s\left(\frac{\pi}{G\bar{\rho}}\right)^{1/2}\right]^3$$

where the subscript m refers to the mass component. The Jeans mass depends on the sound velocity v_s, the matter density, the mean density of the Universe and, consequently, to the cosmic time. Thus, we can find a relation of the size of the perturbations that can grow at different epochs of the Universe.

Another important mass scale that determines the growth of the perturbations is the Hubble mass scale. This is the maximum scale within which fluctuations can interact with each other and there is enough time to grow. It is defined as

$$M_H = \frac{4\pi}{3}\rho\lambda_H^3 \propto \left(\frac{t}{R}\right)^3$$

Therefore, in order for a perturbation to grow, it should have a mass that satisfies the relation

$$M_J \lesssim M \lesssim M_H$$

While baryonic fluctuations have started evolving after the recombination moment, the dark matter fluctuations have started evolving before this moment, and the baryonic component was driven in the gravitational potentials created by the dark matter component. Dark matter weakly interacts with others forms of matter and radiation. The perturbation analysis is the same as for the baryonic fluctuations, with the only exception that all species of perturbations are included (baryonic, radiation, dark matter).

In order to go beyond the linear evolution of perturbations one has to use the crude but useful spherical collapse model. The spherical perturbation is an easy case to examine, although real perturbations have small deviations from sphericity. For the collapse model of the perturbations we will consider spherical perturbation with radius and density given from $r = R(1+a)$ and $\rho = \bar{\rho}(1+\delta)$ respectively. We consider that the perturbation consists of shells, which conserve their mass with time and do not cross each other. The quantity

$$\varepsilon = \frac{\dot{r}^2}{2} - \frac{GM}{r}$$

for every shell determines its behavior. For $\varepsilon < 0$, the expansion of the perturbation decelerates and then recontracts. For $\varepsilon > 0$, the perturbation expands forever, like an open cosmological model. Thus, for a perturbation to collapse, $\varepsilon < 0$ is needed, which can be interpreted as

$$\delta > \frac{3}{5(1+z)}\left(\frac{1}{\Omega_\circ} - 1\right)$$

The evolution of the spherical density perturbation using linear theory (linear approximation ψ) will be

$$\delta_L \simeq \left(\frac{3}{4}\right)^{2/3} \frac{3}{5}(\psi - \sin\psi)^{2/3}$$

by which we can derive the following epochs:

- The onset of the non-linear regime (when $\delta_l \approx 0.57$)
- The onset of collapse - Maximum expansion (when $\delta_l \approx 1.06$)
- The full collapse (when $\delta_l \approx 1.686$). Perturbation turns around, collisionless matter collapses rapidly and a stable distribution in virial equilibrium is produced. This process is called violent relaxation. The radius of the final structure is exactly the half of the radius at maximum expansion.

1.2 Large Scale Structure

1.2.1 Galaxies

Galaxies are the basic unit of distribution of matter in the Universe. They are concentrations of stars, dust and gas in various proportions and have sizes of a few kpc. Galaxies are classified by Hubble in 1926 mainly by their shape (cf. [37], [38], [39] and [40]). His classification is shown in the ″tuning-fork‟ diagram (fig. 2) and includes the three main categories, ellipticals, spirals and irregulars, as well as subcategories for every category. The position of every galaxy in the tuning-fork is determined by the size of its nucleus and spiral arms. The galaxies in the left are called early-type galaxies, while the ones in the right are the late-type galaxies (cf. [98]). The observed fraction of the galaxy types are 10% ellipticals, 20% SO's, 65% spirals and 5% irregulars.

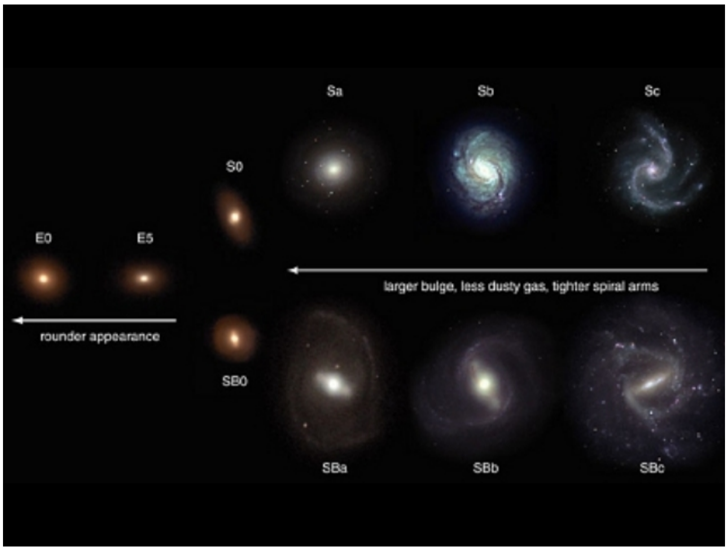

Figure 2: The tuning-fork diagram of the galaxy classification of Edwin Hubble.

Elliptical galaxies are ellipsoidal systems with little gas, old population of stars and a wide variety of mass; we observe dwarf ellipticals with $M \sim 10^7 M_\odot$ and supergiant ellipticals with $M \sim 10^{12} M_\odot$. Their surface brightness distribution follows de Vaucouleus model (cf. [22])

$$I_s = I_e e^{-7.67\left[\left(\frac{r}{r_e}\right)^{0.25} - 1\right]}$$

where r_e is the effective radius that encloses the half of the total light. $I(r)$ falls off slower than r^{-2} for $r < r_e$ and more rapidly for $r > r_e$. This formula also fits the bulges of SO's.

Figure 3: Example of two elliptical galaxies: ESO 325-G004 on the left and M87 on the right.

Spiral galaxies consist of their disk, the bulge and the halo. The disk is very thin, only a few hundred of pc's, has a large amount of gas and many star-forming regions. The spiral structure has formed by the rotation of density waves that produce shocks in the gas regions and, therefore, star formation. The surface brightness of the stars falls exponentially with radius r

$$I_s = I_\circ e^{-r/b}$$

where b is the scale-length of the disk.

Figure 4: Example of two spiral galaxies: NGC 1300, a barred galaxy, on the left and M31 (Andromeda galaxy) on the right.

Figure 5: Example of an irregular galaxy: NGC 1569.

Luminosity distribution

The galaxy luminosity function $\Phi(L)dL$ is the number density of galaxies with observed luminosity in the integral $(L, L + dL)$. The Schechter function (cf. [85]) best fits the observational data of galaxies

$$\Phi(L) = \frac{\phi_*}{L_*}\left(\frac{L}{L_*}\right)^{\alpha} e^{-L/L_*}$$

where L is the luminosity of the galaxy, $\alpha = -1.23 \pm 0.02$, $\phi_* = 0.9 \pm 0.07 \cdot 10^{-2} h^3 Mpc^{-3}$ and L_* is calculated from the luminosity with absolute magnitude M_* relation presented in 1.3.1 by using $M_* - 5 \log h = -20.73 \pm 0.04$, all calculated in the r band (cf. [56]). Constant L_* separates the power law from the exponential law, the faint from the bright galaxies. The mean luminosity density that corresponds to this function is

$$\langle L \rangle = \int L\Phi(L)dL \approx 2 \cdot 10^8 h L_\odot Mpc^{-3}$$

The distance that corresponds to the knee of the luminosity function is the characteristic distance and can be defined, by neglecting cosmological corrections, as

$$D_* = 10^{0.2(m_\circ - M_* - 25)}$$

where M_* is the absolute magnitude that corresponds to L_*. There is also the $\Phi(M)dM$ form of the Schechter function, which is the number density of galaxies with absolute magnitude in the integral $(M, M + dM)$. The shape of the luminosity function is constant with environment for each individual Hubble type:

- All giant types of galaxies (spirals, ellipticals, SO's) have a maximum in their luminosity function. Spirals and SO's have a Gaussian distribution of luminosities.
- Dwarf elliptical galaxies are approximately the 70% of the population in galaxy clusters.
- The luminosity function of individual types of galaxies are similar in high and low density regions.
- The galaxies' relative abundance has an environmental dependence; higher fraction of ellipticals and SO's are observed in high density regions. It is not yet known whether this is caused by an evolutionary effect or a galaxy formation process.

Peculiar velocity field

The velocities of the galaxies relatively to the origin in the expanding Universe with expanding coordinates $\mathbf{r} = x/R(t)$ are

$$\mathbf{v} = \mathbf{r}\dot{R}(t) + R(t)\dot{\mathbf{r}}$$

where $R(t)\dot{\mathbf{r}}$ is their peculiar velocity. The peculiar velocity field of the outermost parts of the galaxies, using the linear theory, is

$$v(\mathbf{r}) = \frac{2\mathbf{g}(\mathbf{r})}{3\Omega_\circ^{0.4} H_\circ}$$

where $\mathbf{g}(\mathbf{r})$ is the peculiar gravitational acceleration.

1.2.2 Clusters of galaxies

Galaxy clusters are large groups of galaxies, the most X-ray luminous objects in the sky (along with AGN's) and are the largest gravitationally bound structures in the Universe. They contain great amounts of dark matter, hot gas and hundreds of galaxies. Clusters with less than 10-20 galaxies are called groups of galaxies (cf. [57]). Cluster's gas is at very high temperatures $\sim 10^6 - 10^7$ K, ionised and emitting X-rays. Diffuse radio emission has also been found in clusters (cf. [48] and [31]. Clusters are great tools for studying large-scale structure, testing structure formation theories and extracting cosmological information (cf. [17] and [4]), as we will analyse below.

Clusters can be classified by several schemes. A first scheme is that of regular and irregulars. Regular clusters are about $\sim$50% of the clusters. They have smooth and symmetric structure, small fractions of spiral galaxies ($< 20\%$), high central density ($\geq 10^3 Mpc^3$), high X-ray luminosity and high velocity dispersion ($\sim 10^3 km/s$). They are believed, due to their observational properties, to be in virial equilibrium. Irregular clusters have evident substructures, higher fraction of spiral galaxies ($\gtrsim 40\%$), lower X-ray luminosity and lower velocity dispersion.

A distinct class of clusters is the one that contains those which have a central huge bright galaxy called BCG or cD. This galaxy is a giant elliptical with mass $\gtrsim 10^{12} M_{\odot}$ and might have multiple nuclei. They might have grown up by galactic cannibalism, by gulping galaxies that spiral towards the cluster center (cf. [55] and [7]). Another opinion states that they might have been created in special locations where clusters are eventually formed by anisotropic accretion of matter (cf. [101]).

In addition, a classification of clusters has been made by Bautz & Morgan (1970) [10]. There are five Bautz-Morgan types of clusters. Bautz-Morgan type I clusters are dominated by a central, supermassive cD galaxy, with extensive optical emission. It was found that these clusters are characterized by a higher number density of galaxies than clusters of other types and that they are dynamically more evolved. Bautz-Morgan type II clusters have their brightest galaxy being intermediate between cD and

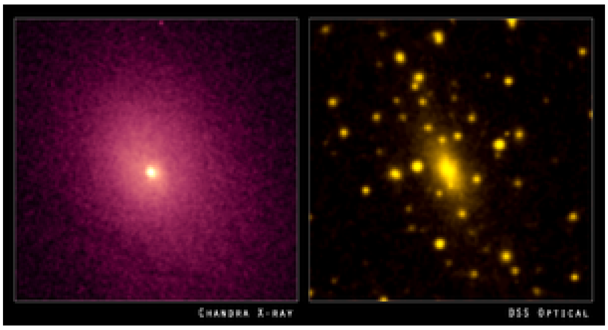

Figure 6: A Bautz-Morgan type I cluster, Abell 2029 in X-rays (left) and optical wavelengths (right).

normal giant ellipticals. Type III clusters have no members significantly brighter than the general bright population, with type I-II and type II-III being intermediate cases.

Figure 7: *Left:* Coma cluster, a representative of Bautz-Morgan type II clusters. *Right:* Virgo cluster, a representative of Bautz-Morgan type III clusters.

Galaxy clusters are flattened structures, even more flattened than the elliptical galaxies, which reflects the initial conditions of their formation and the tidal effects that take place in their early stage of formation; anyway, as we have already mentioned, the initial perturbations in the Universe where not perfectly spherical (cf. [6]). The mean ellipticity is ~ 0.5 and most of them are prolate (cf. [8]). The huge gravitational potential of the cluster causes galaxy members to have large virial velocities and the ″finger of God‟effect occurs; an apparent elongation of the cluster is observed along the line of sight.

A notable feature of clusters is that the seem to point to each other up to 20-30 h^{-1} Mpc distance (cf. [12]). Irregular clusters, which are dynamically young, tend to be more aligned with their neighbors and are usually found in high-density regions (cf. [69] and [88]).

1.2.3 Superclusters, filaments and voids

Superclusters are aggregations of clusters of galaxies, galaxies and groups. They are the largest isolated structures in the Universe, but not dynamically relaxed. Galaxy clusters have peculiar velocities approximately 10^3 km/s, which allows them to move during the Hubble time no more than $10h^{-1}Mpc$, a distance smaller than the size of a typical supercluster; therefore, galaxy clusters have not immigrated from their initial supercluster. This fact make superclusters ideal probes of the initial conditions that created cosmic structures.

Superclusters have a typical size of $\sim 30 - 50h^{-1}Mpc$. The vast majority of them appear to be flattened. In addition, several studies have found elongated bridges of galaxies that connect the rich ones; these are the filamentary and sheet-like structures which are more obvious is 3D surveys (cf. [104],[25],[99], [9] and [96]). In radial velocity surveys, regions with density below the average value have been observed, which are called voids (cf. [64]). Very few galaxies exist in the voids, they are relatively empty of luminous matter, but it is not certain whether dark matter exists in there. It is extremely difficult to identify voids in 2D projections of the sky.

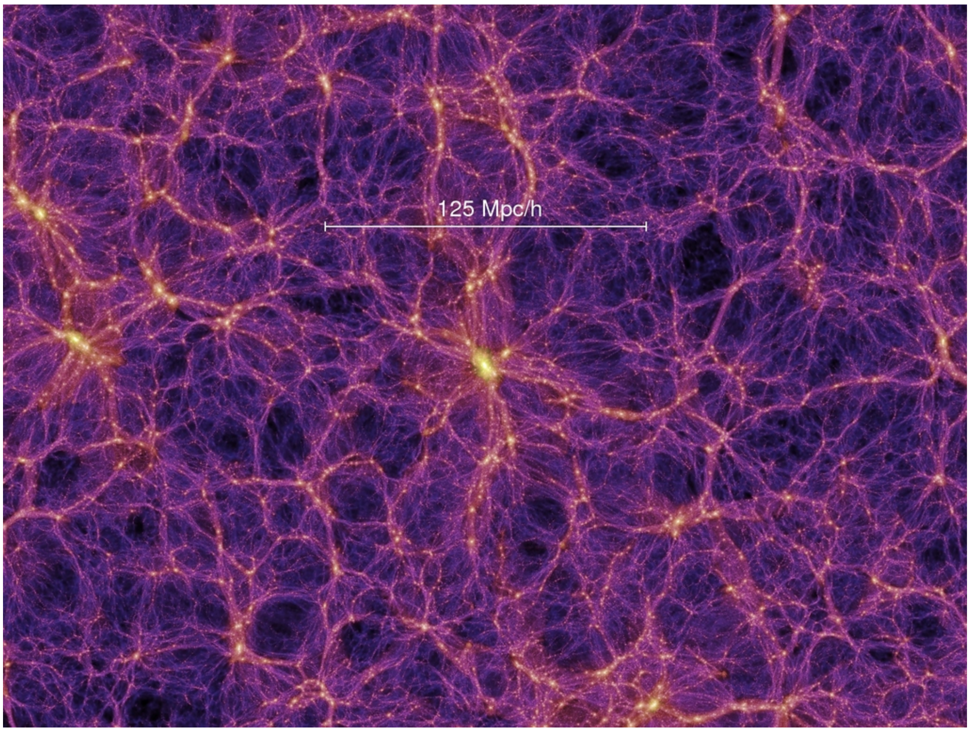

Figure 8: Millennium simulation of the Universe ($z = 0$). This slice is $15h^{-1}Mpc$ thick. Superclusters, filaments and voids are obvious.

1.2.4 Clustering of large scale structure

Galaxy formation theories predict that giant and dwarf galaxies are spatially segregated, since the bright ones are formed at the highest density peaks. Also, it was believed that, dwarf galaxies that have low luminosities could be filling the voids. Nevertheless, Thuan et al. (1987) ([93]) found that dwarf galaxies outline the structures defined by the bright ones and do not fill the voids.

Studies of the galaxy correlation function for different Hubble types have shown that late type galaxies are less correlated than early types, which are less correlated than the dwarf irregular galaxies; dwarf ellipticals are the most correlated and most popular in galaxy clusters. Therefore, bright or low luminosity galaxies are not better or worse tracers of the underlying mass distribution; all different luminosity galaxies are differently biased tracers of the mass.

Clusters of galaxies are also spatially correlated. However, there are several biases that produce inaccuracies in the correlation functions; the enhanced clustering of rich Abell clusters was found to be contaminated by the sample of foreground and background galaxies (cf. [23], [61] and [92]). In summary, in the Abell cluster catalogue the extended region of the clusters tend to increase the galaxy density around them and nearby clusters are revealed that otherwise would not fulfill the selection criteria (cf. [52]). An unbiased catalogue is a catalogue in X-rays (for example, the XMM cluster survey), where clusters' emission is diffuse and has one peak; clusters, along with AGN's, are the most X-ray luminous objects in the sky.

1.3 Observational prerequisites

1.3.1 Apparent magnitudes and distances

In order to conduct surveys of extragalactic objects, such as galaxies, we should measure the distance of the objects we study using their redshift, taken from observational data. This distance also depends on the cosmological model we assume, as is shown below.

Apparent magnitude

The information we get for the Universe comes of the photons we receive. Therefore, we define the apparent luminosity l of a source at distance r from the Earth, with absolute luminosity L, as

$$l = \frac{L}{4\pi r^2} \tag{9}$$

In this relation the loss of energy while propagating in the Universe is not taken into account. With the knowledge of l and L we are able to calculate the distance of the source. To measure the apparent magnitude of a source we use a logarithmic system, by which an object with magnitude 1 is 100 times brighter than an object with magnitude 6. Thus, the definition of the apparent magnitude m of an object with apparent luminosity l at distance r and its absolute magnitude M with absolute luminosity L are, respectively,

$$\begin{aligned} m &= -2.5 \log_{10} l + c_1 \\ M &= -2.5 \log_{10} L + c_2 \end{aligned}$$

where c_1 and c_2 are constants that depend on the filter. The value $m - M$ is called distance modulus μ and is defined by

$$\mu = m - M = 5 \log_{10} r + c_3 \tag{10}$$

where c_3 is fixed to have a value -5 when M is the apparent magnitude of the star with distance 10 pc and a value 25 when the star is at distance 10 Mpc (used in extragalactic astronomy).

The definition of the apparent magnitude is filter dependent, as our observations cover a range $(\nu - d\nu, \nu + d\nu)$ of spectral frequencies and not the whole electromagnetic spectrum. This range depends on the sensitivity of the detector, the frequencies that are allowed to pass the atmosphere which can be all modeled by a sensitivity mask F_ν (or filter). Thus,

$$m_{F_\nu} = -2.5 \log_{10} \left(\int_0^\infty F_\nu I_\nu d\nu \right) + c$$

For $F_\nu = 1$ the apparent magnitude is called bolometric magnitude.

Proper distance

The proper distance is the distance that light travels along a null geodesic. A light signal is emitted at a galaxy at some time and is received by an observer at another time; these two events are connected only by the light signal. Since all observers measure the same speed of light, this distance is a fundamental one. From the Robertson-Walker metric

$$ds^2 = c^2 dt^2 - R^2(t) \left[\frac{dr^2}{1 - kr^2} + r^2 \left(d\theta^2 + \sin^2 \theta d\phi^2 \right) \right]$$

where $R(t)$ is the expansion factor, k is the curvature and (r, θ, ϕ) are polar coordinates, we have, at time t,

$$d_{pro}(t) = R(t) \int_0^{r_1} \frac{dr}{\sqrt{1 - kr^2}} = R(t) r_1, \quad for \quad k = 0$$

where $R(t)$ is the scale factor and r_1 is the dimensionless co-moving coordinate distance of galaxy L_1. For the present time t_0, it is $d_{pro} \approx R(t_0)r_1$, where

$$r_1 \simeq \frac{1}{R(t_0)} \int_0^z \frac{c}{H(z)} dz$$

Luminosity distance

The apparent luminosity l of a source is the product of the rate of the received photons

$$\frac{n}{\delta t_0} = \frac{n}{\delta t_1(1+z)}$$

where t_0 is the time of the emission and t_1 is the time of the reception, of the photon energy

$$\frac{hc}{\lambda_0} = \frac{hc}{\lambda_1(1+z)}$$

where λ_0 is the emission wavelength and λ_1 is the reception wavelength, and of the reverse of the surface area of the detector $4\pi R^2(t_0)r_1^2$, where r_1 is the dimensionless co-moving coordinate distance of the emitter,

$$l = \frac{n}{\delta t_1(1+z)} \frac{hc}{\lambda_1(1+z)} \frac{1}{4\pi R^2(t_0)r_1^2}$$

The total luminosity emitted by the source is

$$L = \frac{n}{\delta t_1} \frac{hc}{\lambda_1}$$

Using equation (9) we can find the distance r of the source, which is now called luminosity distance d_L

$$d_L = (1+z) \int_0^z \frac{c}{H(z)} dz$$

If we have bolometric magnitudes (luminosities integrated over all frequencies), then relations (9) and (10) are changed, because of the expansion of the Universe, to

$$l_{bol} = \frac{L_{bol}}{4\pi r_1^2 R^2(t_0)(1+z)^2}$$

$$m_{bol} - M_{bol} = 5\log_{10} d_L + 25$$

Angular diameter distance

The corresponding distance of the angle that the length x of an extragalactic object subtends at our location is the angular diameter distance, d_θ. The edges of the object have coordinates (r_1, θ_1, ϕ_1) and $(r_1, \theta_1 + d\theta_1, \phi_1)$. The angular diameter distance is defined as

$$d_\theta = \frac{x}{\delta\theta} = r_1 R(t_1) = \frac{r_1 R(t_0)}{1+z} = \frac{1}{1+z} \int_0^z \frac{c}{H(z)} dz \tag{11}$$

From all the above distance definitions we can conclude that

$$d_{prop} = (1+z)d_\theta = \frac{d_L}{1+z}$$

which, for $r_1 \ll 1$ and $z \ll 1$, it is valid that

$$d_{prop} \approx d_\theta \approx d_L \approx R(t_0)r_1$$

1.3.2 Biases and systematics on apparent magnitudes

K-correction

As we have mentioned above, the magnitude measurements of the objects are not the bolometric ones, but they are magnitudes affected by the expansion of the Universe. As a result, a correction in the calculation of the bolometric magnitude should be inserted. This correction comes up due to the fact that, when we measure the magnitude of an object at large distance at a particular wavelength $\lambda_\circ$, we receive light emitted from a different part of the spectrum. The object could be brighter or fainter in this part compared with $\lambda_\circ$. If $L(\lambda_e)d\lambda_e$ is the energy per unit time emitted by the source in the range $(\lambda_e, \lambda_e + \delta\lambda_e)$ and the energy per unit time per unit are received is $l(\lambda_\circ)d\lambda_\circ$, then, by using equation (9) and the luminosity distance, we have

$$l(\lambda_\circ)d\lambda_\circ = \frac{L(\lambda_\circ/(1+z))d\lambda_\circ}{4\pi(1+z)d_L^2}$$

The combination of the detector sensitivity, atmospheric and galactic absorption and other effects bring on energy losses as a function of the wavelength, which can be all included in the factor $F(\lambda_\circ)$, the sensitivity mask. The measured flux would be

$$l = \int_0^\infty F(\lambda_\circ)l(\lambda_\circ)d\lambda_\circ$$

Therefore, the measured magnitude for emitted energy in the range $(\lambda_e, \lambda_e + \delta\lambda_e)$ and received energy in the range $(\lambda_\circ, \lambda_\circ + \delta\lambda_\circ)$ would be

$$m_\circ - M_\circ = 5\log_{10} d_L + 25 + K_\circ(z) \tag{12}$$

where $K_\circ(z)$ is the K-correction,

$$K_\circ(z) = -2.5\log_{10}\left[\frac{\int F(\lambda_\circ)L(\lambda_\circ/(1+z))d\lambda_\circ}{\int F(\lambda_\circ)L(\lambda_\circ)d\lambda_\circ}\right] + 2.5\log_{10}(1+z)$$

By knowing the sensitivity mask, we can calculate the K-correction by integrating. For spiral galaxies, a typical value at $z = 1$ is $K \sim 2$.

Galactic absorption

The interstellar gas and dust of our Galaxy absorb light from background sources. Dust scatters more efficiently the blue light, so the background light appears redder. The simplest model of this effect shows that the flux l_ν of an extragalactic source, transversing a Galactic layer of thickness ds at an angle b from the equatorial plane, suffers losses

$$\frac{\delta l_\nu}{l_\nu} \propto ds\csc(b) \Rightarrow \frac{dl_\nu}{ds} = -\kappa_\nu l_\nu \csc(b)$$

where κ_ν is the absorption coefficient at the spectral frequency ν. By integrating we have

$$l_\nu = l_\nu^\circ \exp(-\mathcal{A}\csc|b|)$$

where l_ν° is the incident, l_ν is the observed flux and $\mathcal{A} = \int \kappa_\nu ds$ is the optical thickness. The observed flux of the object would now be corrected to

$$l_{true} = \frac{l}{\exp(-\mathcal{A}\csc|b|)} = \frac{L}{4\pi r^2}\exp(-\mathcal{A}\csc|b|)$$

The value of $\mathcal{A}$ varies with the frequency band; for the visual we have $\mathcal{A} \sim 0.2$. Equation (10) now gives

$$r_{true} \approx r_{raw}\exp(-\mathcal{A}\csc|b|/2)$$

This means that the distance of an extragalactic object can be overestimated at low galactic latitudes if this effect is not taken into account.

Malmquist bias

When we try to determine distances of extragalactic objects by using apparent magnitude limited samples, such as the Tully-Fisher, Faber-Jackson or D_n-σ relations, we tend to pick a larger fraction of bright objects as we look in greater distances; we sample the brighter end of the luminosity function. It's effect on the distance estimation can be approximated by r_{cor} (see [70])

$$r_{cor} \approx r_{raw} 10^{1.382\sigma^2/5}$$

which means that the distances we calculate are smaller than the true ones. As the distance increases, a smaller fraction of the brighter end of the luminosity function is sampled.

Luminosity evolution

As we look in greater distances, we observe objects that are younger. The luminosity of galaxies is a function of the time the light was emitted. The luminosity of distant objects should be corrected to take into account their luminosity evolution.

By using the luminosity distance, the $K(z)$ correction and the Galactic absorption correction, we obtain a general distance modulus relation

$$m - M = 5 \log_{10} d_L + 25 + K(z) - 1.086\mathcal{A} \csc |b| + ...$$

where any other correction can be added.

1.3.3 Methods of measuring distance

In order to measure distances we use different methods that vary depending on the distance scale of the object. We describe the most frequently used methods, starting from the local to universal distance scales (cf. [81] and [82]).

Trigonometric parallax

It is used to measure the distance of nearby stars out to 60 pc approximately. It is based on the fact that every six months we observe the stars from different point of view, due to the fact that the Earth is on the opposite side of its orbit around the Sun. The parallax angle is the apparent shift of position of object against the background of distant objects. For nearby stars, the parallax angle p is small, so the distance d measured in parsecs is the inverse of the parallax measured in arcseconds, $d = 1/p$.

Main sequence fitting

This method uses the fact that the stars in the globular clusters in our Galaxy are at a similar distance and occupy a certain area on the H-R diagram; their spectral stellar type and absolute luminosity are uniquely correlated. Therefore, having measured the distance of one globular cluster, someone can determine the distance of any other globular cluster by observing its relation of spectral type distribution with apparent magnitude and compare it with the one of the standard globular cluster.

Cepheid variable stars

This method can extend our distance measures up to 20 Mpc approximately, a local extragalactic distance scale. Cepheid stars exhibit a strong relation between their intrinsic luminosity, L, and their pulsation period, P, $L \propto P^{1.3}$. By determining their luminosity, one can measure their distance through the distance modulus equation (10). This method provides the link between the local galactic indicators and the extragalactic ones (cf. [32]).

Scaling relations

Many scaling relations between a distance dependent and a distance independent have been found for indicators at large distances. It was shown that they are distance independent. The Tully-Fisher relation associates the rotational velocity V, of a spiral galaxy to its total infrared, L_{ir}, or blue, L_b, luminosity, $L_{ir} \propto V^4$ and $L_b \propto V^{2.4-2.8}$ respectively (cf. [95]). For elliptical galaxies, there are two similar scaling relations: the Faber-Jackson relation (cf. [29]), which associates the absolute luminosity L of the galaxy, to the stellar velocity dispersion, σ, $L \propto \sigma^{3-4}$, and the $D_n - \sigma$ relation (cf. [24]), which associates its diameter D_n, to the stellar velocity dispersion, $D_n \propto \sigma^{1.2-1.3}$.

Maximum Supernova SNIa brightness

Type Ia supernovae are binary systems, whose white dwarf accretes matter from the red giant, until it reaches the Chandrasekhar limit and explodes (cf. [51]). Those objects have constant maximum luminosity that can be seen out to cosmological distances and for that reason they are great distance indicators for large distances. By measuring their apparent luminosity and already knowing the absolute one, we can calculate their distance.

Surface brightness fluctuation

The discreteness of stars within galaxies that are observed by a detector depend on the distance of the galaxy. We can measure the fluctuations of the starlight pixel by pixel and calibrate the relation to finally provide the distance of the galaxy.

Sunyaev-Zeldovich effect

This method is a direct one, as it does not depend on the measurement of local distances for calibrations. Clusters of galaxies contain hot gas that emits thermal Bremsstrahlung spectrum in $5 \cdot 10^7 - 10^8$ K. The gas distorts the CMB spectrum by Compton scattering, which increases the brightness of the CMB at the longer wavelength range and decreases its brightness in the shorter wavelength range (cf. [91]). By measuring the X-ray flux, gas temperature and angular separation of the cluster on the sky, we can deduct its distance (cf. [13]).

1.4 Clusters as cosmological probes

Clusters are the larger gravitationally bound objects in the Universe and are used in various types of research. They are used to study the evolution of their galaxy members, the creation and evolution of AGN's and supermassive black holes in them, the proportion and distribution of the chemical elements and other applications. On the other hand, due to their great size, they are effectively used in cosmology for many reasons, the most important of which is the measurement of the cosmological parameters.

A rotational mode in clusters would contaminate the velocity dispersion measured, which is used to calculate its mass through the Virial theorem. For this reason, it is important to measure the component of rotation in the velocity distribution of the clusters and accurately calculate its velocity dispersion. The cluster mass is widely used in cosmology and astronomy studies. Below we discuss the most important cosmology applications that use the cluster mass.

1.4.1 Mass-to-light fraction observations

Every astronomical object is characterized by its mass-to-light ratio, M/L, which is scaled to the fraction value for the Sun, $M_\odot/L_\odot$. If the fraction of the object is larger than the Sun's one, this object should consist of a greater portion of dark matter than the Sun. Different classes of extragalactic objects, such as galaxies and clusters, has been proved to have different quantities of mass-to-light ratio. If we estimate the universal luminosity density and calculate the mass-to-light ration of a certain class of objects, we can calculate its contribution to the matter density cosmological parameter Ω_m. A universal value of the mass-to-light ratio can lead to the computation of Ω_m.

Galaxy clusters widely apply to this method under the quite substantial assumption of virial equilibrium. In a virialised cluster its kinetic energy, K, is equal to the half of its potential V:

$$K = -\frac{1}{2}V \Rightarrow \frac{1}{4}\frac{GM(R)}{R} = \frac{1}{2}v_k^2 \Rightarrow M(R) = \frac{2v_k^2 R}{G} \tag{13}$$

where $M(R)$ is the cluster mass, R is its radius, v_k^2 is the velocity dispersion and G is the gravitational constant. Consequently, the calculation of mass-to-light ratio is based on the measurement of the velocity dispersion of the clusters to find their mass and on number-galaxy weighted luminosity estimation. In [70] has been found that

$$(M/L)_{cl} \approx 320^{+170}_{-85} h M_\odot/L_\odot \tag{14}$$

In order to find a global value for Ω_m we use the total density ρ_{tot} we have mentioned in (2), and the mean luminosity density $\langle L \rangle$ calculated by integrating the Schechter luminosity function (cf. [85]).

$$\frac{M}{L} = \frac{\rho}{\langle L \rangle} = \frac{\Omega_m \rho_{tot}}{\langle L \rangle} \simeq 1400 \Omega_m h M_\odot/L_\odot$$

We expect that galaxy clusters represent the Universal mass-to-light ratio value, as they are the deepest potential wells and accumulate matter from large volumes. This is supported by the fact that there is an increasing trend of the mass-to-light ratio value with scale that reaches a plateau at the value of clusters (cf. [3] and [5]). The value of Ω_m we extract from (14) is

$$\Omega_m \simeq 0.23^{+0.12}_{-0.06}$$

1.4.2 Cluster baryon fraction

Galaxy clusters are believed to accrete matter during formation in such scales that there is no segregation between baryonic and dark matter. As a result, the ratio of the baryonic to total matter Ω_B/Ω_m on clusters in representative of the universal value. Galaxies are about the 5% of the cluster mass, while the intracluster gas is about 20%. The addition of those values provides an estimation of Ω_B. We can measure the total mass M_{tot} of the cluster by assuming that the gas traces the cluster mass and the former is in hydrostatic equilibrium; its pressure P_{gas} balances the gravitational force:

$$\frac{dP_{gas}}{dr} = -\rho_{gas}\frac{GM_{tot}}{R^2}$$

where ρ_{gas} is the gas density profile and R its radius. Now, using the relation

$$\frac{\Omega_B}{\Omega_m} = \frac{M_B}{M_{tot}}$$

we can constrain Ω_m (cf. [102] and [27]), which has been found for $h = 0.72$,

$$\Omega_m \simeq 0.35 \pm 0.05$$

1.4.3 Rate of cluster formation evolution

The rate of the perturbations growth varies in universes with different Ω_m. For example, the perturbation growth factor in universes with $\Omega_\Lambda > 0$ present redshift dependence. Nevertheless, in the present epoch it is indistinguishable from the open Universe $\Omega_m = 1 - \Omega_\Lambda$ (cf. [47]). Therefore, there is necessity to constrain Ω_m using the evolution of indicators of cluster formation, especially in ranges where the evolution differs for different models. Ideally we would study the evolution of the cluster mass function, but observationally we can study indicators such as their luminosity function, temperature function and morphology. As a next step, we use the Press-Schechter formalism (cf. [72]) to estimate the cosmological parameters in the cluster mass function that enter through the power spectrum of the perturbations.

From the study of the evolution of the X-ray luminosity function of galaxy clusters, it has been found that a

$$\Omega_m \simeq 1$$

model is expected (cf. [34]). Studying the evolution of the temperature function of the X-ray emitting gas through the iron line emission (cf. [75]) there has been found evolution (cf. [26] and [36]) which leads to

$$\Omega_m \simeq 0.7 - 1$$

or no evolution (cf. [97] and [15]), which leads to

$$\Omega_m \simeq 0.3 - 0.5$$

models. Luminosity-temperature relation is expected to evolve in time in a way depending on the cosmological model (cf. [18]). Many studies have found no evolution of the relation, while another study have found that its evolution matches a

$$\Omega_m \sim 0.35$$

model (cf. [16]).

In an open or flat Universe we expect that clusters are relaxed and do not present indications of substructures. On the other hand, in a critical density model, clusters should continue to form until now and be dynamically activate (cf. [76], [28] and [46]). These expectations could be used in order to constrain the cosmological parameters. Unfortunately, it is difficult to identify cluster substructures due to projection effects and we are not certain about the relaxation time of cluster mergers (cf. [83]). However, we can use some merging criteria (cf. [78], [79], [103] and [86]) that can constrain Ω_m that are based to the fact that galaxies are non-collisional, while gas is collisional:

1. the difference in the peak of gas and galaxy distributions
2. elongation of the X-ray isophotals perpendicularly to the merging direction
3. temperature gradients

The first two indicators are expected to last up to 1 Gyr approximately.

Another morphology evolution criteria that has been observed is the cluster ellipticity. It has been found that cluster ellipticity decreases with redshift in the recent past, $z \lesssim 0.15$, which can be interpreted by a low-Ω_m Universe (cf. [54] and [68]), because merging and anisotropic accretion through filaments would have stopped long ago. The temperature of the X-ray emitting gas as well as its luminosity also follow the same trend (cf. [77]), as it has been confirmed (cf. [68]). However, increase in the clusters' velocity dispersion in lower redshifts due to the virialisation has not been found (cf. [33]). Non-relaxed clusters seem to present increased velocity dispersion due to possible large peculiar velocities of the substructures (cf. [80]).

2 Cluster rotation

2.1 Previous work on cluster rotation

In this section we display some of the previous work on galaxy cluster rotation of galaxy-members or intracluster medium either using observational data or simulations.

Hwang & Lee (2007) [42] search for indications of rotation using spectroscopic data from SDSS and 2dF-GRS. The cluster rotation is reduced to galaxy-members rotations and intracluster gas rotation. They assume that rotation originates either from cluser mergers or from the global rotation of the Universe. The rotating clusters should present spatial segregation of the galaxies with larger and smaller velocities than the mean cluster velocity and should present one peak in the density map. Six clusters were found to rotate. In this study, Hwang & Lee have also found that the rotating clusters are at dynamical equilibrium and have not undergone a recent merger.

Kalinkov et al. (2008) [43] in their study, they are trying to find the maximum gradient in the velocity field of Abell 2107 and they assume that the direction of the maximum linear correlation coefficient presents the major axis of the cluster. The minor axis would be its rotation axis. They use subsamples of cluster's galaxy-members, arranged by their projected distance from the cluster centre. Each subsample contains members of previous subsamples out to projected distance d. This cluster has been widely studied by Oegerle et al. (1992) [59] and already have been found indications of rotation. Generally, Materne et al. (1983) [53] have shown that is very difficult to distinguish a rotating cluster to two overlapping ones either because they merge or they depart from each other. Abell 2107 was found not to consist of two overlapping clusters, due to the one narrow peak in its velocity histogram. The most important indication of rotation is that the positional angle of the axis with the maximum gradient in the velocity field almost coincides with the positional angle of the axis with the larger elongation. However, there is the case that tidal effects would take place in the cluster from structures that are infalling in the cluster centre; nevertheless, those kind of structures were not detected. In the study, the rotation period has been calculated, $2.4 \cdot 10^9$ yrs and its corrected mass due to rotation has been computed, $2.8 \cdot 10^14 M_\odot$ (initial mass $3.21 \cdot 10^14 M_\odot$).

Hamden et al. (2010) [35] are measuring the tangential motion of clusters aiming to map the mean line-of-sight motion of a cluster and detect perspective rotation induced by the projection of the cluster's tangential motion into the line of sight. The most prominent signal would be detected in clusters with large angular extent, symmetric velocity distribution and large number of members. They use three different approaches: measure the line-of-sight motions of individual members, taking spectra of intracluster gas and mapping distortions of the CMB.

Bianconi et al. (2013) [11] study models where the intracluster medium rotates differentially in a massive galaxy cluster. The evaluate through X-ray brightness maps the isophote flattening due to the gas rotation. They constrain the rotational velocities using different rotation laws, rotation curves of clusters and ellipticity profiles of observed clusters.

Chluba & Mannheim (2002) [19] and Cooray & Chen (2002) [21] are studying the effect of the cluster rotation on the temperature and polarisation of CMB, the kinetic SZ effect (Sunyaev-Zeldovich effect). The main results of this effect is the shift of the position of the peak on the temperature fluctuation relative to the cluster centre and the tilt of the direction of the plane of linear polarisation. The SZE has three manifestations: the thermal SZE, due to inverse Compton scattering of the CMB photons off the hot intracluster medium, the kinetic SZE, due to the peculiar velocity of the cluster with respect to the rest frame of the CMB and the rotation-kinetic SZE, due to the rotation of the cluster. Chluba & Mannheim study the rotation-kinetic SZE and the fluctuation of the temperature and polarisation of the CMB. in order to measure the rotational properties of the clusters. They use multi-frequency data to measure the position of the peak of the temperature fluctuation. The relative change of the CMB radiation intensity due to the rotation-kinetic SZE is bipolar. The tilt of the polarisation plane is not frequency dependent and the rotation-kinetic SZE contribution is more severe in the Wien part of the CMB spectrum.

In the work of Fang et al. (2008) [30] hydrodynamical simulations were used to compute the rotation contribution in the non-thermal pressure of the intracluster gas. It was found that this contribution is comparable to the random turbulent motion's. However, the rotation motion is not big enough to be detected through the Doppler effect. The simulation results were compared to observed ellipticity profiles of clusters. In real clusters, the rotation velocities of galaxies in the inner region are much smaller that hose in simulations. In the outer region, the rotational velocities are larger in real clusters or the latter are more centrally concentrated.

2.2 Rotation identification

We will describe the details of two methods used in an attempt to quantify a rotation mode in clusters of galaxies. The first method is developed in this thesis, while the second one is based on Hwang & Lee (2007) [42].

2.2.1 Our method of rotation identification

We introduce a method of identifying the possible rotation of galaxies in galaxy clusters, which can measure the velocity amplitude of rotation and the angle of its rotation axis, projected on the plane of the sky, by using the individual galaxy-member velocities.

Let us assume a cluster of a certain mass containing a certain number of galaxies. Each galaxy has its own three dimensional velocity relatively to the cluster center, while only the line-of-sight velocity component can be measured through the redshift of the galaxy. The basic idea is to split the projected cluster galaxy angular distribution vertically in two semicircles, while galaxies are rotated consecutively by an angle θ according to the Euler transformations for two-dimensional rotation. Angle θ sets off from the horizontal axis and increases counterclockwise. The relative transformation equations of the galaxies are:

$$\begin{aligned} ra' &= ra \cdot \cos\theta - dec \cdot \sin\theta \\ dec' &= ra \cdot \sin\theta + dec \cdot \cos\theta \end{aligned} \tag{15}$$

where (ra, dec) are the original celestial coordinates of each galaxy and (ra', dec') are the new coordinates. A visual illustration of this is provided in figure 9.

Having now two distinct groups of galaxies (one for $dec' > 0$ and one for $dec' < 0$), we calculate the mean line-of-sight velocity of each one (v_{mean1}, v_{mean2}) and the difference between the two mean velocities $v_{dif} = v_{mean1} - v_{mean2}$. Consequently, we obtain the velocity difference v_{dif} as a function of the angle θ. We will use the graph of $v_{dif}(\theta)$, which we will call rotation diagram, as our primary indication for the presence or not of a rotation mode. Of course an interesting issue, which we address further below, is also related to the orientation of the rotational axis with respect to the line of sight.

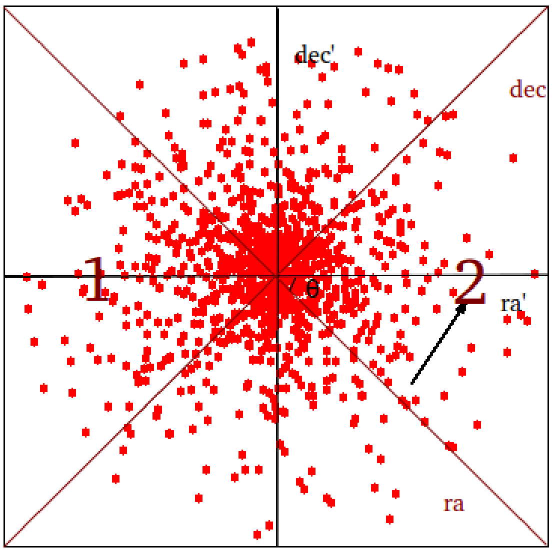

Figure 9: An illustration of our method. The galaxies with coordinates (ra, dec) are turned by angle θ and their new coordinates are (ra', dec'). The cluster is then split in two semicircles, 1 and 2.

For a rotating cluster, this diagram should show a periodic trend and the rotation axis would be at the angle θ of the maximum velocity difference v_{dif}. For example, assume a counterclockwise rotating cluster whose rotation axis is at $\theta = 90°$. We will start rotating the galaxy-members at angles between $0° - 180°$ with a step of $10°$. For $\theta = 0$, we will not observe any significant velocity difference; ideally, at the absence of noise, it would be zero ($v_{dif} = 0$). As θ increases, the velocity difference should increase until it reaches the maximum value at $\theta = 90°$. In this case, the galaxies in the right semicircle would seem to depart and the galaxies in the left semicircle would seem to approach us, with respect to the cluster center. The amplitude of the rotation signal will decrease as θ increases to $180°$ and increase again at $\theta = 270°$ until it approaches zero at $\theta = 360°$. In figure 10 we show the expected graph $v_{dif}(\theta)$ for an ideally rotating cluster with rotation amplitude 600 km/s and rotation axis at $\theta = 90°$. The ideal rotation in this case is achieved by attributing a constant rotational line-of-sight velocity to the galaxy members; the galaxies of the left semiphere (with respect to the vertical rotation axis) are attributed $v_{los} = -300$ km/s, while the galaxies of the right semisphere are attributed with $v_{los} = 300$ km/s.

If a non-rotating cluster has one or more subgroups that approach or depart with respect to the center, then, in the rotation diagram we will observe one or more peaks (or dumpings) in one of the semicircles at the corresponding angle θ of the peak (or dumping). There is a case where rotation and substructures cannot be easily distinguished: two subgroups of galaxies that move inside the cluster and whose line-of-sight velocity component happens to show a periodic signal. But this case is not likely to happen since it requires a fine tunning. In general, the expectations for a non-rotating cluster, with no infalling substructures, is expected to have a random rotation diagram (no systematic dependence of $v_{dif}(\theta)$ on θ) with small values of velocity difference.

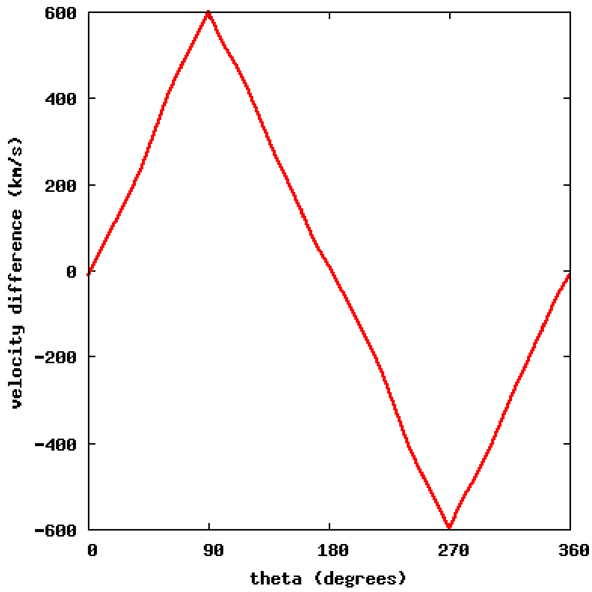

Figure 10: The ideal rotation signal of a clockwise rotating galaxy cluster with an amplitude $v_{dif} = 600 km/s$ (rotation axis at $\theta = 90°$).

2.2.2 The method of Hwang & Lee

Below we will compare our method with that of Hwang & Lee (2007) [42]. To this end we present the details of the latter method. Hwang & Lee use a sinusoidal relation to compute the angle of the rotation axis Θ_o and the rotational velocity v_{rot}:

$$v_p(\Theta) = v_{sys} + v_{rot} \cdot \sin(\Theta - \Theta_o) ,$$

where v_p is the observed radial velocity of each galaxy, v_{sys} is the peculiar velocity of the cluster and Θ is the projected on the plane of the sky position angle of each galaxy, setting off from North to East.

From now on we set $v_{sys} = 0$, because the recessional velocity of every galaxy is subtracted from the mean cluster velocity. As long as the velocities v_p are known (from the redshifts of the galaxies), we need to calculate the angle Θ of every galaxy, using its coordinates (ra, dec) (translated to the cluster rest-frame, ie., for a cluster center at $(0, 0)$).

	$dec > 0$	$dec < 0$
$ra > 0$	$\Theta = \arctan(ra/dec)$	$\Theta = \arctan(ra/dec) + 180^o$
$ra < 0$	$\Theta = \arctan(ra/dec)$	$\Theta = \arctan(ra/dec) + 180^o$

We then use a χ^2 minimization procedure to determine the correct values of Θ_o and v_{rot}. Namely, we use a grid of Θ_o and v_{rot} and calculate χ^2 for each pair:

$$\chi^2 = \sum_i \frac{(v_{p_i} - v_{los_i})^2}{\sigma_i^2} \tag{16}$$

where v_{los_i} is the line-of-sight velocity of every galaxy and σ_i its measurement error. For the purpose of these tests and since we use ideal velocities we set $\sigma_i = 1$.

2.3 Validation of our method

Before applying our method to real galaxy cluster data, we should validate and confirm that it can provide unambiguously an indication of rotation.

To this end, we construct, using the Monte-Carlo simulation method, a virialised cluster with a mass of $4 \times 10^{14} M_\odot$, radius $R_{cl} = 1$ Mpc, core radius $r_c = 0.1$ Mpc and having a King's profile density distribution

$$\rho(r) = \frac{\rho_0}{(1 + (r/r_c)^2\,)^{3/2}}\ , \tag{17}$$

where $\rho(r)$ is the density included within radius r and ρ_0 is the density in the center of the cluster. To estimate the value of ρ_0 we use the cluster mass M_{cl},

$$M(R_{cl}) = \frac{4}{3}\pi R^3 \rho(R) \Rightarrow M_{cl} = \frac{4}{3}\pi R^3 \frac{\rho_0}{(1 + (r/r_c)^2\,)^{3/2}}$$

from which we extract the $\rho_0 = 6.56036 \times 10^{-12}$ kg/km^3. Although it is known that the NFW (Navarro-Frenk-White [58]) profile is a more accurate representation of the dark matter and/or galaxy density profile of clusters of galaxies, while the King's profile is applicable mostly to the intracluster gas (cf. [44]), it is acceptable to use the latter for the purpose of testing our methodology. To construct the cluster using this galaxy distribution we follow the usual ″rejection method‟ (eg., see *Numerical Recipes in Fortran 77*, [73], pg. 281) procedure:

- Take random values (uniform distribution) between $-R_{cl}$ and R_{cl} for the coordinates (x, y, z) of each galaxy and find the distance r from the center of the cluster $(0, 0, 0)$. Turn down the mock galaxies that have $r > R_{cl}$.
- Find $\rho(r)$ from the King profile (equation (17)).
- For each selected ″mock‟ galaxy estimate the probability that it falls within the expectation of the King profile.
- Take a random value ρ_2 in the interval $(0, \rho_0)$. Reject the galaxies that have $\rho_2 > \rho$.

A realisation of one such Monte-Carlo cluster can be seen in figure 11.

Every galaxy is given a three dimensional velocity which could be: (a) one with a random orientation with respect to the cluster center of mass and an amplitude given by the Virial expectation, (b) a rotational velocity with amplitude being a fraction of the Virial expectation, or (c) the vectorial sum of both of them.

Another useful property of the cluster, which we will come across later, is the velocity dispersion v_σ. It is defined by the relation

$$v_\sigma^2 == \frac{1}{n-1}\sum_{i=1}^{n}(v_{los} - v_m)^2 \Rightarrow v_\sigma = \sqrt{\frac{1}{n-1}\sum_{i=1}^{n}(v_{los} - v_m)^2} \tag{18}$$

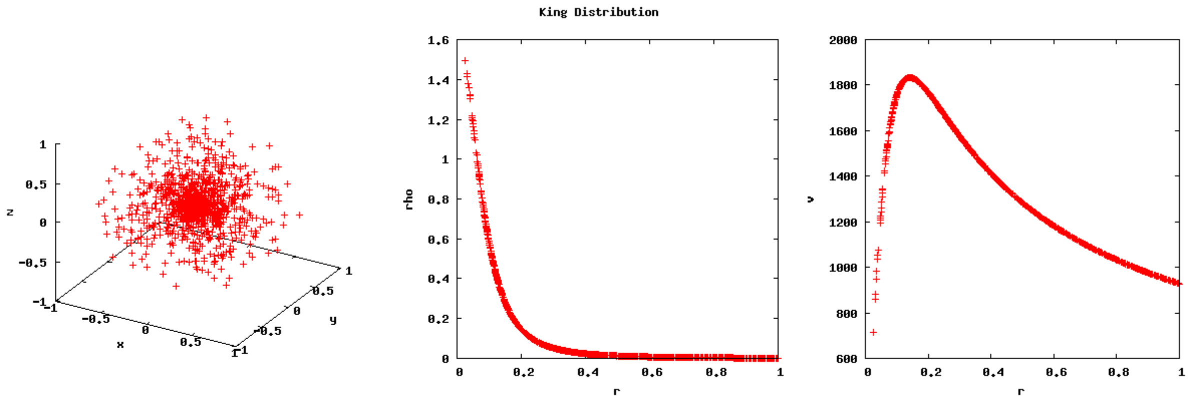

Figure 11: (a) The 3D cluster, (b) the density ρ as a function of the cluster-centric distance r, (c) velocity as a function of the distance r from the cluster center.

where n is the number of galaxy-members and v_m is the mean line-of-sight velocity of the cluster. Velocity dispersion is a way to express the level of mobility of the galaxies in the cluster and is related to the cluster gravitational potential via the Virial theorem.

2.3.1 Ideal 2D rotation

Initially, we will check our method in ideal conditions, ie., using a cluster with an ideal (projected on the plane of the sky) rotation of the galaxy members. Galaxies in one of the semicircles ($dec > 0$) are assigned a constant line-of-sight velocity of $v_{los} = -300$ km/s and in the other semicircle ($dec < 0$) are assigned $v_{los} = 300$ km/s. Therefore, the rotation amplitude of this configuration is 600 km/s. In order to investigate also sampling effects we produce the rotation diagrams for a cluster with 50 and 1000 galaxies, in figures 12 and 13 respectively, where we also check for different orientations of the rotation axis.

Our method (red lines in the figures) seem to recover sufficiently well both the expected rotation amplitude and the orientation of the rotation axis (corresponding to the peak of the $v_{dif}(\theta)$ diagram) for both cases (figures 12 and 13). For the high-sampling case (figure 13), the Hwang & Lee's method identifies the rotation axis accurately but not the rotation amplitude, which is found to be approximately 400 km/s instead of 600 km/s; i.e., it recovers only $\sim 2/3$ of the input one. The same is true for the low sampling case (figure 12), but there is also a deviation of the recovered rotation axis angle with respect to the input one. Observing the results of these two cases we can conclude, as anticipated, that the richer the cluster the easier the rotation signal can be identified and the more accurately the rotation properties can be estimated.

It is interesting to note that based on the rotation diagrams we can deduce the clockwise or anti-clockwise nature of the rotation, from the quadrant of the angle θ of the maximum velocity difference. If the angle θ is in the first or third quadrant ($0 \leq \theta < 90$ or $180 \leq \theta < 270$), the rotation is clockwise; otherwise ($90 \leq \theta < 180$ or $270 \leq \theta < 360$), the rotation is counterclockwise.

2.3.2 A more realistic rotation in 3D

To have a more realistic rotation profile of the cluster, we assign to each galaxy a random orientation (virial in amplitude) velocity and, in addition, a rotation velocity as a percentage of the virial one. From the components v_x, v_y, v_z of the overall velocity of a galaxy, v (figure 14), we calculate the line-of-sight velocity of each galaxy from the relation:

$$v_{los} = v_x \cdot \cos\phi + v_z \cdot \cos(90^\circ - \phi)$$

where ϕ is the vertical angle between the line of sight and axis x. For $\phi = 0$, the line of sight coincides with the x-axis; as angle ϕ increases, we take into account in the line-of-sight velocity also the z-component of the velocity. For $\phi = 90^\circ$, the line of sight coincides with the z-axis (figure 14).

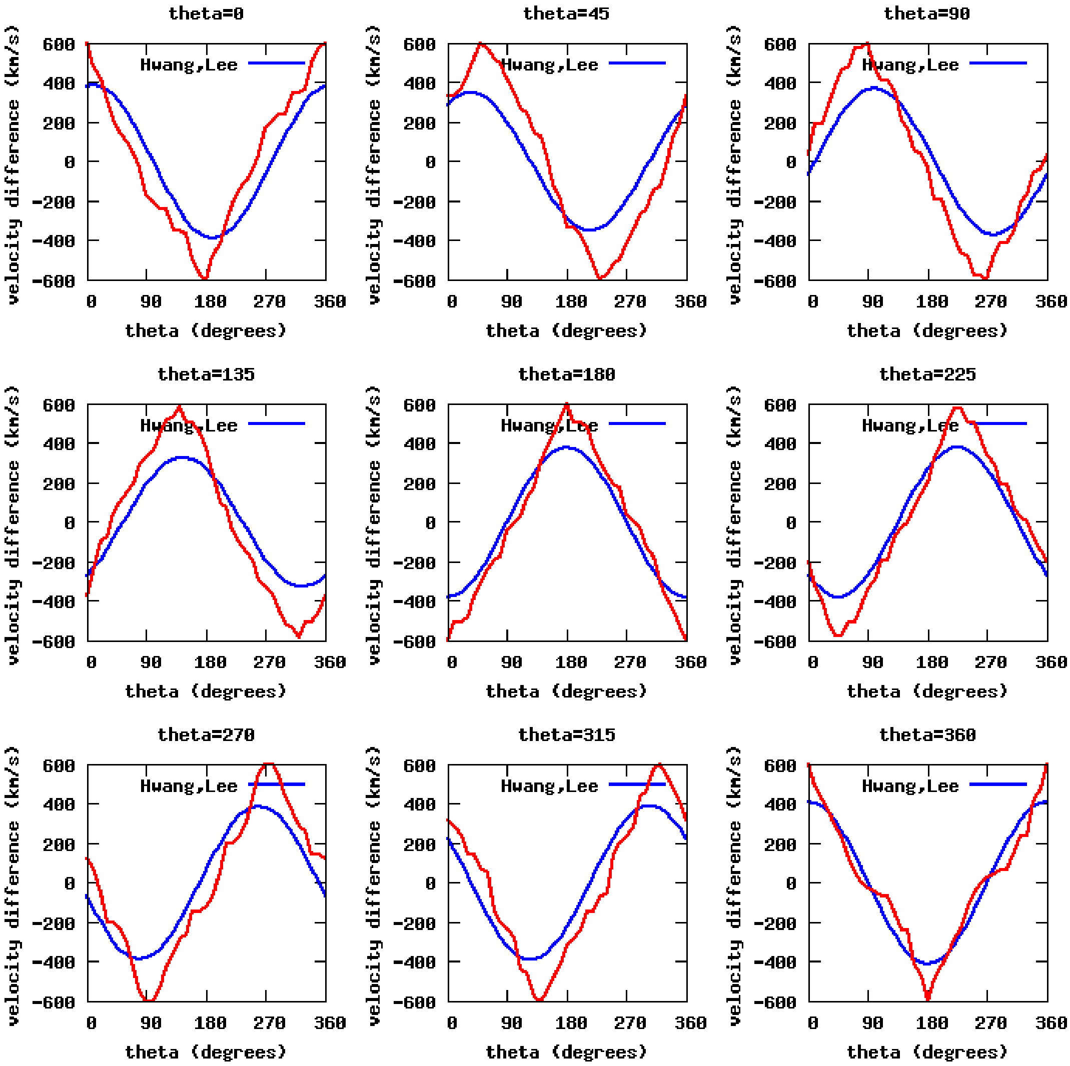

Figure 12: The results of our method (red lines) and of the Hwang & Lee's method (blue lines) for a cluster with 50 galaxies with θ the angle of the rotation axis setting off from the horizontal axis and increasing counterclockwise.

Assuming that the cluster is dynamically relaxed (virialised) we can estimate the amplitude of the expected 3-dimensional velocity, v_k, of each galaxy from (13), which depends on its distance from the cluster center of mass:

$$v_k^2 = \frac{1}{2}\frac{GM(r)}{r} \Rightarrow$$
$$v_k(r) = \sqrt{\frac{1}{2}\frac{GM(r)}{r}} = \sqrt{\frac{2}{3}\frac{G\pi\rho_0 r^2}{(1+(\frac{r}{r_c})^2)^{3/2}}}\,, \tag{19}$$

where $M(r)$ is the mass within a sphere of radius r. Each component $v_{k_x}, v_{k_y}, v_{k_z}$ of the virial velocity $v_k(r)$ is randomly orientated[2] such that it satisfies the relation (19).

The amplitude of the rotational velocity is set as a percentage of the virial velocity, while its counter-

[2]We use the *ran1* random number generator from the Numerical Recipes in Fortran 77, [73], pg. 271.

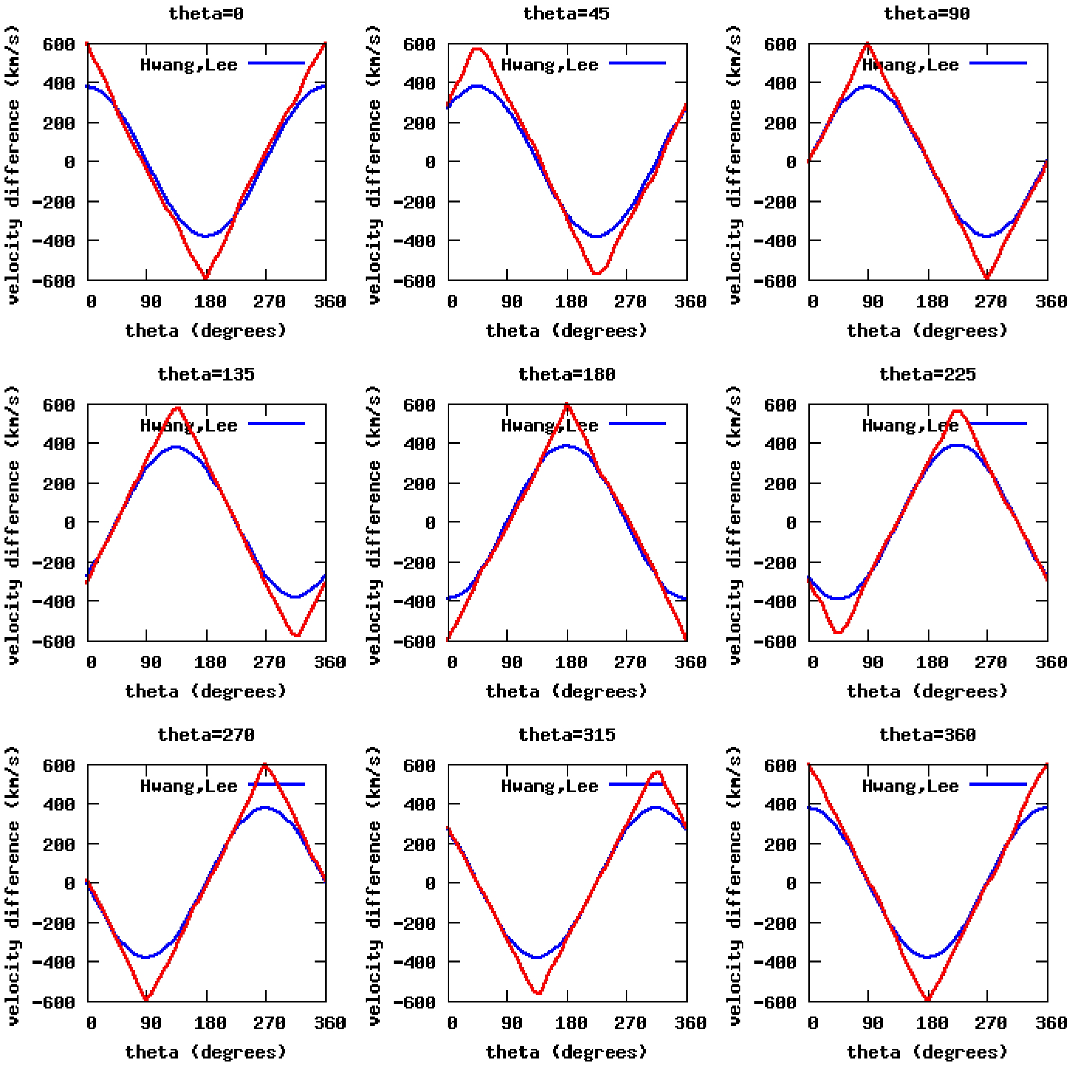

Figure 13: As in figure 12 but for a cluster with 1000 galaxy-members.

clockwise direction is set by the velocity components $v_{rot_x}, v_{rot_y}, v_{rot_z}$, which emerge from the relations

$$\vec{v_{rot}} \cdot \vec{r} = 0$$
$$v_{rot}^2 = v_{rot_y}^2 + v_{rot_x}^2$$

The first relation comes from the fact that the coordinate vector $\vec{r}$ is perpendicular to the rotation velocity vector $\vec{v_{rot}}$. The second one comes from the analysis of the $\vec{v_{rot}}$ in its coordinates. The z-component of the velocity is set 0, in order the rotational velocities to be perpendicular to the rotation axis z. Consequently, we obtain the following relations for the components $v_{rot_x}, v_{rot_y}, v_{rot_z}$:

$$v_{rot_z} = 0$$

	$y > 0$	$y < 0$
$x > 0$	$v_{rot_y} = \left(x^2 v_{rot}^2/(x^2+y^2)\right)^{1/2}$	$v_{rot_y} = \left(x^2 v_{rot}^2/(x^2+y^2)\right)^{1/2}$
$x < 0$	$v_{rot_y} = -\left(x^2 v_{rot}^2/(x^2+y^2)\right)^{1/2}$	$v_{rot_y} = -\left(x^2 v_{rot}^2/(x^2+y^2)\right)^{1/2}$

$$v_{rot_x} = -\frac{y}{x} v_{rot_y}$$

We now wish to investigate the effect of different orientations of the 3-dimensional rotational axis with respect to the line-of-sight. To this end, we set the rotation axis at angle $\theta = 90°$ from the horizontal

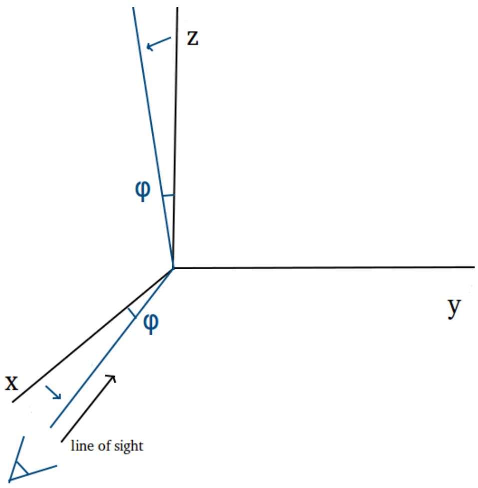

Figure 14: The triaxial coordinate system and the line of sight direction (blue line). Y axis remains intact.

axis. We will turn the rotation axis with respect to the vertical position, so that it forms an angle ϕ with the line of sight in the interval $(0°, 90°)$ until it is aligned with the line of sight. Firstly, we will apply this procedure to a cluster with 1000 galaxies of which the rotational velocity is 30% of the corresponding virial velocity v_p (but no virial velocities are assigned). The results for different values of the orientation of the rotation axis with respect to the line-of-sight are shown in figure 15. From equation (19), we have that the 3D rotation amplitude is ~ 600 km/s.

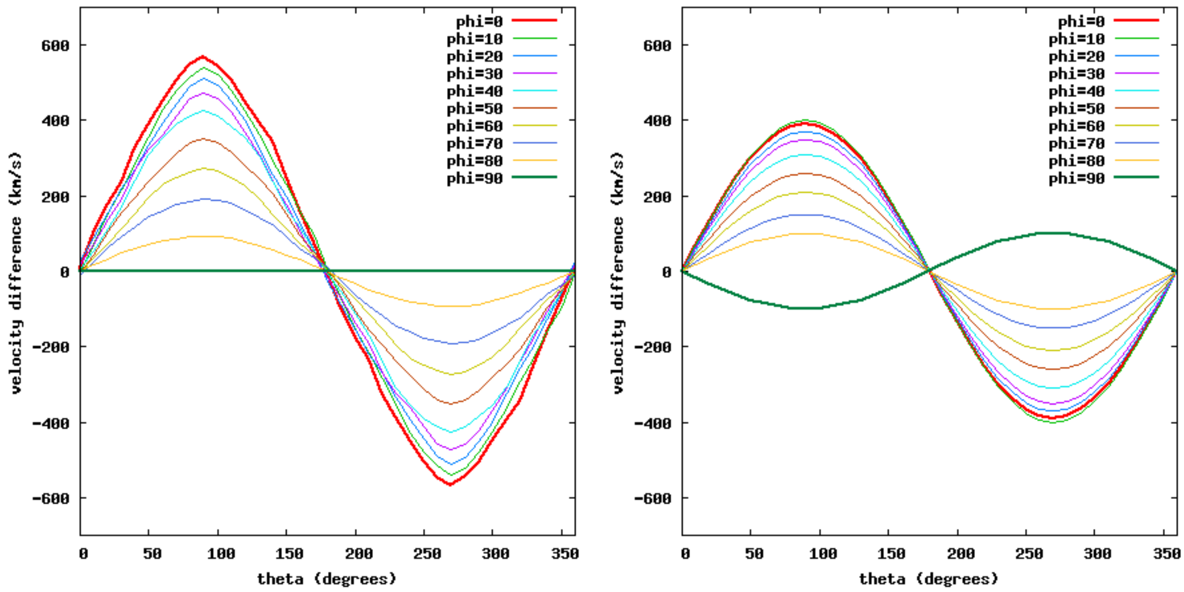

Figure 15: The rotation diagram for a cluster with a 3D rotational velocity of 600km/s as the rotation axis shifts from perpendicular to parallel to the line of sight ($\phi = 0° - 90°$). *Left Panel:* Results based on our method. *Right Panel:* Results based on Hwang & Lee's method.

As we expect, the rotation signal becomes weaker (the rotation amplitude decreases) as the angle ϕ increases. The counterclockwise direction of rotation is apparent in figure 15 from the occurrence of the peak in 90°. For $\phi = 90°$, rotation cannot be identified, as the rotation component of the velocity of the galaxies is perpendicular to the line of sight and thus it cannot be observed. Our method gives a flat rotation diagram in this case, as it should, while the Hwang & Lee's method gives a ″fake‟ signal showing a rotation axis at $\theta = 270°$. Their method appears again, as in the ideal 2D case presented previously, to have problems in recovering the correct input rotation amplitude for any value of ϕ.

We will now repeat the same test, using a cluster with 1000 galaxies, but having both a virial and a rotational velocity component. The latter are set to 30% of the former one. The results are shown in figure 16.

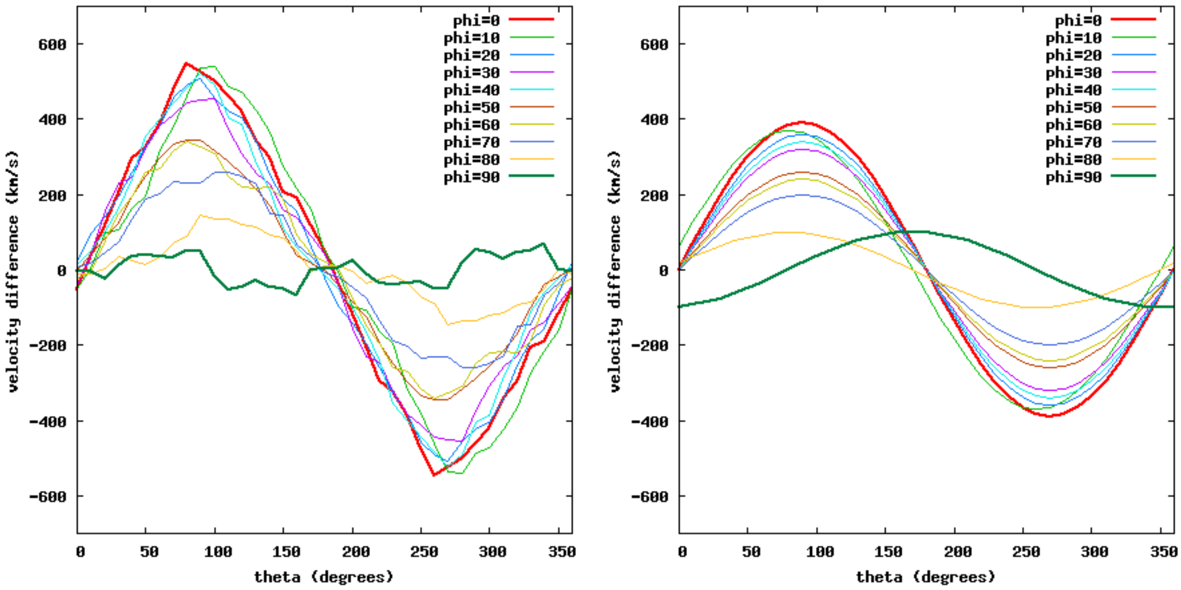

Figure 16: Similar rotation diagram as in figure 15 but now for a cluster with a more realistic 3D velocity, composed of a random oriented virial component and a rotational component, being $\sim 30\%$ of the former.

As expected the rotation signal decreases as a function of increasing ϕ. Furthermore, the accuracy of the recovered rotation axis angle is fairly good (it decreases slightly with increasing of ϕ). When the rotation axis and the line of sight are aligned, our method gives a noisy rotation diagram, indication of no rotation, as indeed expected due to the orientation of the cluster, but again the Hwang & Lee's method has the same problems as discussed in the previous case (fake rotation signal at $\phi = 90°$ and underestimation of the rotation amplitude at lower-ϕ's).

As a next step, we are testing the effect on the rotation signal of the rotational center, not coinciding with the cluster center, but being in a small distance from it, for reasons that may have to do with a recent merging effect, for example. We use the same simulated cluster with 1000 galaxies, which have virial velocity and rotational velocity (the 30% of the virial one). We study nine different rotational centers, whose one or both coordinates are 0.1 Mpc distant from the cluster center; we rotate the galaxy-members around the new rotational center. We compare those signals to the signal from the real rotational center, which is (0,0) - the cluster center. We also show the results of Hwang & Lee (figure 17).

The rotation signal appears to have only small variations in the rotation amplitude and rotation axis for the different rotational centers near the real rotational center (0,0). This result is also valid for the Hwang & Lee's method.

2.3.3 A more realistic rotation in 2D

We return now to investigate systematics related to the identification of rotation on the plane of the sky. We therefore keep the rotation axis perpendicular to the line of sight ($\phi = 0$) and rotate it at different angles θ, on the plane of the sky, as we did for the ideal 2D rotation in the previous section. The galaxies will be assigned with virial and rotational velocities (30% of the former). To study sampling effects we will again use two cases; a cluster with 1000 (figure 18) and a cluster with a 50 galaxies (figure 19).

Black lines correspond to the input rotation signal and as we can see in figure 18, both methods recover well the orientation of the rotational axis, while only our method manages to recover fully the amplitude of the rotational velocity (as seen also in the previous tests). However, as can be seen in figure 19 both

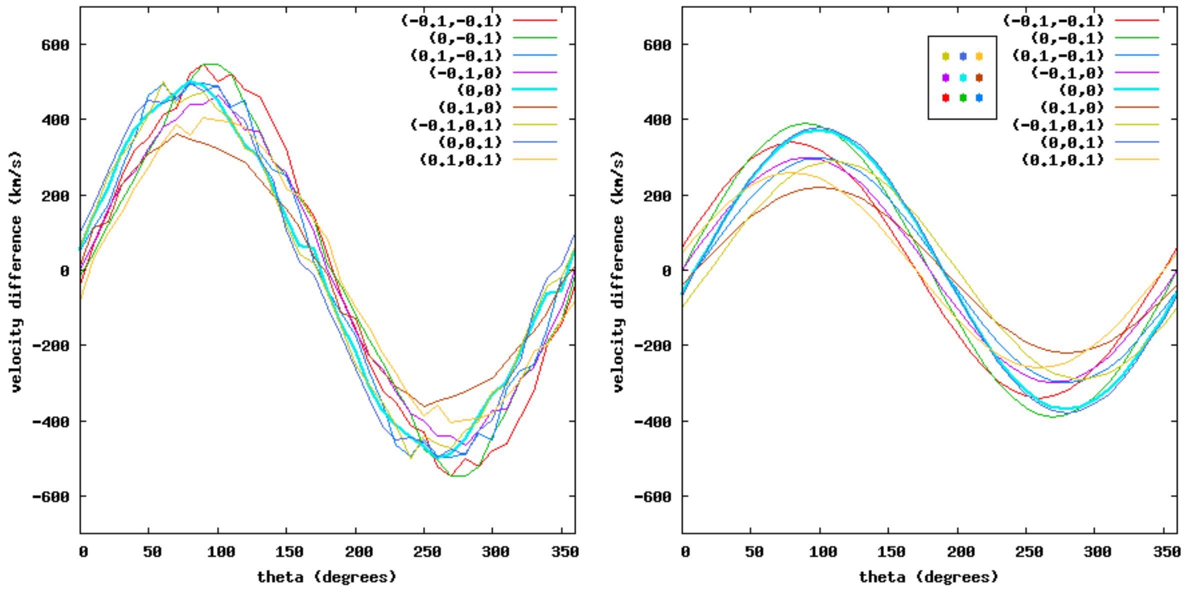

Figure 17: The rotation diagram for a cluster with a 3D rotational velocity of 600km/s for nine different rotational center candidates. The real rotational center is the (0,0). *Left Panel:* Results based on our method. *Right Panel:* Results based on Hwang & Lee's method.

methods have difficulties in determining accurately the rotation amplitude and the orientation angle of the axis for the case of a cluster with only 50 members. There is considerable noise in the rotation signal in our method due to sampling effects and the dominance of the virial, with respect to the rotational, velocity of galaxies. We can see cases ($\theta = 90°, \theta = 270°$) where the recovery is satisfactory, and cases ($\theta = 135°$, $\theta = 225°$) where it is not. Therefore, sampling effects are important and using clusters with a small number of galaxy redshifts should be avoided.

A next test for systematics is to to simulate 50 Monte Carlo clusters, all with the same statistical properties but of which the rotational velocity is an increasing fraction of the virial one ($0\% - 100\%$), keeping the rotation axis set to $\theta = 45°$. We are going to calculate the mean and standard deviation of the recovered rotation amplitudes and angles of rotation axis, in order to find the range for a successful application of our method. In order to investigate further also the sampling issue discussed earlier, we simulate 4 sets of clusters containing $N_g = 1000$, 50, 30 and 10 galaxies for each case, respectively, and apply the above procedure for all sets.

In figures 20, 21, 22 and 23 we present the mean and standard deviation of the recovered rotation amplitudes (left panels) and of the recovered rotation axis angle (right panels) as a function of the ratio v_{rot}/v_{virial}, where $v_{virial} \simeq 1800$ km/s. In the ideal case of very good sampling (figure 20), we see that our method correctly recovers the rotation amplitude with negligible uncertainty except for the case of no rotational velocity (0% of virial), while the already identified problem of the Hwang & Lee's method, that of underestimating the rotation amplitude, is shown here as well to be independent of v_{rot}/v_{virial}. Generally, we observe that in all different N_g cases our method recovers more accurately the rotational velocity amplitude for $v_{rot}/v_{virial} > 0.2$, while the Hwang & Lee's method performs slightly better in recovering, on average, the correct angle of orientation axis (especially for the low sampling cases; $N_g = 30, 10$). In the lower sampling cases ($N_g = 30, 10$) the uncertainties are very large and recovery of the underlying rotation mode extremely inaccurate.

A general result from this analysis is that one may not expect to recover the characteristics of an existing rotation mode if the amplitude of the rotation is less than $\sim 10\% - 20\%$ of the virial velocity and the sampling of the cluster members is low (less than ~ 30 galaxies/cluster).

As a final test for systematics, we are simulating 1000 Monte-Carlo clusters, with a small number of galaxy-members (20 in this case) and with no rotational velocities, only virial ones. The aim is to compute the fraction of clusters that will be found to rotate, while this rotation signal would be false. As we analyse in forthcoming sections, 2.4.4 and 2.6.1, we use two different groups of indications of rotation;

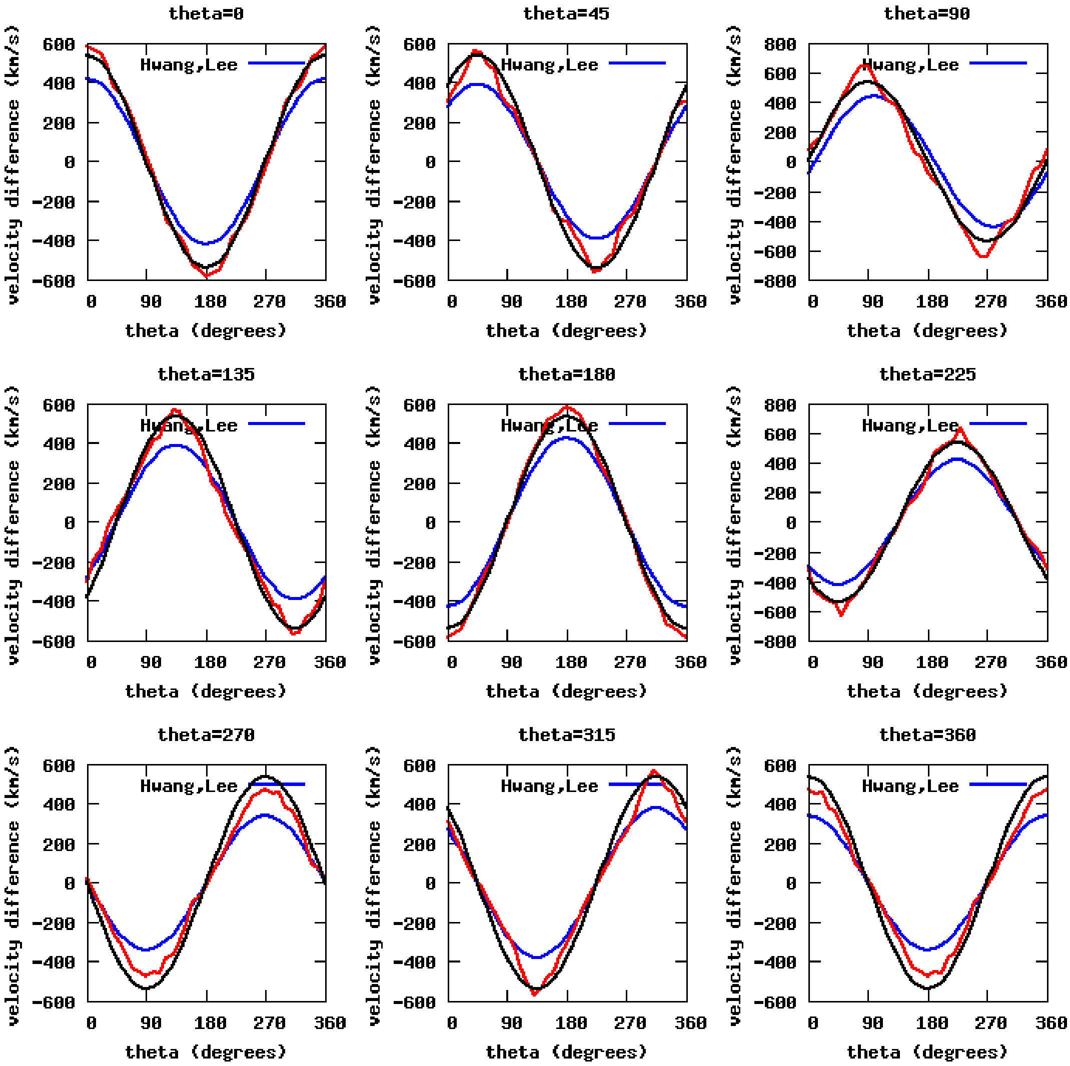

Figure 18: The results of our method (red lines) and of Hwang & Lee's method (blue lines) for a cluster with 1000 galaxies. The angle θ of the cluster rotation axis sets off from the horizontal axis increasing counterclockwise. Black lines is the expected signal for a cluster with ideal rotation of the same amplitude (no virial velocities).

the former one indicates that the cluster is rotating ($prob_{KS} < 0.01$, $\chi^2_{id} \lesssim 1$, $\chi^2_r > 1$ and $\chi^2_{id}/\chi^2_r \ll 1$) and the latter indicates a possible rotating clusters ($prob_{KS} < 0.08$, $\chi^2_{id} \lesssim 1$, $\chi^2_r > 1$ or $prob_{KS} < 0.08$, $\chi^2_{id} \lesssim 1$, $\chi^2_r < 1$,$\chi^2_{id}/\chi^2_r < 0.25$). To this end, we have found that 51 out of 1000 clusters were found to be rotating clusters (5.1% of the sample) and 110 out of the 1000 were found to be possibly rotating clusters (11%, the former clusters are included in this value). Those fractions are small enough to let us conclude that the rotation signal of ever a poor cluster is not likely to be fake, but real, even if this signal is weak.

2.4 Observational data

2.4.1 Data acquisition

We have selected a random subsample of the Abell clusters (cf. [1]) with $z \lesssim 0.1$ so that it covers relatively homogeneously all five Bautz-Morgan morphology types. The clusters in our sample are shown in the table 1. The cluster data (redshift, right ascension, declination) are from the NASA-NED database (ned.ipac.caltech.edu).

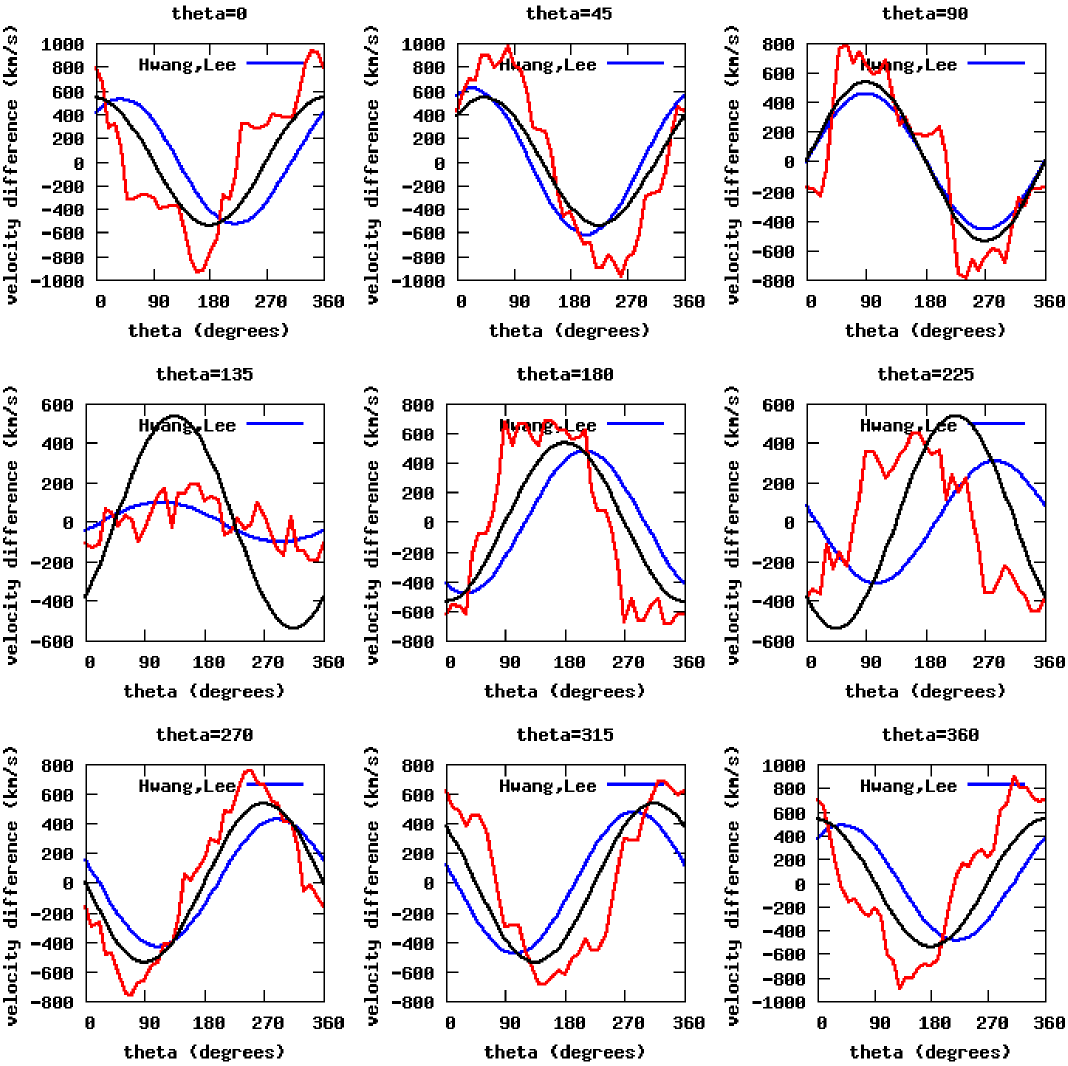

Figure 19: As in figure 18 but for a cluster with 50 galaxy-members.

In order to acquire the galaxy-members of each cluster from the SDSS spectroscopic database (Sloan Digital Sky Survey, skyserver.sdss3.org/dr9), we compute the limits of an equal-area rectangular region that has a diameter equal to 2.5 h^{-1}Mpc on rest frame. For that reason, we calculate the angular diameter distance d_θ for each cluster (in Mpcs) taken from (11) with the Hubble function $H(z)$ taken from (6). The angular diameter θ of a linear distance 2.5 Mpcs from the center of the cluster (column 5 of table 1), using its angular diameter distance, is

$$\sin\theta = \frac{2.5}{d_\theta} \Rightarrow \theta = \arcsin\left(\frac{2.5}{d_\theta}\right)$$

Initially, we need to equal-area rectangular region centered on the center of every cluster. The equal area will be achieved by projecting the region $(-ra, ra), (-dec, dec)$ of the celestial sphere in a plane which crosses the cluster center. This is because of the curvature of the celestial sphere, and the effect increases as the declination moves away from the equator. The projected region will have boundaries

upper limit	*lower limit*
$ra_c - \theta\cos(dec_c)$	$ra_c + \theta\cos(dec_c)$
$dec_c - \theta$	$dec_c + \theta$

where (ra_c, dec_c) are the equatorial coordinates of the center. After computing the boundaries of this rectangular region, we extract the SDSS galaxy-data of the above region for every cluster.

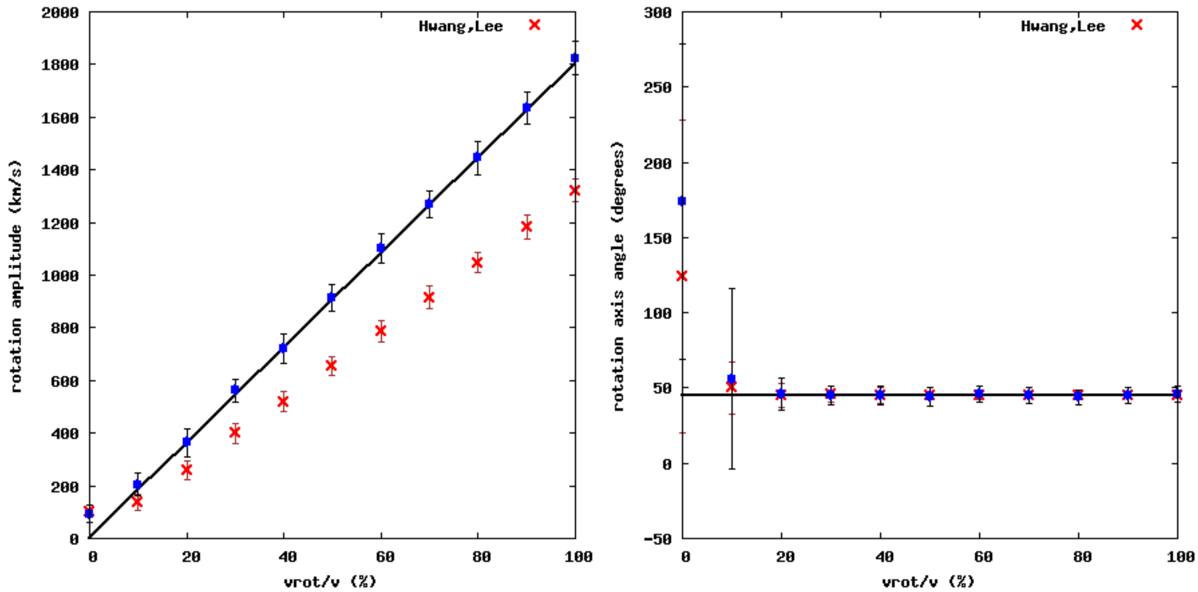

Figure 20: Case with $N_g = 1000$ with blue and red symbols representing results of our and Hwang & Lee's method, respectively. *Left Panel:* Recovered rotation amplitudes as a function of v_{rot}/v_{virial}. The black line indicates the input rotation amplitude. *Right Panel:* Recovered rotation axis angle as a function of the ratio v_{rot}/v_{virial}. The black line indicates the actual angle of the rotation axis.

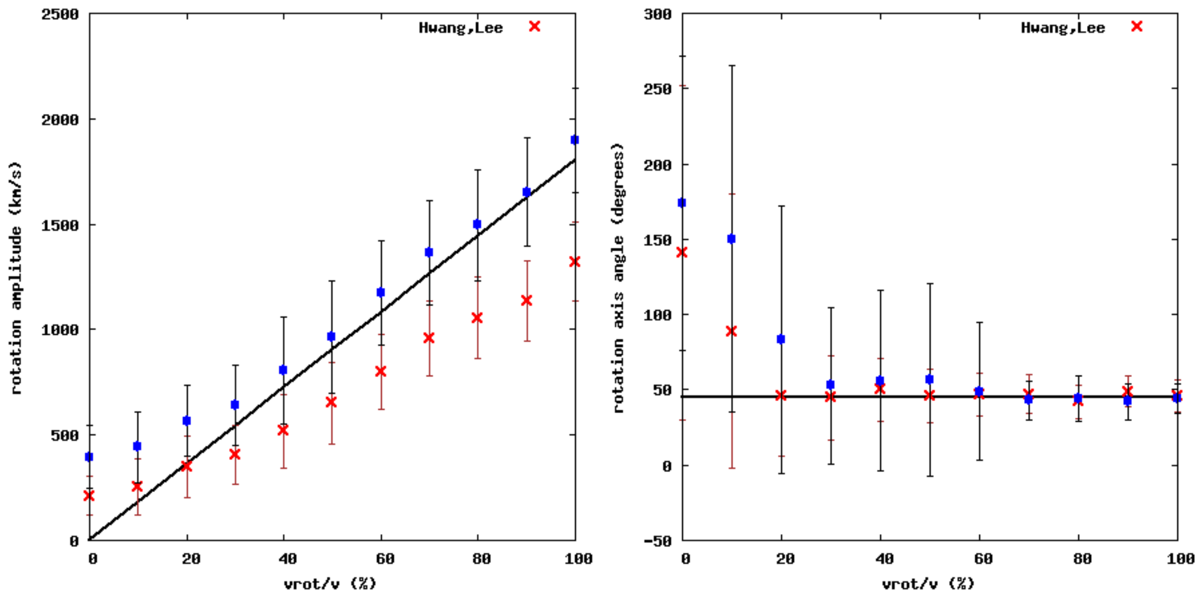

Figure 21: Same as in figure 20 but for $N_g = 50$.

The SDSS data consist of objects that are found in the square region we requested, but spanning any redshift. For every object there is information for the redshift z, its right ascension and declination, the apparent magnitude in five bands (we download only the r-band) and other information that we are not concerned with. Firstly, we will keep the objects that are declared as galaxies, with measured redshift, that is in a range of ± 0.01 of the central redshift of each cluster (known from NASA NED); this means we assume that galaxies in the cluster will have a maximum velocity of 3000 km/s relatively to the center, which is a fact only in a few extreme cases.

The rotation analysis is then performed using galaxies within a circular region around the center with a certain radius (1.5 or 2.5 Mpc). The angular distance θ_{gal} of every galaxy from the cluster center is

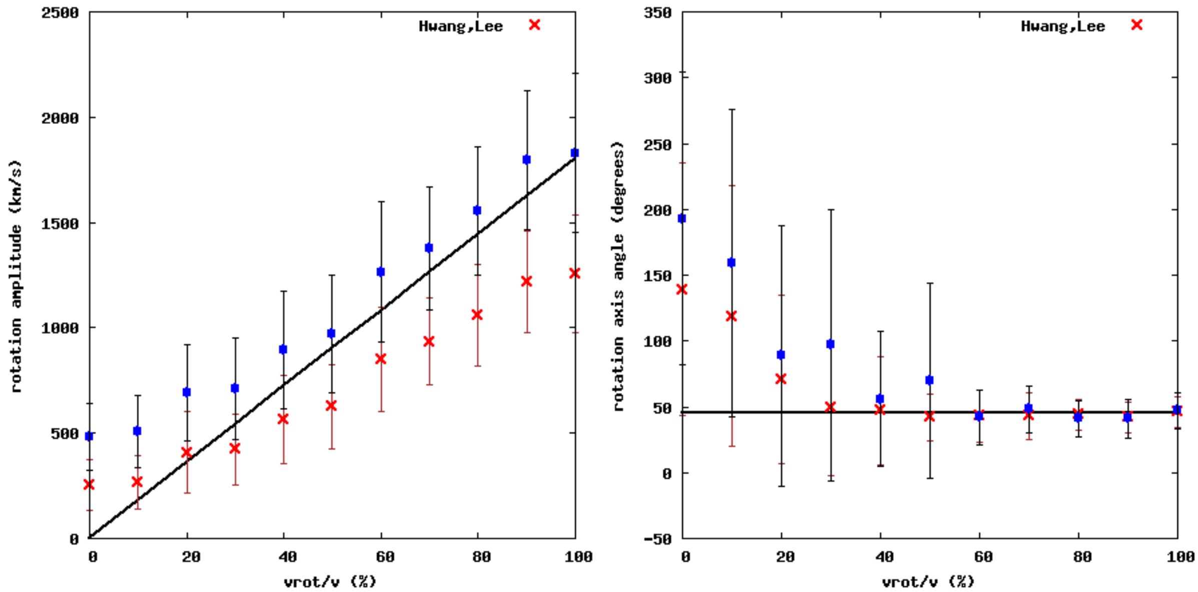

Figure 22: Same as in figure 20 but for $N_g = 30$.

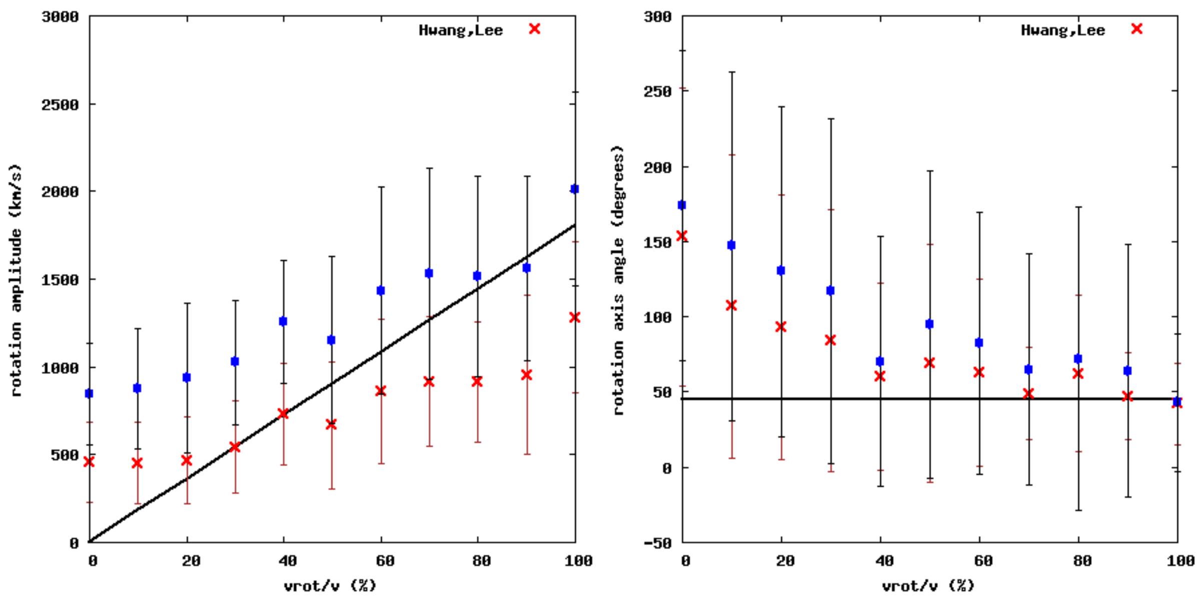

Figure 23: Same as in figure 20 but for $N_g = 10$.

estimated by the cosine law of the spherical triangle galaxy-cluster-earth's pole:

$$\cos\theta_{gal} = \cos(90^o - dec)\cdot\cos(90^o - dec_c) + \sin(90^o - dec)\cdot\sin(90^o - dec_c)\cdot\cos(ra - ra_c)$$

where (ra, dec) are the equatorial coordinates of the galaxy and (ra_c, dec_c) are the equatorial coordinates of the cluster center. The linear distance r of the galaxy from the center is calculated using the triangle that is formed by the cluster center, the galaxy and the observer, and is

$$r = d_\theta \cdot \sin\theta_{gal}$$

where d_θ is the angular diameter distance of the cluster. In this way, every galaxy with $r > 1.5$ Mpc or $r > 2.5$ Mpc will be rejected from being considered a cluster member.

We are studying circular areas as well as circular rings of the cluster. We want to find out whether the cluster's rotation comes from the outer parts or from the inner parts. If the virialised clusters seem

Cluster name	Redshift z	ra (deg)	dec (deg)	Ang. diam. (deg)
A85	0.055061	10.4075	-9.3	0.62381
A168	0.045000	18.7908	0.2	0.75419
A279	0.079700	29.0929	1.1	0.44366
A646	0.129200	125.5400	47.1	0.28974
A671	0.050200	127.1221	30.4	0.68027
A690	0.078800	129.8092	28.8	0.44825
A734	0.071900	135.1613	16.3	0.48731
A957	0.043600	153.4888	-0.9	0.77711
A971	0.092900	154.9446	41.0	0.38652
A1027	0.069001	157.7354	53.4	0.50606
A1177	0.031600	167.3654	21.7	1.05688
A1213	0.046900	169.1213	29.3	0.72528
A1291	0.052700	173.0413	56.0	0.64993
A1468	0.084400	181.4088	51.4	0.42126
A1516	0.076900	184.7388	5.2	0.45831
A1569	0.073500	189.0779	16.6	0.47760
A1650	0.083838	194.6925	-1.8	0.42380
A1656	0.023100	194.9529	28.0	1.43106
A1738	0.115400	201.2967	0.2	0.31932
A1775	0.071700	205.4817	26.4	0.48855
A1795	0.062476	207.2521	26.6	0.55462
A1800	0.075500	207.4225	28.1	0.46604
A1913	0.052800	216.7158	16.7	0.64878
A1983	0.043600	223.1833	16.7	0.77711
A1991	0.058700	223.6258	18.6	0.58767
A2029	0.077280	227.7333	5.7	0.45626
A2079	0.068984	232.0196	28.9	0.50617
A2089	0.073130	233.1721	28.0	0.47981
A2107	0.041148	234.9125	21.8	0.82100
A2124	0.065625	236.2471	36.1	0.52998
A2147	0.035000	240.5717	15.9	0.95812
A2199	0.030151	247.1604	39.6	1.10575
A2244	0.096800	255.6833	34.0	0.37262
A2255	0.080600	258.1292	64.1	0.43916
A2356	0.116100	323.9429	0.1	0.31765
A2428	0.085100	334.0613	-9.4	0.41813
A2593	0.041300	351.1292	14.6	0.81813
A2670	0.076186	358.5571	-10.4	0.46221

Table 1: The clusters we have studied. The first column is the Abell name of the cluster, the second is its redshift, the third is its right ascension of the center in degrees, the fourth is the declination of the center in degrees and the fifth is the angular diameter of 2.5 Mpc in the redshift of the cluster in degrees. All these data are taken from NASA-NED.

to be the most usual rotating clusters, due to an initial acquired angular momentum, then the extraction of the inner area in our rotation study will cause the rotation signal to weaken. On the other hand, if the rotation in clusters is caused by mergers, then we would expect that the outer parts of the cluster would have a more prominent rotation velocity distribution and the extraction of the inner cluster-members from the study would cause the rotation signal to strengthen. As a result, there are cases where we want to study the probable rotation in circular annuli, excluding the central regions where projections along the line-of-sight are more severe. Furthermore, we wish to also study the outskirt regions of the clusters. Consequently, we will investigate the cluster rotation for each cluster using four different angular configurations (there are some cases where an additional configuration is used, as explained in each case):

1. the circular area within 1.5 Mpc radius
2. the circular ring with inner boundary 0.3 Mpc and outer boundary 1.5 Mpc
3. the circular area within 2.5 Mpc radius
4. the circular ring with inner boundary 0.5 Mpc and outer boundary 2.5 Mpc

Before we apply our rotation algorithm we wish to clear our galaxy members of possible outliers, which could affect our results. To this end we plot the relative to the cluster-center galaxy velocity frequency distribution for each cluster, which has a mean value of 0. We expect that a virialised cluster should have roughly a Gaussian frequency distribution. Therefore a Gaussian is fitted to the data using the usual χ^2 minimization procedure and then all galaxies that have velocities $> 3\sigma$ away from the mean are rejected. This procedure is repeated iteratively until no galaxies are rejected.

2.4.2 Cluster richness

In order to determine the cluster richness, we will calculate the number of bright galaxies of each cluster, using the Schechter luminosity function mentioned in the introduction. We use the $\Phi(M)$ form, with M^* taken from Montero-Dorta & Prada (2008) [56],

$$M^* - 5\log h = -20.73 \pm 0.04$$

for the SDSS galaxies in the r band. The corresponding magnitude m^* is calculated by equation (12), but with an additional evolutionary correction component

$$m^* - M^* = 5\log d_L + 25 + K(z) + EC(z)$$

The values of K-correction as well as the evolutionary correction we enter is taken from Poggianti (1996) [71] for the r band. Galaxies with magnitude smaller than m^* are the bright ones for each cluster. The number of bright galaxies compared with the overall number of galaxies stands for the cluster richness.

2.4.3 Choosing the correct rotational center

The clusters are now ready to be studied with our method, which we discussed in section 2.2.1. Instead of using the (ra, dec) coordinates of the galaxies, we use the equal-area projection of the galaxy distribution:

$$y \Rightarrow ra \cdot \cos(dec_c)$$
$$x \Rightarrow dec$$

We also use the line-of-sight velocities of the galaxies, which are calculated from their redshift z using the relation

$$v_{los} = c \cdot x$$

Generally, the center of mass of the cluster, which we have used in all the above procedures (taken from NASA-NED), is not necessarily the rotational center of the cluster. For that reason, we apply our method of rotation identification to the cluster using 9 different possible rotational centers, which form a rectangle whose center is the center of mass of the cluster. In figure 24 this configuration is shown. The distances (dy, dx) are calculated for every cluster from the relations:

$$dy = 20\% \cdot cluster\ radius \cdot \cos(dec_c)$$
$$dx = 10\% \cdot cluster\ radius$$

where dec_c is the declination of the cluster center and cluster radius is 1.5 or 2.5 Mpc. Thus, the rotation algorithm is applied 9 times for each cluster, using the equations (15), in the form

$$y' = y \cdot \cos\theta - x \cdot \sin\theta$$
$$x' = y \cdot \sin\theta + x \cdot \cos\theta$$

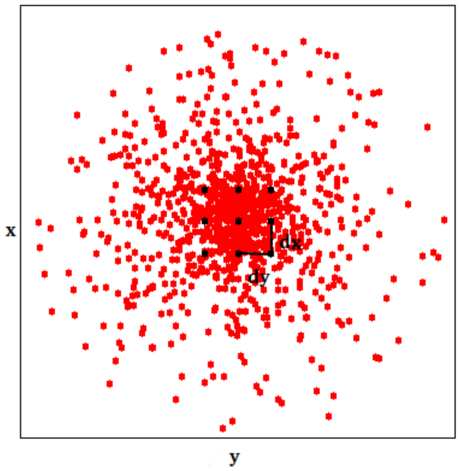

Figure 24: The formation of the different rotational centers (black dots) that we study for each cluster. dy,dx are the sides of the small rectangles (in this case dy=dx).

The line that splits the cluster in two semicircles is $x' = 0$. But how do we identify the "correct" rotational center?

In order to decide which is the rotational center of the cluster, we use as our basic criteria the smoothest of the sinusoidal curve, which should represent better the ideal rotation with the maximum amplitude observed in the data-curve. The latter, which we call ideal rotation diagram, is introduced by the following procedure:

For every rotational center, we find the angle θ where the maximum rotational velocity v_{max} is observed in the rotation diagram. This angle splits the cluster in two semispheres; we attach to each galaxy of the first semisphere a velocity $v_{los} = v_{max}/2$ and to each galaxy of the second semisphere a velocity $v_{los} = -v_{max}/2$. We now repeat our algorithm of rotation identification using those ideal line-of-sight velocities for the galaxies of the cluster and create the ideal rotation diagram. The next step is to conduct a statistical test (χ^2 minimization) to compute the real, v_i, and ideal, v_{id_i}, rotation curves and quantify their difference. We use relation (16), which now is,

$$\chi^2 = \sum_i \frac{(v_i - v_{id_i})^2}{\sigma_i^2} \tag{20}$$

where the error σ_i^2 is given by

$$\sigma_i^2 = \sigma_{v_i}^2 + \sigma_{v_{id_i}}^2$$

σ_{v_i} is the error of computing the rotational velocity of the data

$$\sigma_{v_i} = \sqrt{\left(\frac{v_{disp_{1_i}}}{\sqrt{n_{1_i}}}\right)^2 + \left(\frac{v_{disp_{2_i}}}{\sqrt{n_{2_i}}}\right)^2}$$

where $v_{disp_{1_i}}$ and $v_{disp_{2_i}}$ are the velocity dispersions of the galaxies in semicircles 1 and 2 respectively and n_{1_i} and n_{2_i} are the number of galaxies in semicircles 1 and 2 respectively, each time they are rotated by angle θ. The velocity dispersions are found using the equation (18). $\sigma_{v_{id_i}}$ is the error of computing the ideal rotational velocity of the data and is calculated using exactly the same relations, only this time the galaxies are attributed with the ideal rotational velocities. The center whose difference χ^2 has the smaller value (smaller difference between the curves) is the one we identify as the rotation center.

2.4.4 Rotation identification

After having chosen the "best" rotational center, it is time to make a decision whether a cluster is rotating or not. We will combine several tests in order to draw the safest conclusion for each cluster. We will use parameters such as the ideal rotation curve we mentioned before, the random rotation curve and a Kolmogorov-Smirnov test. The procedures described below have been applied to each of the clusters.

A first test is provided by using the ideal rotation curve for the selected center and compute the χ^2 value between the real and ideal rotation curve, which will now name χ^2_{id}.

The next test is to perform a similar χ^2 comparing between our data rotation curve and one that corresponds to the random rotation curve. To this end, we keep the same coordinates of the galaxies of the cluster, but we shuffle their line-of-sight velocities randomly. Then, our algorithm of rotation is applied on them, again using the selected rotational center of the cluster. This process is repeated 10000 times and the final rotation curve, v_{r_i}, of this cluster is the mean of all the random rotation curves, $v_{r_{i_j}}$, and its error $\sigma_{v_{r_i}}$ is the statistical standard deviation of the mean.

$$v_{r_i} = \frac{1}{n}\sum_{j=1}^{n} v_{r_{i_j}}$$

$$\sigma_{v_{r_i}} = \sqrt{\frac{1}{n-1}\sum_{i=1}^{n}\left(v_{r_{i_j}} - v_{r_i}\right)^2}$$

where $n = 10000$. We calculate the value of χ^2 between the real rotation curve and the random curve, as we did for the ideal curve in (20). The reason of conducting this test is that we can measure the statistical importance of the possible rotation of a cluster by comparing χ^2_{id} with χ^2_r. If the first is significantly smaller than the second, then we can claim that the rotation model represents the data rotation curve more efficiently. If the opposite occurs, then the cluster in not likely to be rotating. The ratio χ^2_{id}/χ^2_r is also a useful parameter for concluding the rotation. The smaller this ratio is (as it approaches zero) while the value of χ^2_{id}/df (df are the degrees of freedom) remains $\lesssim 1$, the better the cluster is described by our rotation model.

We are also applying the Kolmogorov-Smirnov two-sample test (the algorithm *kstwo* is taken from Numerical Recipes in Fortran 77, [73], pg. 619) to the distributions of the line-of-sight velocities of the galaxies of the two semicircles of the cluster for each angle θ. This test calculates the probability that the two distributions have the same paternal distribution. The bigger the probability the more likely is the two distributions to belong to the same distribution. For a rotating cluster, we expect the smaller probability to occur at the angle of the maximum velocity difference of the rotation diagram.

As a result, we have four parameters that can be used to deduce the rotation of the clusters:

- χ^2_{id}/df between the real and ideal rotation curve, which should be less or equal to 1 for a rotating cluster,
- χ^2_r/df between the real rotation curve and random curve, which should be $\gg 1$ for a rotating cluster,
- χ^2_{id}/χ^2_r , which should approach zero for a rotating cluster, and
- the Kolmogorov-Smirnov probability between the redshift distribution of the two semicircles of maximum velocity difference, which should have a significantly small value (< 0.01), at the angle θ of the maximum velocity difference of the rotation diagram.

2.5 Application on individual clusters and results

Below we report our results for each cluster of our sample, separately. We have constructed eight diagrams for each cluster: a set of two plots for each of the four angular configurations. The first plot displays the rotation diagram for each of the 9 tested rotational centers, while the second plot displays, for the finally selected rotational center, the spatial distribution of the galaxies (in the upper left panel), the histogram of the line-of-sight velocities along with the fitted Gaussian (in the upper right panel), the rotation diagram with the real, ideal rotation and random rotation curves (and their uncertainties) in the bottom left panel, and the Kolmogorov-Smirnov probability diagram as a function of rotation angle θ in the bottom right panel.

Note that in the upper left panel, where we plot the spatial distributions of galaxies, the faint crosses represent the rejected galaxies due to the angular criteria, the black crosses indicate the rejected galaxies due to velocity criteria, while the blue and red dots represent galaxies moving towards and away the observer, respectively. The black square is the NASA-NED cluster center and the black triangle is the final rotational center. We present all the rotation center diagrams discussed above as an example only for one case, that of Abell 85. For every other cluster we present the diagram of the final rotational center for a radius 1.5 Mpc and, if this diagram does not show rotation mode, but at another radius configuration does, we present also the final rotational center diagram for that configuration too. All such plots, for all clusters, except for Abell 85, are shown in the appendix.

Along with the diagrams, we present tables of the results of the χ^2 minimization tests and Kolmogorov-Smirnov probability test we conducted for each of the angular configurations. Tables 2, 3, 4 and 5 also show the number of galaxies finally included as cluster-members, their mean redshift, which is the new cluster redshift, the rotation amplitude, which is the maximum velocity difference v_{dif} in the rotation diagram, the direction or rotation (clockwise is represented by value 1 and counterclockwise is represented by value 2) and the angle θ of the rotation axis, which is the angle of the maximum velocity difference. Some clusters have a and b components, which are the substructures as studied in section 2.5.6. In addition, table 2 and 4 contain less clusters, because some clusters had less than 10 members in those configurations and were not studied at all.

Abell clusters are sorted by their Bautz-Morgan type to present the results, and there is a final category of clusters that are likely to have two or three substructures, which are studied individually.

2.5.1 Bautz-Morgan type I clusters

Firstly, we present the results of the Bautz-Morgan type I clusters, which are characterized by a higher number density of galaxies than clusters of other types and are dynamically more evolved, as we mentioned in section 1.2.2.

Abell 85

Abell's 85 X-ray image (figure 25) can confirm its Bautz-Morgan type: it has a spherical shape, as is expected for a virialised cluster.

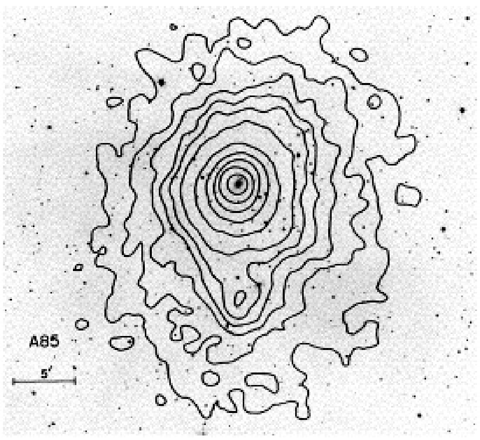

Figure 25: The X-ray isophotals of Abell 85 taken from Einstein IPC (1999).

It has a NASA-NED redshift 0.055061 and is a rather rich cluster; the number of members varies from 60 to 155 for each angular configuration. Below we present the rotation diagrams for all the four angular configurations. We remark that the cluster seems to show a rotation signal in 1.5 Mpc and 0.3-1.5 Mpc configurations (as confirmed by the Kolmogorov-Smirnov probability diagram, table 2 and 4), but this signal disappears at the other two configurations, where the outer radius of the cluster is 2.5 Mpc and more outer galaxy-members are included. This trend can be caused from a possible different velocity distribution of the outer galaxies with respect to the inner ones; maybe they are falling in the cluster center and thus these velocities reflect infall velocities. Our result is that Abell 85 is a probable rotating cluster within a 1.5 Mpc radius.

Abell 690

Abell 690 has a NASA-NED redshift 0.0788 and contains few members. We present the 1.5 Mpc radius configuration, where a weak rotation signal can be identified as well as on the other configurations. Values of χ^2 fraction at tables 2, 3, 4 and 5 show that the rotation diagram of this cluster

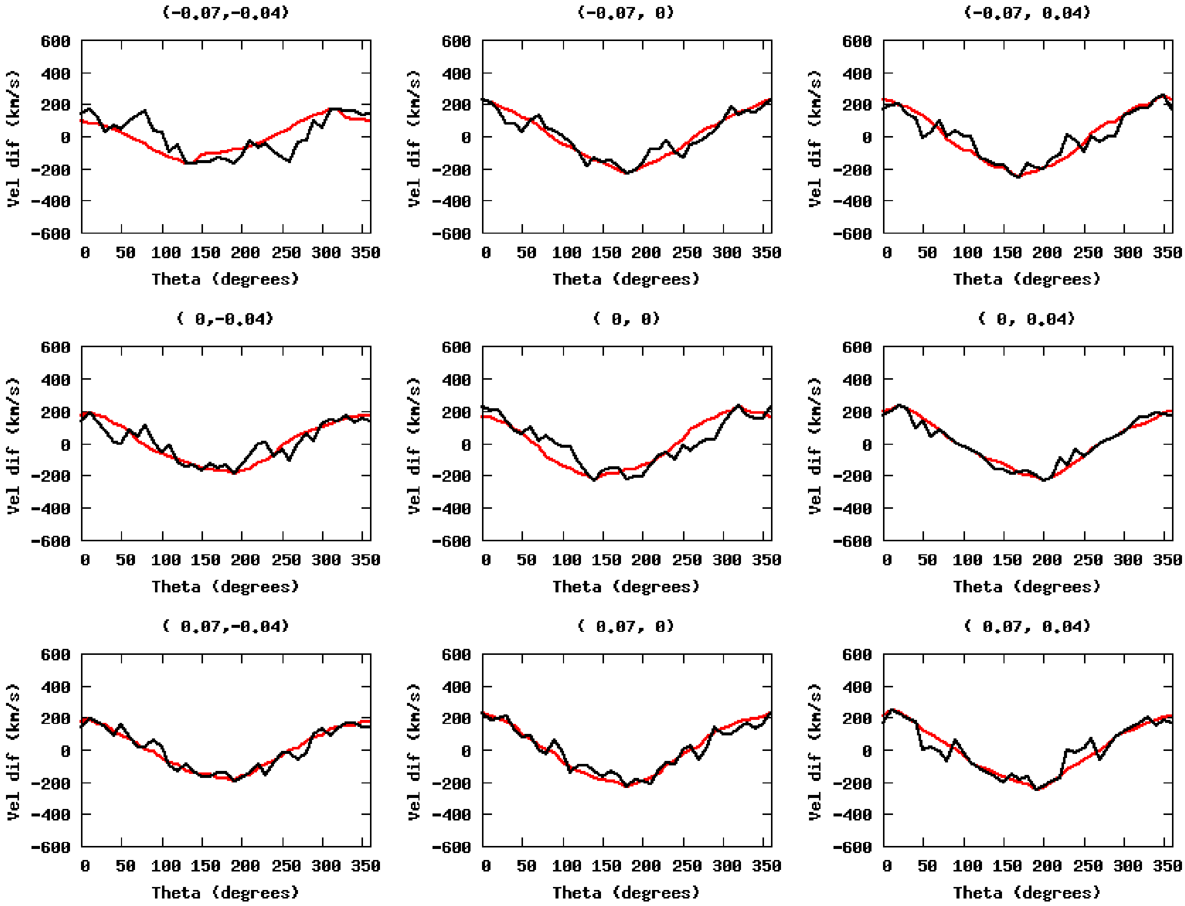

Figure 26: The rotation diagrams for all the candidate rotational centers for Abell 85 ($r < 1.5$ Mpc). Black lines are the real rotation curves and red lines are the ideal rotation curves. Above each panel we indicate the coordinates (dy, dx) of the rotational center.

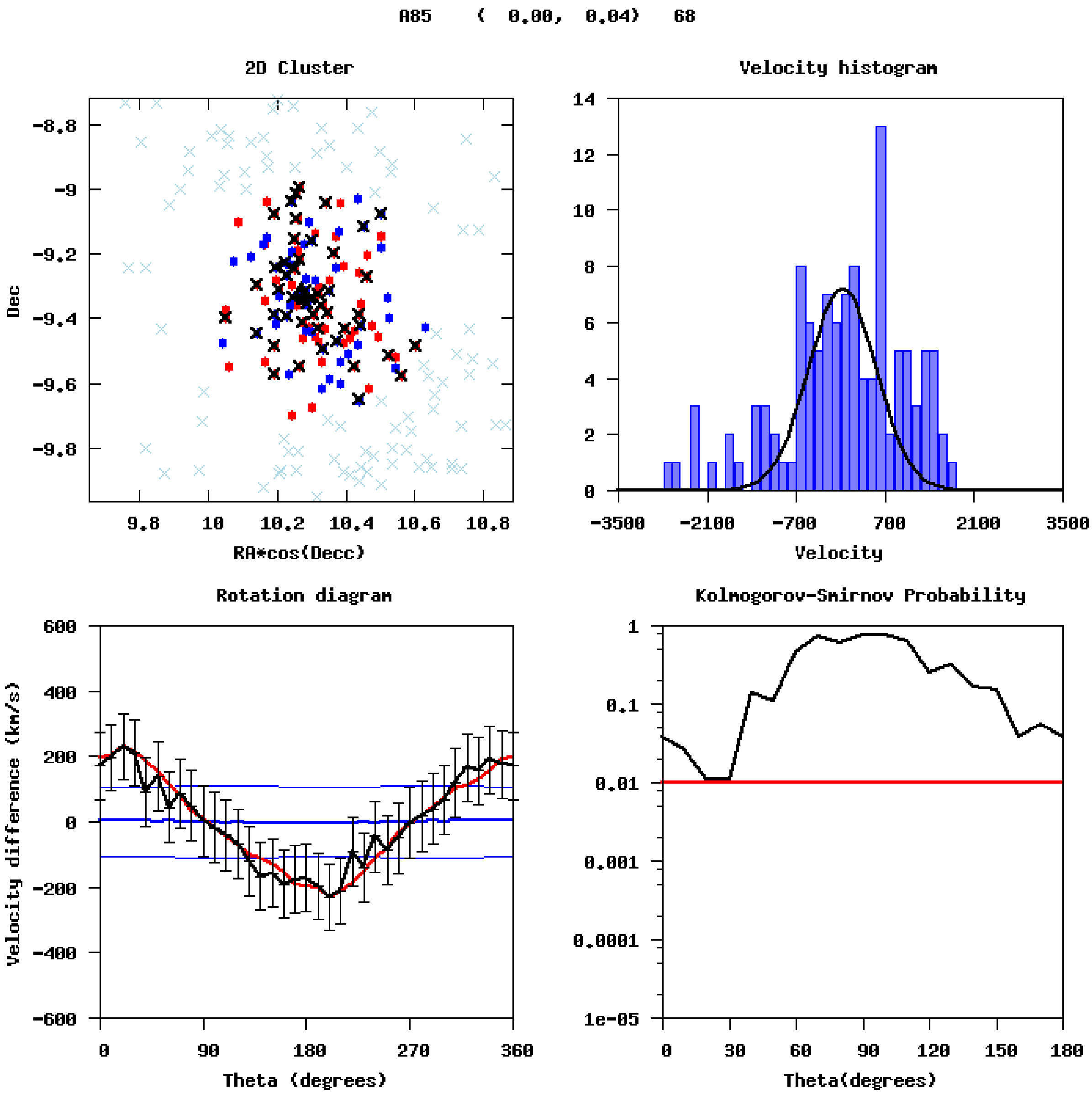

Figure 27: Abell 85 with a radius of 1.5 Mpc. The title of the figure indicates the coordinates of the final selected rotational center (dy, dx) and the number of galaxies included in the study.

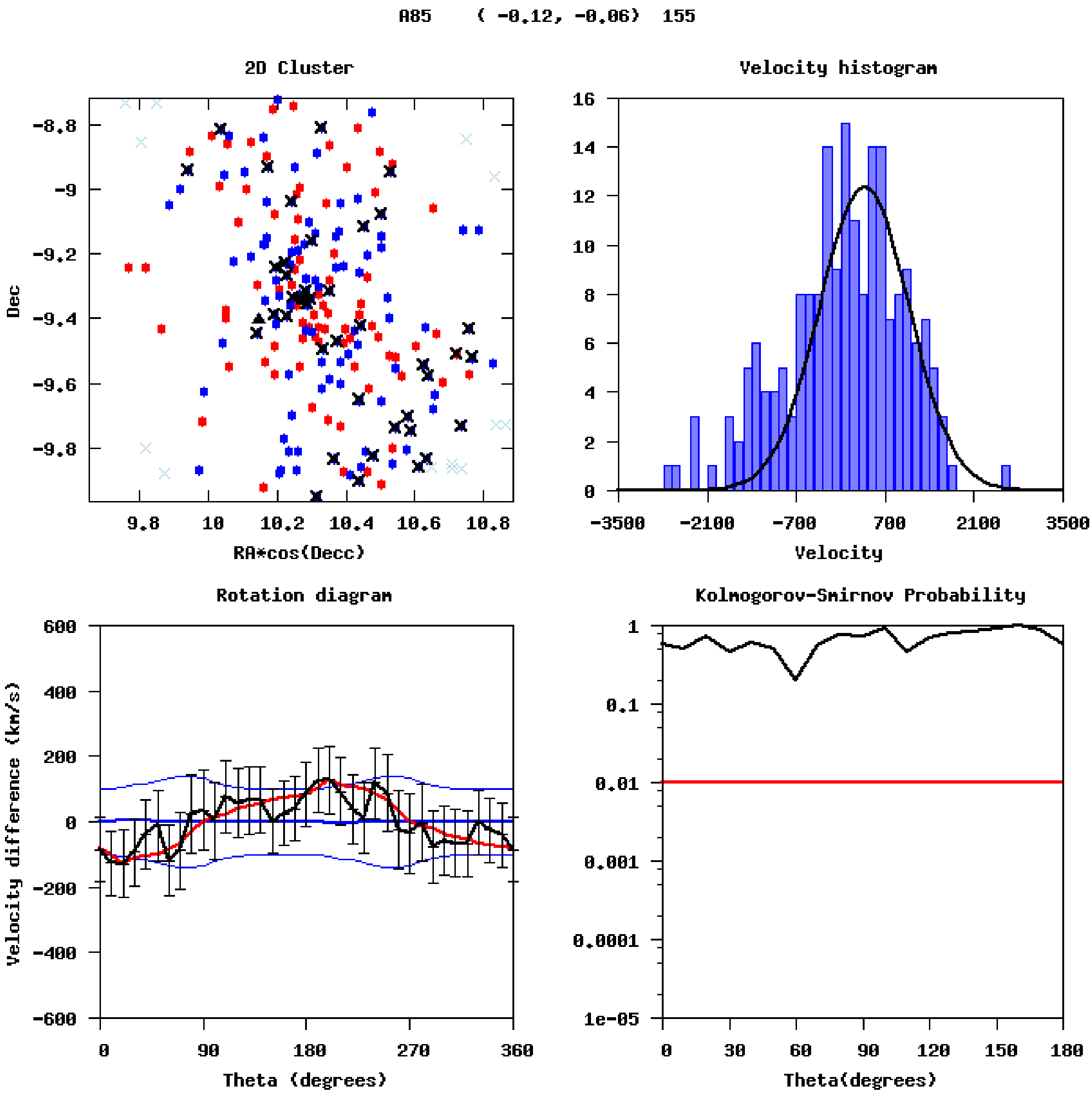

Figure 28: Abell 85 with a radius of 2.5 Mpc. The title of the figure indicates the coordinates of the final selected rotational center (dy, dx) and the number of galaxies included in the study.

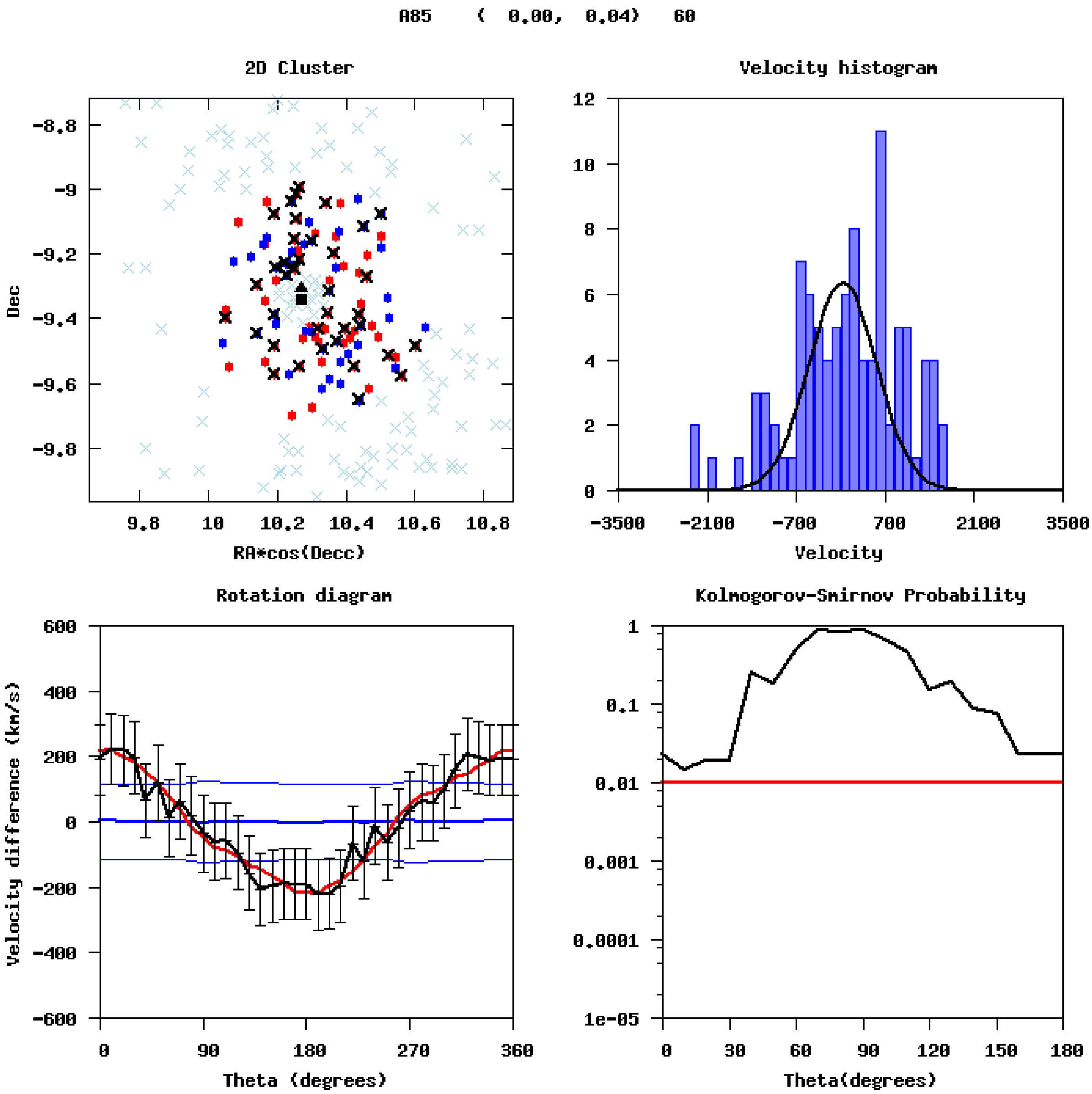

Figure 29: Abell 85 with radius between 0.3 and 1.5 Mpc. The title of the figure indicates the coordinates of the final selected rotational center (dy, dx) and the number of galaxies included in the study.

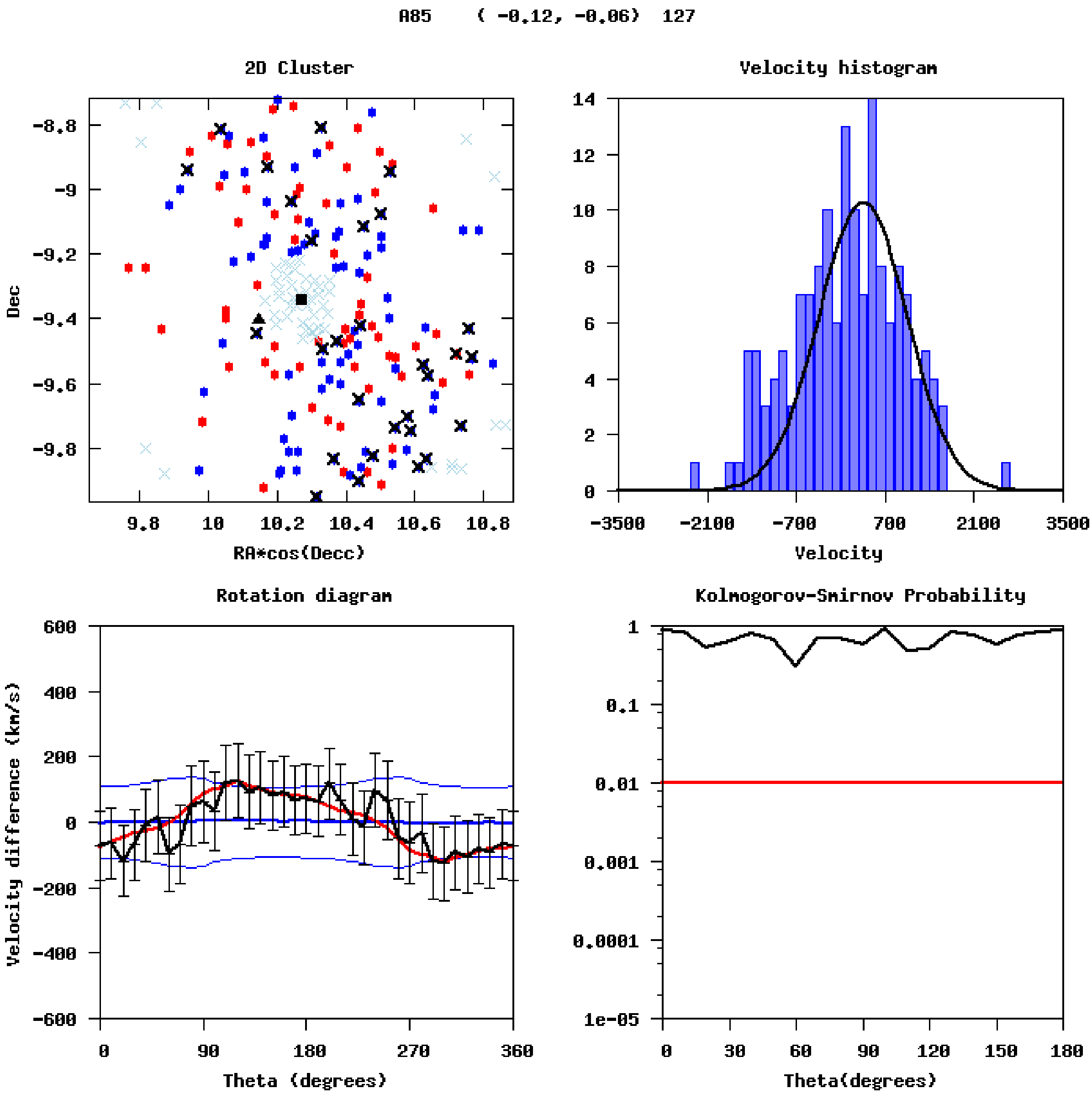

Figure 30: Abell 85 with radius between 0.5 and 2.5 Mpc. The title of the figure indicates the coordinates of the final selected rotational center (dy, dx) and the number of galaxies included in the study.

Cluster	z	n_{mem}	$v_{rot}/km \cdot s^{-1}$	Rot. axis $\theta/°$	Rot. dir.	$prob_{KS}$	χ^2_{id}/df	χ^2_r/df	χ^2_{id}/χ^2_r
A85	0.055180	68	228.9	20	1	0.010875	0.10101	0.8088	0.125
A168	0.044975	142	60.2	330	-	0.183787	0.1347	0.0597	2.256
A279	0.079800	66	479.9	140	2	0.015100	0.1413	1.3526	0.104
A646	0.126789	19	239.7	300	-	0.341447	0.0826	0.0907	0.911
A671	0.047440	44	80.9	330	-	0.367889	0.0481	0.0956	0.503
A690	0.080212	40	214.1	270	2	0.099250	0.0934	0.2694	0.347
A734	0.074386	14	310.9	120	-	0.102396	0.0684	0.3120	0.219
A957	0.044902	61	341.7	300	-	0.112386	0.0859	0.6095	0.141
A971	0.092674	38	321.0	320	-	0.094171	0.1715	0.1312	1.308
A1177	0.032136	38	233.5	190	1	0.040671	0.2482	1.2181	0.204
A1213	0.046824	68	83.1	340	-	0.187147	0.2408	0.1346	1.788
A1291a	0.051032	43	486.1	340	2	0.000175	0.0700	2.3912	0.029
A1291b	0.058009	39	430.8	230	1	0.105567	0.0623	0.9273	0.067
A1413	0.138170	10	306.4	210	-	0.180311	0.1357	0.1351	1.004
A1468	0.084903	26	256.1	0	1	0.002684	0.0388	0.5730	0.068
A1516	0.076980	37	147.8	340	-	0.197631	0.1648	0.2869	0.574
A1569a	0.069389	28	336.4	90	2	0.021409	0.1774	1.1275	0.157
A1569b	0.079419	27	242.5	200	1	0.026556	0.0883	0.5605	0.158
A1650	0.083056	39	190.8	290	-	0.087363	0.1524	0.2038	0.748
A1656	0.023236	482	178.8	220	1	0.042582	0.1372	0.5855	0.234
A1691	0.072370	59	463.1	190	-	0.052466	0.1696	0.7669	0.221
A1738	0.116653	24	506.9	100	2	0.011671	0.0985	0.9831	0.100
A1775a	0.065371	22	478.9	270	2	0.009365	0.1125	1.7262	0.065
A1775b	0.075206	55	165.9	240	-	0.298312	0.2228	0.2771	0.804
A1795	0.062689	84	287.5	260	-	0.062623	0.2790	0.3836	0.727
A1800	0.075949	48	278.7	190	-	0.170881	0.1562	0.4235	0.369
A1913	0.053028	102	447.5	50	1	0.000008	0.2416	2.4736	0.098
A1983	0.045365	103	67.0	60	-	0.194663	0.0699	0.1272	0.550
A1991	0.058928	69	135.3	160	-	0.368198	0.1653	0.3821	0.433
A2029	0.078864	52	324.9	310	-	0.060347	0.0465	0.4959	0.094
A2079	0.066018	60	245.8	140	-	0.198195	0.0840	0.1838	0.457
A2089	0.073433	55	168.0	250	-	0.242238	0.3096	0.1579	1.961
A2107	0.041323	110	525.2	160	2	0.000706	0.0965	1.8334	0.053
A2124	0.066183	60	138.3	240	-	0.309192	0.2136	0.0974	2.193
A2147	0.035735	223	268.9	140	2	0.000282	0.333	0.9859	0.337
A2199	0.030488	212	366.4	90	2	0.001061	0.1468	1.9951	0.074
A2244	0.099414	69	472.2	230	-	0.083436	0.0866	0.4017	0.215
A2255	0.079756	65	974.2	50	1	0.000046	0.1184	1.6329	0.073
A2356	0.118824	33	490.7	220	-	0.060384	0.1610	0.3696	0.436
A2399	0.057446	82	248.2	250	1	0.002198	0.1098	0.9272	0.118
A2428	0.083962	32	115.5	210	-	0.509875	0.1778	0.0739	2.407
A2593	0.041806	103	271.8	220	-	0.040228	0.1156	0.812	0.142
A2670	0.076136	93	450.0	250	1	0.002885	0.0938	0.9227	0.102

Table 2: The clusters with 1.5 Mpc radius. The first column is the Abell name of the cluster, the second is the mean redshift of the members, the third is the number of members included, the fourth is the rotation amplitude, the fifth is the angle θ of the rotation axis, the sixth is the minimum value of the Kolmogorov-Smirnov probability, and the last three columns are χ^2_{id}, χ^2_r, χ^2_{id}/χ^2_r respectively.

approaches better an ideal rotation curve than a random one. However, the rotation cannot be confirmed by the Kolmogorov-Smirnov probability tests, although they are more optimistic in the 2.5 Mpc and 0.5-2.5 Mpc configurations.

Cluster	z	n_{mem}	$v_{rot}/km \cdot s^{-1}$	Rot. axis $\theta/^{\circ}$	Rot. dir.	$prob_{KS}$	χ^2_{id}/df	χ^2_r/df	χ^2_{id}/χ^2_r
A85	0.056332	155	128.4	200	-	0.195518	0.1519	0.2251	0.675
A168	0.044839	184	157.1	70	-	0.133911	0.1860	0.3245	0.573
A279	0.079889	79	407.4	130	2	0.033038	0.2042	1.1632	0.176
A646	0.126861	23	273.7	220	-	0.366184	0.1043	0.1338	0.779
A671	0.047484	57	160.3	130	-	0.218951	0.1090	0.4745	0.230
A690	0.080403	64	300.4	20	1	0.042322	0.1075	0.7917	0.136
A734	0.074449	20	265.1	130	-	0.207477	0.2286	0.5721	0.400
A957	0.044862	66	312.5	300	-	0.039013	0.0920	0.5598	0.164
A971	0.092879	41	201.2	90	-	0.297295	0.0720	0.0831	0.867
A1027	0.064109	19	465.6	310	-	0.108000	0.1776	0.3214	0.552
A1177	0.031783	51	377.3	130	2	0.000956	0.1011	2.0569	0.049
A1213	0.047149	105	236.8	170	-	0.066707	0.2268	1.0365	0.219
A1291a	0.050854	61	535.6	320	2	0.000001	0.1206	5.0179	0.024
A1291b	0.058268	55	688.5	220	1	0.002886	0.2386	3.7460	0.064
A1413	0.138392	15	221.1	100	-	0.540248	0.0653	0.1102	0.593
A1468	0.084823	28	233.6	0	1	0.018986	0.0701	0.4428	0.158
A1508	0.094757	13	501.7	120	2	0.006403	0.1752	3.1830	0.055
A1516	0.076861	55	121.2	270	-	0.165937	0.0888	0.2690	0.330
A1569a	0.070020	55	438.5	50	1	0.000835	0.0734	2.2497	0.033
A1569b	0.079366	31	240.1	190	1	0.026912	0.0943	0.8113	0.116
A1650	0.083098	56	115.7	300	-	0.087561	0.1009	0.1597	0.632
A1656	0.023499	578	51.0	230	-	0.094035	0.1349	0.1022	1.320
A1691	0.072552	77	318.6	200	-	0.06308	0.2015	0.5407	0.373
A1738	0.116645	25	399.8	80	1	0.037716	0.1480	0.5569	0.266
A1775a	0.065121	30	254.2	290	2	0.010504	0.0733	0.8811	0.083
A1775b	0.075322	77	218.3	160	-	0.046153	0.1196	0.7181	0.167
A1795	0.062594	123	216.6	160	-	0.131338	0.7245	0.2636	2.749
A1800	0.075375	85	213.2	320	-	0.226402	0.0771	0.2223	0.347
A1913	0.052850	140	481.8	50	1	0.000017	0.5962	4.7843	0.125
A1983	0.045326	146	42.4	90	-	0.073739	0.1316	0.0821	1.602
A1991	0.058844	92	77.4	220	-	0.363569	0.2011	0.1705	1.179
A2029	0.077224	145	252.8	50	-	0.052519	0.1681	0.4343	0.387
A2079	0.065881	93	138.7	290	-	0.408894	0.1046	0.1959	0.534
A2089	0.073709	76	225.0	190	1	0.003650	0.0646	0.5334	0.121
A2107	0.041771	135	224.6	170	2	0.025348	0.1201	0.7864	0.153
A2124	0.066328	82	382.4	30	-	0.087591	0.0778	0.7548	0.103
A2147	0.036179	388	255.8	250	1	0.000876	0.1616	1.3653	0.118
A2199	0.030602	320	381.8	70	1	0.000005	0.2251	3.1694	0.071
A2244	0.099290	84	417.2	280	-	0.019161	0.2325	0.3405	0.683
A2255	0.079580	79	335.8	60	-	0.095175	0.1520	0.3140	0.484
A2356	0.119131	47	332.9	230	-	0.181572	0.2979	0.3832	0.777
A2399	0.057539	103	281.7	240	1	0.000231	0.1864	1.3798	0.135
A2428	0.083963	44	169.7	140	-	0.259234	0.2307	0.2647	0.872
A2593	0.041807	152	153.4	190	1	0.041332	0.1398	1.0642	0.131
A2670	0.076027	120	293.5	250	1	0.018442	0.1965	0.7958	0.247

Table 3: The clusters with 2.5 Mpc radius. The first column is the Abell name of the cluster, the second is the mean redshift of the members, the third is the number of members included, the fourth is the rotation amplitude, the fifth is the angle θ of the rotation axis, the sixth is the minimum value of the Kolmogorov-Smirnov probability, and the last three columns are χ^2_{id}, χ^2_r, χ^2_{id}/χ^2_r respectively.

Abell 734

Abell 734 has a redshift of 0.0719 and very few members (10-20 depending on the configuration). Its small richness causes large errorbars to show up in the rotation diagrams and, therefore, not

Cluster	z	n_{mem}	$v_{rot}/km \cdot s^{-1}$	Rot. axis $\theta/°$	Rot. dir.	$prob_{KS}$	χ^2_{id}/df	χ^2_r/df	χ^2_{id}/χ^2_r
A85	0.055201	60	221.8	10	1	0.014495	0.0910	0.8010	0.114
A168	0.044930	114	76.7	320	-	0.168188	0.1471	0.1018	1.445
A279	0.079756	45	512.0	140	2	0.014518	0.2229	1.6295	0.137
A646	0.126666	17	346.5	300	-	0.278951	0.0808	0.1597	0.506
A671	0.047613	30	189.2	80	-	0.083635	0.1181	0.3286	0.359
A690	0.080331	30	192.0	270	2	0.342223	0.0860	0.1267	0.679
A734	0.074198	12	195.4	120	-	0.378833	0.1227	0.1450	0.846
A957	0.045270	38	423.8	310	-	0.156537	0.0699	0.7667	0.091
A971	0.092716	26	490.8	320	-	0.017970	0.2527	0.3229	0.783
A1177	0.032176	30	344.1	220	1	0.020980	0.1144	1.6668	0.069
A1213	0.046735	56	86.4	260	-	0.141352	0.1885	0.0927	2.032
A1291a	0.051058	35	482.2	340	2	0.000965	0.0610	1.8240	0.033
A1291b	0.058009	28	509.5	230	1	0.116581	0.0684	1.0219	0.067
A1413	0.138057	9	372.8	210	-	0.198367	0.1236	0.2012	0.614
A1468	0.084814	23	231.5	0	1	0.004049	0.0773	0.4204	0.184
A1516	0.076957	33	154.9	0	-	0.126991	0.1875	0.288	0.651
A1569a	0.069416	25	384.9	90	2	0.039843	0.1892	1.2179	0.155
A1569b	0.079176	23	174.1	90	2	0.251732	0.0749	0.3496	0.214
A1650	0.083092	34	190.7	290	-	0.091115	0.1728	0.2233	0.774
A1656	0.023322	394	226.2	220	1	0.029947	0.1544	0.686	0.225
A1691	0.072350	51	411.4	190	-	0.126964	0.2225	0.4937	0.451
A1738	0.116644	20	284.7	110	2	0.075909	0.0672	0.5191	0.129
A1775a	0.065371	22	478.9	270	2	0.009365	0.1125	1.7262	0.065
A1775b	0.074983	41	153.7	170	-	0.378213	0.1087	0.1741	0.624
A1795	0.062784	72	250.6	260	-	0.128078	0.2860	0.2035	1.405
A1800	0.076037	40	224.5	280	-	0.335052	0.1072	0.2294	0.467
A1913	0.053043	97	468.9	50	1	0.000008	0.1803	2.5935	0.070
A1983	0.045370	92	193.2	60	1	0.007554	0.1238	0.9597	0.129
A1991	0.058883	59	127.0	210	-	0.351775	0.1696	0.2921	0.580
A2029	0.078821	47	221.1	330	-	0.262640	0.1101	0.3984	0.276
A2079	0.066021	56	284.2	140	-	0.155385	0.0775	0.2447	0.317
A2089	0.073592	46	229.3	180	1	0.089105	0.1268	0.2754	0.460
A2107	0.041277	82	491.5	160	2	0.000176	0.0550	1.6297	0.034
A2124	0.066237	49	146.3	110	-	0.201610	0.1918	0.0658	2.914
A2147	0.035739	189	316.5	130	2	0.000118	0.306	1.2406	0.246
A2199	0.030482	179	424.4	90	2	0.000210	0.0804	2.1073	0.038
A2244	0.099523	62	349.1	240	-	0.163202	0.2010	0.2538	0.792
A2255	0.080032	53	860.9	60	1	0.000604	0.1185	1.5244	0.078
A2356	0.119265	28	847.1	210	-	0.028307	0.2016	0.8918	0.226
A2399	0.057434	68	275.6	250	1	0.003979	0.1177	0.9529	0.124
A2428	0.084034	27	202.8	130	-	0.372538	0.1318	0.2073	0.636
A2593	0.041886	85	343.7	220	1	0.008922	0.1181	1.3691	0.086
A2670	0.076105	82	495.6	250	1	0.006278	0.0978	1.2326	0.079

Table 4: The clusters in the 0.3-1.5 Mpc radius circular ring. The first column is the Abell name of the cluster, the second is the mean redshift of the members, the third is the number of members included, the fourth is the rotation amplitude, the fifth is the angle θ of the rotation axis, the sixth is the minimum value of the Kolmogorov-Smirnov probability, and the last three columns are χ^2_{id}, χ^2_r, χ^2_{id}/χ^2_r respectively.

allowing to detect any possible rotation signal in any configuration. The stronger signal is that in the 2.5 Mpc configuration, presented in the appendix, which could correspond to a rotation signal confirmed by table 3.

Cluster	z	n_{mem}	$v_{rot}/km \cdot s^{-1}$	**Rot. axis** $\theta/°$	**Rot. dir.**	$prob_{KS}$	χ^2_{id}/df	χ^2_r/df	χ^2_{id}/χ^2_r
A85	0.056264	127	126.3	120	-	0.297261	0.1190	0.2449	0.486
A168	0.044725	139	86.1	10	-	0.335141	0.1499	0.1444	1.038
A279	0.079957	54	411.5	130	2	0.054366	0.1186	1.0160	0.117
A646	0.126678	20	216.7	220	-	0.324131	0.0990	0.0967	1.024
A671	0.047673	38	111.8	340	-	0.146176	0.1367	0.2669	0.512
A690	0.080588	51	219.5	20	1	0.204829	0.0538	0.3585	0.150
A734	0.074331	18	162.7	240	-	0.545283	0.0783	0.2184	0.359
A957	0.045527	29	200.5	160	-	0.236582	0.1212	0.0753	1.611
A971	0.093290	24	604.8	330	-	0.086413	0.1021	0.3301	0.309
A1027	0.064109	19	465.6	310	-	0.108000	0.1776	0.3214	0.552
A1177	0.031753	38	481.0	120	2	0.000249	0.1419	2.7653	0.051
A1213	0.046992	74	169.8	200	-	0.082983	0.1812	0.5238	0.346
A1291a	0.050852	49	613.9	330	2	0.000006	0.1436	4.2446	0.034
A1291b	0.058836	34	790.0	190	1	0.001976	0.0689	3.0190	0.023
A1413	0.138537	12	146.7	110	-	0.338987	0.0354	0.0277	1.279
A1468	0.084831	18	569.3	0	1	0.002913	0.0768	1.6356	0.047
A1508	0.094757	13	501.7	120	2	0.006403	0.1752	3.1830	0.055
A1516	0.076798	48	98.8	270	-	0.487337	0.0972	0.1420	0.685
A1569a	0.070131	41	541.2	40	1	0.000281	0.0954	2.6523	0.036
A1569b	0.079181	24	134.0	120	2	0.236963	0.1187	0.2460	0.483
A1650	0.083125	46	251.4	280	-	0.035635	0.1318	0.7974	0.165
A1656	0.023254	519	178.3	160	2	0.060236	0.1208	0.8365	0.144
A1691	0.072680	56	303.4	190	-	0.143088	0.1230	0.3729	0.330
A1738	0.116505	16	247.0	130	2	0.046532	0.0157	0.4243	0.037
A1775a	0.065136	29	263.9	290	2	0.018096	0.0779	0.7264	0.107
A1775b	0.075225	57	356.5	150	-	0.003410	0.2339	1.5031	0.156
A1795	0.062643	101	384.8	150	-	0.031193	0.8605	0.5932	1.451
A1800	0.075223	71	242.2	320	-	0.200303	0.1962	0.2242	0.875
A1913	0.052774	119	491.4	50	1	0.000031	0.5750	4.5403	0.127
A1983	0.045280	121	134.9	50	-	0.057424	0.1187	0.5156	0.230
A1991	0.058729	77	91.5	130	-	0.345015	0.2355	0.0849	2.776
A2029	0.077281	120	378.4	60	-	0.006981	0.1236	0.8985	0.138
A2079	0.065776	82	118.9	150	-	0.409541	0.1764	0.0935	1.886
A2089	0.073732	64	317.8	190	1	0.000406	0.1335	1.3009	0.103
A2107	0.041681	97	236.1	150	2	0.053652	0.1556	0.5396	0.288
A2124	0.066428	61	318.1	40	-	0.068489	0.1855	0.4856	0.382
A2147	0.036252	328	317.2	240	1	0.000258	0.1698	1.8690	0.091
A2199	0.030610	264	435.9	70	1	0.000005	0.1514	4.0372	0.037
A2244	0.099076	63	431.3	300	-	0.005910	0.1845	0.4238	0.435
A2255	0.079132	46	277.4	280	-	0.177970	0.1316	0.1593	0.826
A2356	0.119494	38	294.6	330	-	0.389655	0.1457	0.3187	0.457
A2399	0.057433	80	179.7	260	1	0.022628	0.1574	0.4689	0.336
A2428	0.084030	34	161.3	140	-	0.363970	0.1023	0.1293	0.791
A2593	0.041838	127	162.8	190	1	0.079246	0.1772	1.2495	0.142
A2670	0.075962	94	292.5	280	2	0.013054	0.1860	0.6419	0.290

Table 5: The clusters in the 0.5-2.5 Mpc radius circular ring. The first column is the Abell name of the cluster, the second is the mean redshift of the members, the third is the number of members included, the fourth is the rotation amplitude, the fifth is the angle θ of the rotation axis, the sixth is the minimum value of the Kolmogorov-Smirnov probability, and the last three columns are χ^2_{id}, χ^2_r, χ^2_{id}/χ^2_r respectively.

Abell 1027

Abell 1027, with NASA-NED redshift 0.069001 was only studied in the configuration 2.5 Mpc and

0.5-2.5 Mpc, due to the very small number of members on the rest two configurations (below 5). The large errorbars do not allow the detection of a possible rotation signal.

Abell 1177

Abell 1177 has a NASA-NED redshift 0.0316. It has approximately 40-50 members. We present the 1.5 Mpc and 2.5 Mpc configurations. We can see a rotation signal in the 1.5 Mpc configuration when looking the rotation diagram and table 2. The Kolmogorov-Smirnov probability diagram does not show a certain rotation signal. This signal is shown by all means in 2.5 Mpc configuration. Abell 1177 is a rotating cluster candidate.

Abell 1413

Abell 1413 has NASA-NED redshift 0.1427 and its spherical X-ray isophotals show a virialised cluster. It has minimal number of members and rotation signal cannot be detected as shown in the rotation diagram.

Abell 1468

Abell 1468 has 0.0844 NASA-NED redshift. In all configurations the rotation diagram corresponds to a rotating cluster's rotation diagram. This rotation is confirmed by the values of χ^2_{id}/χ^2_r and Kolmogorov-Smirnov probability of tables 2, 3, 4 and 5 that are consistent with rotation. Consequently, Abell 1468 is a rotating cluster. We also study another angular configuration, the circular area within 1 Mpc radius, in case the cluster radius is smaller and rotation would be detected. However, the rotation signal is weaker in this configuration, which means that outer galaxies in this cluster also have rotation velocity distribution (the results table is shown at the end of the section and the diagram is in the appendix).

Abell 1508

Abell 1508 has an initial redshift 0.0966 and a minimal number of only 13 galaxy-members and this is the reason it has been studied only in the 2.5 Mpc and 0.5-2.5 Mpc configurations. In the appendix we present the rotation diagram of the 2.5 Mpc configuration, which presents a rotation signal, which can be confirmed by the values of χ^2_{id}, χ^2_r and χ^2_{id}/χ^2_r of table 3. The same results apply also for the 0.5-2.5 Mpc configuration. However, we cannot draw a safe conclusion about the rotation or not of Abell 1508, since the rotation signal could easily be produced by two groups infalling in their common center of mass from different directions along the line of sight. These substructures can be seen in the spatial distribution of the galaxies in the appendix. This signal would be verified if we possessed more data of galaxy-members.

Abell 1738

Abell 1738 has NASA-NED redshift 0.1154 and contains approximately 25 members. Again, the small number of galaxy-members does not help us to make safe conclusions about its rotation. It presents weak rotation signal in all configurations (the stronger is in the 1.5 Mpc configuration) which is confirmed by tables 2, 3, 4 and 5.

Abell 1795

Abell 1795 has NASA-NED redshift 0.062476 and is a rather rich cluster. Its X-ray isophotals are spherical as expected for a Bautz-Morgan I type cluster. No rotation signal or other indications of rotation have been found in any of the four angular configurations.

Abell 1991

Abell 1991 has initial redshift 0.0587 and is also a rich cluster. No rotational signal in any configuration seems to be confirmed, neither by the Kolmogorov-Smirnov probability diagram nor by the χ^2_{id}, χ^2_r and χ^2_{id}/χ^2_r values.

Abell 2029

Abell 2029 has NASA-NED redshift 0.0773 and is also a rich cluster. It is a virialised cluster, as seen from its X-ray isophotals. In the 1.5 Mpc and 0.5-2.5 Mpc configurations a rotation signal can be detected, which is consistent with the value of χ^2_{id}/χ^2_r of tables 2 and 5. In the other two angular configurations a weaker signal is detected. We study the cluster also in the 1 Mpc configuration, because it seems that the inner area of the cluster is denser and this could be its radius. This case is confirmed, and the rotation signal as well as the indications of rotation are stronger for this rich cluster (the results table is shown at the end of the section and the diagram is in the appendix).

Abell 2107

Abell 2107 is another rich cluster with NASA-NED redshift 0.0411. There is a clear rotation signal in both 1.5 Mpc and 0.3-1.5 Mpc configuration, which is obvious from the rotation diagram, the Kolmogorov-Smirnov probability diagram and the χ^2_{id}/χ^2_r values of tables 2 and 4. This signal is weakened in 2.5 Mpc and 0.5-2.5 Mpc configurations as happened for the Abell 85. We assume that the outer galaxies have a different velocity distribution, not virialised, and probably they are infalling.

Abell 2199

Abell 2199 is a virialised and very rich cluster; contains hundreds of galaxies detected in the optical band of the SDSS spectroscopic survey. It has NASA-NED redshift 0.030151. It shows great indications of rotation in every parameter we use to deduct it and in every angular configuration. The two peaks in its rotation diagram could mean that the rotation signal is caused by the presence of substructures. Abell 2199 is a rotating cluster candidate.

2.5.2 Bautz-Morgan type I-II clusters

Bautz-Morgan type I-II clusters are intermediate cases between type I and II clusters, as we have already mentioned.

Abell 279

Abell 279 has NASA-NED redshift 0.0797. This cluster presents rotation signal and has χ^2_{id}/χ^2_r values that are consistent with rotation in all configurations. This cluster is a rotating cluster.

Abell 957

Abell 957 has redshift 0.0436. Its rotation diagrams in 1.5 Mpc, 2.5 Mpc and 0.3-1.5 Mpc configurations present weak rotation signal and weak indications of rotation have been found in tables 2, 3 and 4. However, the rotation signal along with the indications is completely lost in the 0.5-2.5 Mpc configuration. This would mean that the intermediate-distance galaxy members, in 0.3-0.5 Mpc distance from the cluster center, contaminate the rotation signal.

Abell 1650

Abell 1650 is a medium richness cluster in our study and has NASA-NED redshift 0.083838. Rotation mode cannot be identified in three of the four angular configurations. In the 0.5-2.5 Mpc configuration, a weak rotation signal is detected and also weak indications of rotation are found in table 5. On the one hand, the cluster is rotating and the inner members contaminate the rotation signal due to projection effects; on the other hand, this signal is caused by two substructures moving at an angle along the line of sight at distance 0.5-2.5 Mpc from the cluster center.

Abell 2244

Abell 2244 is cluster with NASA-NED redshift 0.0968. In the 1.5 Mpc and 0.3-1.5 Mpc configurations its velocity (redshift) distribution is sparse and seems to consist of substructures; this possibility is amplified due to the existence of multiple peaks in the rotation diagram of all the configurations. There are indications of rotation and a weak rotation signal in 1.5 Mpc and 0.5-2.5 Mpc configurations, but they are not enough to conclude in the rotation of the cluster.

Abell 2670

Abell 2670 is a rich cluster with 0.076186 NASA-NED redshift. It displays strong rotation signal and indications of rotation in χ^2_{id}/χ^2_r values in 1.5 Mpc and 0.3-1.5 Mpc configurations. In the 2.5 Mpc and 0.5-2.5 Mpc configurations, mupliple peaks appear in the rotation diagrams and Kolmogorov-Smirnov probability diagrams, which show that maybe substructures exist in the outer region of the cluster that also contaminate its rotation signal. We conclude that Abell 2670 is a rotating cluster.

2.5.3 Bautz-Morgan type II clusters

Bautz-Morgan type II clusters are the ones that have their brightest galaxy being intermediate between cD and normal giant ellipticals.

Abell 971

Abell 971 has NASA-NED redshift 0.0929 and has ~ 40 galaxy-members. Rotation signal cannot be extracted from the rotation diagram of none of the angular configurations and there are no indications of rotation in tables 2, 3, 4 and 5.

Abell 1656

Abell 1656 is the richest cluster in our study. It has NASA-NED redshift 0.0231. It presents weak rotation signal and weak indications of rotation in the 1.5 Mpc, 2.5Mpc and 0.3-1.5 Mpc configurations. The rotational mode is lost in the 2.5 Mpc configuration, probably due to contaminations in the rotation velocity distribution of the outer and inner members. The cluster is studied also in the 1 Mpc configuration, where the cluster is denser, and a greater rotation signal was found, confirmed by the indications of rotation (the results table is shown at the end of the section and the diagram is in the appendix). Abell 1656 is a rotating cluster.

Abell 1691

Abell 1691 has NASA-NED redshift 0.072093. There are weak indications of rotation and weak rotation signal in all configurations, but they are not supported by the Kolmogorov-Smirnov probability diagram.

Abell 1800

Abell 1800 has NASA-NED redshift 0.0755. In 1.5 Mpc and 2.5 Mpc angular configurations, there is weak rotation signal that is lost in the other two configuration. It is possible that the inner galaxies contaminate the signal due to projection effects.

Abell 2089

Abell 2089 is a cluster with NASA-NED redshift 0.07313. In the 2.5 Mpc 0.5-2.5 Mpc configurations a strong rotation signal is detected confirmed by the indications of rotation in tables 3 and 5. In the 0.3-1.5 Mpc configuration the signal is weakened and in the 1.5 Mpc is completely lost. It is possible that in the inner region of the cluster velocity-projections along the line of sight weaken the rotation signal. Abell 2089 is a rotating cluster candidate.

Abell 2428

Abell 2428 is not a rich cluster with NASA-NED redshift 0.0968. No indications of rotation and no detectable rotation signal exist in any angular configuration.

Abell 2593

Abell 2593 is a rich cluster with NASA-NED redshift 0.0413. It presents indications of rotation in all configurations mainly in the χ^2_{id}/χ^2_r values. In the 0.3-1.5 Mpc configuration especially, the rotation diagram as well as the Kolmogorov-Smirnov probability diagram there is the strongest evidence of rotation mode (see table 4). Abell 2593 is a rotating cluster.

2.5.4 Bautz-Morgan type II-III clusters

Bautz-Morgan type II-III clusters are intermediate cases between Bautz-Morgan type II and Bautz-Morgan type III clusters.

Abell 168

Abell 168 is at NASA-NED redshift 0.045. It presents no indications of rotation in none of the four angular configurations. The χ^2 tests show that its rotation curve resembles more a random than an ideal one.

Abell 1516

Abell 1516 is at NASA-NED redshift 0.0769. It does not show any strong rotation mode or any other indications of rotation.

Abell 2079

Abell 2079 is at 0.068984 NASA-NED redshift. It also does not show indications of rotation in none of the angular configurations. The final rotation diagram of the 1.5 Mpc configuration is shown in the diagram's appendix.

Abell 2255

Abell 2255 is not a rich cluster, with NASA-NED redshift 0.0806. It provides a very strong rotation signal (approximately 1000 km/s rotation amplitude) both in 1.5 Mpc and 0.3-1.5 Mpc configurations, which is confirmed by the χ^2 tests and the Kolmogorov-Smirnov probability test. This signal is weakened and lost, as for Abell 85, in the 2.5 Mpc and 0.5-2.5 Mpc configurations. Probably the outer members have different velocity distribution profiles and they are not yet virialised. Abell 2255 is a strong candidate for a rotating cluster with a radius $\sim$ 1.5 Mpc.

Abell 2356

Abell 2356 is at NASA-NED redshift 0.1161. It is a distant cluster with few members that cause large errorbars to show up in the rotation diagrams. The weak rotation signal cannot be confirmed by the weak indications of rotation in all configurations and, therefore, we cannot safely conclude in the rotation or not of Abell 2356.

2.5.5 Bautz-Morgan type III clusters

Bautz-Morgan type III clusters have no members significantly brighter than the general bright population of galaxy members.

Abell 646

Abell 646 is at NASA-NED redshift 0.1292. It has few galaxy-members with available redshift on SDSS, probably because of the fact that is a distant cluster. As a result, a rotation mode cannot be detected in none of the angular configurations.

Abell 1213

Abell 1213 is at NASA-NED redshift 0.0469. It does not show indications of rotation in the 1.5 Mpc and 0.3-1.5 Mpc configurations. However, a rotation signal as well as indications of rotation appear in the 2.5 Mpc and 0.5-2.5 Mpc configurations. The outer galaxy-members seem to have a rotation velocity distribution , in comparison with the inner ones.

Abell 1913

Abell 1913 is a rather rich cluster with NASA-NED redshift 0.0528. It appears to be a rotating cluster in all angular configurations, as a fact that is based on all the parameters that we use to deduce rotation.

Abell 1983

Abell 1983 is another rich cluster of the study with NASA-NED redshift 0.0436. It does not provide any indications of rotation in three of the angular configurations (1.5 Mpc, 2.5 Mpc and 0.5-2.5 Mpc). The χ^2 tests indicate that the velocity distribution of the galaxy-members is more likely random than ideally rotating in those configurations. However, a weak rotation signal and weak indications of rotation are presented in the 0.3-1.5 Mpc configuration.

Abell 2147

Abell 2147 is a cluster containing hundreds of galaxies at NASA-NED redshift 0.035. It presents indications of rotation by all means (rotation diagram, Kolmogorov-Smirnov probability diagram, χ^2 test values) in all configurations. It was also studied in the 1 Mpc configuration, where a stronger rotation signal has been found (the results table is shown at the end of the section and the diagram is in the appendix). Abell 2147 is a rotating cluster candidate.

Abell 2399

Abell 2399 is at NASA-NED redshift 0.0579. It also shows strong rotation indications in all configurations and in all the parameters we use. The signal is a bit weakened in the 0.5-2.5 Mpc configuration, possibly because of the different velocity distribution of some of the outer members. The cluster has been studied in the 1 Mpc configuration, where we could detect a larger density in the spatial distribution diagram. We have detected a stronger rotation signal and more prominent indications of rotation (the results table is shown at the end of the section and the diagram is in the appendix). Abell 2399 is a rotating cluster candidate.

2.5.6 Clusters containing substructures

In this section we investigate clusters whose velocity distribution show substructures along the line of sight. Substructure with the lowest mean redshift will be called a, the one with the next larger mean redshift will be called b and so on.

Abell 671

Abell 671 is a Bautz-Morgan type II-II cluster at NASA-NED redshift 0.0502. In our velocity distribution diagram (figure 88) it appears to consist of three substructures along the line of sight, at slightly different redshifts. Because of the small number of members of the cluster, we only can study the rotation of the largest and more close substructure, which has approximately 50 members. This substructure does not show clear indications of rotation in any of the parameters we use. We would expect that the substructures had an amount of angular momentum that would lead to rotation, but this does not seem to be the case in Abell 671.

Abell 1291

Abell 1291 is a Bautz-Morgan type II cluster at NASA-NED redshift 0.0527. This cluster shows strong indications of substructures in the velocity distribution diagram. When we study the cluster as one structure, it does not present rotation signal (2.5 Mpc configuration, figure 89). As a next step, we study the two substructures of the cluster in all configurations, and we observe a rotation mode in all of them and in both the substructure a and substructure b of the cluster. We show the diagrams of the 2.5 Mpc configuration; figure 90 and 91. The two substructures seem to have opposite directions of angular momentum - the one is rotating clockwise while the other rotates counterclockwise. Finally, we study the case that substructure b consists of two substructures; we study the rotation only of one of them (figure 92) - the second one is very small. We find that it presents weaker indications of rotation. We assume that the two large substructures of the cluster are two different groups in a very small distance, which have undergone a merge and now have opposite angular momentum.

Lauer (1988) [49] has also found two interacting substructures in Abell 1291 and an additional low-luminosity elliptical galaxy that does not interact with the other substructures. Blakeslee & Tonry (1992) [14] have stated that Abell 1291 has undergone a merger and Ramella et al. (2007) [74] have also detected its substructures.

Abell 1569

Abell 1569 is a Bautz-Morgan type II cluster at NASA-NED redshift 0.0735. The rotation diagram of the cluster is very noisy and a weak rotation signal is detected. The velocity distribution shows two main substructures that we study individually. Substructure a presents a prominent rotation signal in all configurations. Substructure b presents a weaker signal, mainly detected in 1.5 Mpc and 2.5 Mpc configurations, which means that inner-member non-rotational velocities that are projected on the plane of the sky contaminate the rotation signal. We also study the case of substructure a in the 2.5 Mpc configuration consisting of two smaller substructures. We study them also individually, but we cannot detect a rotation mode with certainty, as their galaxy-members are few. There is a possibility that the rotation signal of substructure a is not due to rotation, but due to the existence of the substructures.

Abell 1775

Abell 1775 is a Bautz-Morgan type I cluster at NASA-NED redshift 0.0717. When we study this cluster individually it shows an very strong rotation signal, confirmed by all parameters we use. This rotation signal is not due to rotation velocity distribution of the galaxies, but due to the existence of substructures. Obviously, when looking at the velocity distribution, it consists of two substructures that we study individually. Substructure a also presents rotation mode in all configurations, but, on the contrary, substructure b presents strong rotation signal only in 2.5 Mpc and 0.5-2.5 Mpc configurations.

Abell 2124

Abell 2124 is a Bautz-Morgan type I cluster at NASA-NED redshift 0.065625. This cluster presents a weak rotation signal in the 0.5-2.5 Mpc and 2.5 Mpc configurations, and weak indications of rotation (the Kolmogorov-Smirnov test and the χ^2 tests). In these two configurations it appears to be consisting of two substructures, which we study; there is the case that its rotation signal is due to those substructures. None of them though presents strong indications of rotation.

Cluster	z	n_{mem}	$v_{rot}/km \cdot s^{-1}$	**Rot. axis** $\theta/°$	**Rot. dir.**	$prob_{KS}$	χ^2_{id}/df	χ^2_r/df	χ^2_{id}/χ^2_r
A1468	0.084888	21	170.5	0.	1	0.062063	0.0899	0.2199	0.409
A2029	0.078977	31	534.5	320.	1	0.003741	0.0790	0.9737	0.081
A1656	0.023207	326	247.9	220.	1	0.003243	0.0644	0.8352	0.077
A2147	0.035760	128	423.3	160.	2	0.002562	0.0799	1.4618	0.055
A2399	0.057582	55	421.1	240.	1	0.000944	0.1187	1.7087	0.069

Table 6: The clusters that were also studied in the 1 Mpc radius circular area. The first column is the Abell name of the cluster, the second is the mean redshift of the members, the third is the number of members included, the fourth is the rotation amplitude, the fifth is the angle θ of the rotation axis, the sixth is the minimum value of the Kolmogorov-Smirnov probability, and the last three columns are χ^2_{id}, χ^2_r, χ^2_{id}/χ^2_r respectively.

2.6 Basic results

2.6.1 Fraction of rotating clusters

In this section we present some basic statistics of the results of our study. In the 1.5 Mpc configuration we have found that 13 out of the 43 clusters have strong indications of rotation ($prob_{KS} \lesssim 0.01$, $\chi^2_{id} < 1$, $\chi^2_r \gtrsim>$ and $\chi^2_{id}/\chi^2_r \ll 1$), which is the ∼30% of our sample. 11 of them presented strong indications of rotation both in the 1.5 Mpc and 0.3-1.5 Mpc configurations (Abell 279, Abell 1291a, Abell 1738, Abell 1775a, Abell 1913, Abell 2107, Abell 2147, Abell 2199, Abell 2255, Abell 2399, Abell 2670), one of them presented strong indications of rotation only in the 0.3-1.5 Mpc configuration (Abell 1983) and one of them presented weak indications of rotation ($prob_{KS} \lesssim 0.04$, $\chi^2_{id} < 1$ and $\chi^2_{id}/\chi^2_r < 0.4$) on the 1.5 Mpc configuration and strong indications of rotation in the 0.3-1.5 Mpc configuration (Abell 2593). Additionally, 6 more clusters presented weak indications of rotation in the 1.5 Mpc configuration (Abell 85, Abell 1177, Abell 1468, Abell 1569a, Abell 1569b, Abell 1656) and overall 19 out of the 43 clusters presented at least weak indications of rotation either in the 1.5 Mpc configuration or the 0.3-1.5 Mpc configuration. This is ∼44% of the sample.

We have found possible substructures in 3 of the clusters mentioned above (Abel 2199, Abell 2670, Abell 1569a). If those substructures actually exist, then our previous fractions are a little changed. We have 11 out of 43 clusters rotating (∼25% of the sample) and 16 out of 43 clusters at least possibly rotating in the 1.5 Mpc or 0.3-1.5 Mpc configuration (∼37% of the sample). These fractions are also shown in the table below.

1.5 Mpc and 0.3-1.5 Mpc configurations

	Rotating clusters	**Possibly rotating clusters**
No substructures	∼30%	∼44%
Clusters with substructures	∼25%	∼37%

In the 2.5 Mpc we have found 9 out of the 45 cluster that present strong indications of rotation (Abell 1177, Abell 1291a, Abell 1291b, Abell 1508, Abell 1569a, Abell 1913, Abell 2147, Abell 2199, Abell 2399), which is the 20% of the sample. Additionally, 10 more clusters present weaker indications or rotation (Abell 279, Abell 1775a, Abell 2593, Abell 690, Abell 1468, Abell 1569b, Abell 1738, Abell 2089, Abell 2107, Abell 2670) and there is not a cluster that presents indications of rotation in the 0.5-2.5 Mpc configuration but not in the 2.5 Mpc one. Overall, 19 out of the 45 clusters of the sample are rotating either in the 2.5 Mpc or the 0.5-2.5 Mpc configuration, which is the ∼42% of our cluster sample.

There is the possibility that 5 of the clusters mentioned above (Abell 2199, Abell 1508, Abell 1291b, Abell 1569a, Abell 2670) may contain substructures and their rotation signal may not be realistic. Our statistics would be affected in this case. If all the clusters that are possible to contain substructures do contain, then 5 out of 45 clusters are rotating (∼11% of the cluster-sample) and 14 out of the 45 clusters, the ∼31% of the sample, are possibly rotating. These results are summarized in the table.

2.5 Mpc and 0.5-2.5 Mpc configurations

	Rotating clusters	**Possibly rotating clusters**
No substructures	∼20%	∼42%
Clusters with substructures	∼11%	∼31%

Taking into account the rotation in all configurations, 15 out of 45 clusters are rotating (∼33% of the sample) and 8 additional clusters are possible to rotate (overall ∼50% of the sample). If the substructures detected actually exist, then 18 out of the 45 clusters are certainly or possibly rotating, the ∼40% of our sample.

There are 3 cases where the rotation signal is strengthened when moving from the 1.5 Mpc configuration to the 2.5 Mpc configuration (Abell 1177, Abell 2399, Abell 1291b) and there are also 6 cases where the exact opposite case occurs (Abell 279, Abell 1738, Abell 1775a, Abell 2107, Abell 2255, Abell 2670). In the former case we would conclude that the outer parts of the cluster are rotating and this rotation was probably caused by recent mergers of clusters. In the latter case, one would conclude that rotation is due to initial angular momentum of clusters, attributed during their formation and preserved until their virialisation. It seems that the latter case is more likely to occur. However, due to the small statistical sample of these events, we cannot conclude for the origin of rotation of clusters.

Finally, we do not find a preferable clockwise or counterclockwise direction of rotation among the rotating or possibly rotating clusters, as we expected.

2.6.2 Special cases

There were some cases, where the 0-1 Mpc angular configuration was also studied. This occurred for clusters that we had visual evidence their radius extended up to 1 Mpc. They either presented small vacuum areas in their spatial distribution of galaxies or they had a denser core. Almost all of them presented greater indications of rotation in this configuration, which confirms our speculation (Abell 2029, Abell 1656, Abell 2147, Abell 2399). The one that did not present more prominent rotation signal consisted of a small number of members (Abell 1468).

2.7 Correlations between rotation parameters and virial index

We try to find correlations between several observational properties and indications of rotation of the clusters. We use the Spearman Rank-Order Correlation Coefficient test (Numerical Recipes in Fortran 77, [73], p.635). In the next, r_s is the correlation coefficient between two values and $probr_s$ the statistical significance of this result. Positive correlation coefficient means positive correlation, while negative correlation coefficient means anti-correlation; zero value means the two objects are not correlated. A small value of $probr_s$ indicates a significant correlation or anti-correlation.

First of all, we find that the number of galaxies of a cluster is correlated with the number of its bright galaxies; the larger the number of galaxies, the larger the number of bright galaxies. This confirms the fact that rich clusters have a large number of bright galaxies. We also find that the number of galaxies of the clusters is anti-correlated with their redshift, as we expected. As we observe at more distant areas in the Universe, we observe less galaxies and, therefore, less rich clusters. These results come up in all configurations; those for 1.5 Mpc and 2.5 Mpc configurations are shown in the table below and in figure 31 for the 2.5 Mpc configuration.

We would also like to confirm that the Bautz-Morgan type of the clusters is correlated with their X-ray isophotals' shapes. This means that the virial state of the cluster is reflected in its X-ray emission shape; a virialised cluster should have spherical isophotals. This is confirmed in all configurations and the results of the 1.5 Mpc and 2.5 Mpc configurations are shown.

	Angular config.	r_s	$probr_s$
Number of bright galaxies - Number of galaxies	0-1.5	0.512	0.00271688
Number of bright galaxies - Number of galaxies	0-2.5	0.644	0.00002289
Redshift - Number of galaxies	0-1.5	-0.561	0.00082995
Redshift - Number of galaxies	0-2.5	-0.559	0.00038962

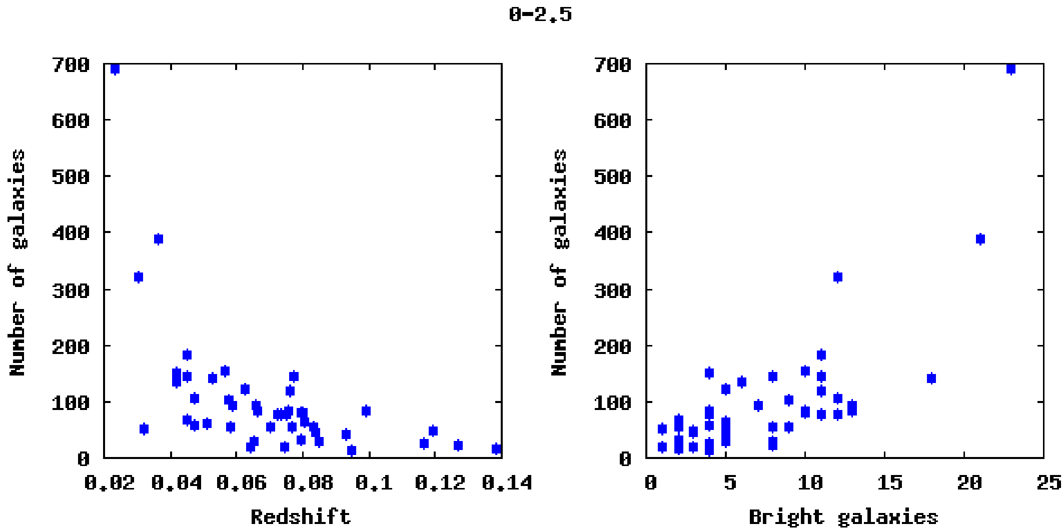

Figure 31: *Left:* Number of galaxies as a function of cluster redshift. *Right:* Number of galaxies as a function of the number of bright galaxies. Both are shown for the 2.5 Mpc configuration.

	Angular config.	r_s	$probr_s$
X-ray isophotals - Bautz-Morgan type	0-1.5	0.426	0.02664495
X-ray isophotals - Bautz-Morgan type	0-2.5	0.459	0.01064785

We are now checking the correlation between the indications of rotation we use to deduct rotation. We find that the value of the Kolmogorov-Smirnov probability, the value of the fraction of χ^2 minimization test between the ideal and real rotation diagrams to the χ^2 minimization test between the random and real rotation diagrams and the optical identification of rotation from the rotation diagram are all correlated with each other in all angular configurations. As a result, all three can deduct rotation; on condition that one of them shows rotational signal, the other two will also show rotational signal. The results for the 1.5 Mpc and 2.5 Mpc configurations are shown in the table below; for the 2.5 Mpc configuration also look at figure 32.

	Angular config.	r_s	$probr_s$
Kolmogorov-Smirnov probability - Fraction of χ^2	0-1.5	0.719	0.00000238
Kolmogorov-Smirnov probability - Fraction of χ^2	0-2.5	0.826	0.00000000
Kolmogorov-Smirnov probability - Optical identification	0-1.5	0.790	0.00000005
Kolmogorov-Smirnov probability - Optical identification	0-2.5	0.833	0.00000000
Fraction of χ^2 *- Optical identification*	0-1.5	0.784	0.00000007
Fraction of χ^2 *- Optical identification*	0-2.5	0.860	0.00000000

We have found significant correlations between the rotation amplitude and the three indications of rotation. The larger the rotation amplitude, the stronger indications of rotation appear on the cluster. These results are valid in all configurations, but those for the 1.5 Mpc and 2.5 Mpc configurations are shown; some of them are plotted in figure 32.

In the 2.5 Mpc configuration we have found correlation between the X-ray isophotal shape of the

	Angular config.	r_s	$probr_s$
Rotation amplitude - Kolmogorov-Smirnov probability	0-1.5	-0.719	0.00000240
Rotation amplitude - Kolmogorov-Smirnov probability	0-2.5	-0.644	0.00002233
Rotation amplitude - Fraction of χ^2	0-1.5	-0.676	0.00001597
Rotation amplitude - Fraction of χ^2	0-2.5	-0.623	0.00005003
Rotation amplitude - Optical identification	0-1.5	-0.571	0.00051731
Rotation amplitude - Optical identification	0-2.5	-0.485	0.00271012

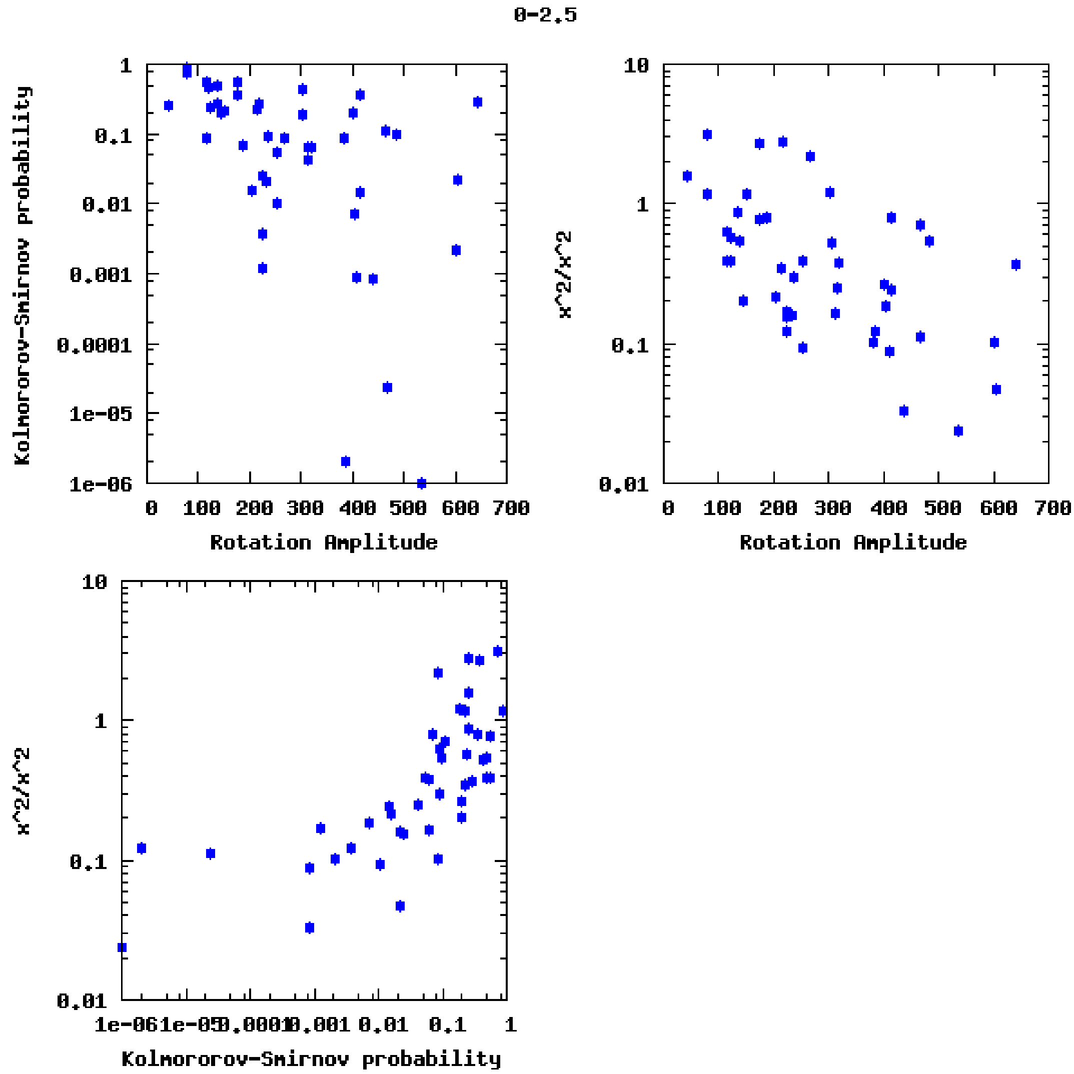

Figure 32: *Top Left:* Rotation amplitude as a function of the Kolmogorov-Smirnov probability value. *Top Right:* Rotation amplitude as a function of the value of the fraction of χ^2 minimization test between the ideal and real rotation diagrams to the χ^2 minimization test between the random and real rotation diagrams. *Bottom:* Rotation amplitude as a function of the optical rotation identification. All are shown for the 2.5 Mpc configuration.

clusters and the fraction of χ^2 minimization test values as well as the Kolmogorov-Smirnov probability test values. The correlations indicate that there is dependence of the rotation with the virial state of the cluster, which is associated with the X-ray isophotal shape and, consequently, the Bautz-Morgan type of the clusters. It is more often that clusters with non-spherical isophotals seem to present indications of rotation. There is also a correlation between the X-ray isophotal shape and the rotation amplitude of the clusters; this means that if the isophotals are not spherical, the rotation amplitude detected is bigger.

It is possible that the large angular momentum of the cluster has caused the distortion of the spherical shape of the isophotals. These correlations are shown in the table below, for the 2.5 Mpc configuration.

	Angular config.	r_s	$probr_s$
X-ray isophotal shape - Kolmogorov-Smirnov probability	0-2.5	-0.347	0.05999119
X-ray isophotal shape - Fraction of χ^2	0-2.5	-0.494	0.00552332
X-ray isophotal shape - Rotation amplitude	0-2.5	0.455	0.01143488

Correlation has been found in the 1.5 Mpc configuration between the number of galaxies and the optical identification as well as the number of bright galaxies and the optical configuration. There has been also found correlation between the number of galaxies and the Kolmogorov-Smirnov probablility test values. The smaller number of galaxy-members (or bright members) the cluster contains, the less prominent its optical identification or Kolmorogov-Smirnov indication of rotation is. The results of the correlations are shown for the 1.5 Mpc configuration in the table below.

	Angular config.	r_s	$probr_s$
Number of bright galaxies - Optical identification	0-1.5	-0.308	0.08628161
Number of galaxies - Optical identification	0-1.5	-0.349	0.05016239
Number of galaxies - Kolmogorov-Smirnov probability	0-1.5	-0.368	0.03841897

We have also found some additional correlations in the 2.5 Mpc configuration: the cluster redshift is correlated with both the Kolmogorov-Smirnov probability and the fraction of χ^2 values. The more distant the cluster is, the more difficult is to detect its rotation. In addition, we have found correlation between the number of bright galaxies of the cluster and the angle of its rotation axis.

	Angular config.	r_s	$probr_s$
Redshift - Kolmogorov-Smirnov probability	0-2.5	0.321	0.05650315
Redshift - Fraction of χ^2	0-2.5	0.336	0.04500924

In the 0.3-1.5 Mpc configuration we found that the number of galaxy-members is anti-correlated with the Kolmogorov-Smirnov probability value. This means that the smaller the number of members, the most prominent is to deduct the rotation using the Kolmogorov-Smirnov probability test. We have also found correlations between the Kolmogorov-Smirnov probability test value and the cluster redshift, Bautz-Morgan type and number of bright members. This correlation mean that: the more distant and less rich the object, the less prominent its rotation identification is, and, last but not least, the less virialised the cluster, the stronger the Kolmorogov-Smirnov indication of rotation is.

	Angular config.	r_s	$probr_s$
Redshift - Kolmogorov-Smirnov probability	0.3-1.5	0.321	0.05650315
Number of bright galaxies - Kolmogorov-Smirnov probability	0.3-1.5	0.336	0.04500924
Bautz-Morgan type - Kolmogorov-Smirnov probability	0.3-1.5	0.336	0.04500924

We have not found any correlations between the number of galaxies and the rotation amplitude, as we should; we did not want our method to be biased by the number of members or richness of the cluster. We have not also found correlation between the Bautz-Morgan type and the number of galaxies or redshift, as we expected.

3 Conclusions

In this thesis we studied the possible rotation of a sample of clusters. We developed a new algorithm in order to be able to deduce rotation using the line of sight velocities of the galaxy members. We checked the results of this algorithm by applying it on various constructed Monte-Carlo simulated clusters. We also compared our results with the ones based on the Hwang & Lee's method.

Afterwards, we applied our algorithm on a sample of Abell clusters on the SDSS spectroscopic database. We used four parameters in order to deduce the rotation: the χ^2 between the real and ideal rotation curve, the χ^2 between the real rotation curve and the random curve, their expectation ratio and the Kolmogorov-Smirnov probability of galaxy velocities between the two semispheres of the cluster. We calculated the rotation amplitude, direction of rotation axis, projected direction of rotation and rotation center. We found 27 possible rotating clusters, some of them probably having the rotation signal being due to substructures, among the 45 of our sample ($\sim$60% of the sample). This result has an outcome: calculations of the cluster mass in cosmological research using the virial equilibrium of the cluster should be corrected to include the rotation of the galaxies, as we mentioned in section 1.4. This is a very important result, as galaxy clusters are widely and effectively used as cosmological probes to constrain cosmological parameters and determine the current cosmological model. Unfortunately, we could not conclude for the origin of the rotation in clusters or on the parts of the clusters where the rotation velocity distribution is more prominent.

Finally, we sought for correlations between the cluster rotation and its dynamical state. We found that the three indications of rotation are correlated with each other as expected and, as a result, even one of them can be used to deduce a possible cluster rotation. The amplitude of the rotation is also correlated with the indications of rotation, which means that the larger the rotation amplitude, the more significant are the indications of rotation. This implies that small amplitude rotation may not be easy to identify, and thus it could pass undetected. We have also found correlation between the X-ray isophotal shape of the clusters and the indications of rotation, which means that virialised clusters tend to show less prominent indications of rotation. This hints to the cause of rotation being due to early anisotropic accretion of matter having significant angular momentum.

A X-ray isophotals

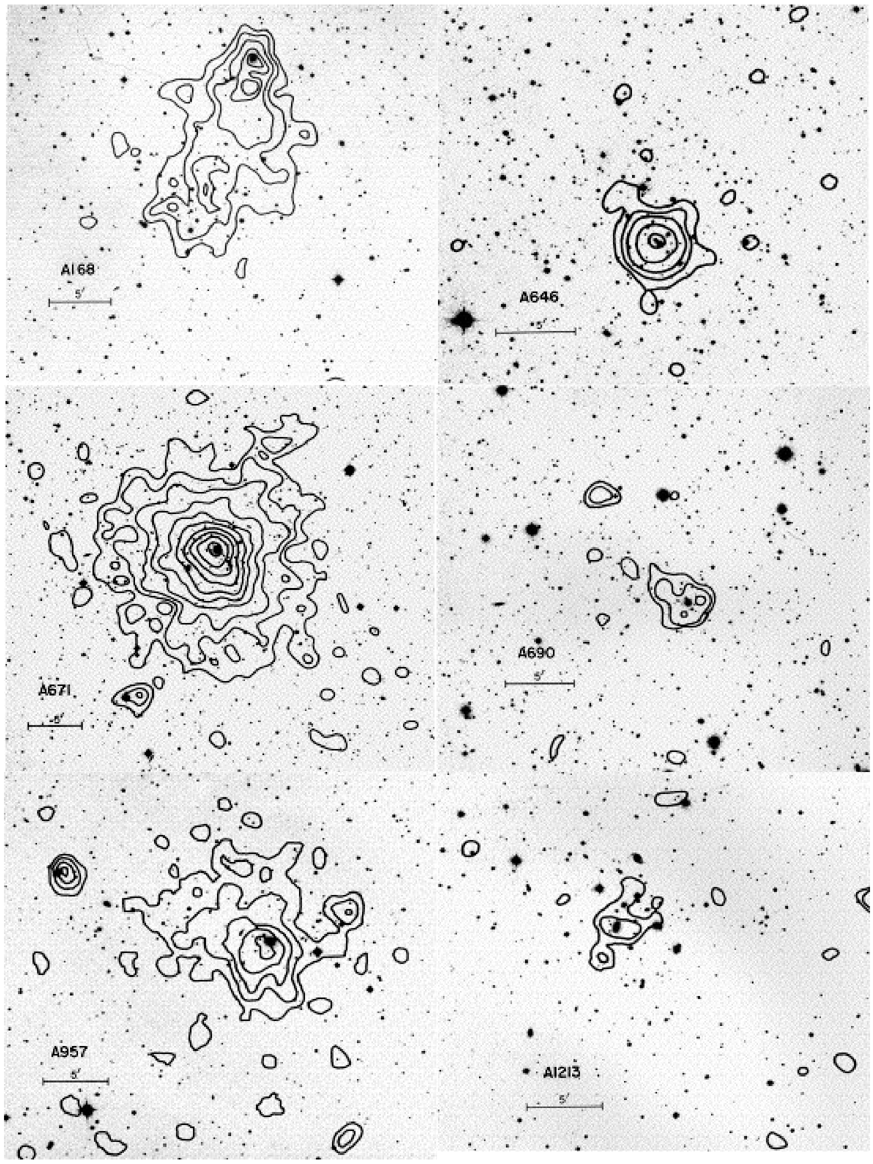

Figure 33: The X-ray isophotals of Abell 168, Abell 646, Abell 671, Abell 690, Abell 957 and Abell 1213 taken from Einstein IPC (1999).

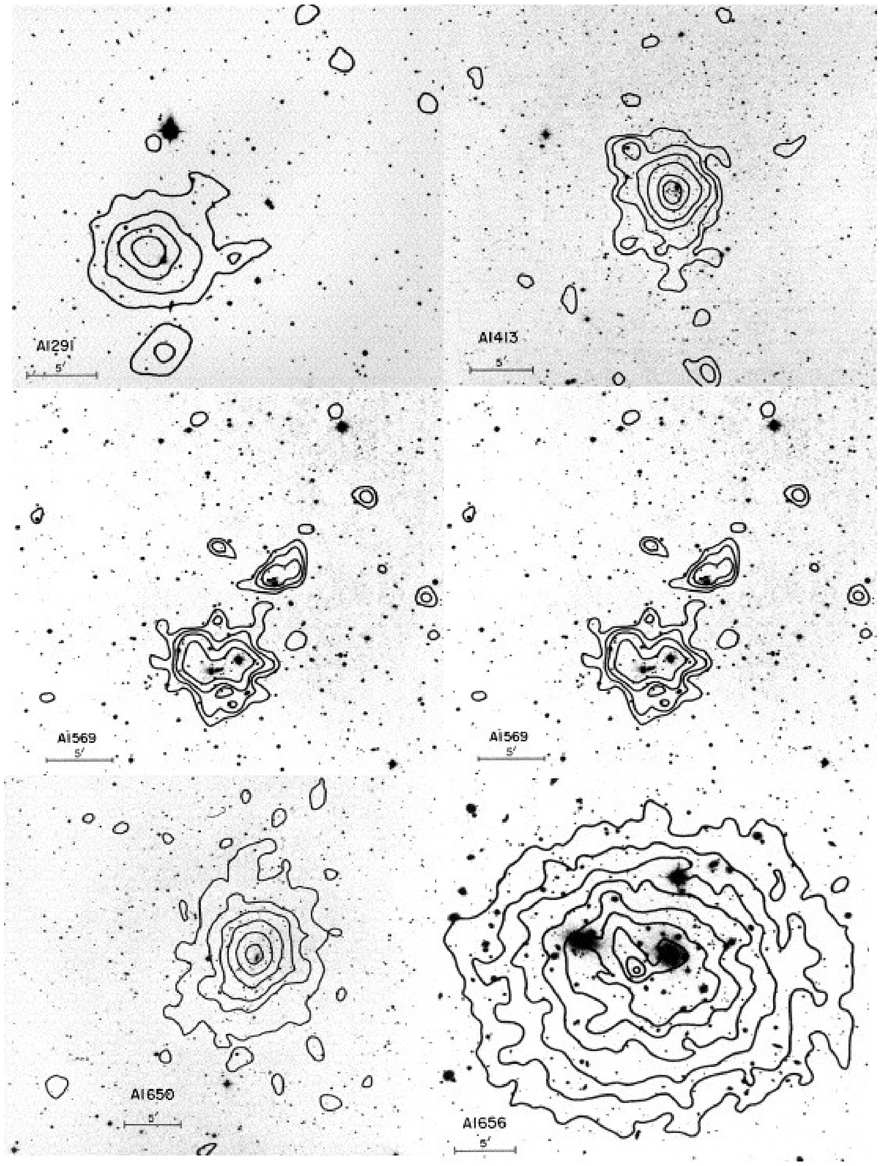

Figure 34: The X-ray isophotals of Abell 1291, Abell 1413, Abell 1569, Abell 1650, Abell 1656 and Abell 1775 taken from Einstein IPC (1999).

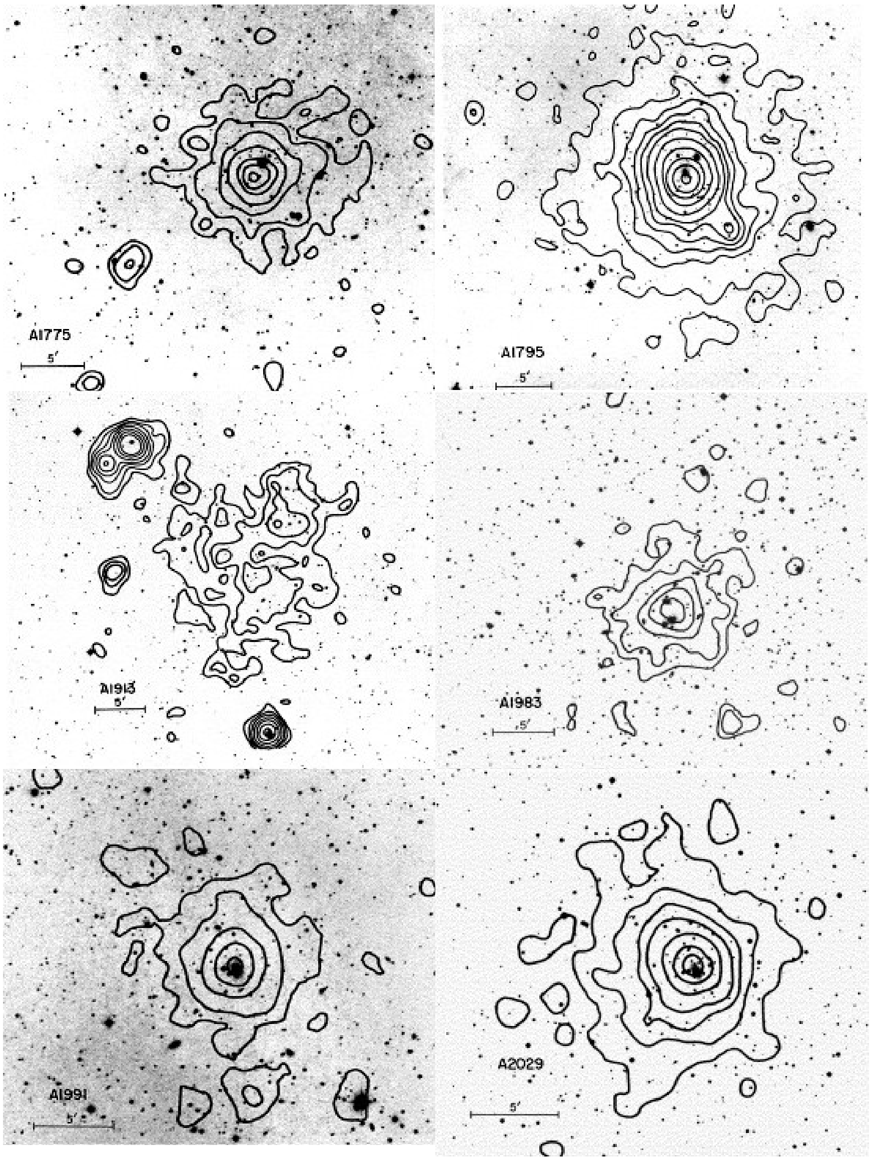

Figure 35: The X-ray isophotals of Abell 1795, Abell 1913, Abell 1983, Abell 1991, Abell 2029 and Abell 2079 taken from Einstein IPC (1999).

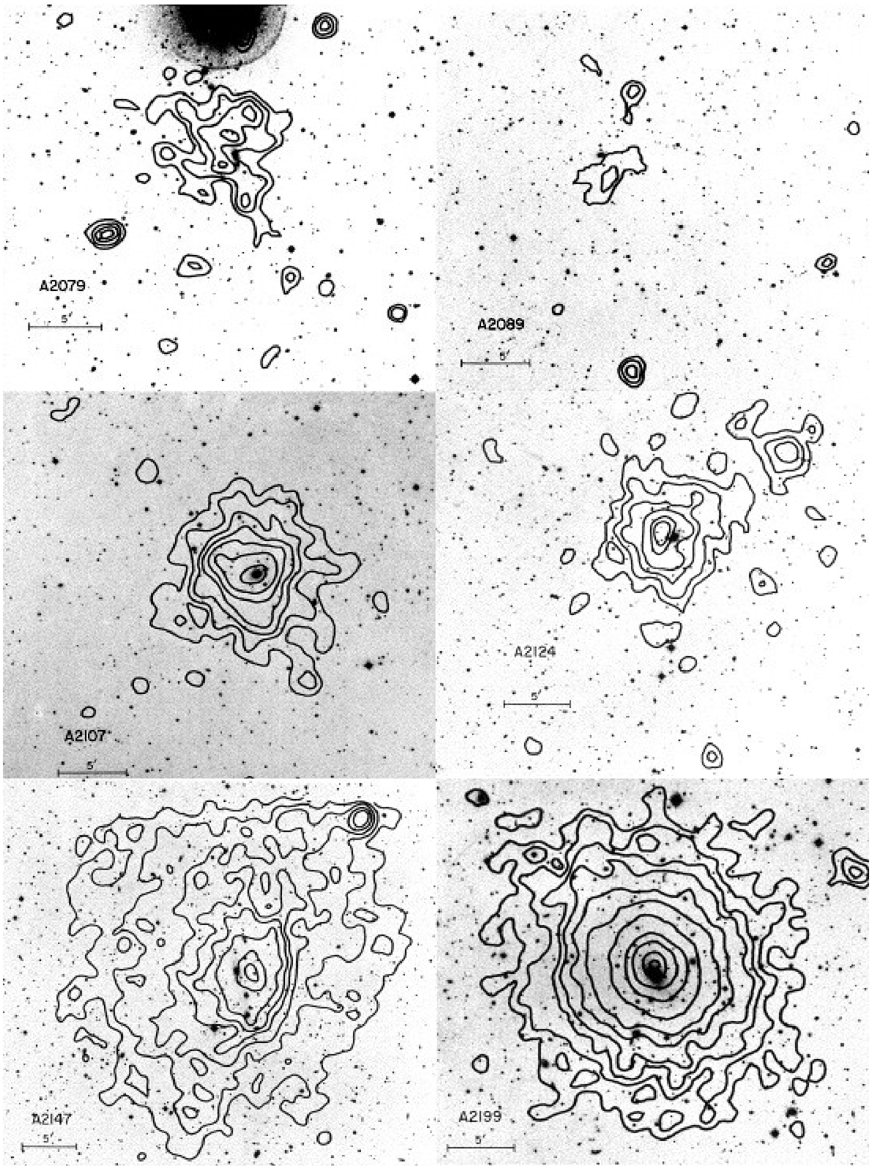

Figure 36: The X-ray isophotals of Abell 2089, Abell 2107, Abell 2124, Abell 2147, Abell 2199 and Abell 2244 taken from Einstein IPC (1999).

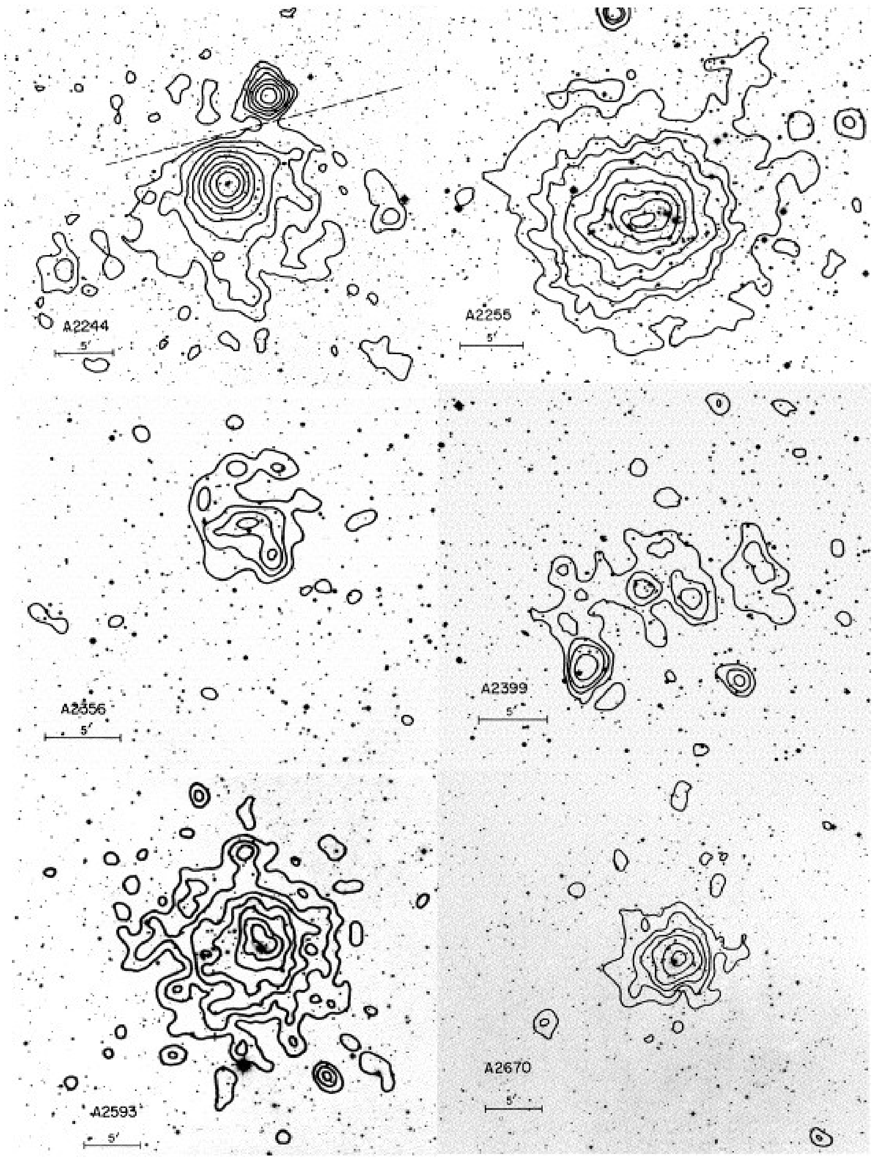

Figure 37: The X-ray isophotals of Abell 2255, Abell 2356, Abell 2399, Abell 2593, Abell 2670 and Abell 1213 taken from Einstein IPC (1999).

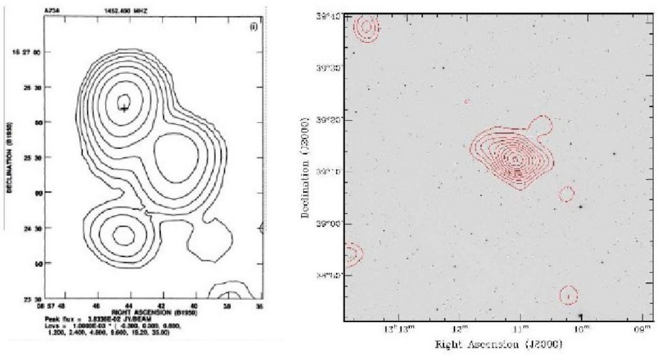

Figure 38: The X-ray isophotals of Abell 734 in the left (by Bagchi & Kapahi (1994)) and Abell 1691 in the right taken from ROSAT.

B Rotation diagrams

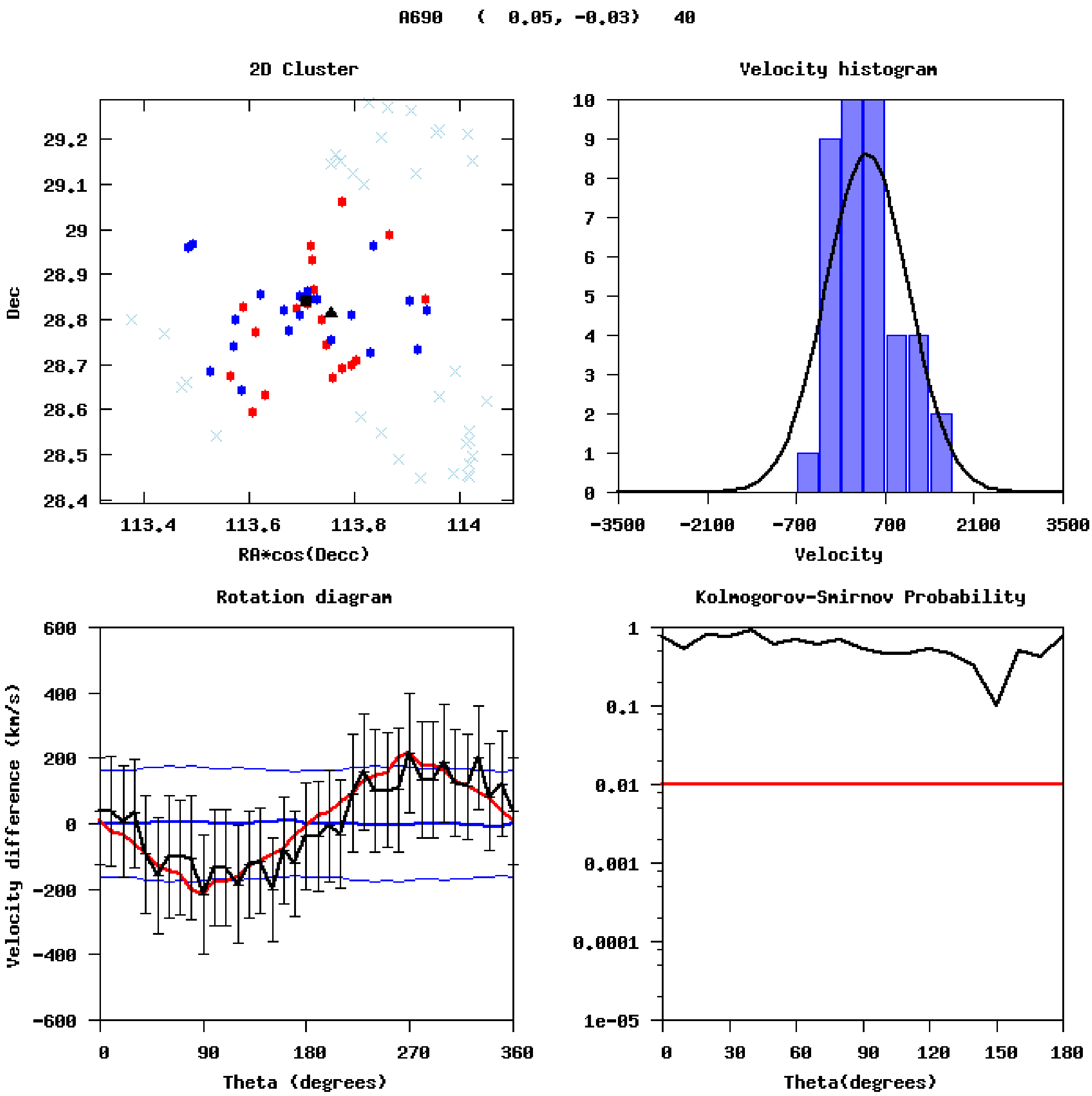

Figure 39: Abell 690 with radius of 1.5 Mpc. The title of the figure indicates the coordinates of the final selected rotational center (dy, dx) and the number of galaxies included in the study.

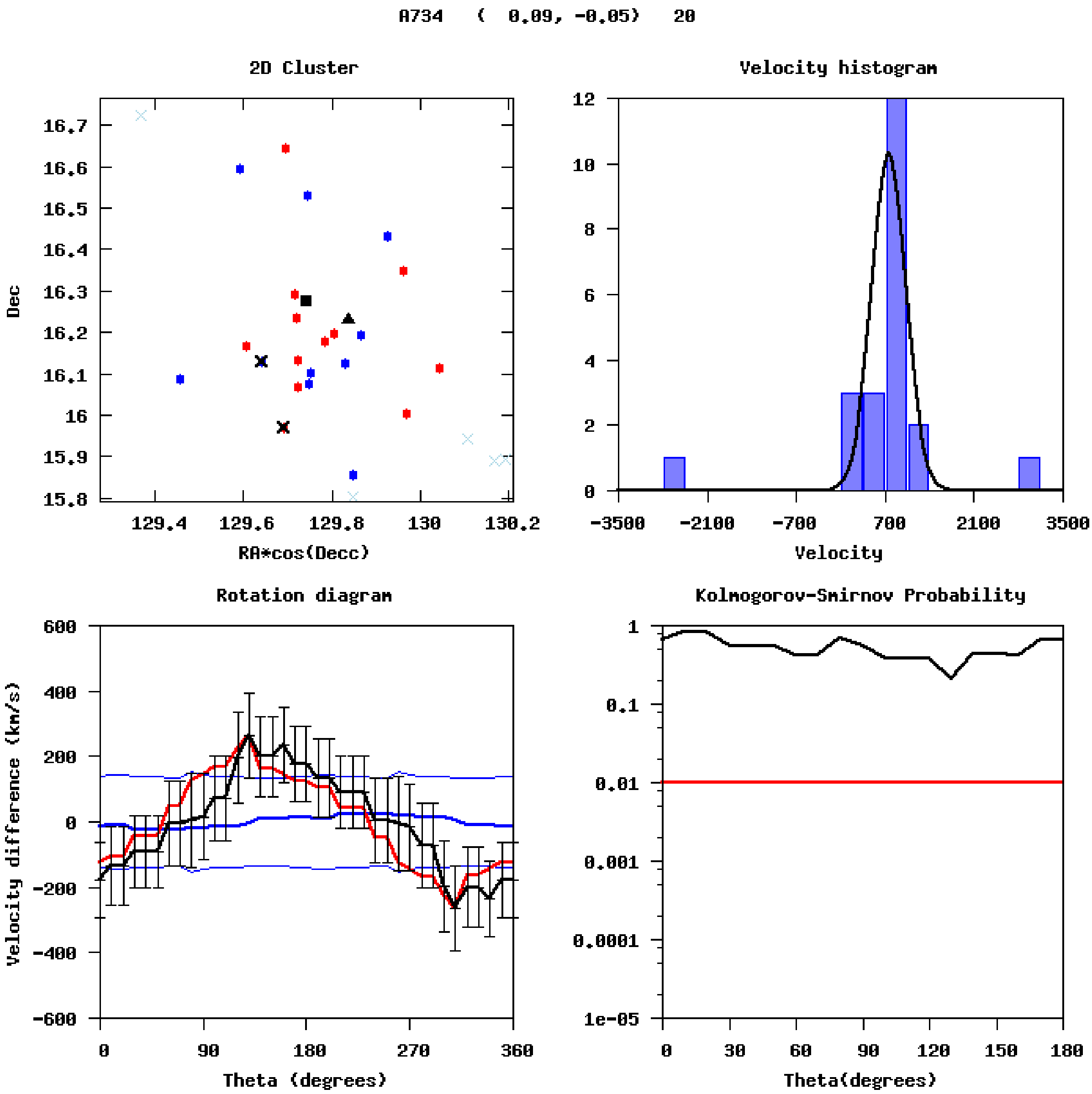

Figure 40: Abell 734 with radius of 2.5 Mpc. The title of the figure indicates the coordinates of the final selected rotational center (dy, dx) and the number of galaxies included in the study.

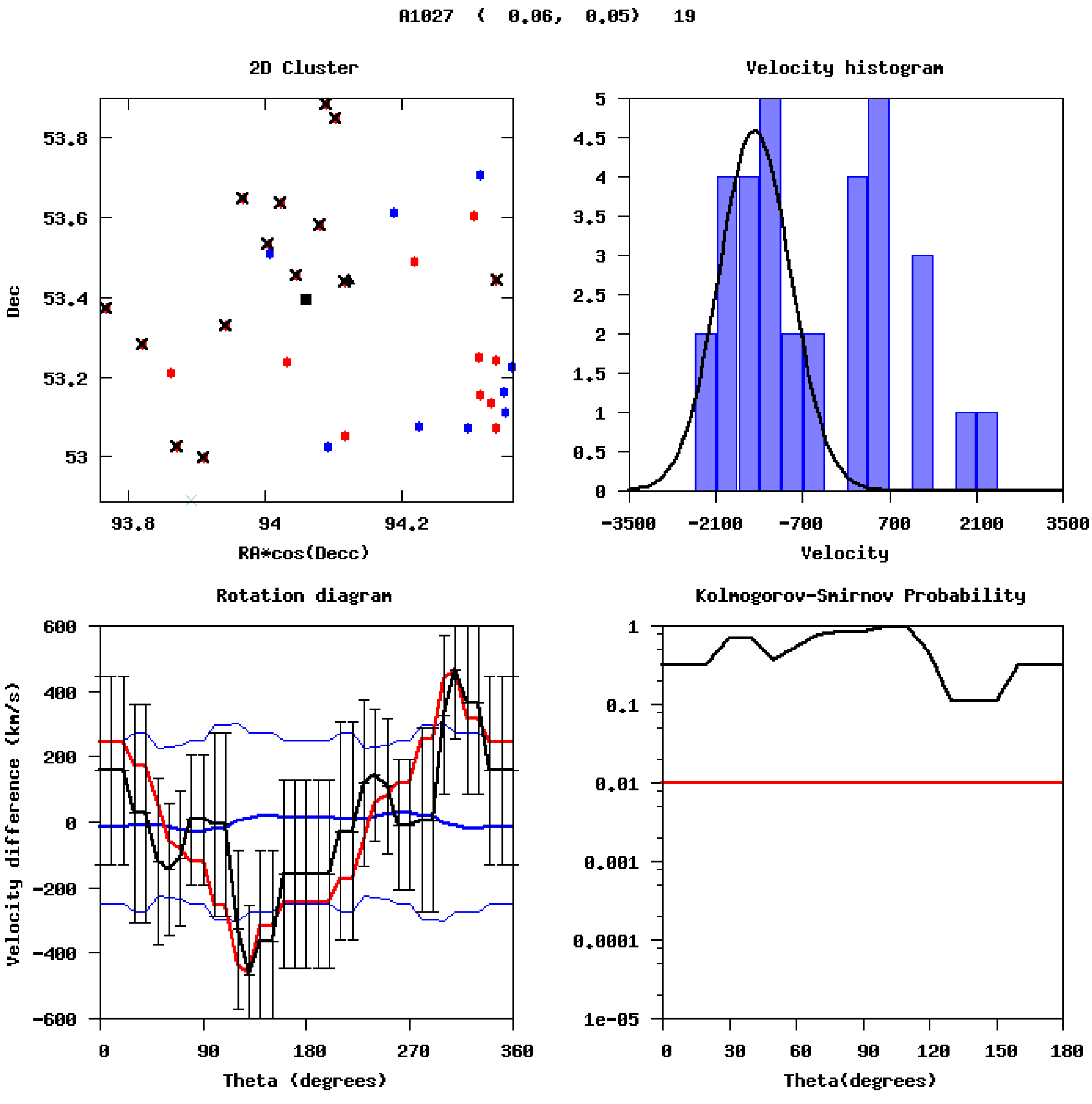

Figure 41: Abell 1027 with radius of 2.5 Mpc. The title of the figure indicates the coordinates of the final selected rotational center (dy, dx) and the number of galaxies included in the study.

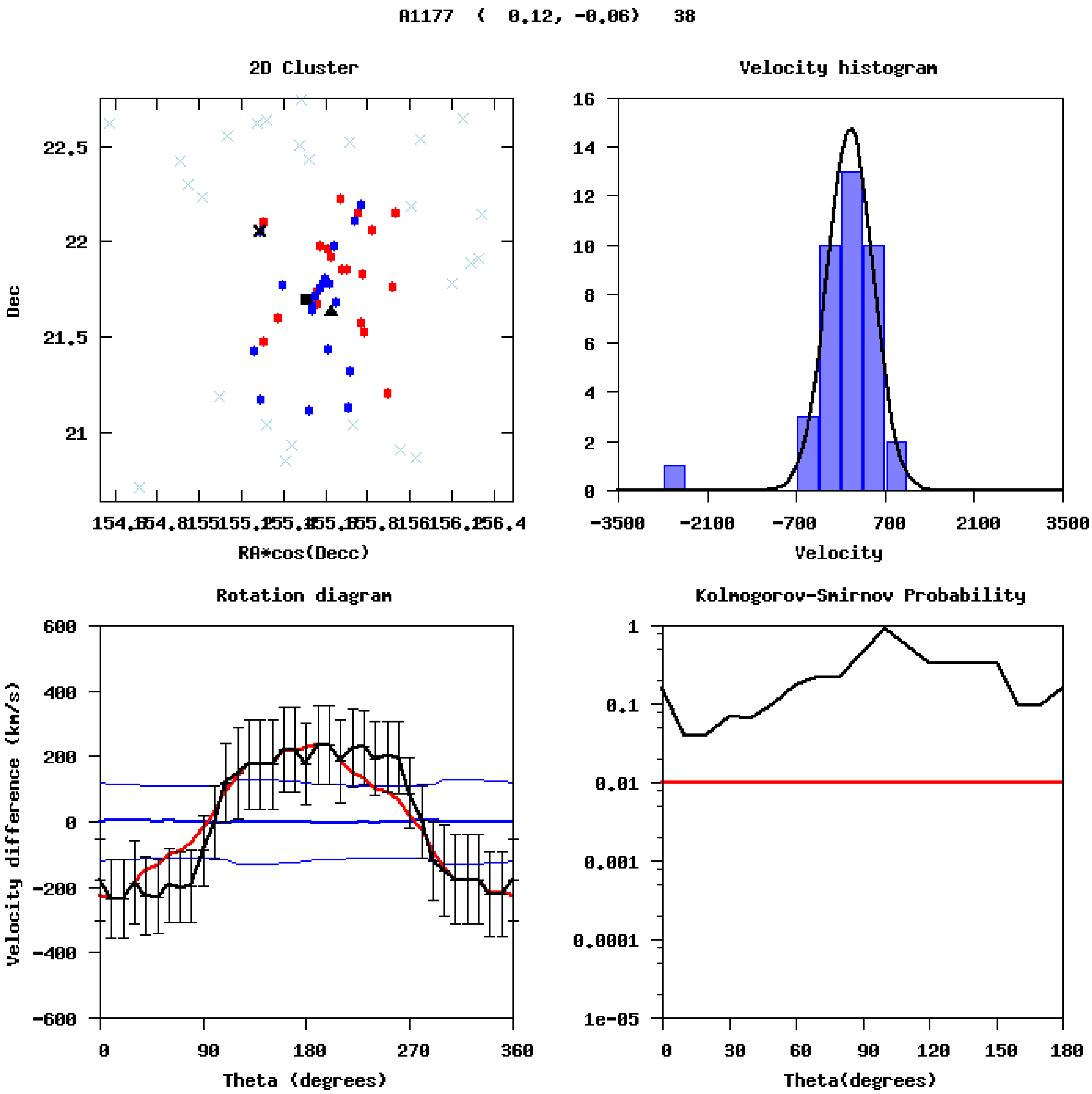

Figure 42: Abell 1177 with radius of 1.5 Mpc. The title of the figure indicates the coordinates of the final selected rotational center (dy, dx) and the number of galaxies included in the study.

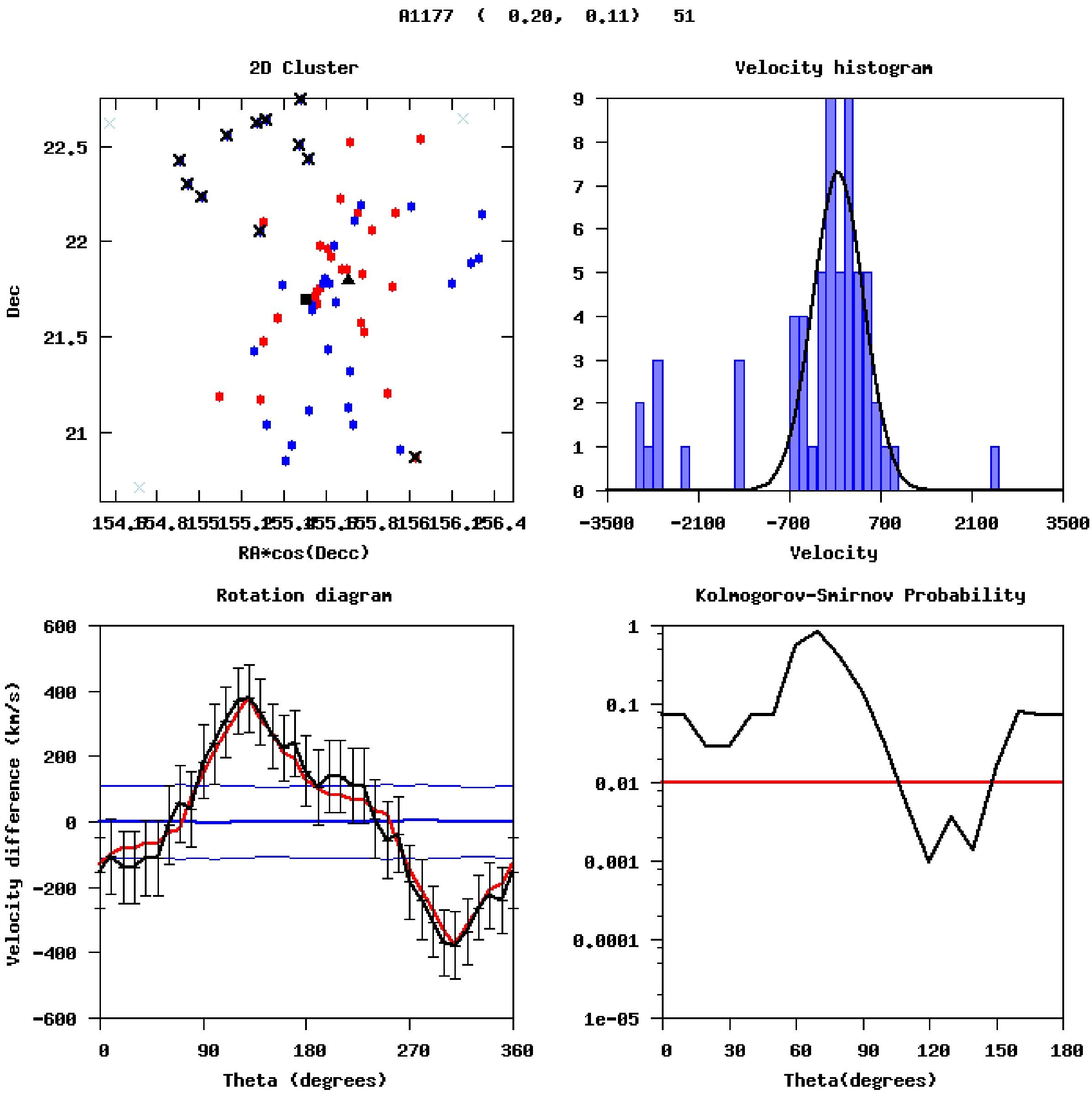

Figure 43: Abell 1177 with radius of 2.5 Mpc. The title of the figure indicates the coordinates of the final selected rotational center (dy, dx) and the number of galaxies included in the study.

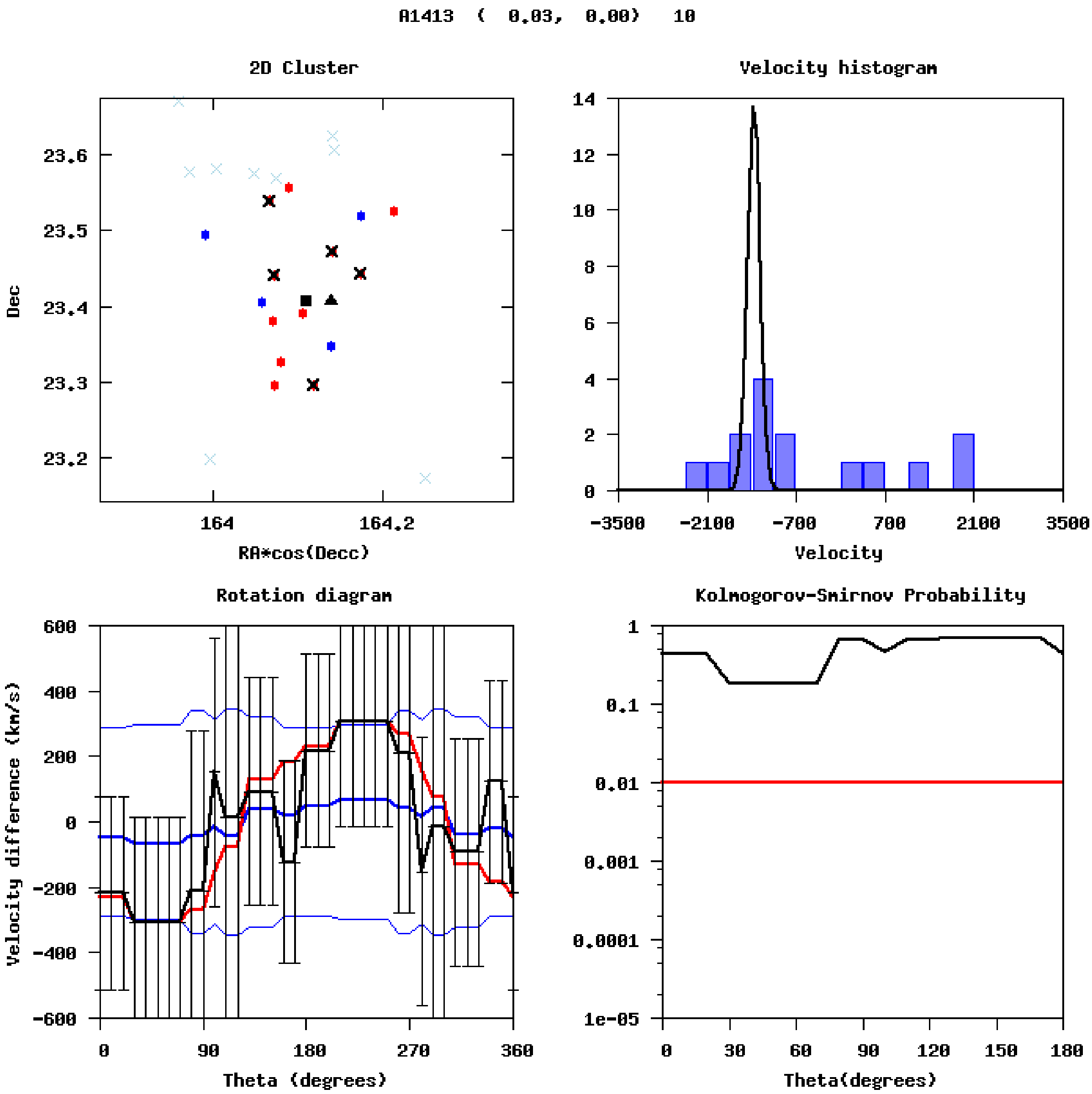

Figure 44: Abell 1413 with radius of 1.5 Mpc. The title of the figure indicates the coordinates of the final selected rotational center (dy, dx) and the number of galaxies included in the study.

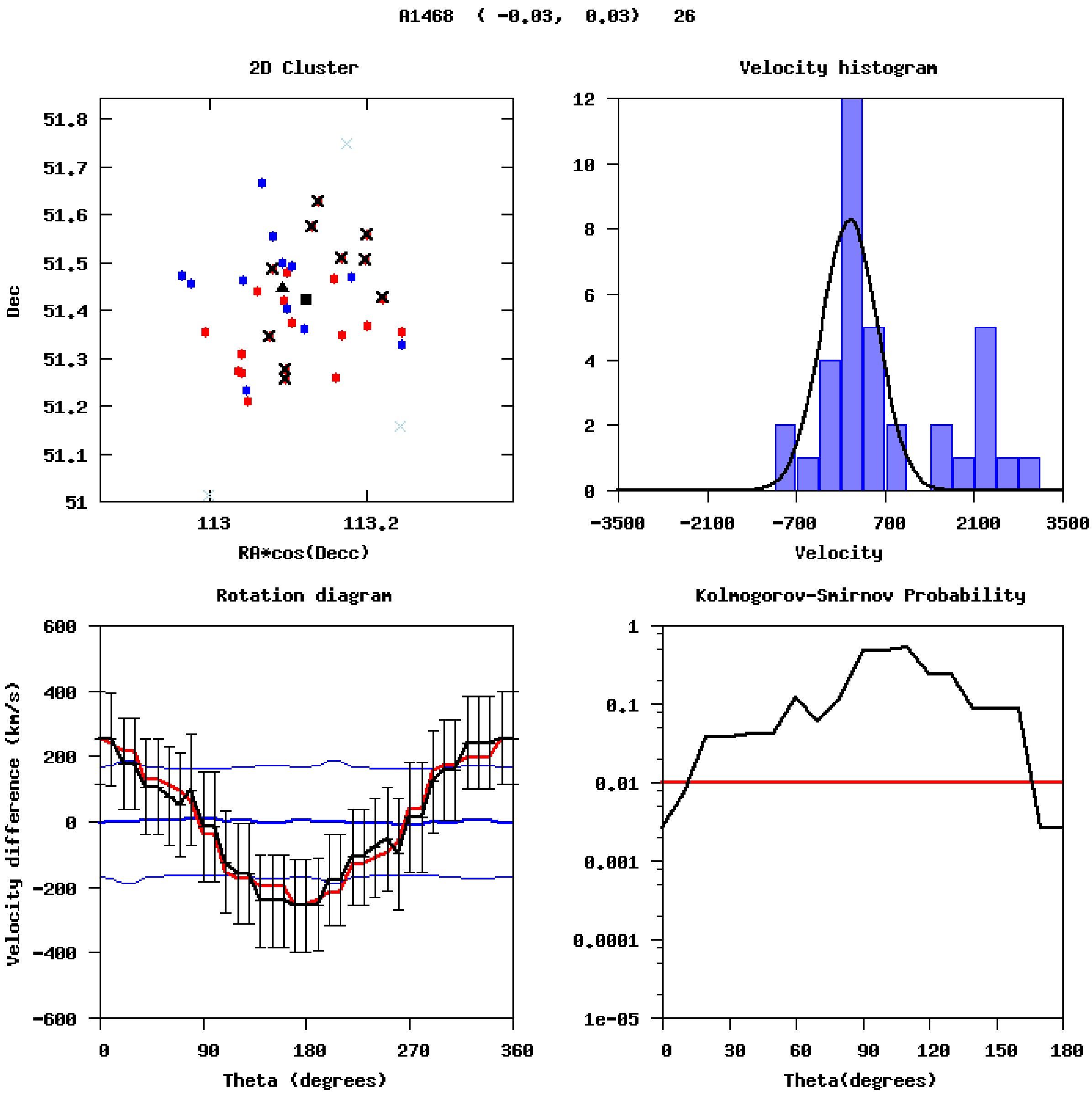

Figure 45: Abell 1468 with radius of 1.5 Mpc. The title of the figure indicates the coordinates of the final selected rotational center (dy, dx) and the number of galaxies included in the study.

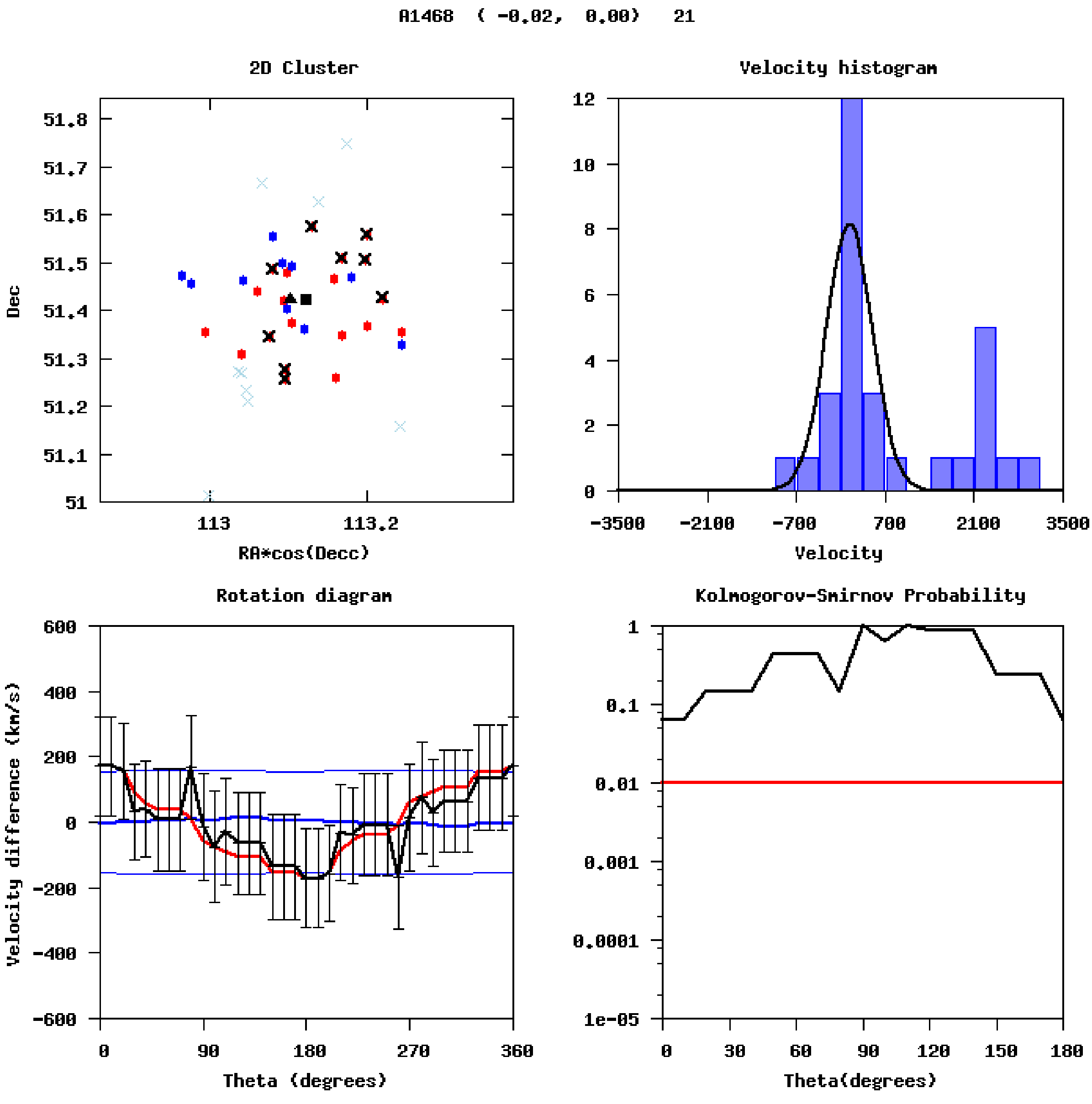

Figure 46: Abell 1468 with radius of 1 Mpc. The title of the figure indicates the coordinates of the final selected rotational center (dy, dx) and the number of galaxies included in the study.

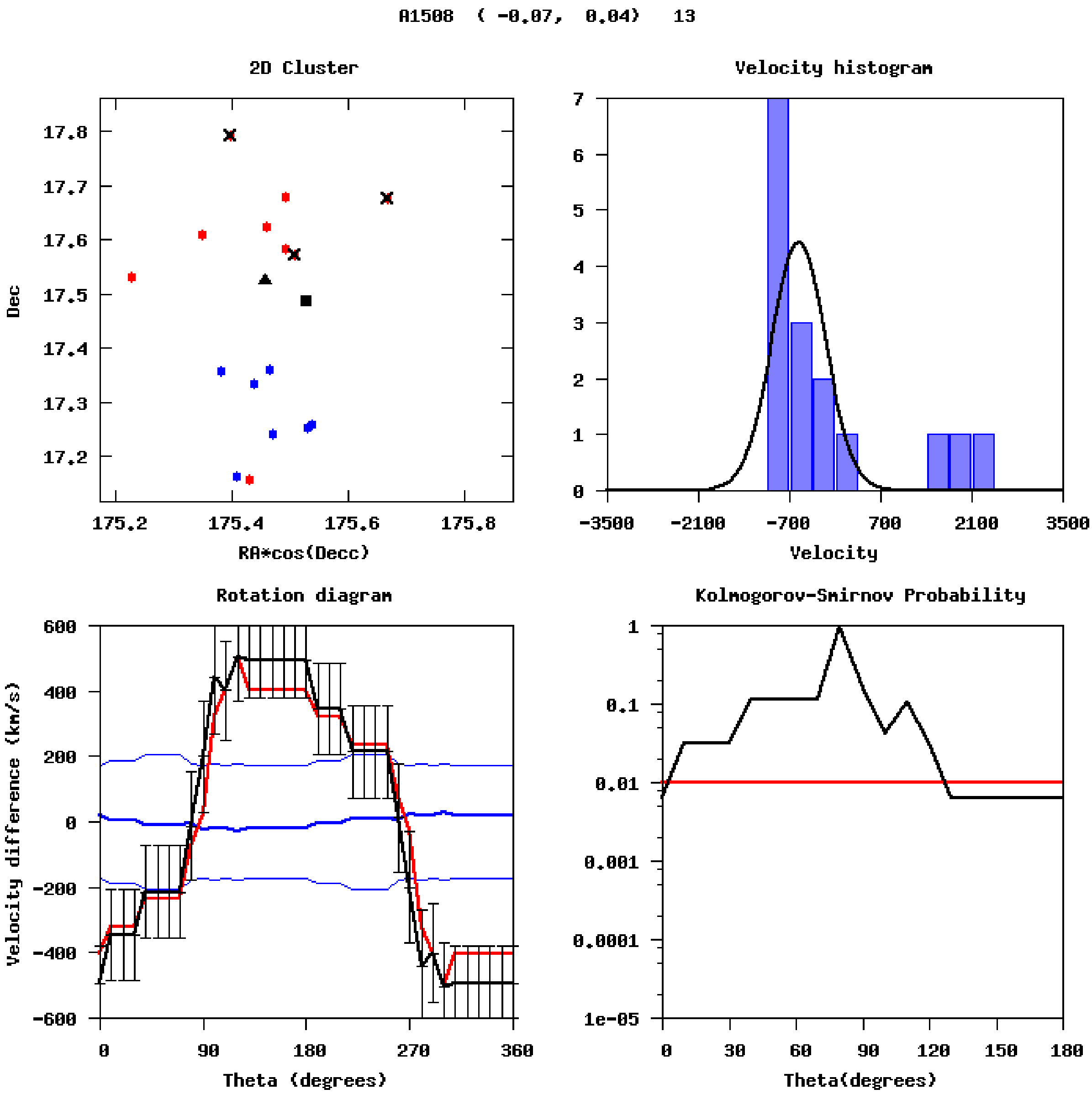

Figure 47: Abell 1508 with radius of 2.5 Mpc. The title of the figure indicates the coordinates of the final selected rotational center (dy, dx) and the number of galaxies included in the study.

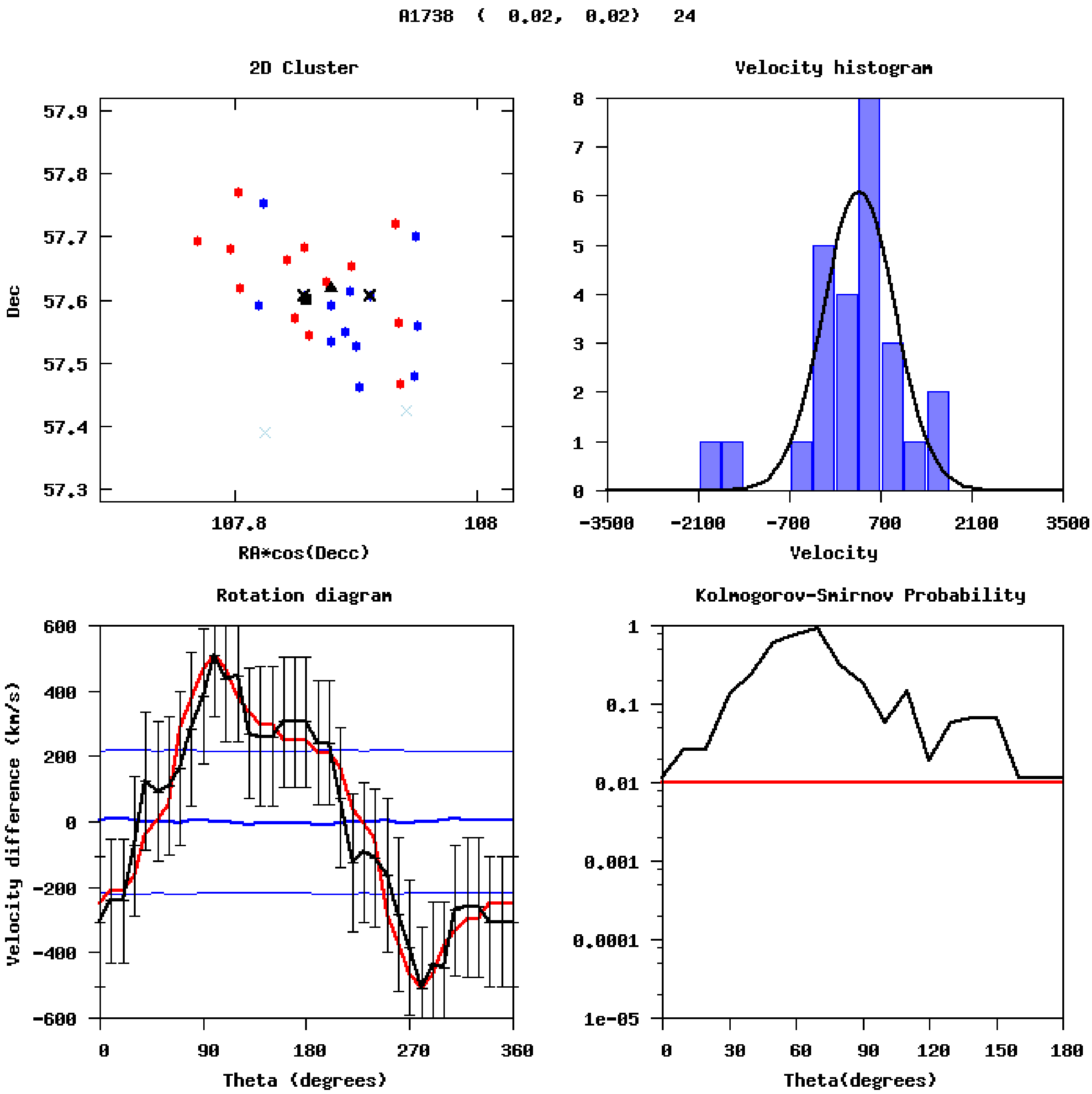

Figure 48: Abell 1738 with radius of 1.5 Mpc. The title of the figure indicates the coordinates of the final selected rotational center (dy, dx) and the number of galaxies included in the study.

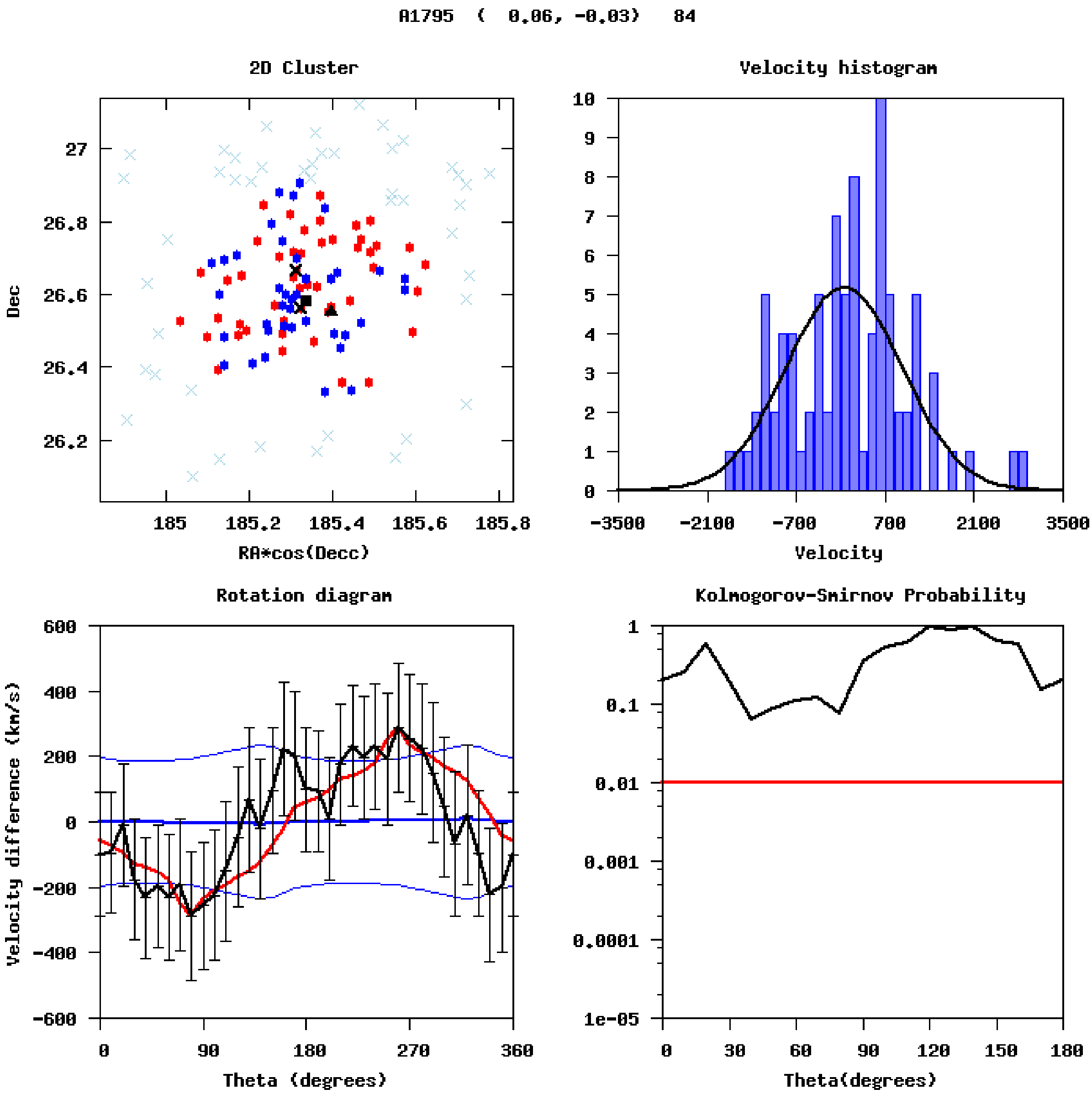

Figure 49: Abell 1795 with radius of 1.5 Mpc. The title of the figure indicates the coordinates of the final selected rotational center (dy, dx) and the number of galaxies included in the study.

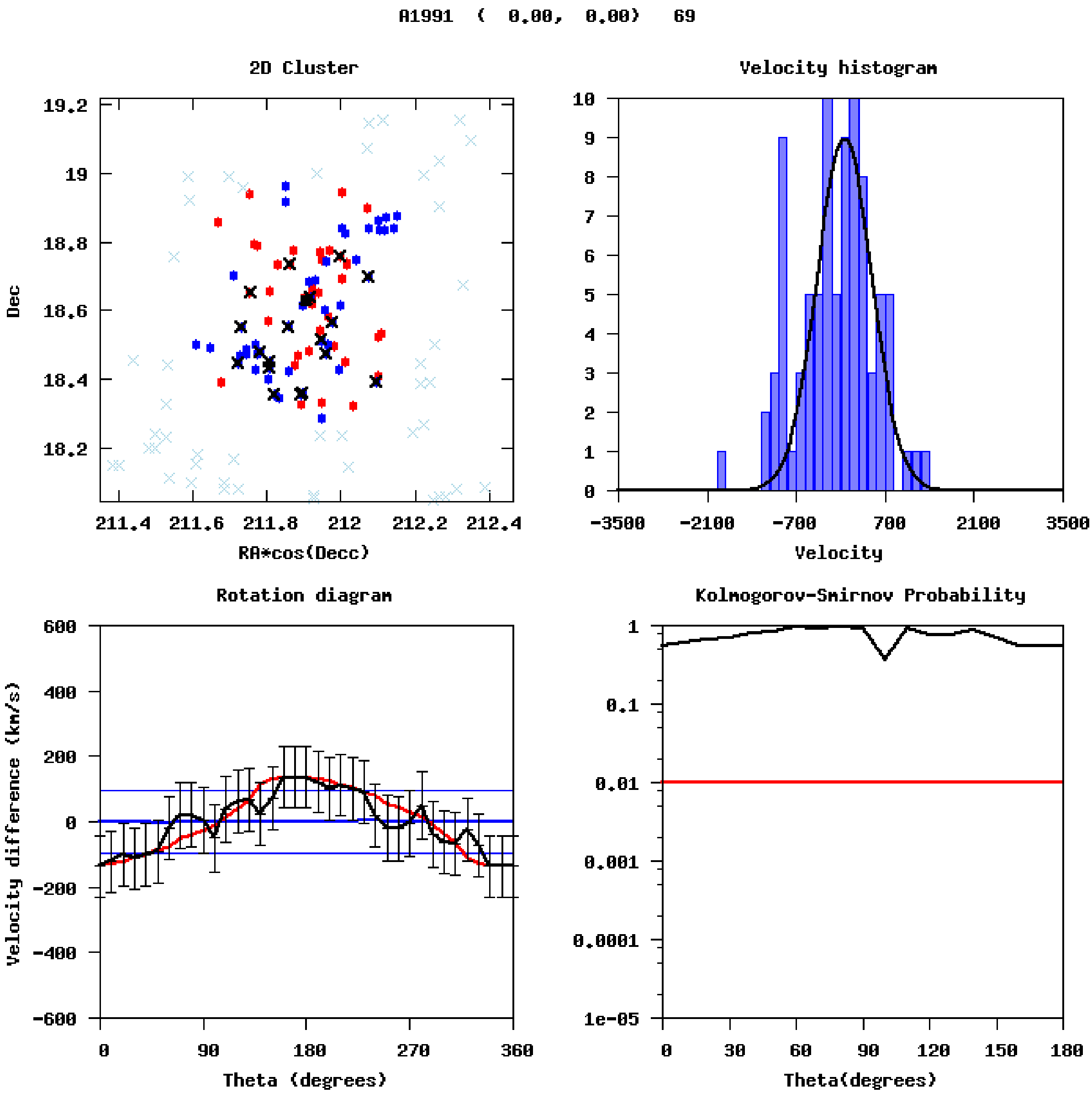

Figure 50: Abell 1991 with radius of 1.5 Mpc. The title of the figure indicates the coordinates of the final selected rotational center (dy, dx) and the number of galaxies included in the study.

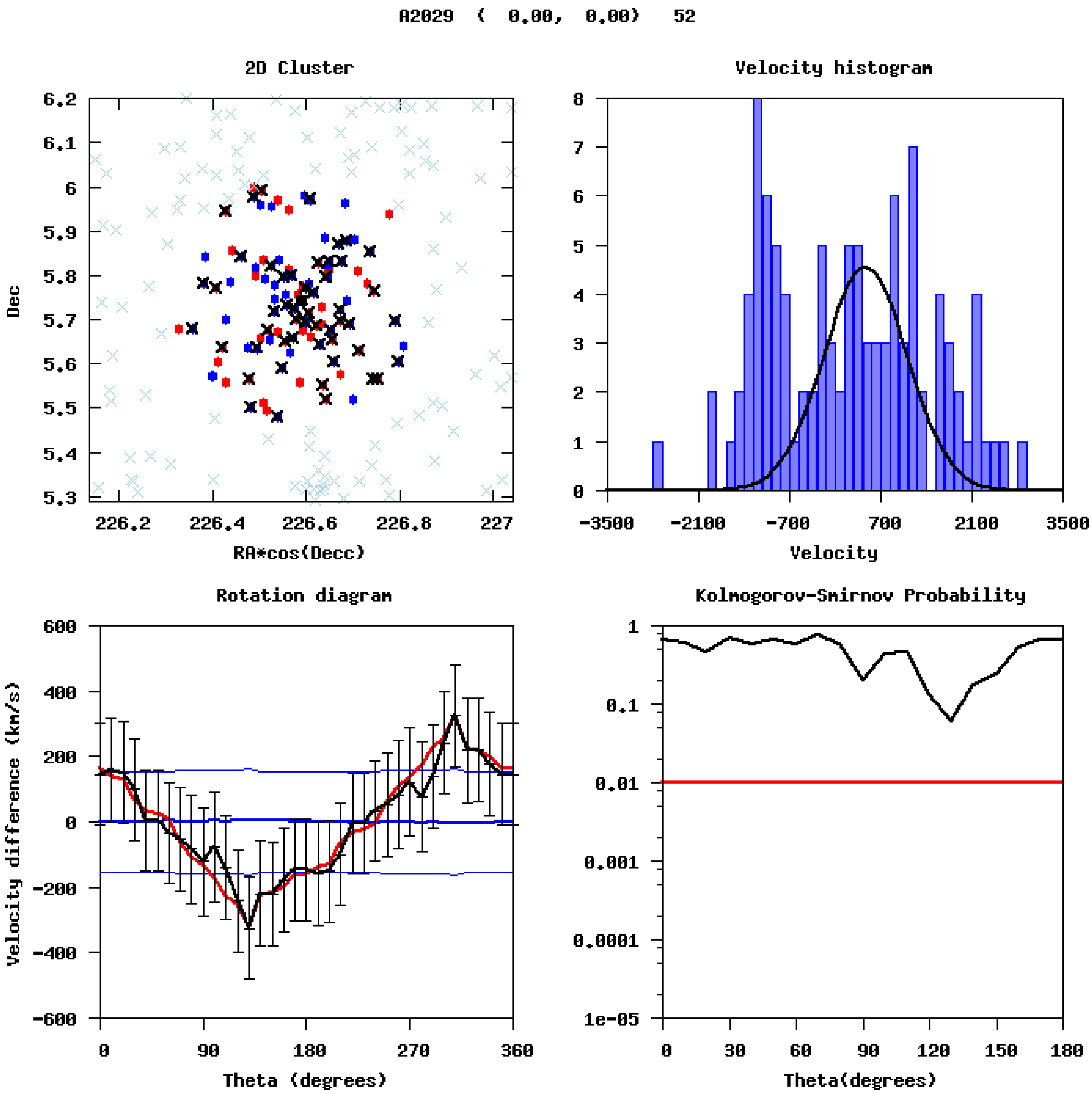

Figure 51: Abell 2029 with radius of 1.5 Mpc. The title of the figure indicates the coordinates of the final selected rotational center (dy, dx) and the number of galaxies included in the study.

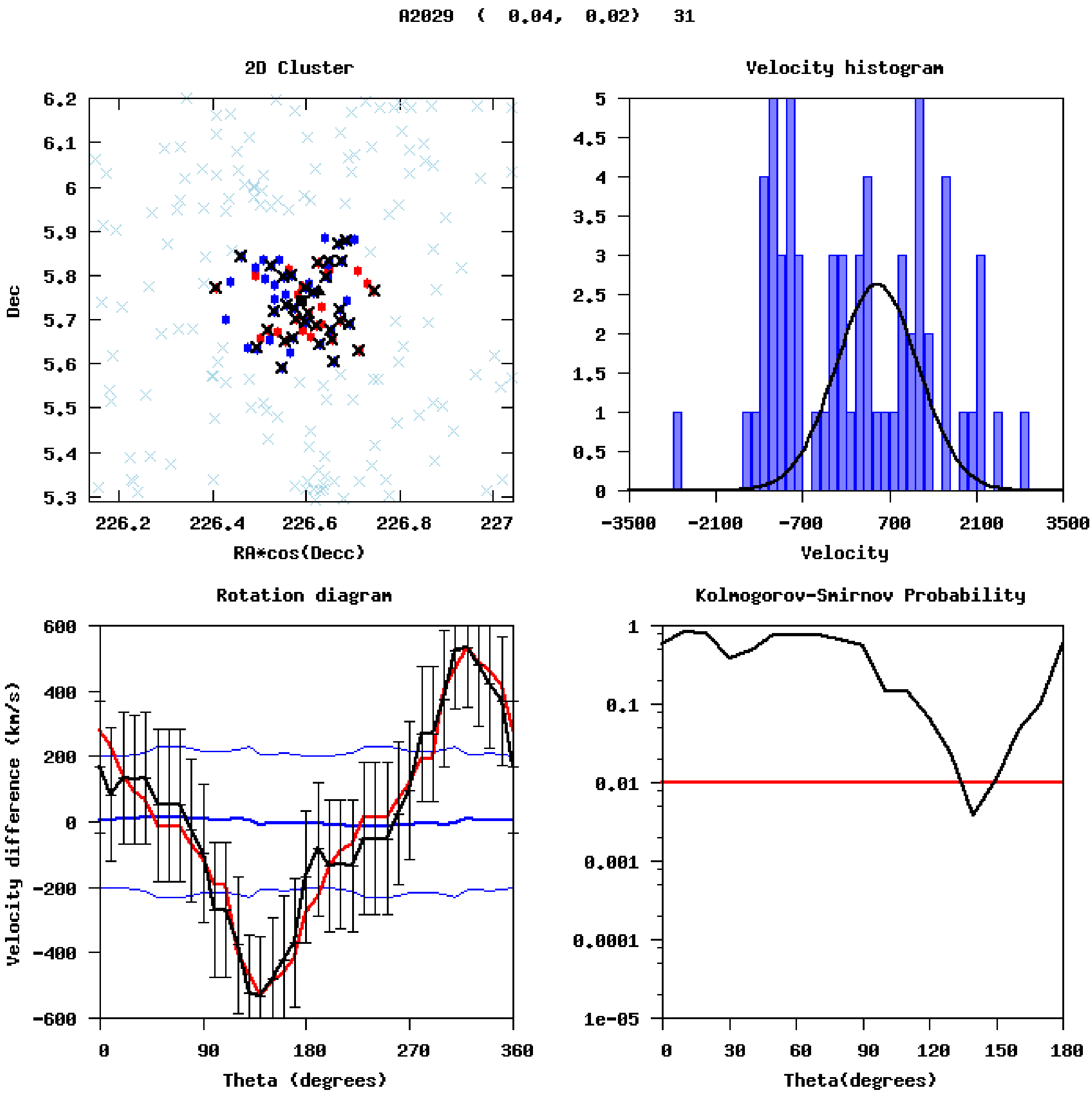

Figure 52: Abell 2029 with radius of 1 Mpc. The title of the figure indicates the coordinates of the final selected rotational center (dy, dx) and the number of galaxies included in the study.

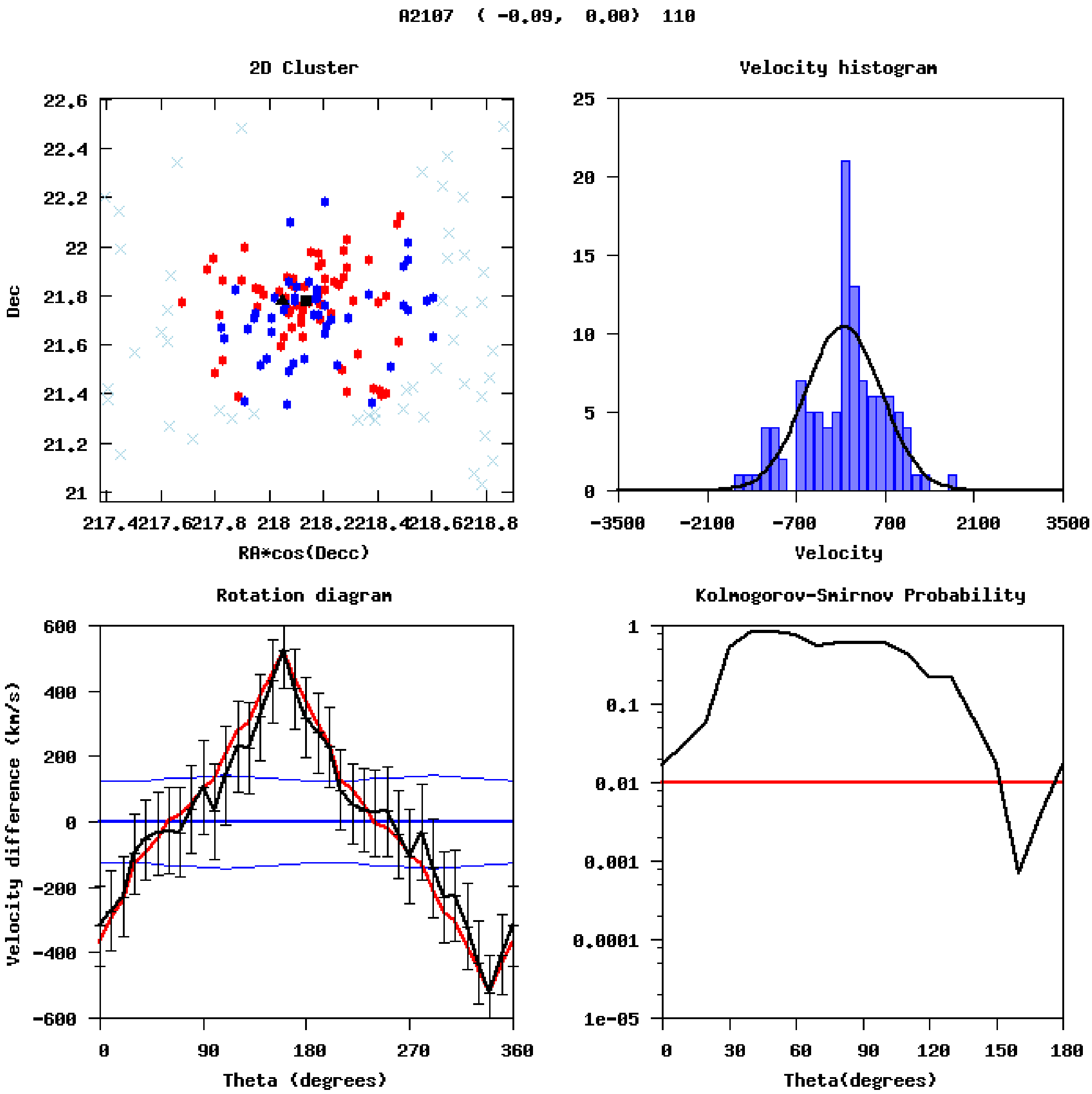

Figure 53: Abell 2107 with radius of 1.5 Mpc. The title of the figure indicates the coordinates of the final selected rotational center (dy, dx) and the number of galaxies included in the study.

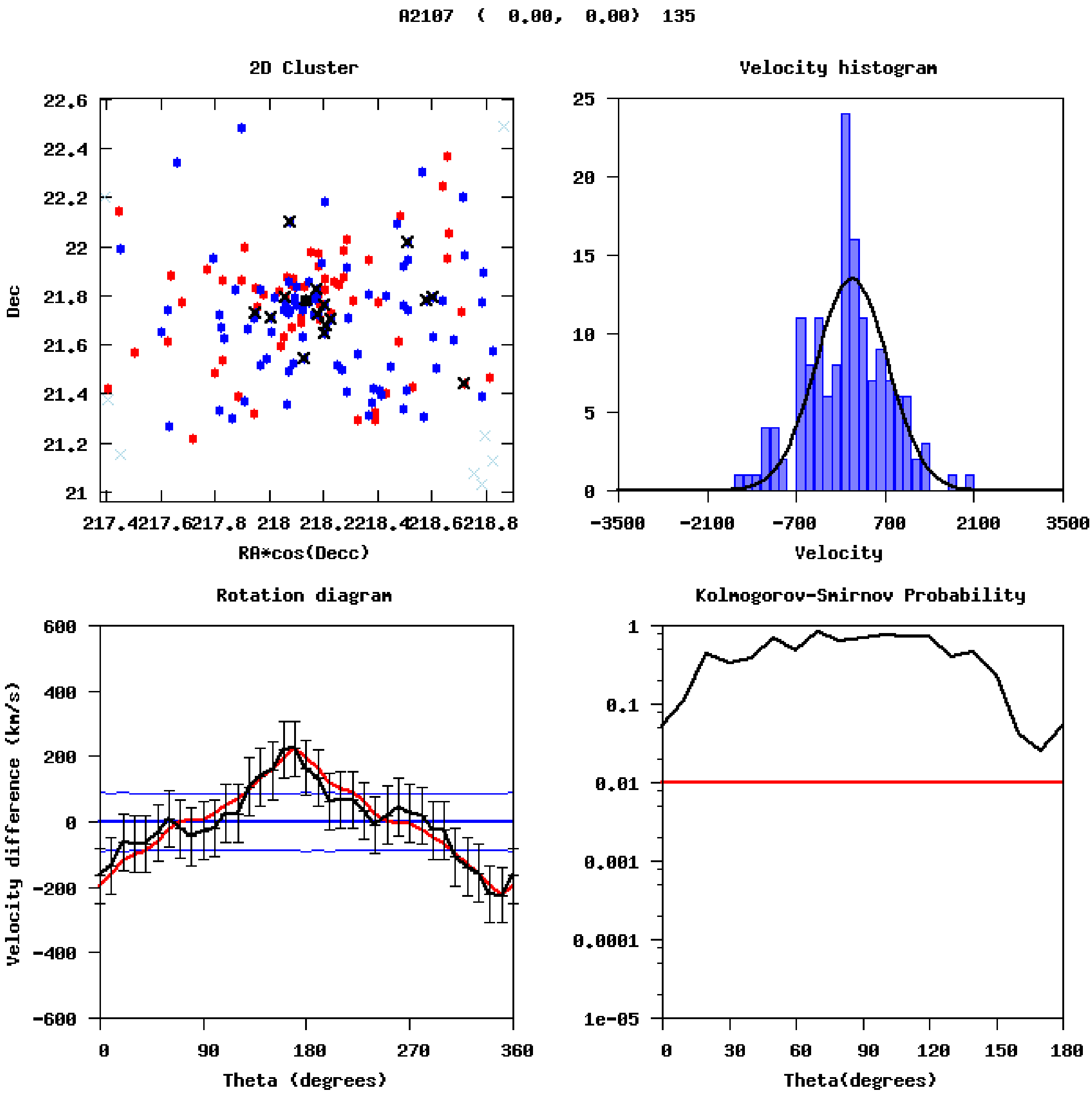

Figure 54: Abell 2107 with radius of 2.5 Mpc. The title of the figure indicates the coordinates of the final selected rotational center (dy, dx) and the number of galaxies included in the study.

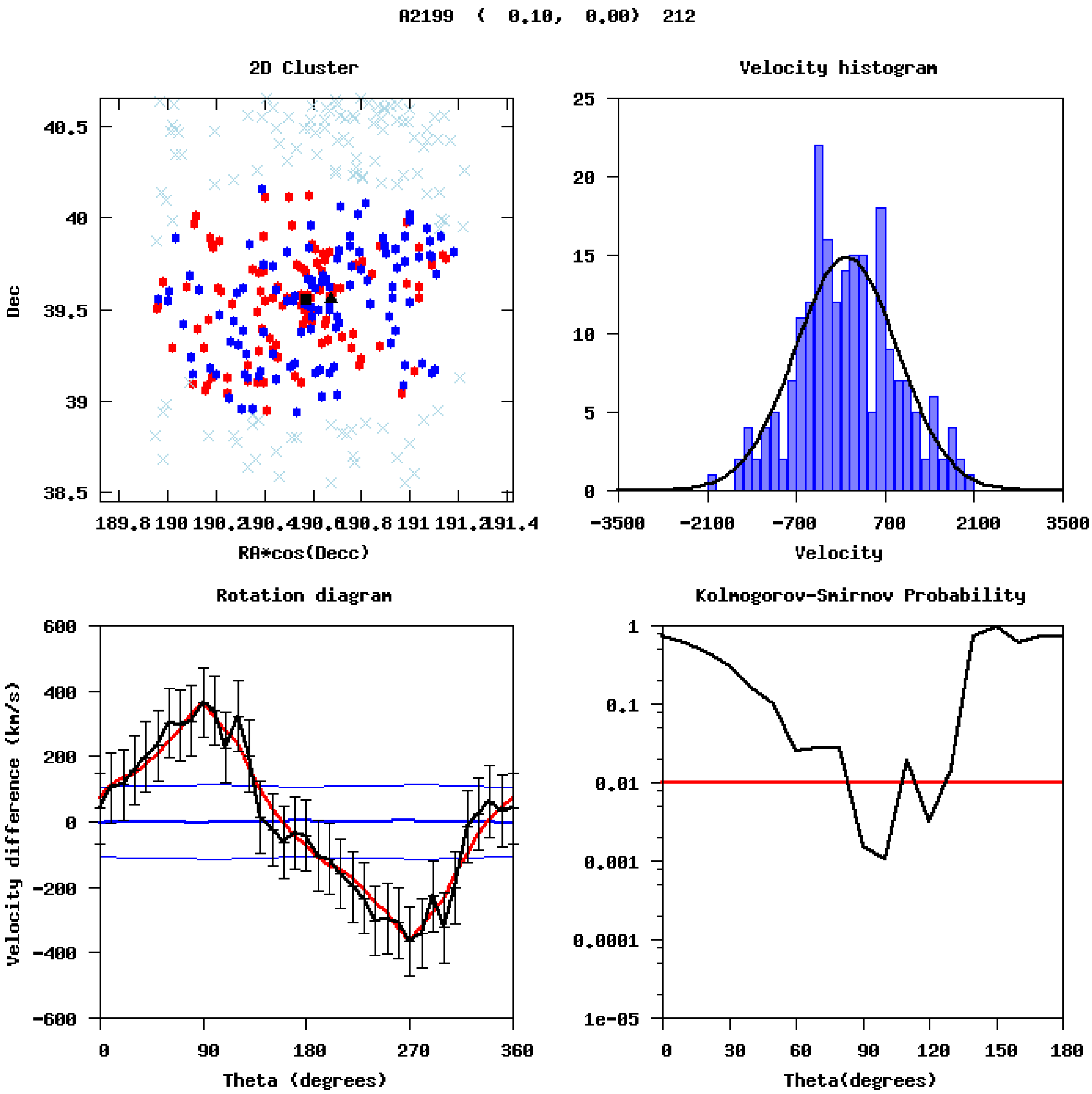

Figure 55: Abell 2199 with radius of 1.5 Mpc. The title of the figure indicates the coordinates of the final selected rotational center (dy, dx) and the number of galaxies included in the study.

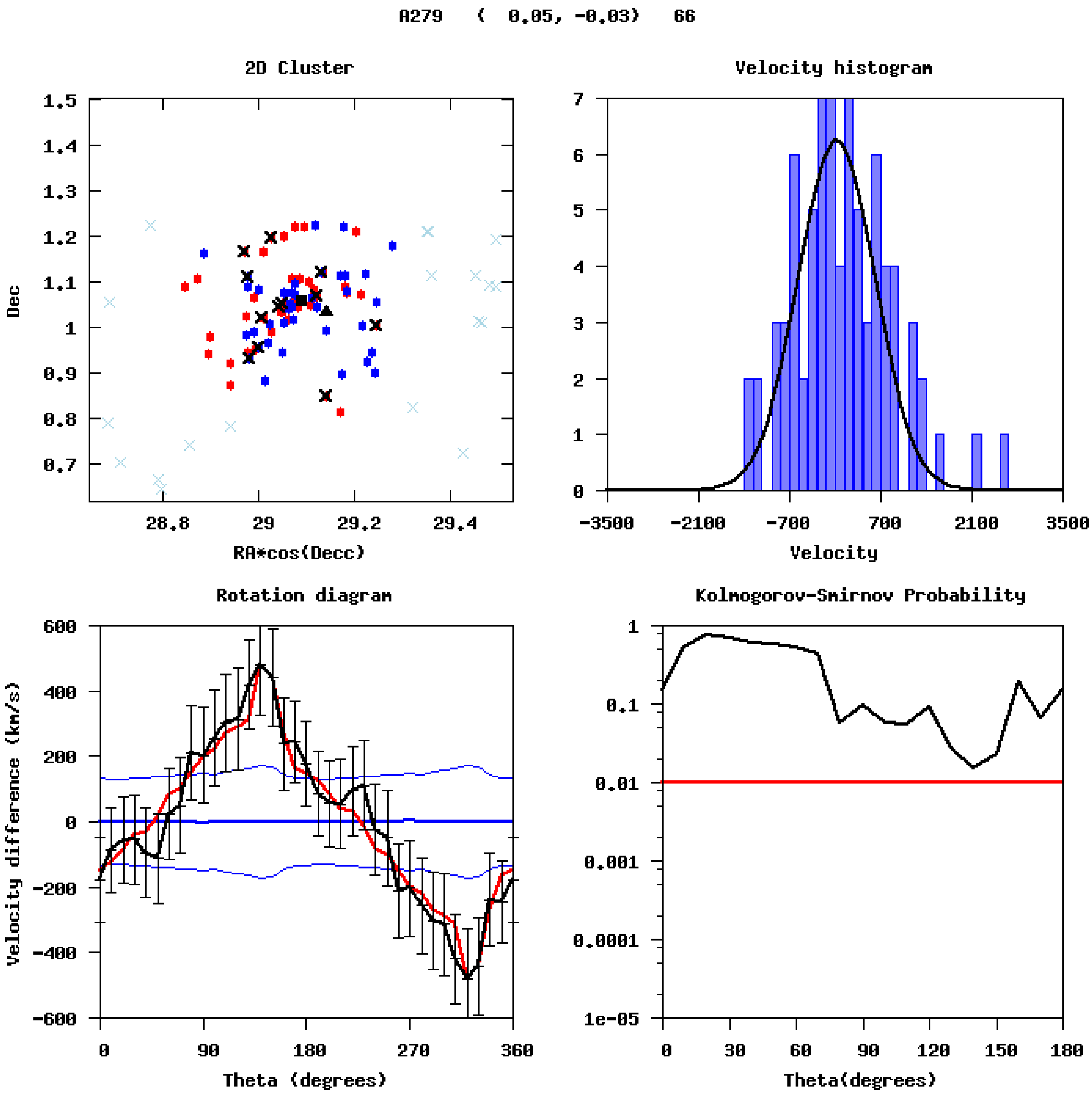

Figure 56: Abell 279 with radius of 1.5 Mpc. The title of the figure indicates the coordinates of the final selected rotational center (dy, dx) and the number of galaxies included in the study.

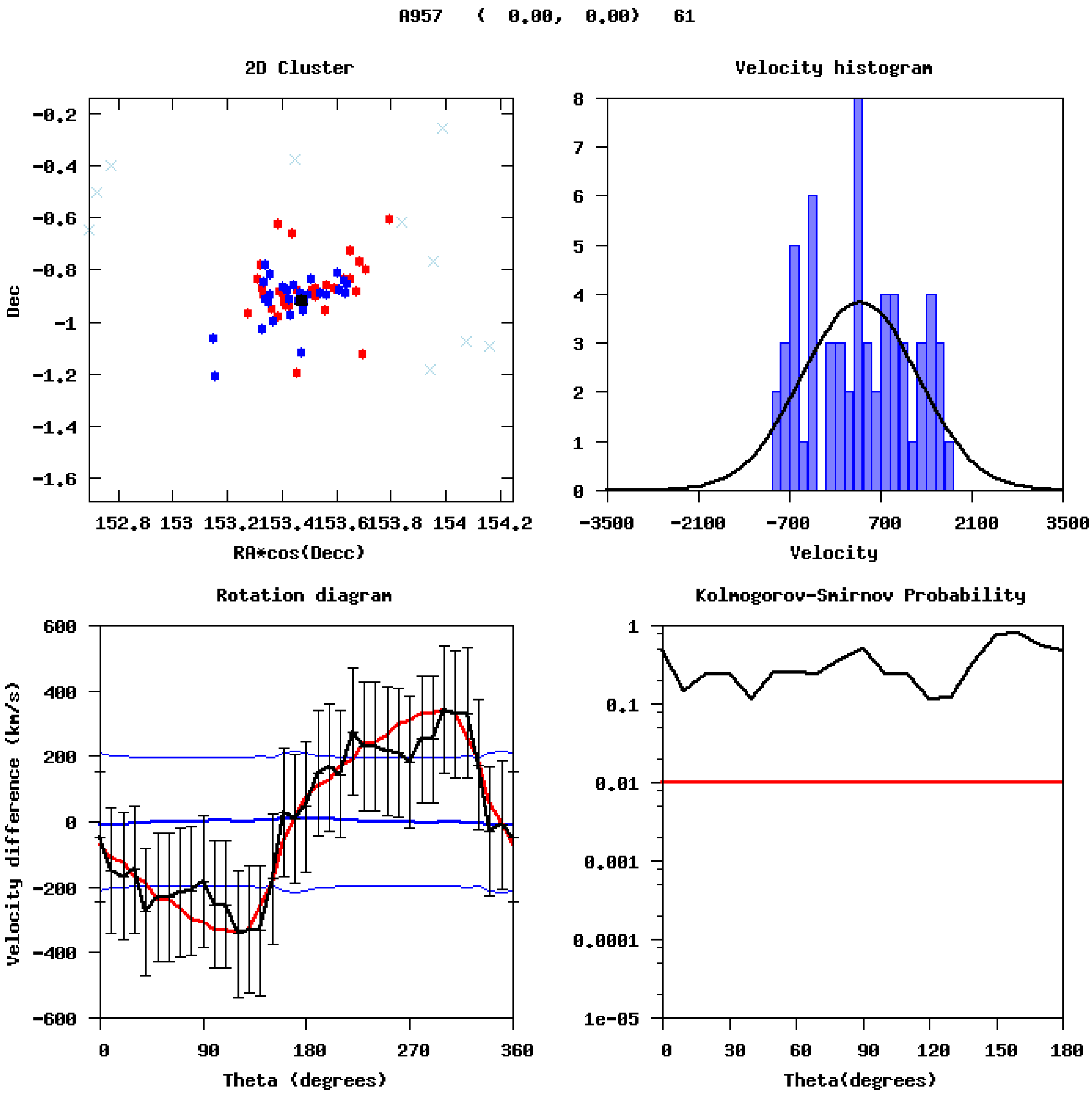

Figure 57: Abell 957 with radius of 1.5 Mpc. The title of the figure indicates the coordinates of the final selected rotational center (dy, dx) and the number of galaxies included in the study.

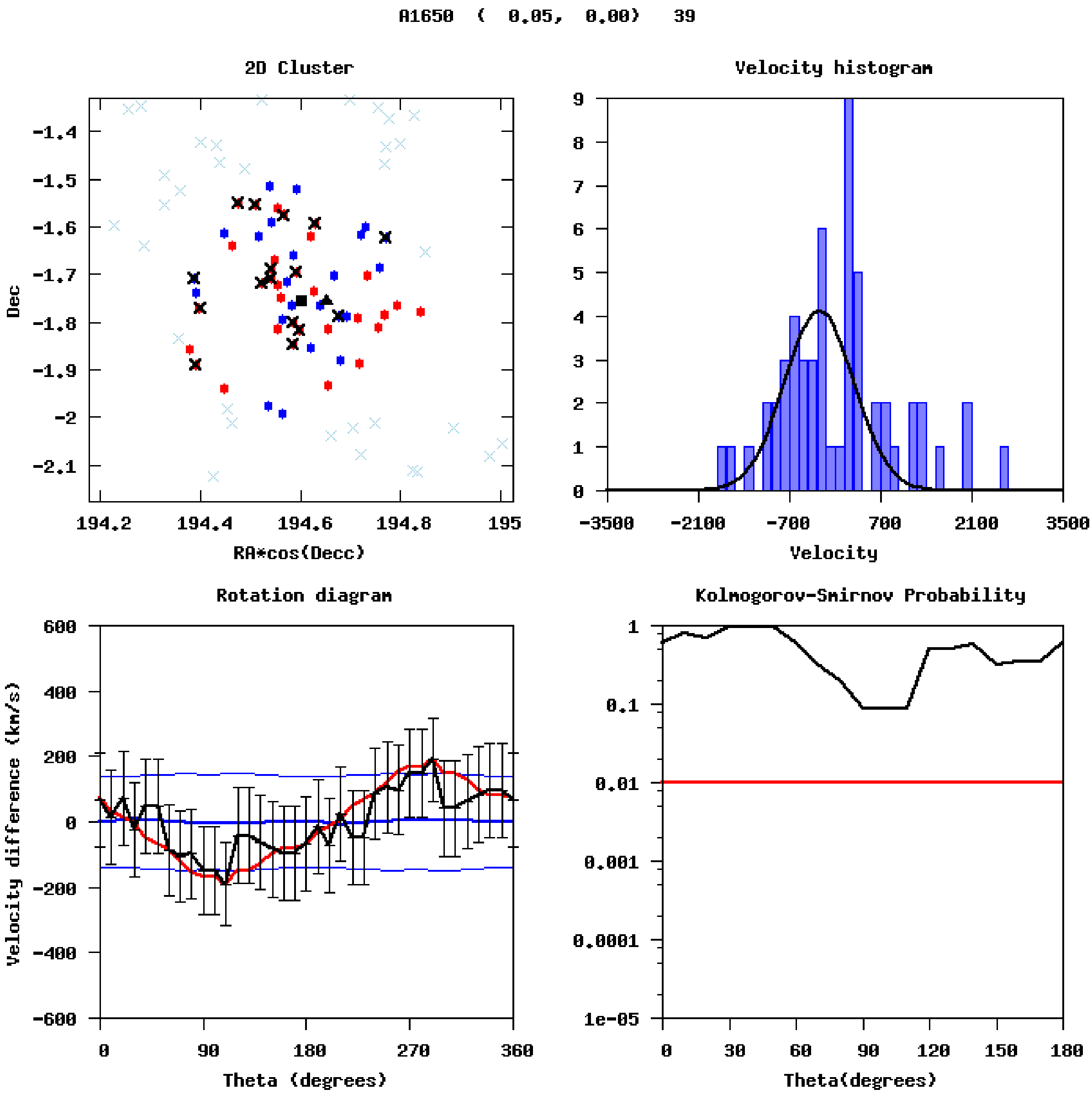

Figure 58: Abell 1650 with radius of 1.5 Mpc. The title of the figure indicates the coordinates of the final selected rotational center (dy, dx) and the number of galaxies included in the study.

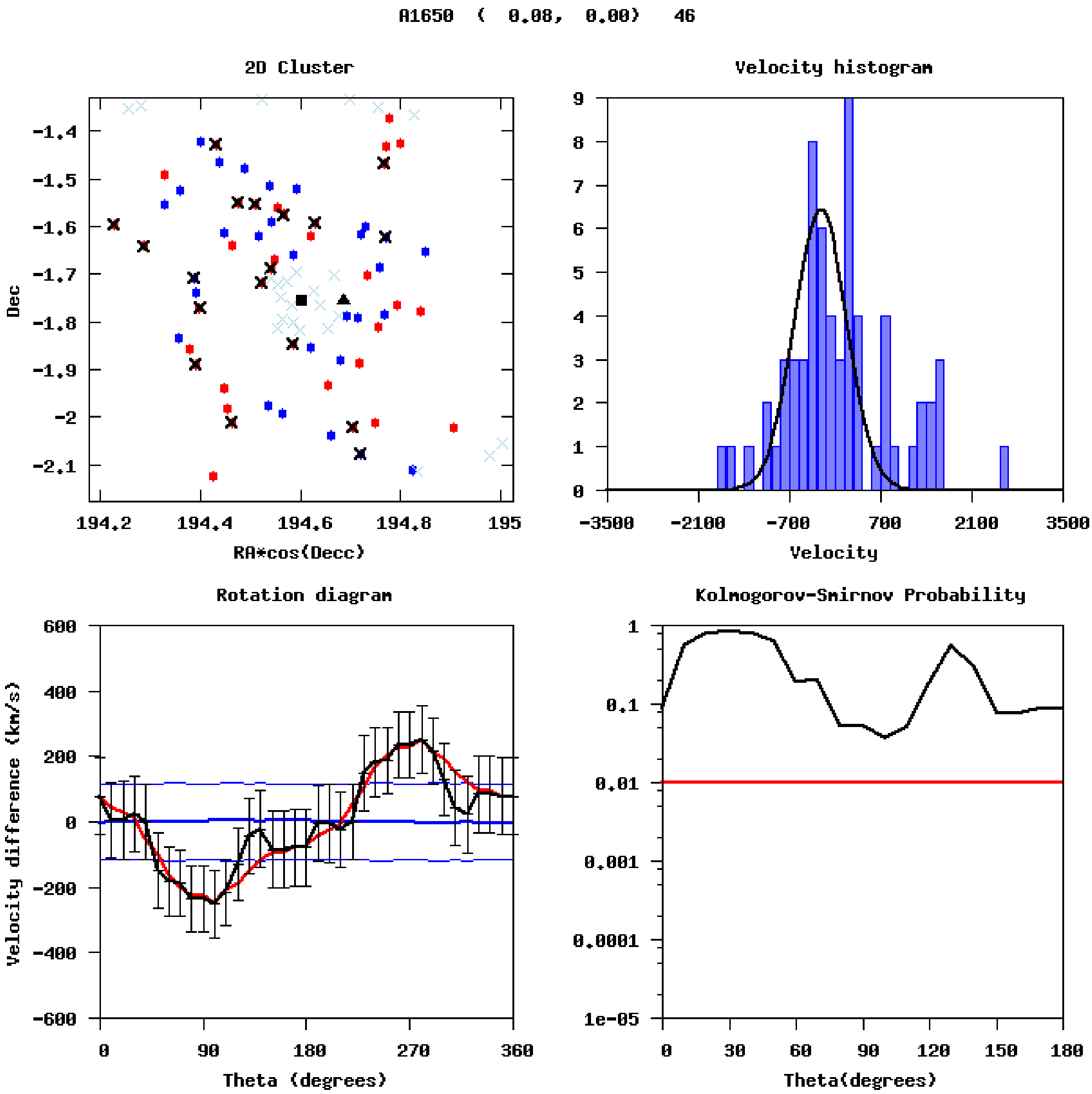

Figure 59: Abell 1650 with radius between 0.5 and 2.5 Mpc. The title of the figure indicates the coordinates of the final selected rotational center (dy, dx) and the number of galaxies included in the study.

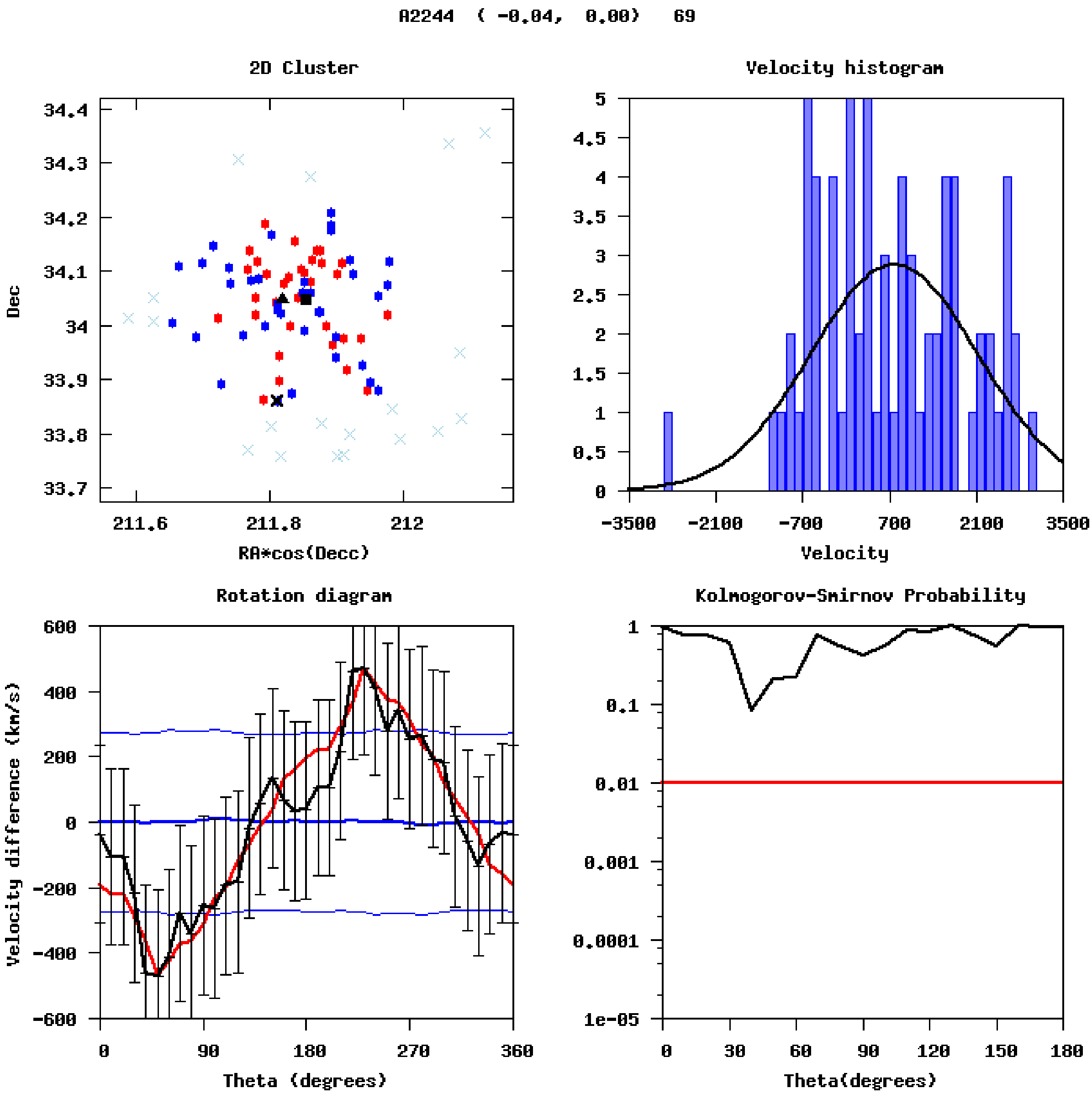

Figure 60: Abell 2244 with radius of 1.5 Mpc. The title of the figure indicates the coordinates of the final selected rotational center (dy, dx) and the number of galaxies included in the study.

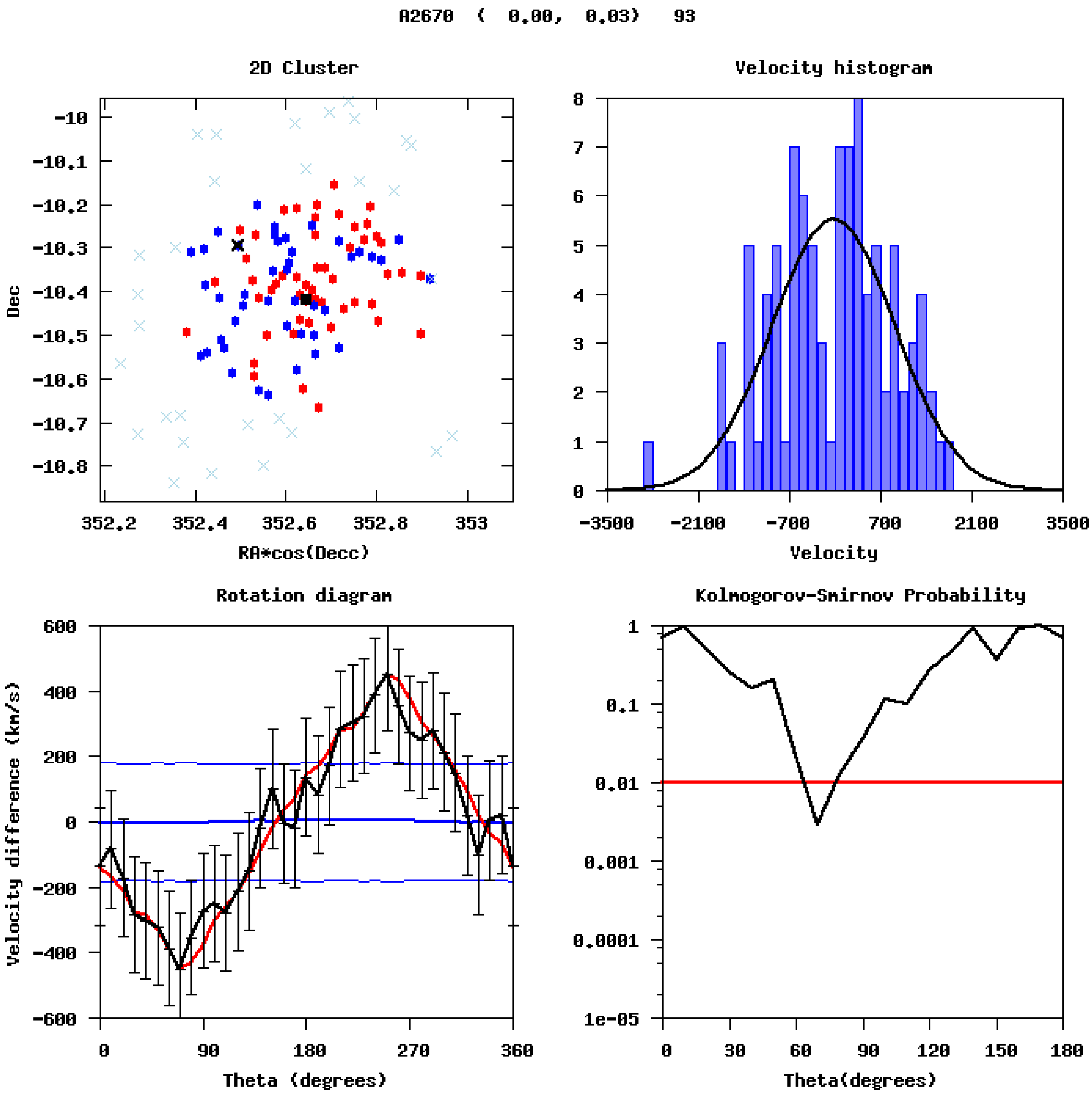

Figure 61: Abell 2670 with radius of 1.5 Mpc. The title of the figure indicates the coordinates of the final selected rotational center (dy, dx) and the number of galaxies included in the study.

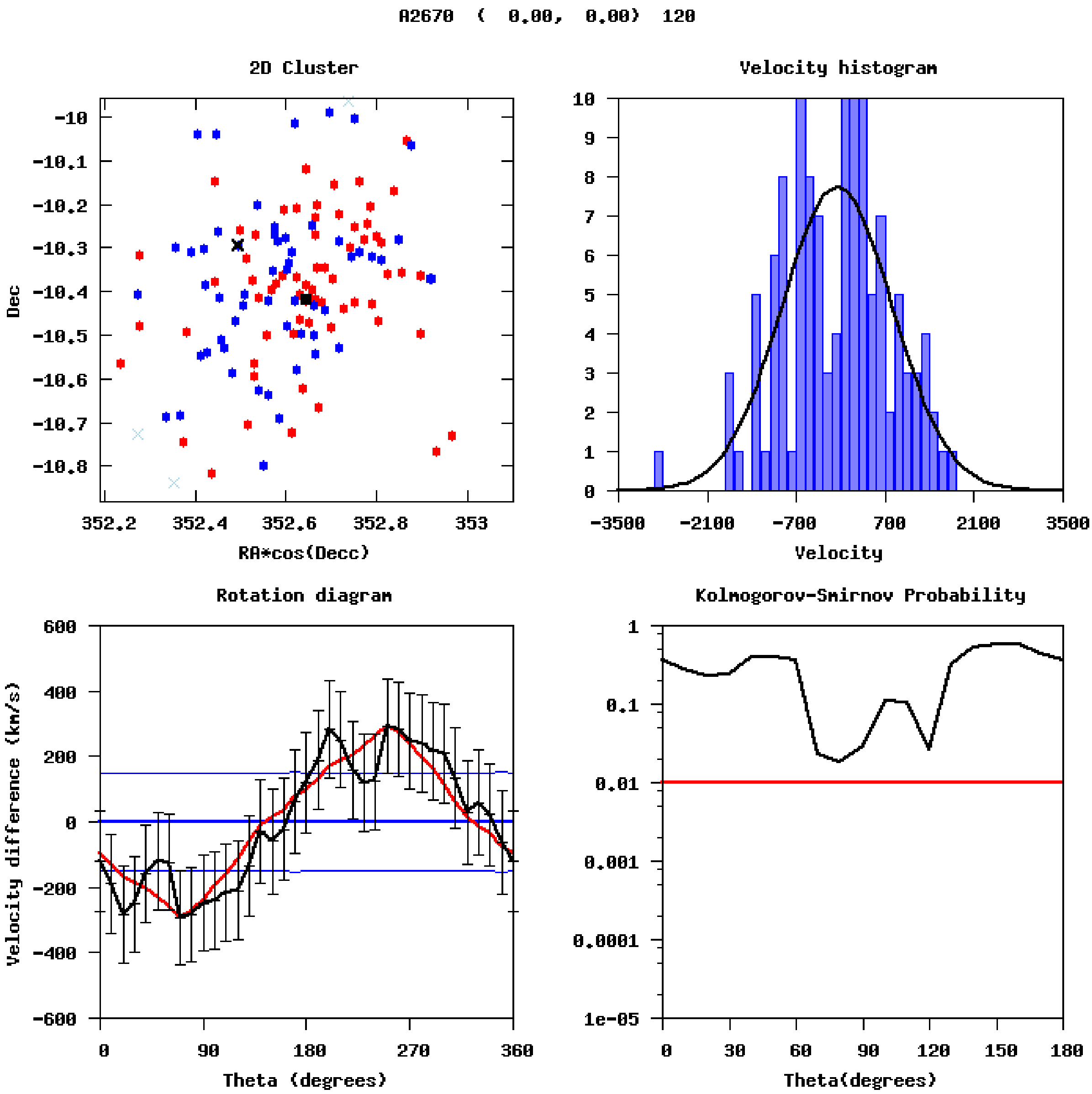

Figure 62: Abell 2670 with radius of 2.5 Mpc. The title of the figure indicates the coordinates of the final selected rotational center (dy, dx) and the number of galaxies included in the study.

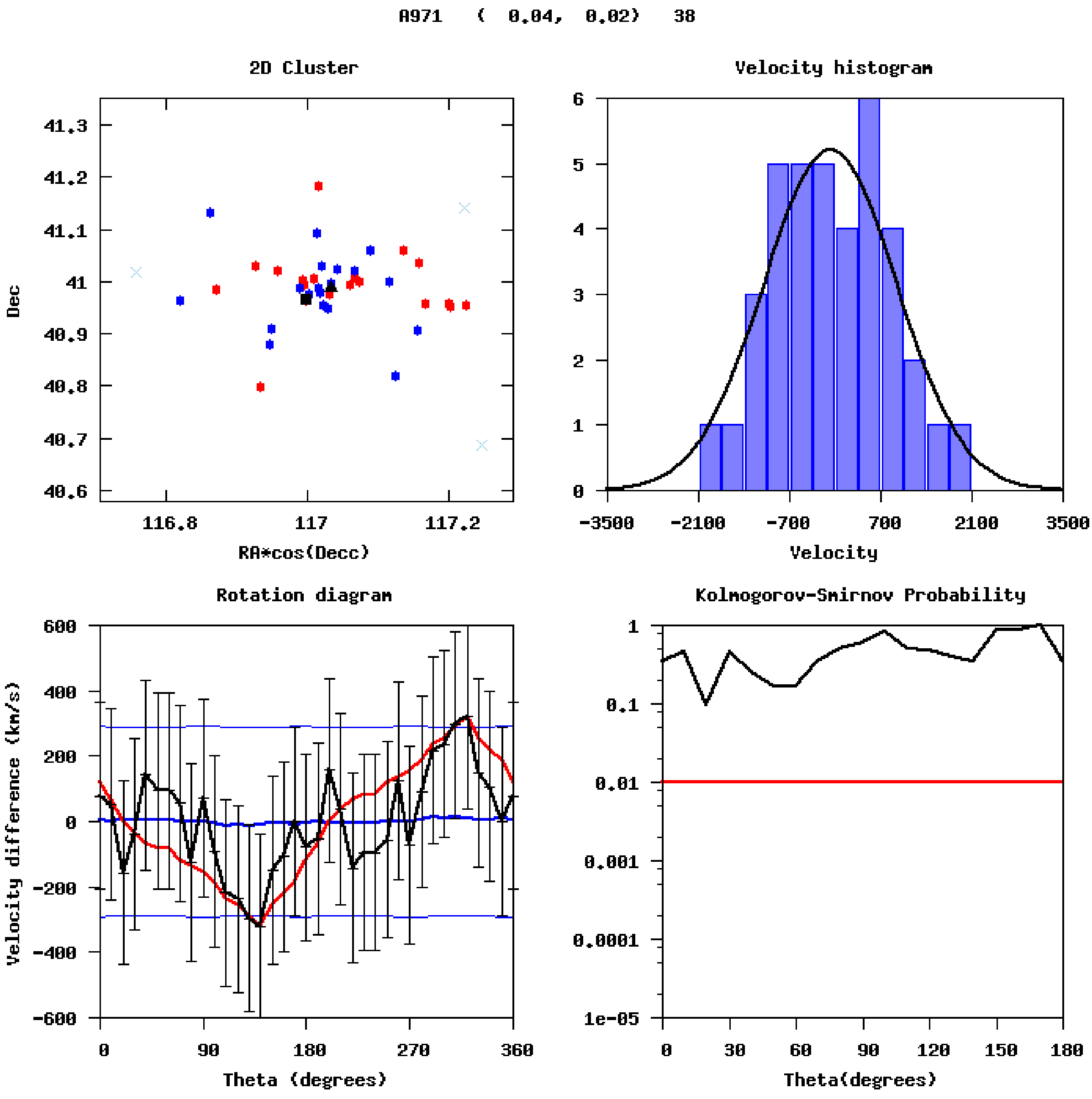

Figure 63: Abell 971 with radius of 1.5 Mpc. The title of the figure indicates the coordinates of the final selected rotational center (dy, dx) and the number of galaxies included in the study.

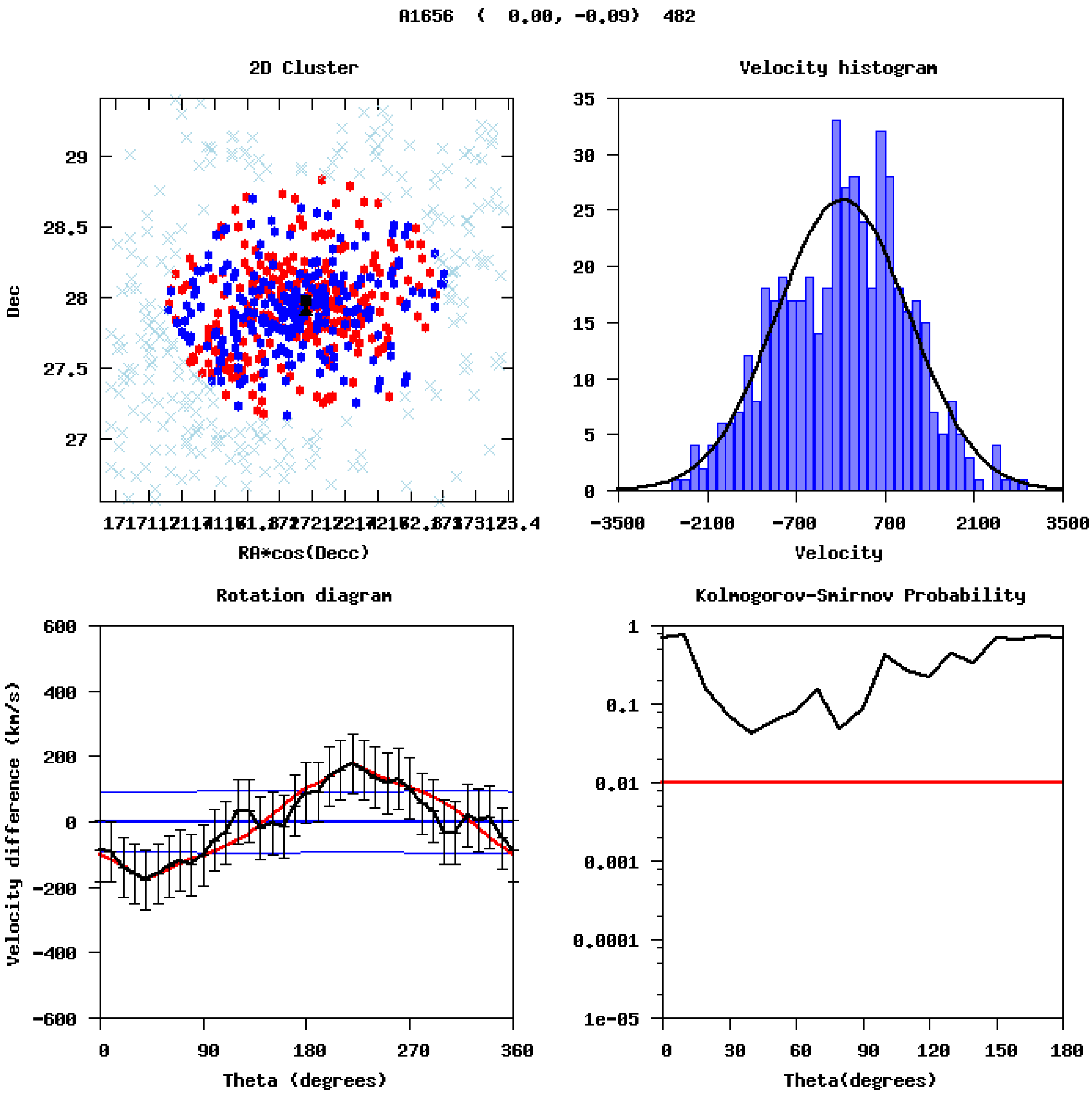

Figure 64: Abell 1656 with radius of 1.5 Mpc. The title of the figure indicates the coordinates of the final selected rotational center (dy, dx) and the number of galaxies included in the study.

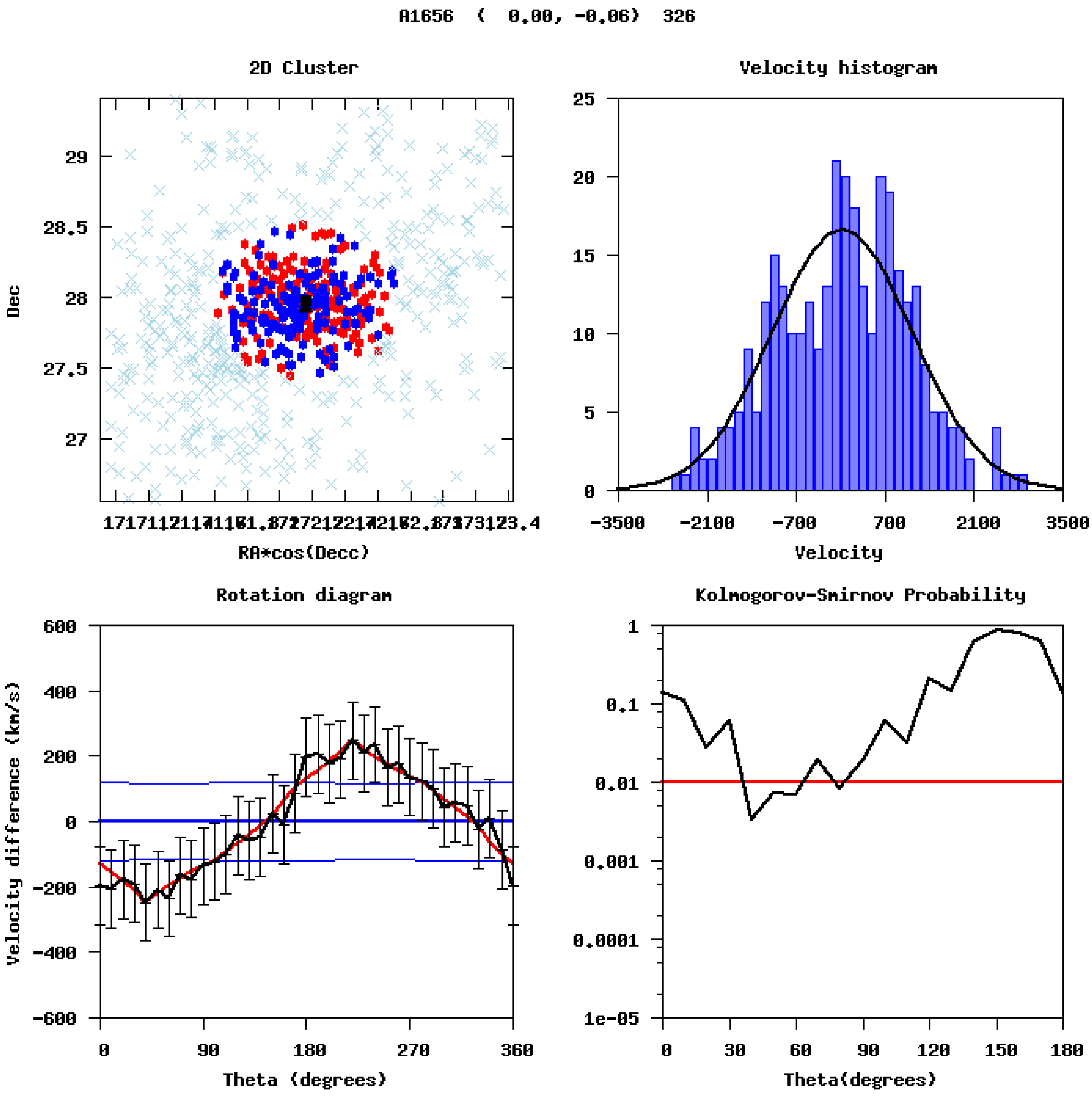

Figure 65: Abell 1656 with radius of 1 Mpc. The title of the figure indicates the coordinates of the final selected rotational center (dy, dx) and the number of galaxies included in the study.

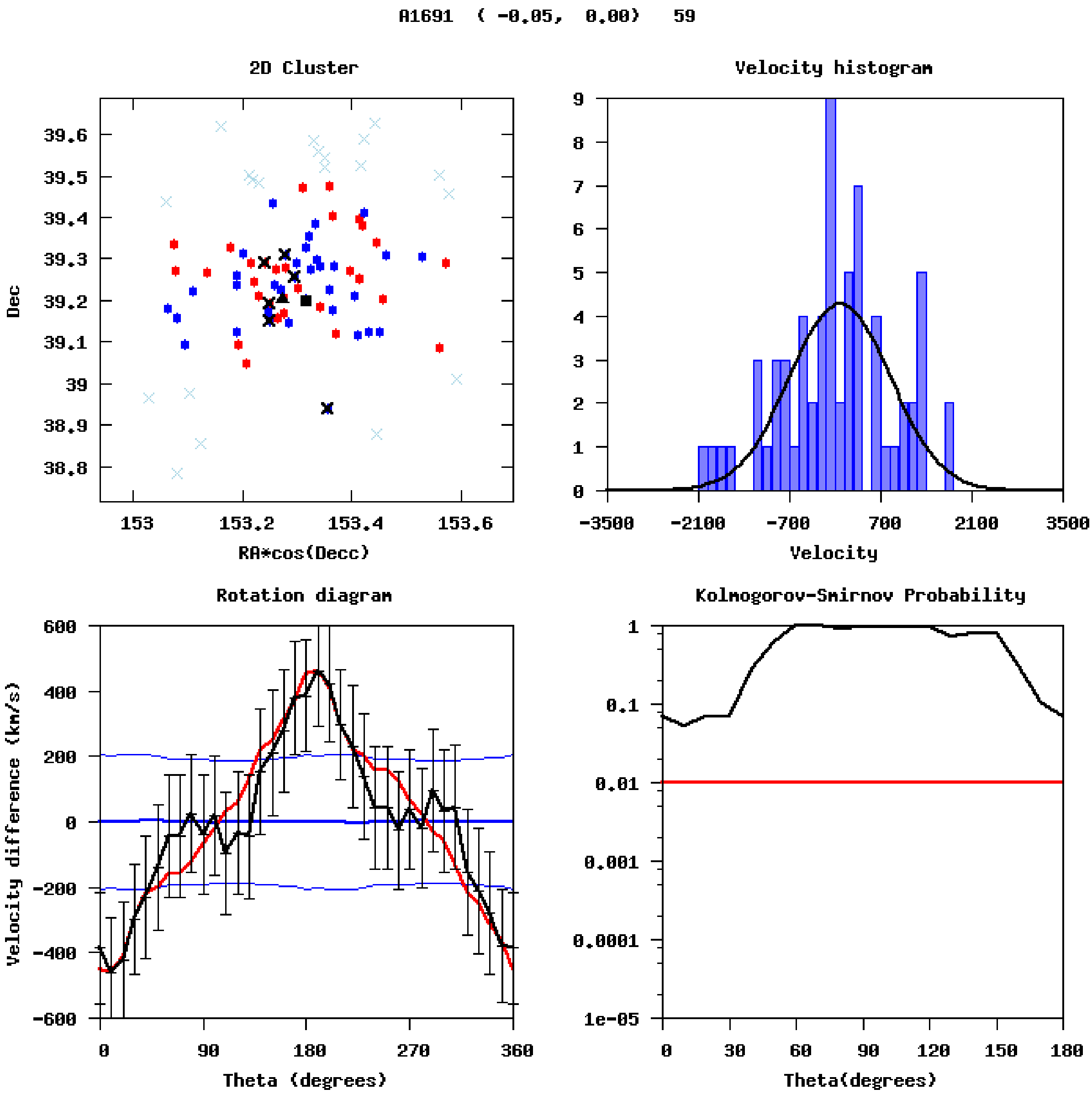

Figure 66: Abell 1691 with radius of 1.5 Mpc. The title of the figure indicates the coordinates of the final selected rotational center (dy, dx) and the number of galaxies included in the study.

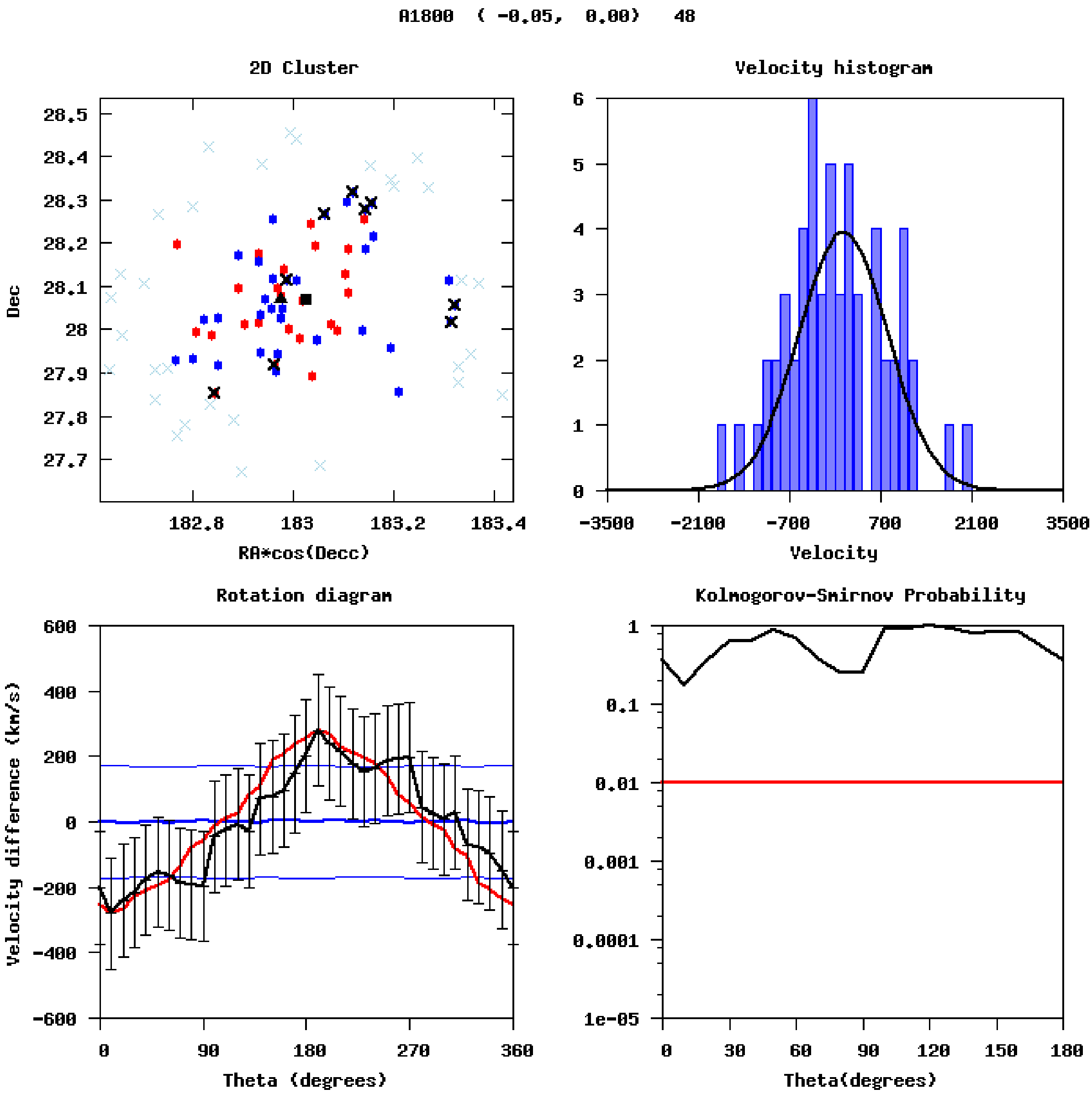

Figure 67: Abell 1800 with radius of 1.5 Mpc. The title of the figure indicates the coordinates of the final selected rotational center (dy, dx) and the number of galaxies included in the study.

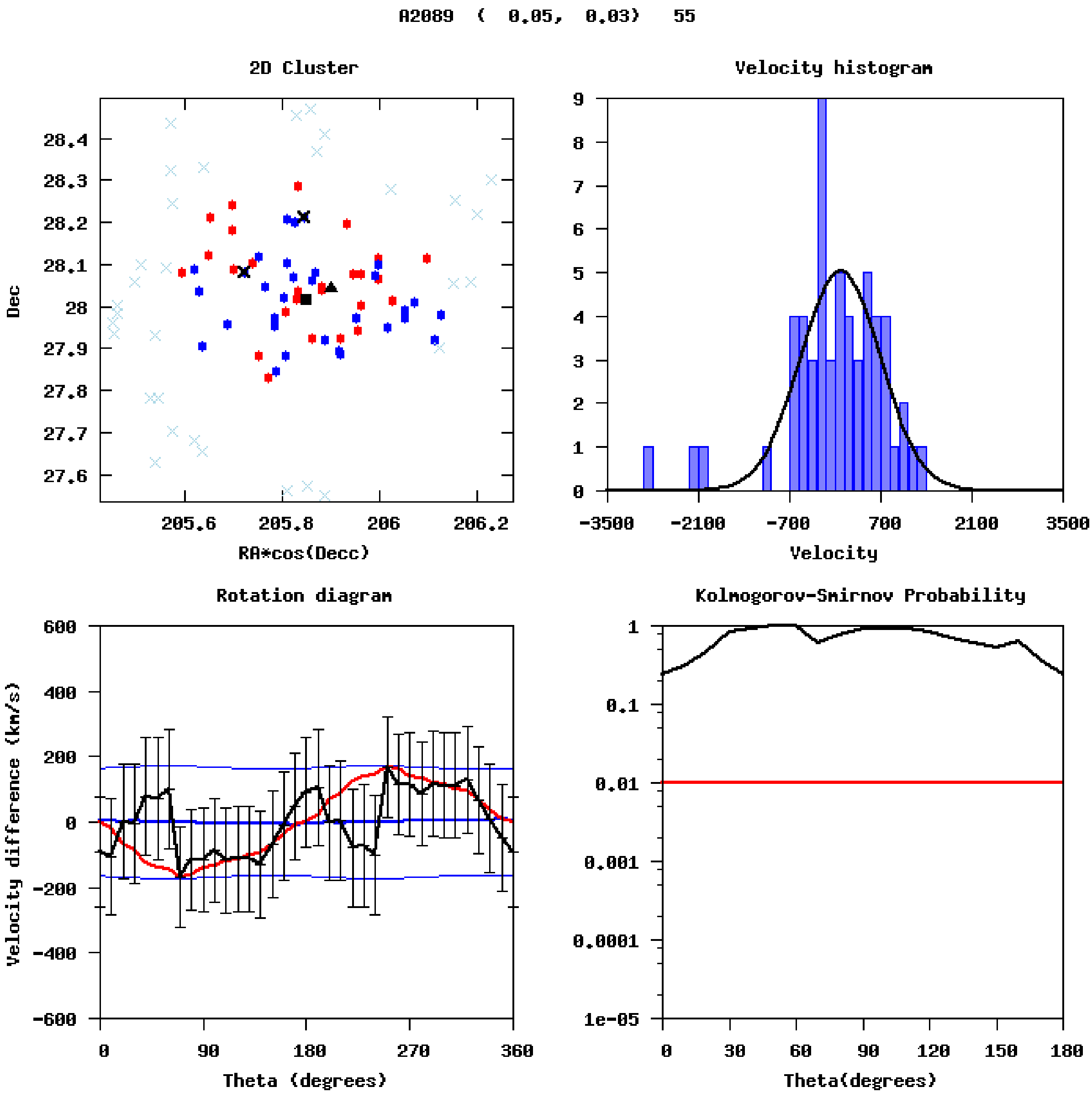

Figure 68: Abell 2089 with radius of 1.5 Mpc. The title of the figure indicates the coordinates of the final selected rotational center (dy, dx) and the number of galaxies included in the study.

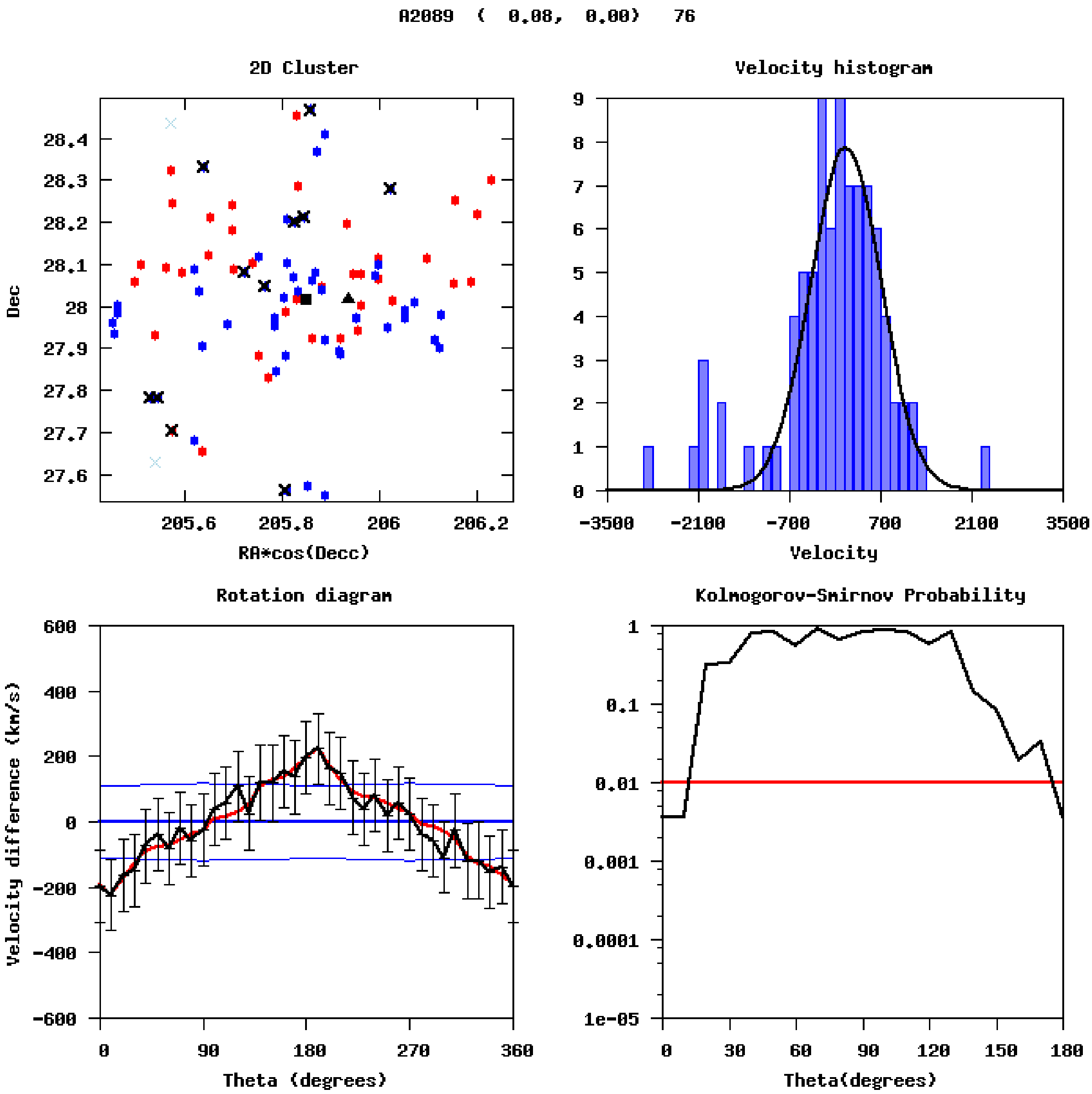

Figure 69: Abell 2089 with radius of 2.5 Mpc. The title of the figure indicates the coordinates of the final selected rotational center (dy, dx) and the number of galaxies included in the study.

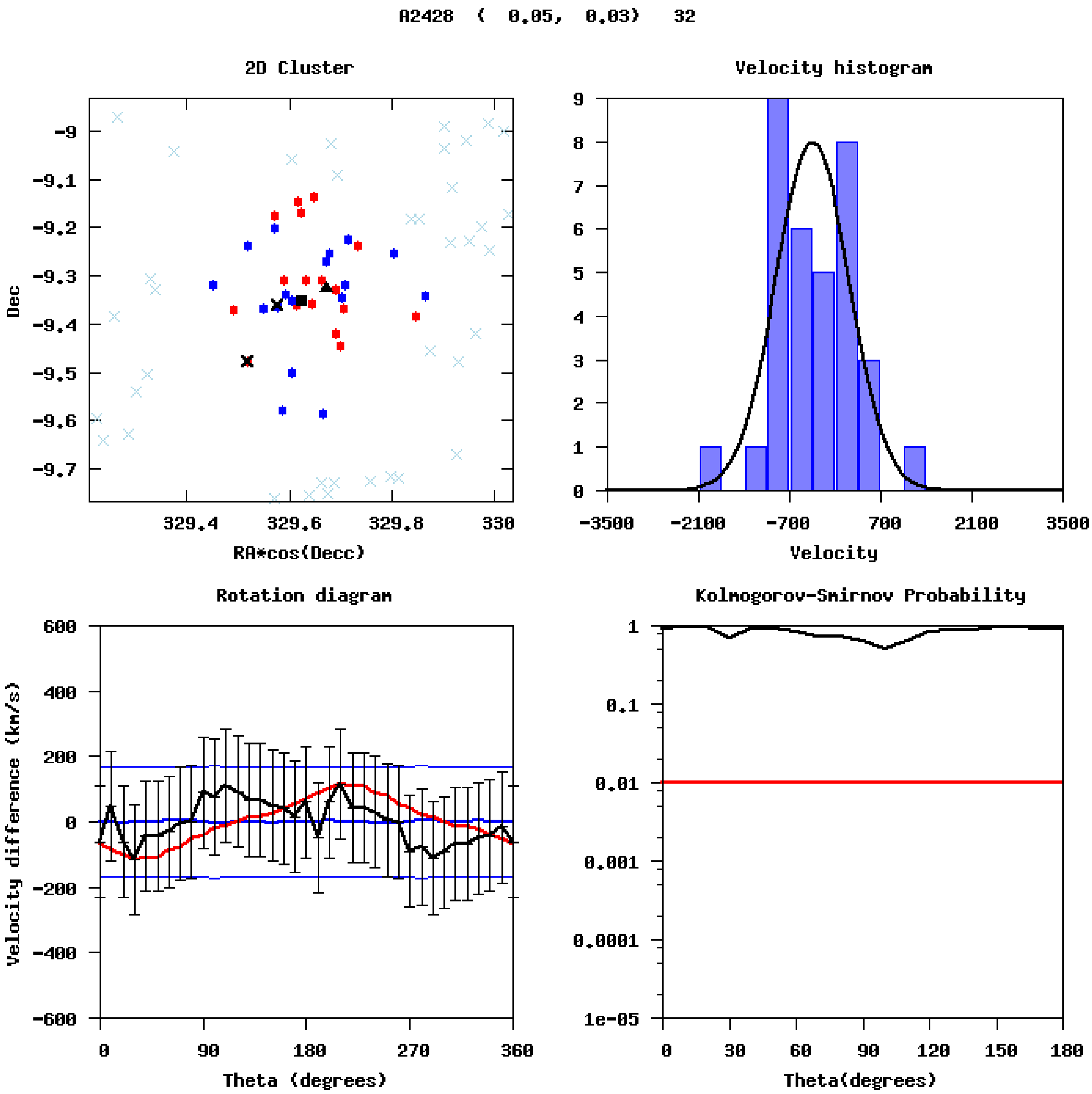

Figure 70: Abell 2428 with radius of 1.5 Mpc. The title of the figure indicates the coordinates of the final selected rotational center (dy, dx) and the number of galaxies included in the study.

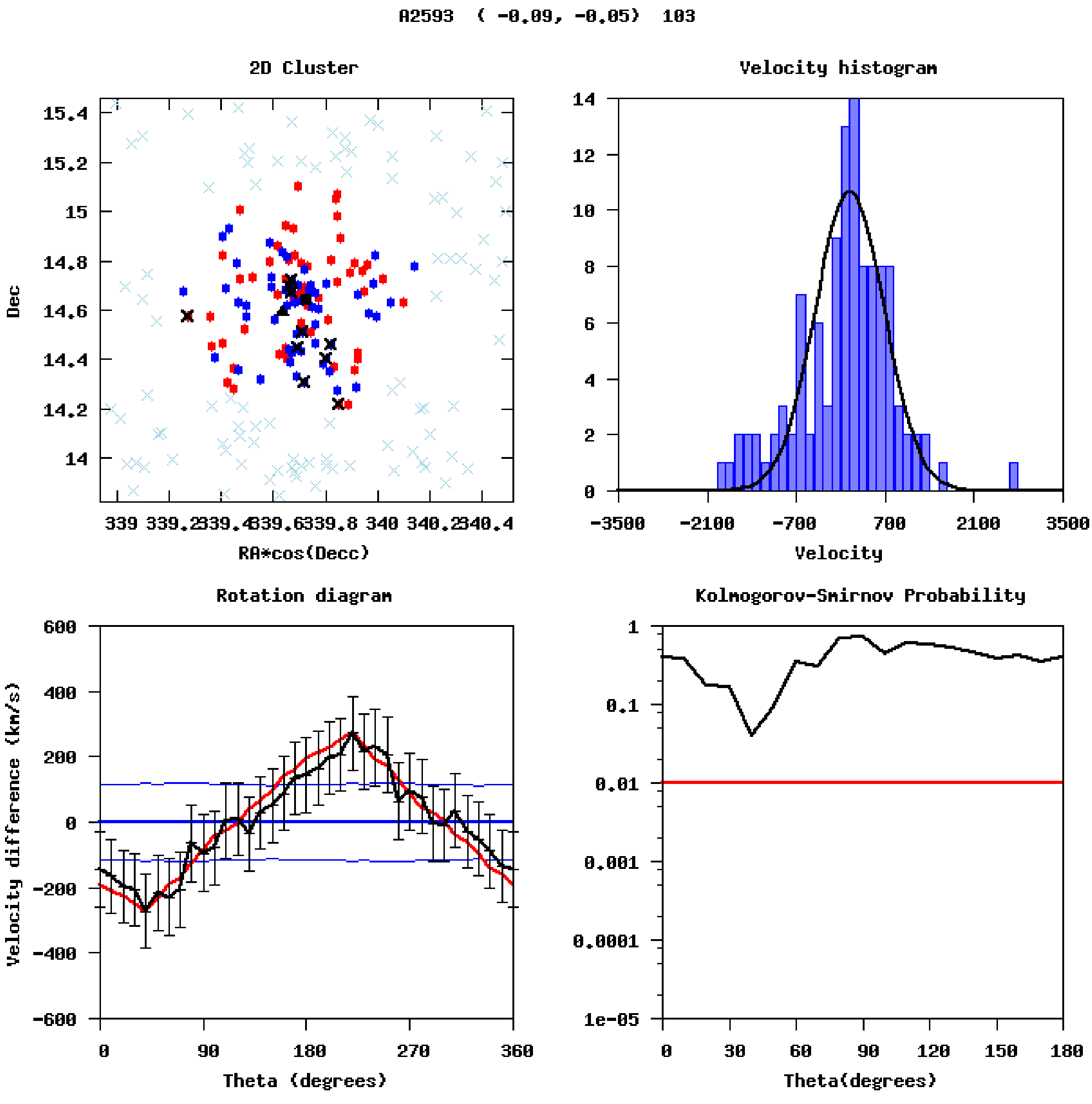

Figure 71: Abell 2593 with radius of 1.5 Mpc. The title of the figure indicates the coordinates of the final selected rotational center (dy, dx) and the number of galaxies included in the study.

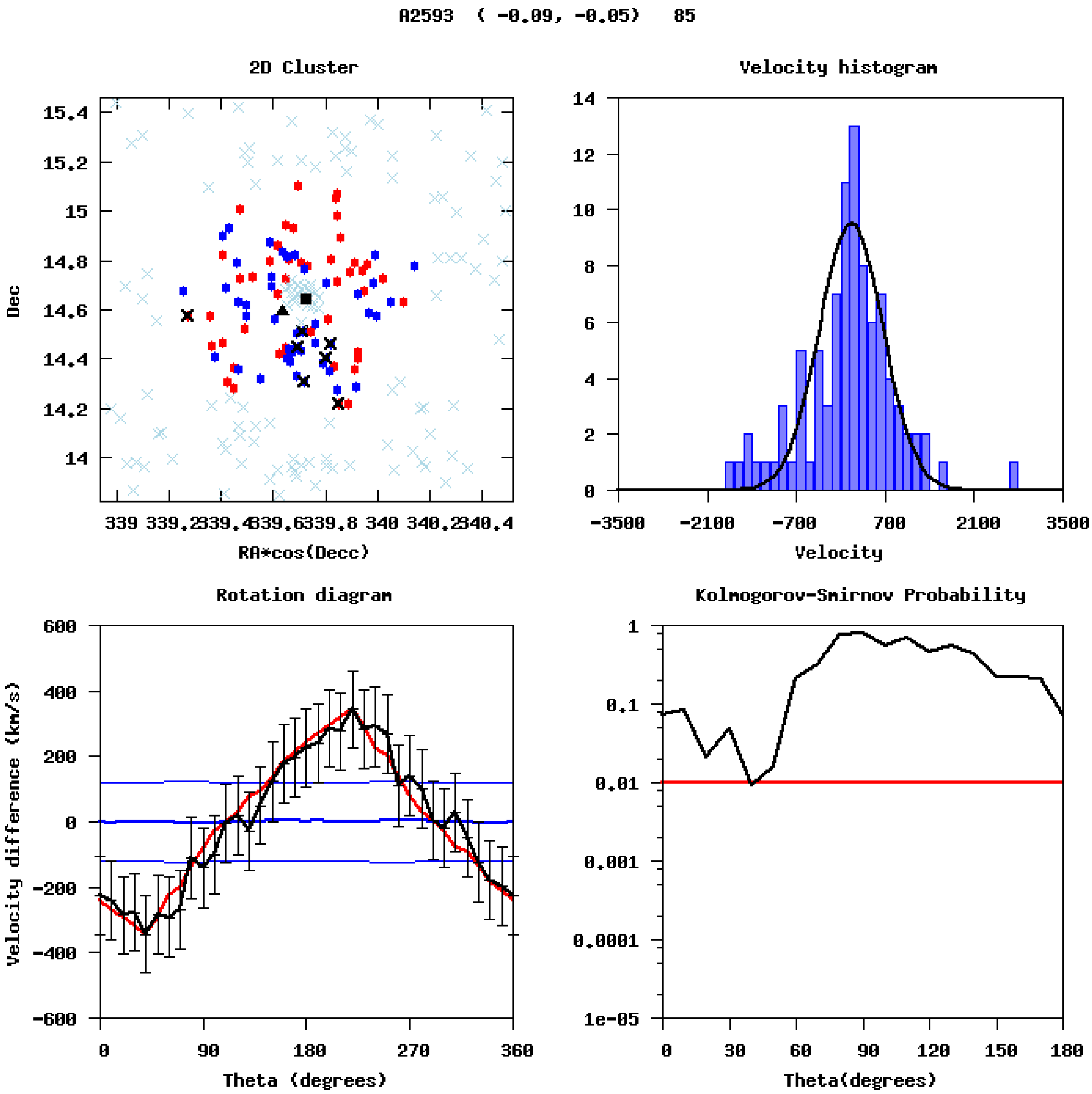

Figure 72: Abell 2593 with radius between 0.3 and 1.5 Mpc. The title of the figure indicates the coordinates of the final selected rotational center (dy, dx) and the number of galaxies included in the study.

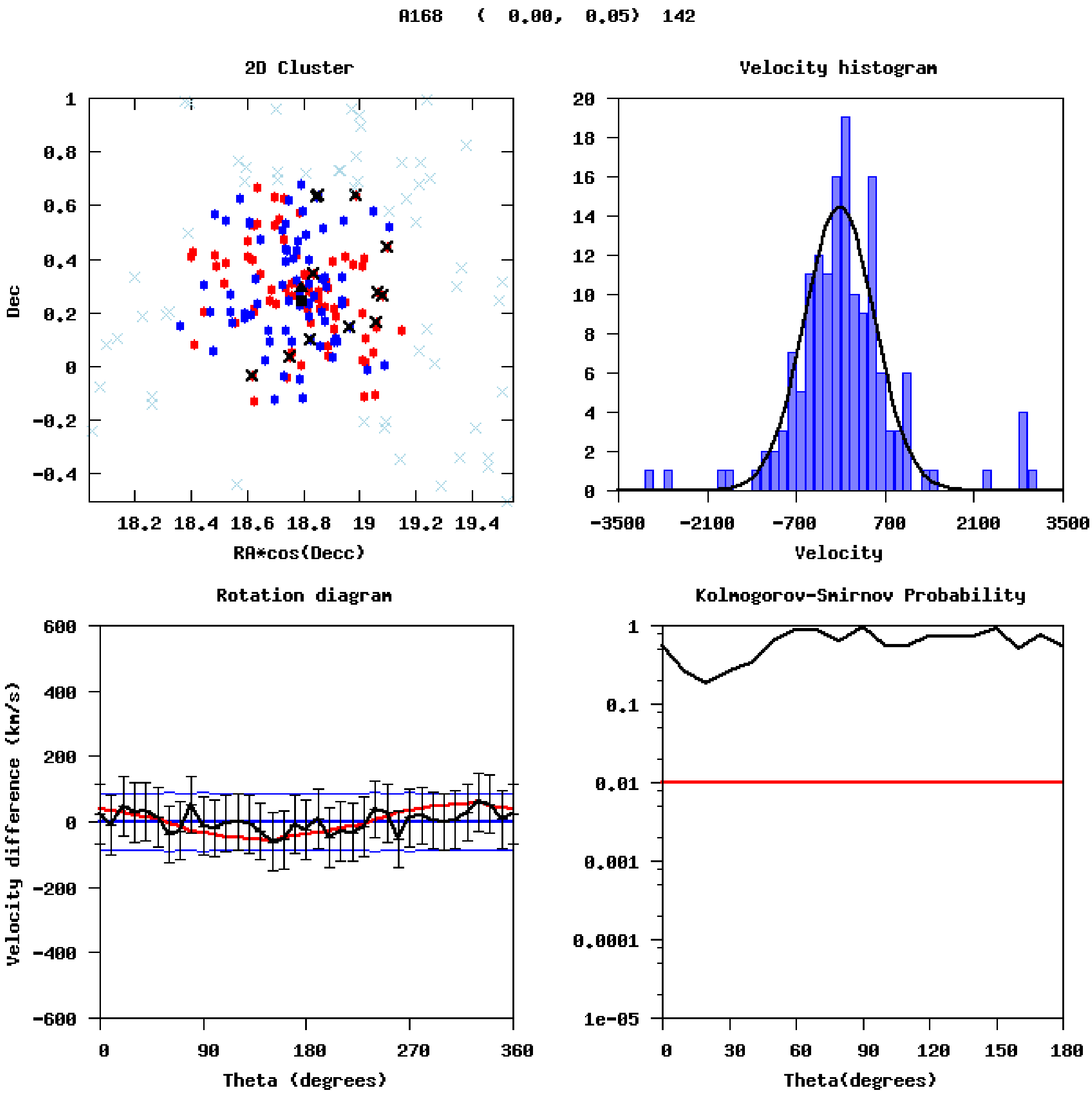

Figure 73: Abell 168 with radius of 1.5 Mpc. The title of the figure indicates the coordinates of the final selected rotational center (dy, dx) and the number of galaxies included in the study.

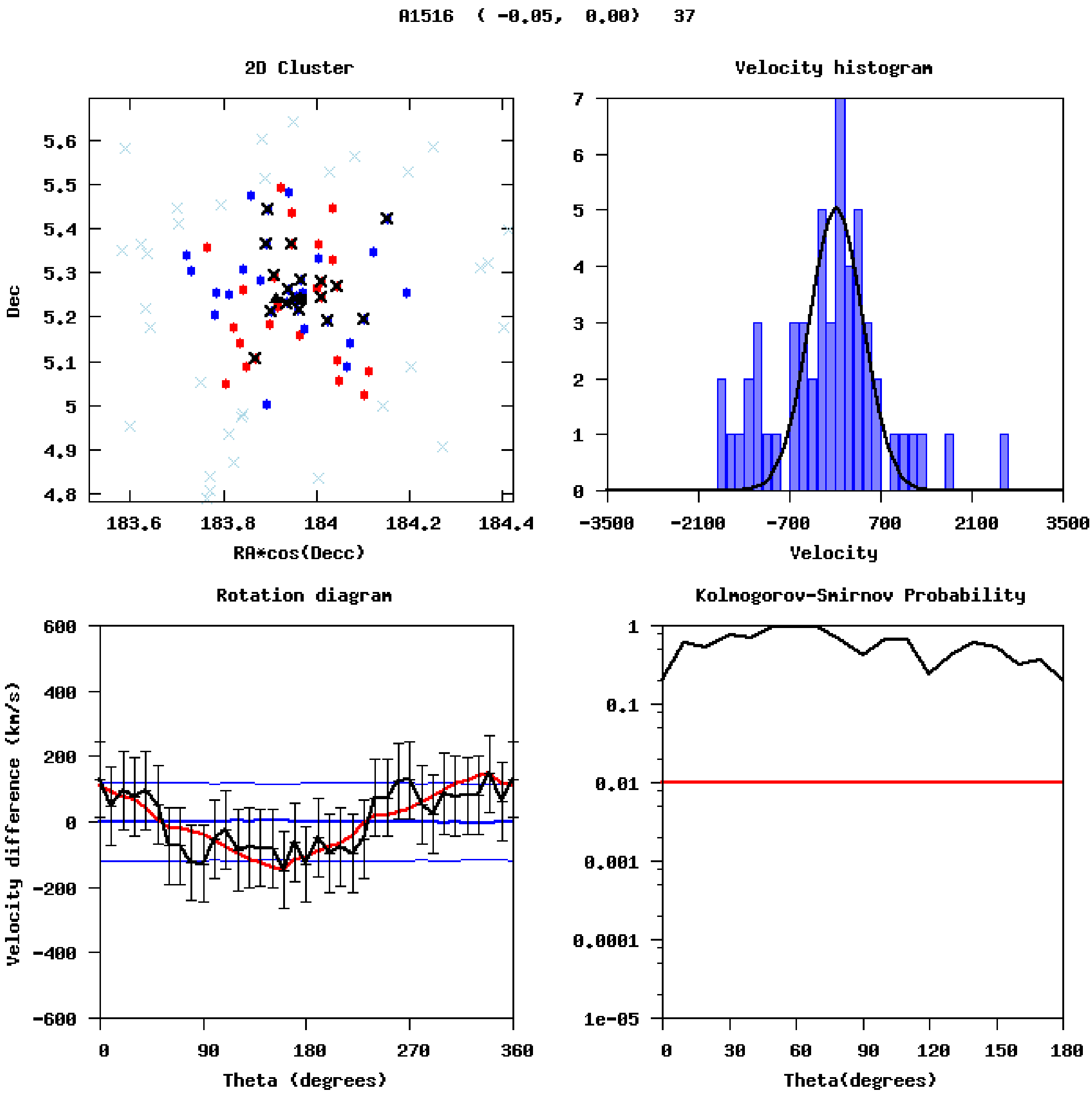

Figure 74: Abell 1516 with radius of 1.5 Mpc. The title of the figure indicates the coordinates of the final selected rotational center (dy, dx) and the number of galaxies included in the study.

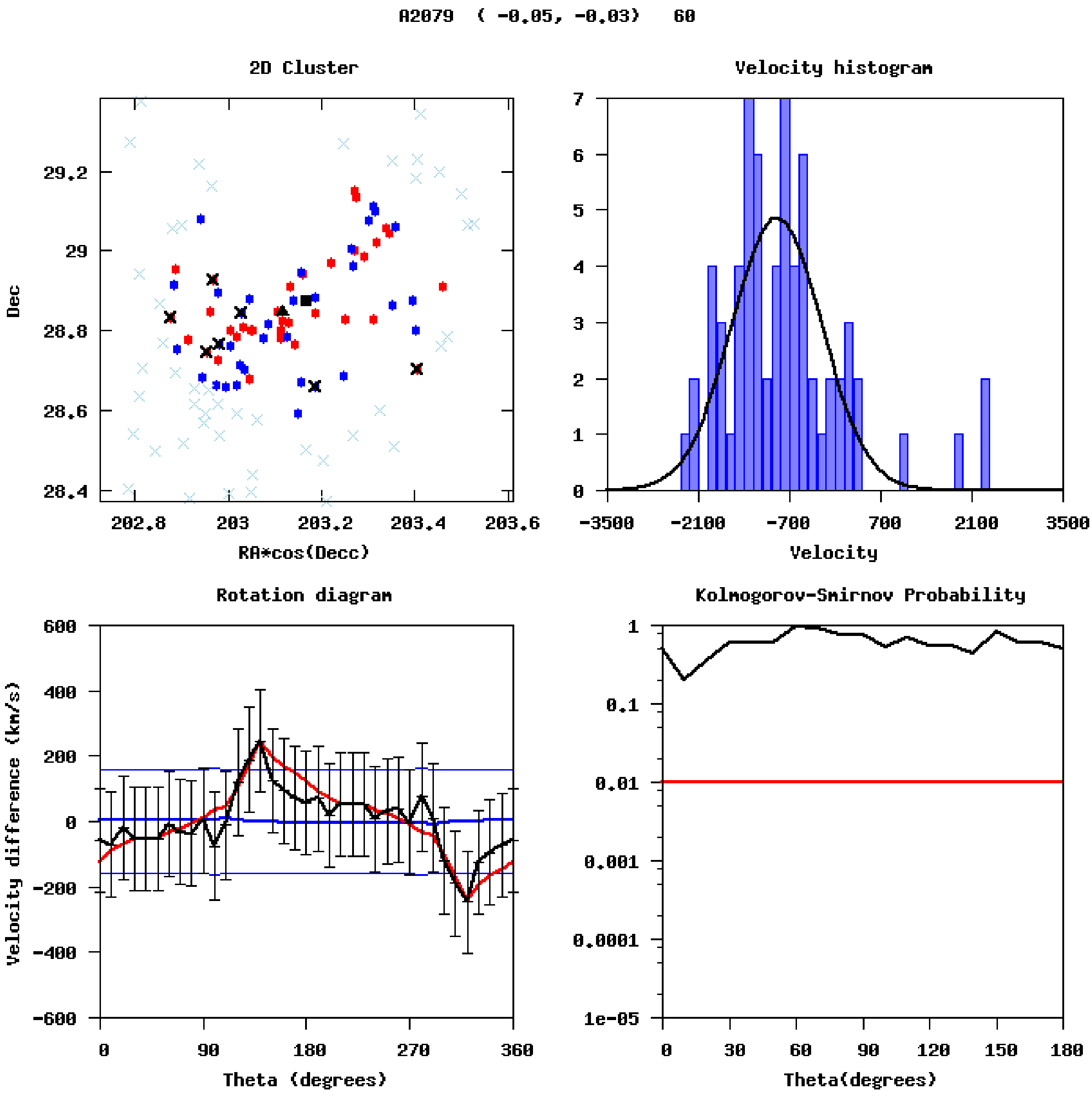

Figure 75: Abell 2079 with radius of 1.5 Mpc. The title of the figure indicates the coordinates of the final selected rotational center (dy, dx) and the number of galaxies included in the study.

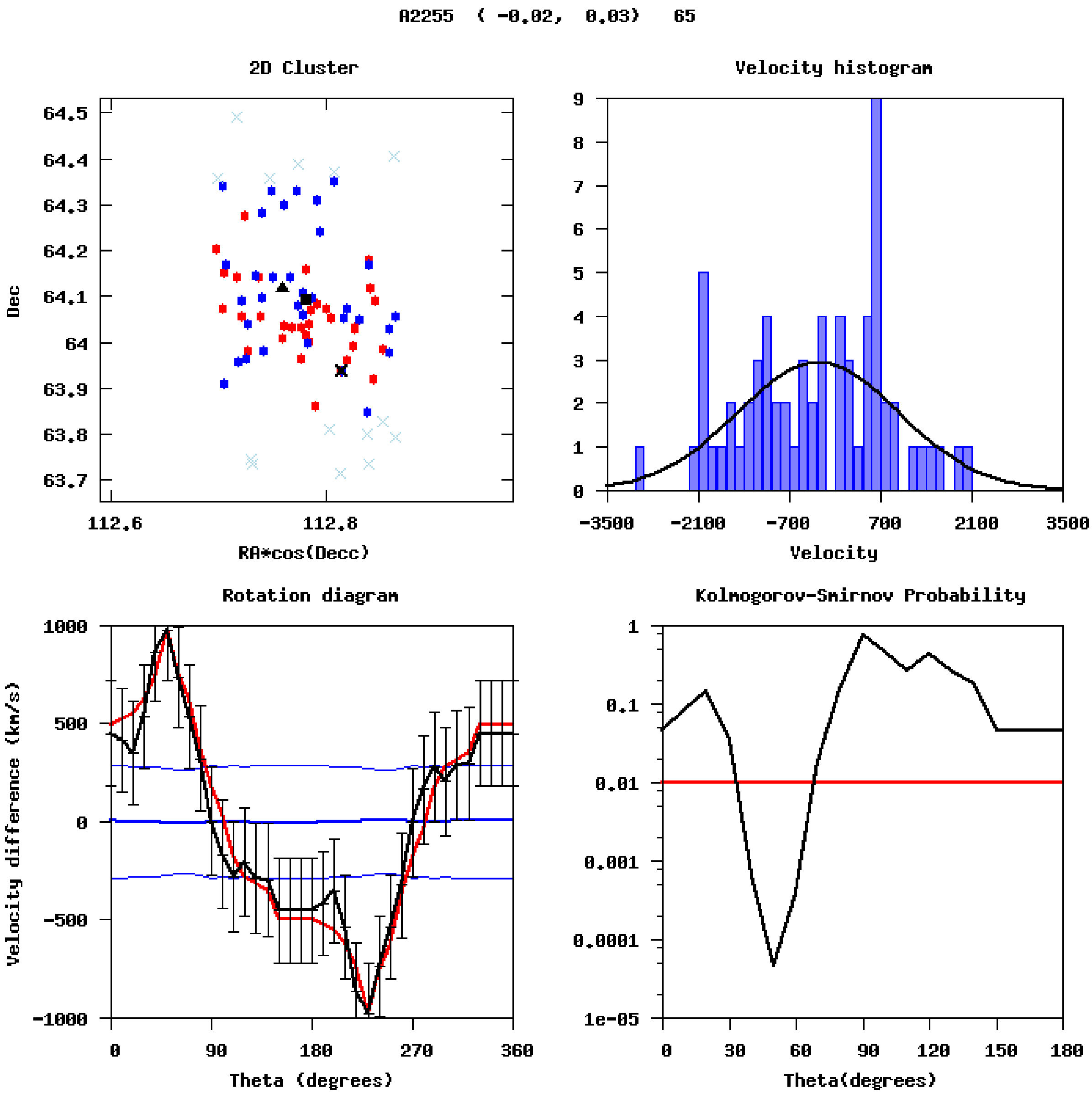

Figure 76: Abell 2255 with radius of 1.5 Mpc. The title of the figure indicates the coordinates of the final selected rotational center (dy, dx) and the number of galaxies included in the study.

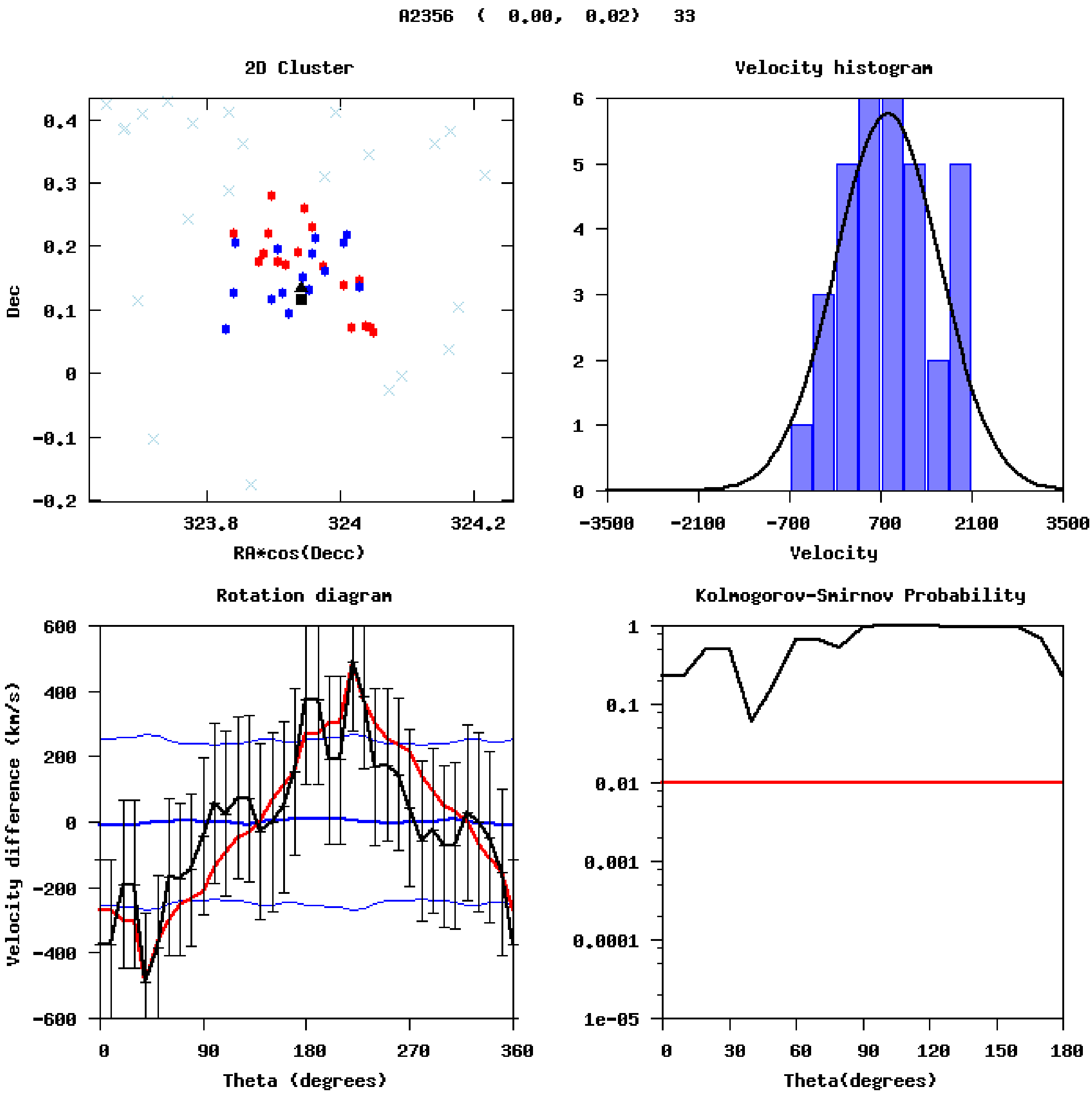

Figure 77: Abell 2356 with radius of 1.5 Mpc. The title of the figure indicates the coordinates of the final selected rotational center (dy, dx) and the number of galaxies included in the study.

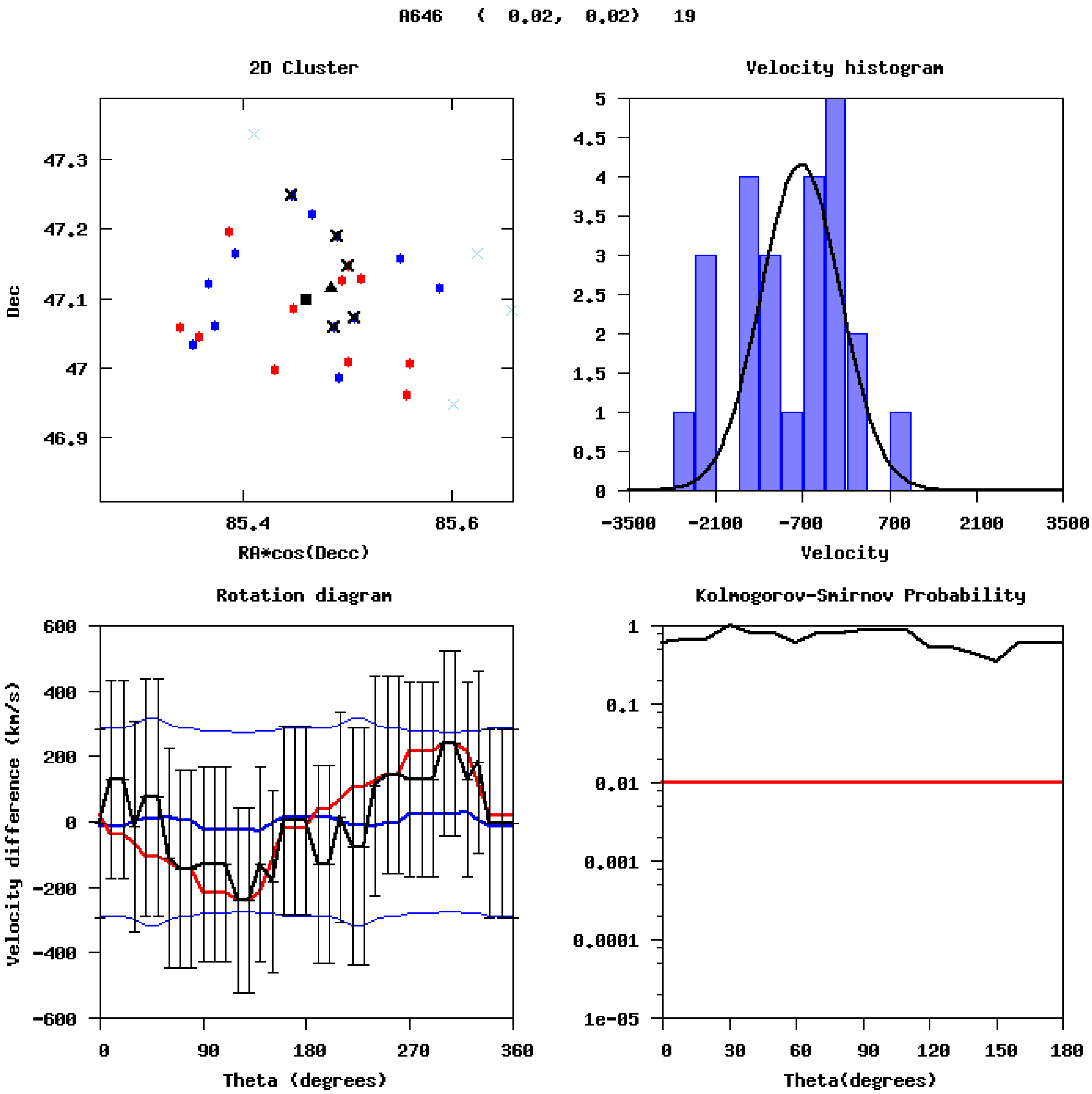

Figure 78: Abell 646 with radius of 1.5 Mpc. The title of the figure indicates the coordinates of the final selected rotational center (dy, dx) and the number of galaxies included in the study.

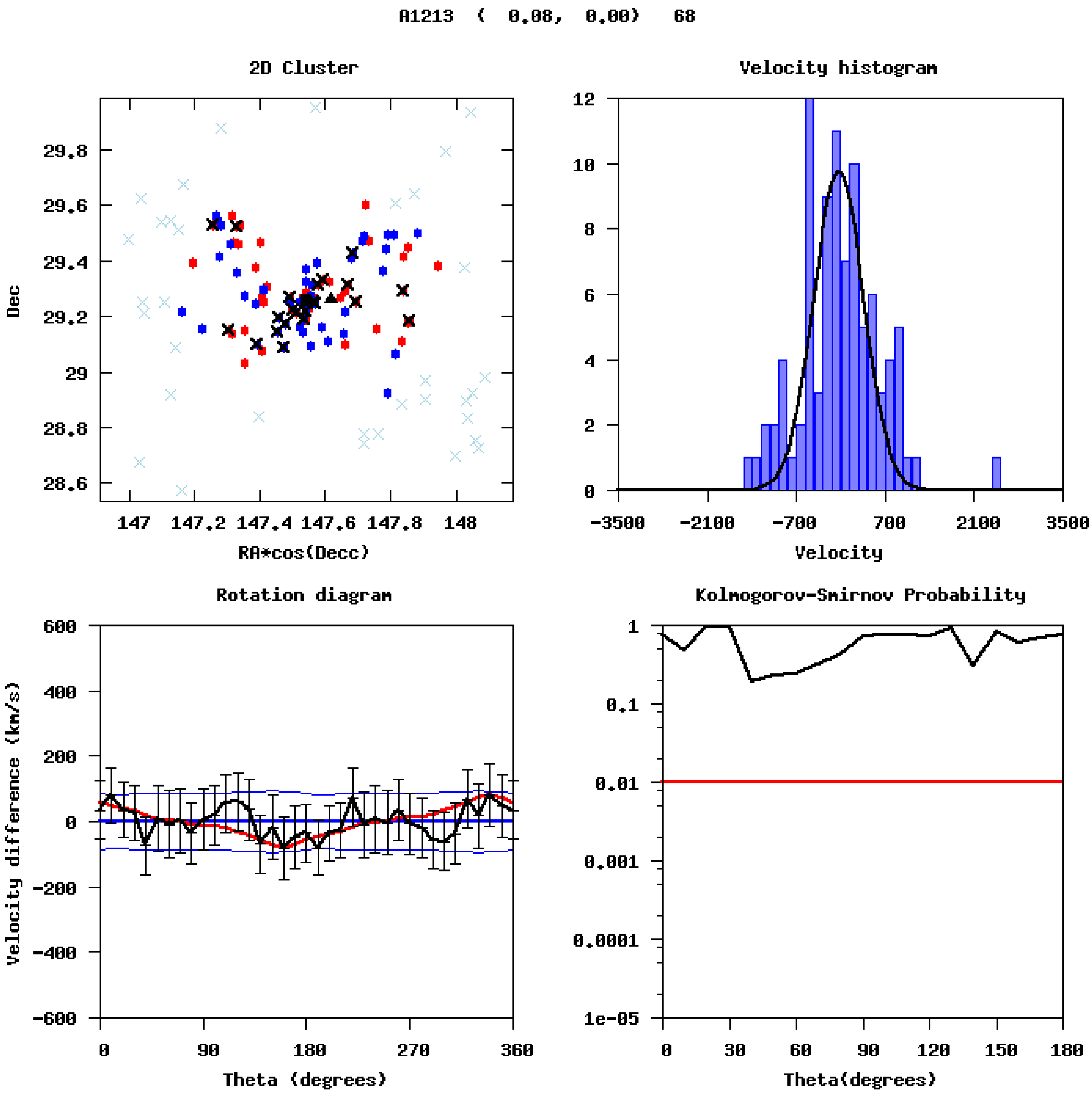

Figure 79: Abell 1213 with radius of 1.5 Mpc. The title of the figure indicates the coordinates of the final selected rotational center (dy, dx) and the number of galaxies included in the study.

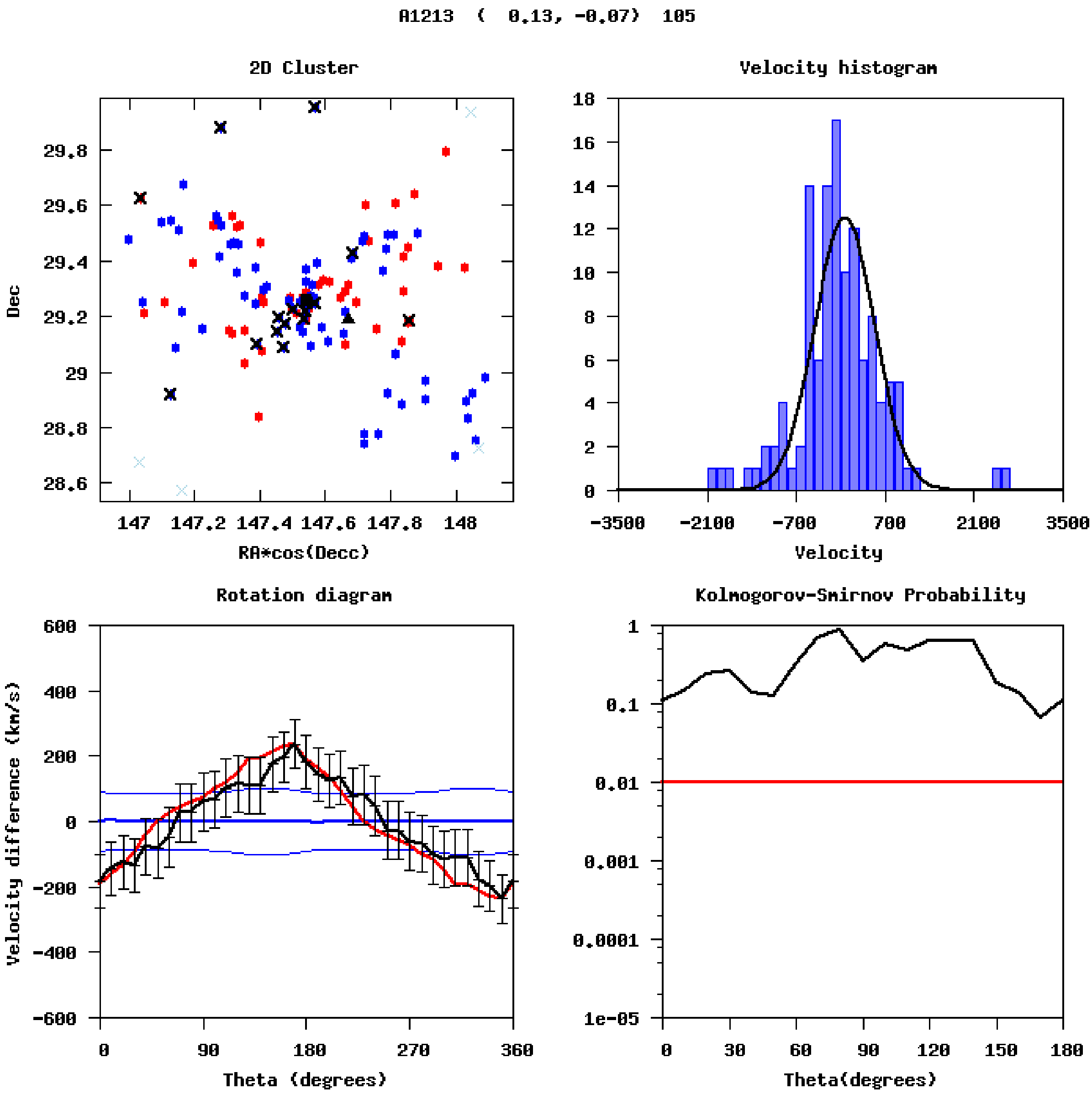

Figure 80: Abell 1213 with radius of 2.5 Mpc. The title of the figure indicates the coordinates of the final selected rotational center (dy, dx) and the number of galaxies included in the study.

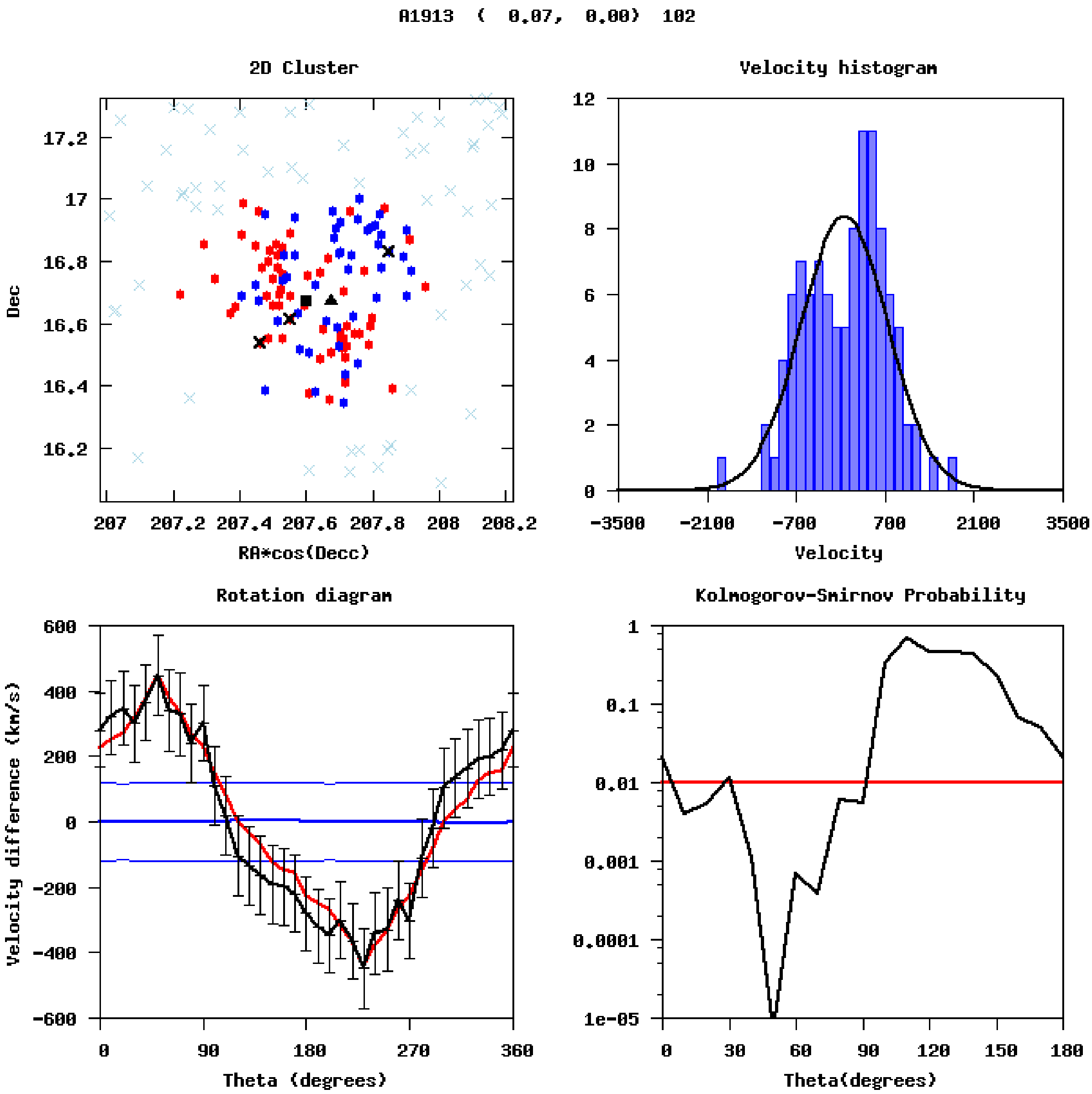

Figure 81: Abell 1913 with radius of 1.5 Mpc. The title of the figure indicates the coordinates of the final selected rotational center (dy, dx) and the number of galaxies included in the study.

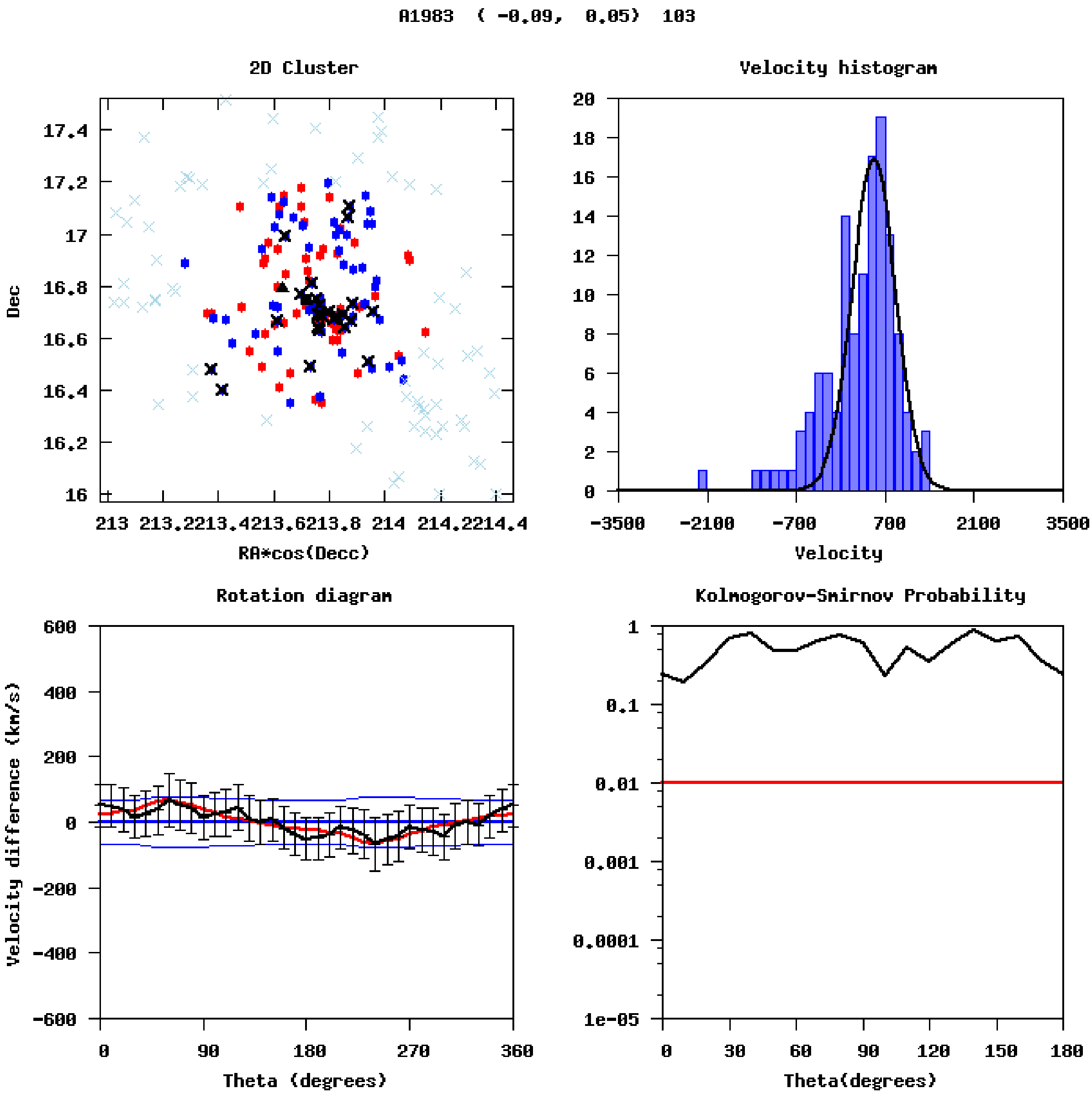

Figure 82: Abell 1983 with radius of 1.5 Mpc. The title of the figure indicates the coordinates of the final selected rotational center (dy, dx) and the number of galaxies included in the study.

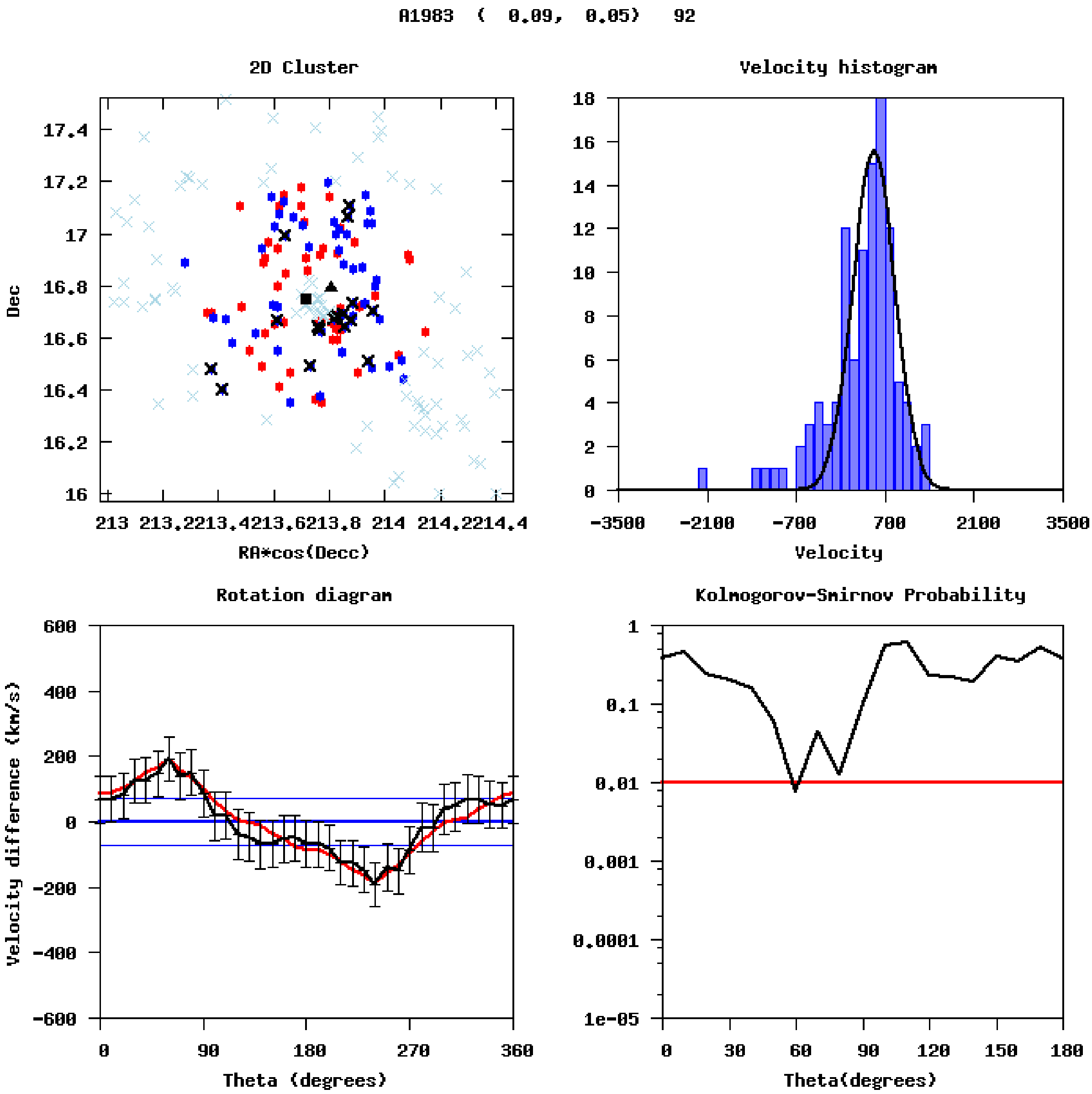

Figure 83: Abell 1983 with radius between 0.3 and 1.5 Mpc. The title of the figure indicates the coordinates of the final selected rotational center (dy, dx) and the number of galaxies included in the study.

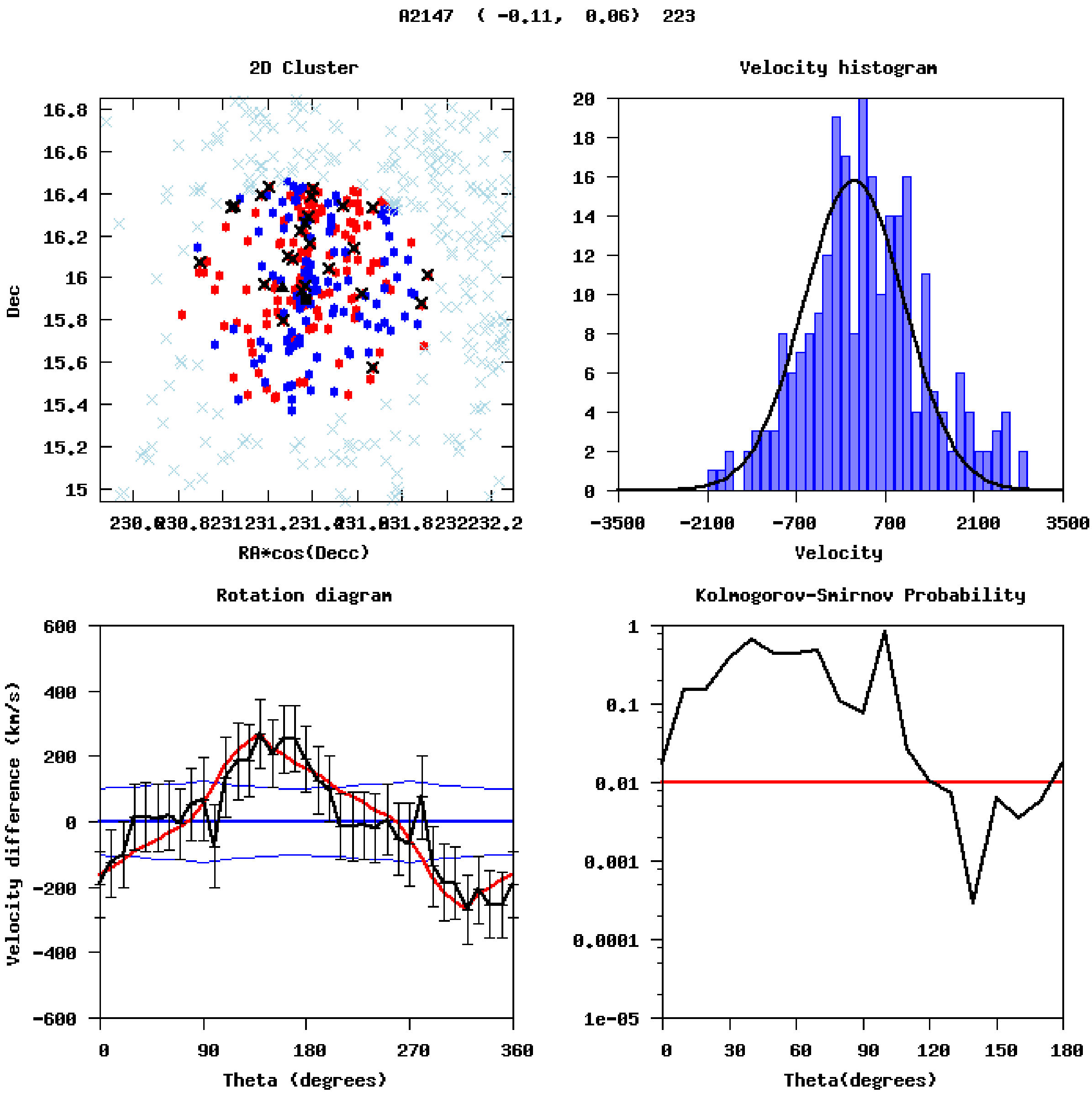

Figure 84: Abell 2147 with radius of 1.5 Mpc. The title of the figure indicates the coordinates of the final selected rotational center (dy, dx) and the number of galaxies included in the study.

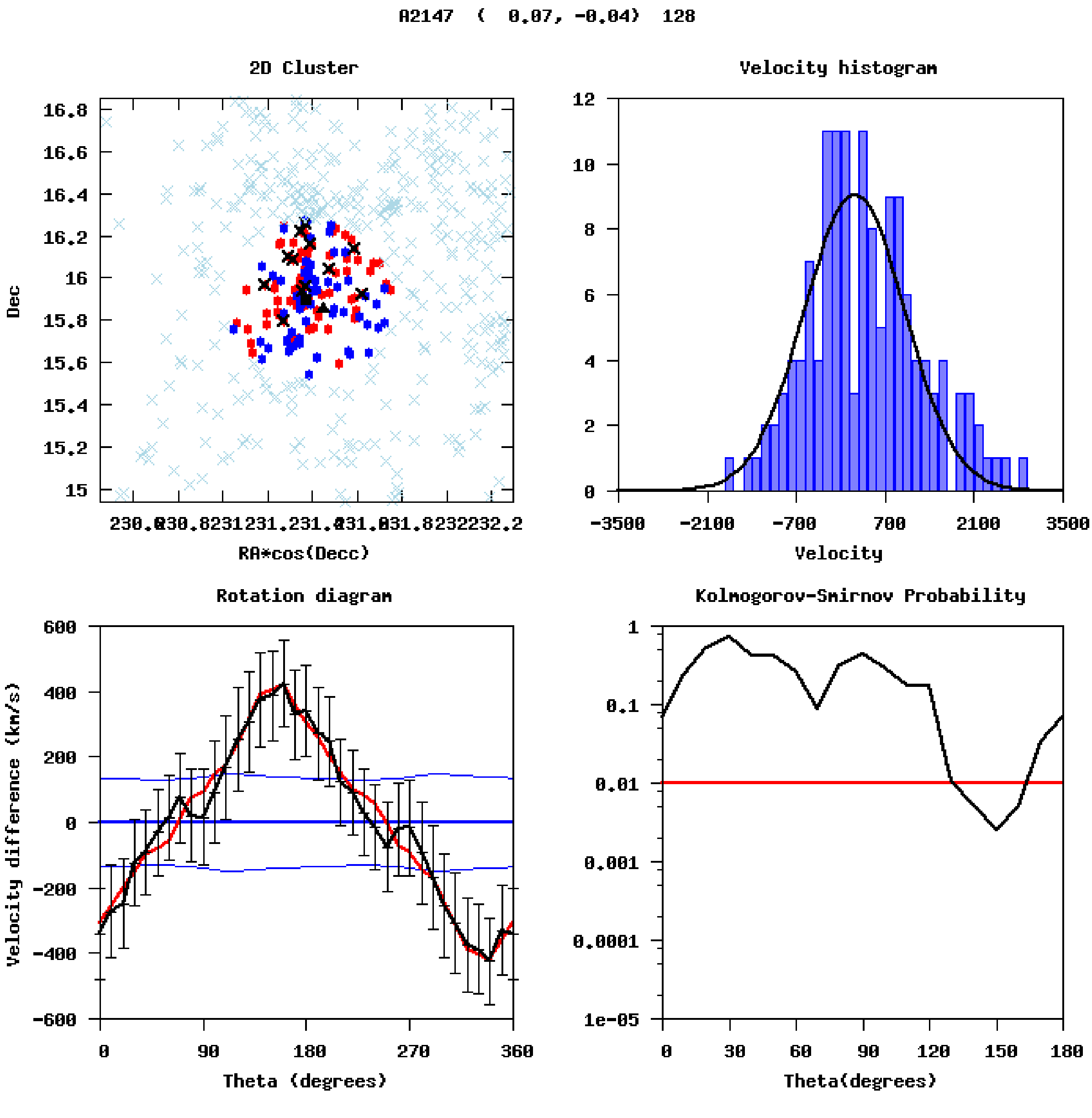

Figure 85: Abell 2147 with radius of 1 Mpc. The title of the figure indicates the coordinates of the final selected rotational center (dy, dx) and the number of galaxies included in the study.

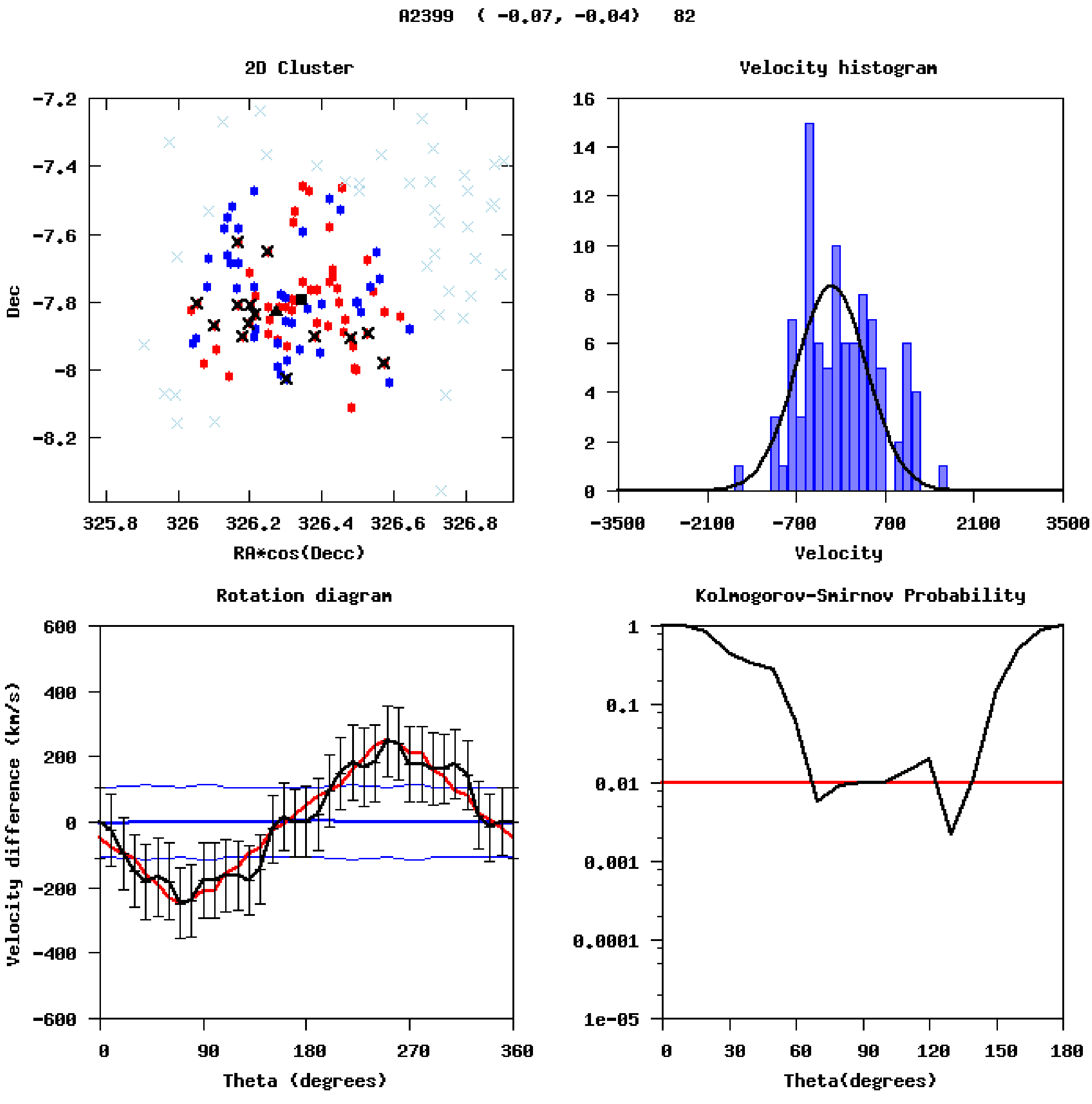

Figure 86: Abell 2399 with radius of 1.5 Mpc. The title of the figure indicates the coordinates of the final selected rotational center (dy, dx) and the number of galaxies included in the study.

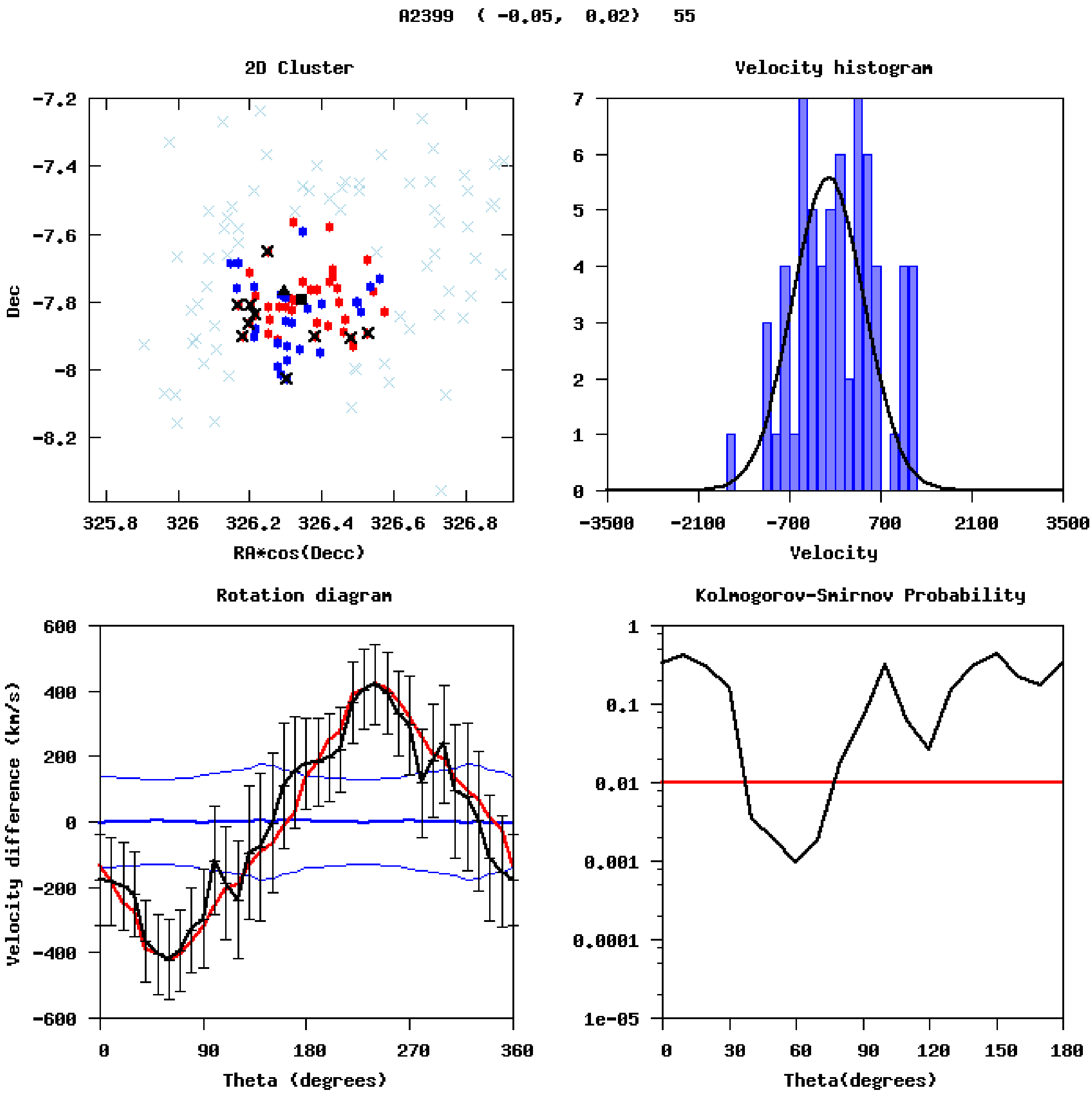

Figure 87: Abell 2399 with radius of 1 Mpc. The title of the figure indicates the coordinates of the final selected rotational center (dy, dx) and the number of galaxies included in the study.

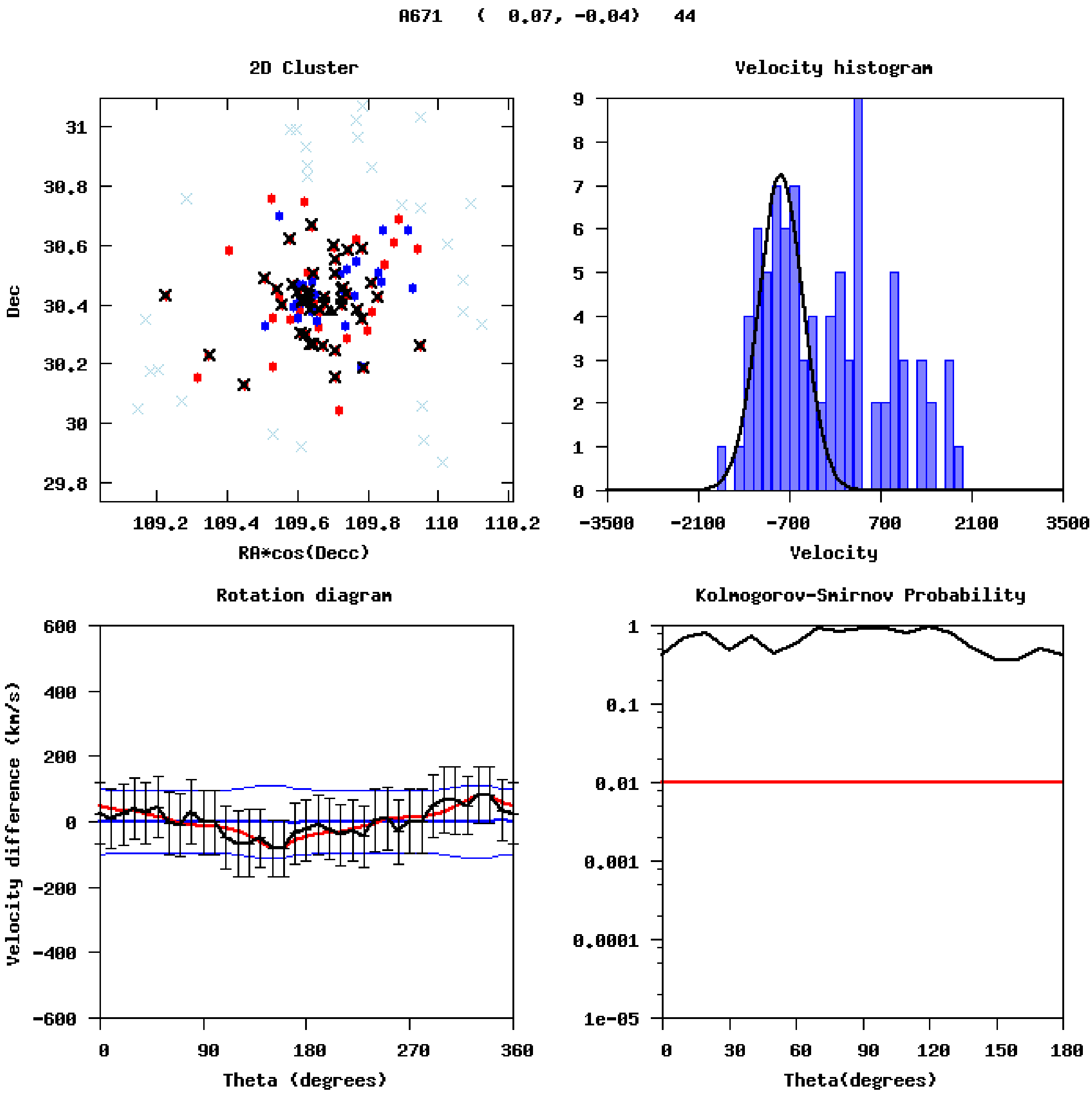

Figure 88: Abell 671 with radius of 1.5 Mpc. The title of the figure indicates the coordinates of the final selected rotational center (dy, dx) and the number of galaxies included in the study.

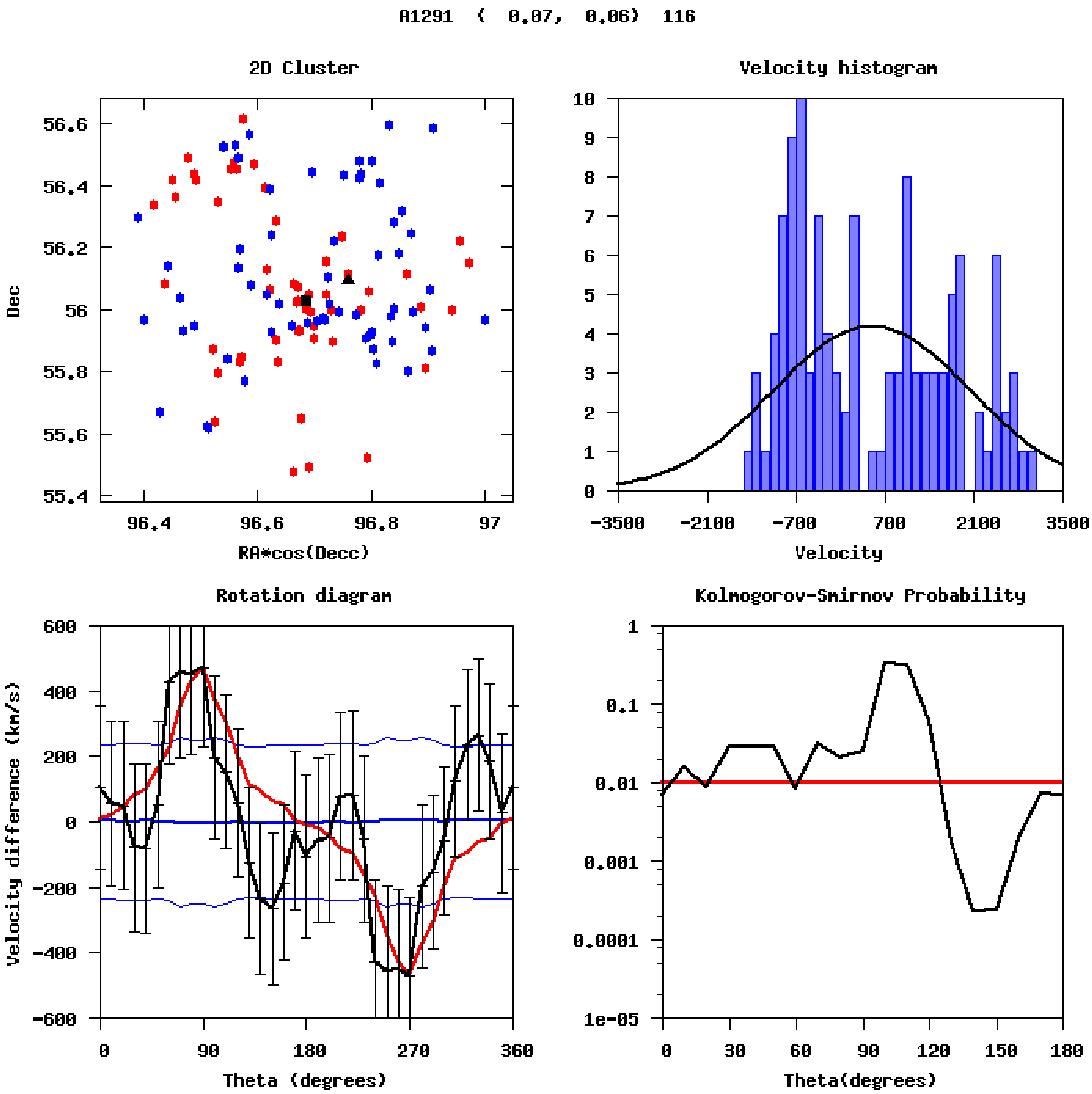

Figure 89: Abell 1291 with radius of 2.5 Mpc. The title of the figure indicates the coordinates of the final selected rotational center (dy, dx) and the number of galaxies included in the study.

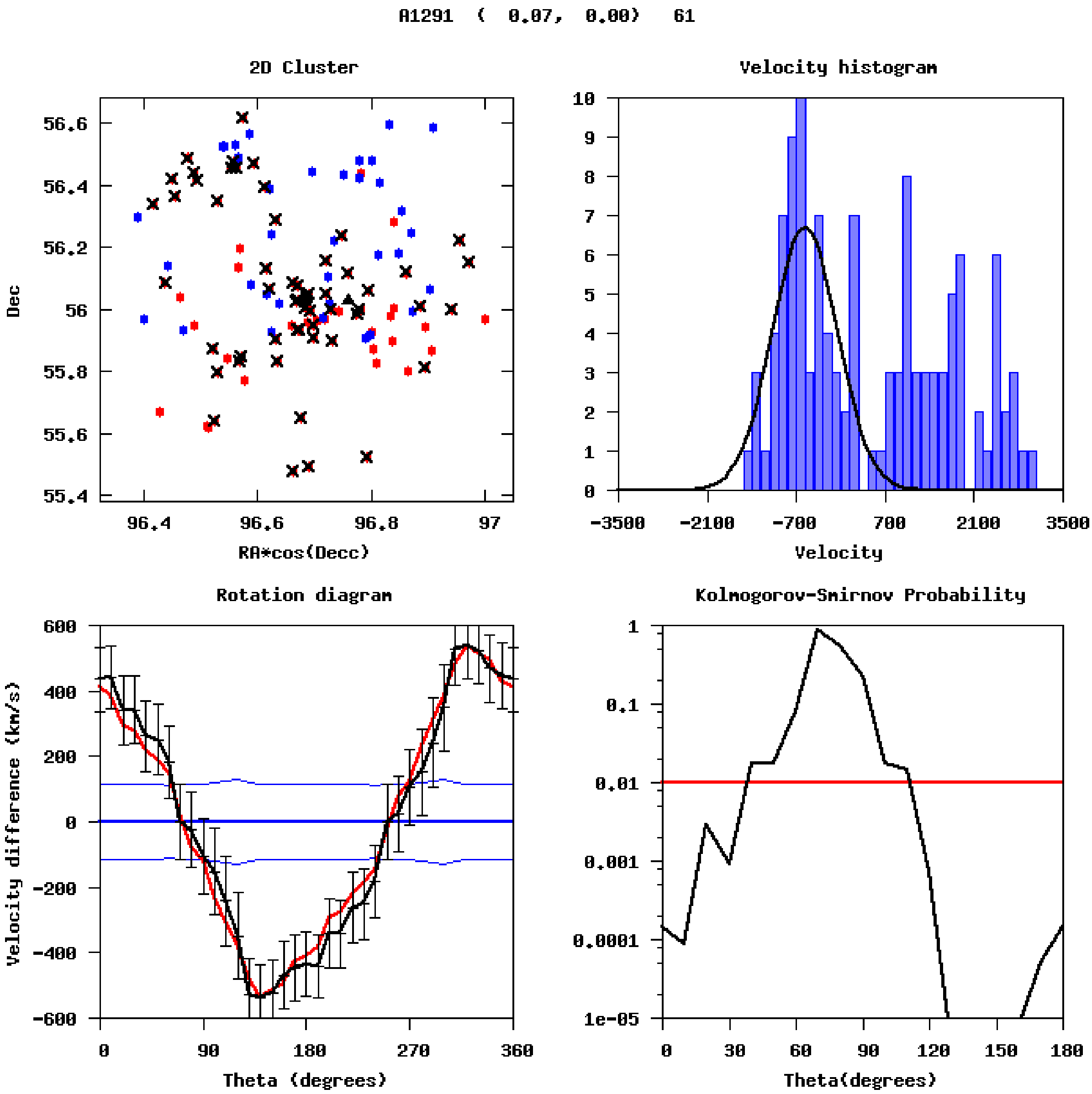

Figure 90: Substructure a of Abell 1291 with radius of 2.5 Mpc. The title of the figure indicates the coordinates of the final selected rotational center (dy, dx) and the number of galaxies included in the study.

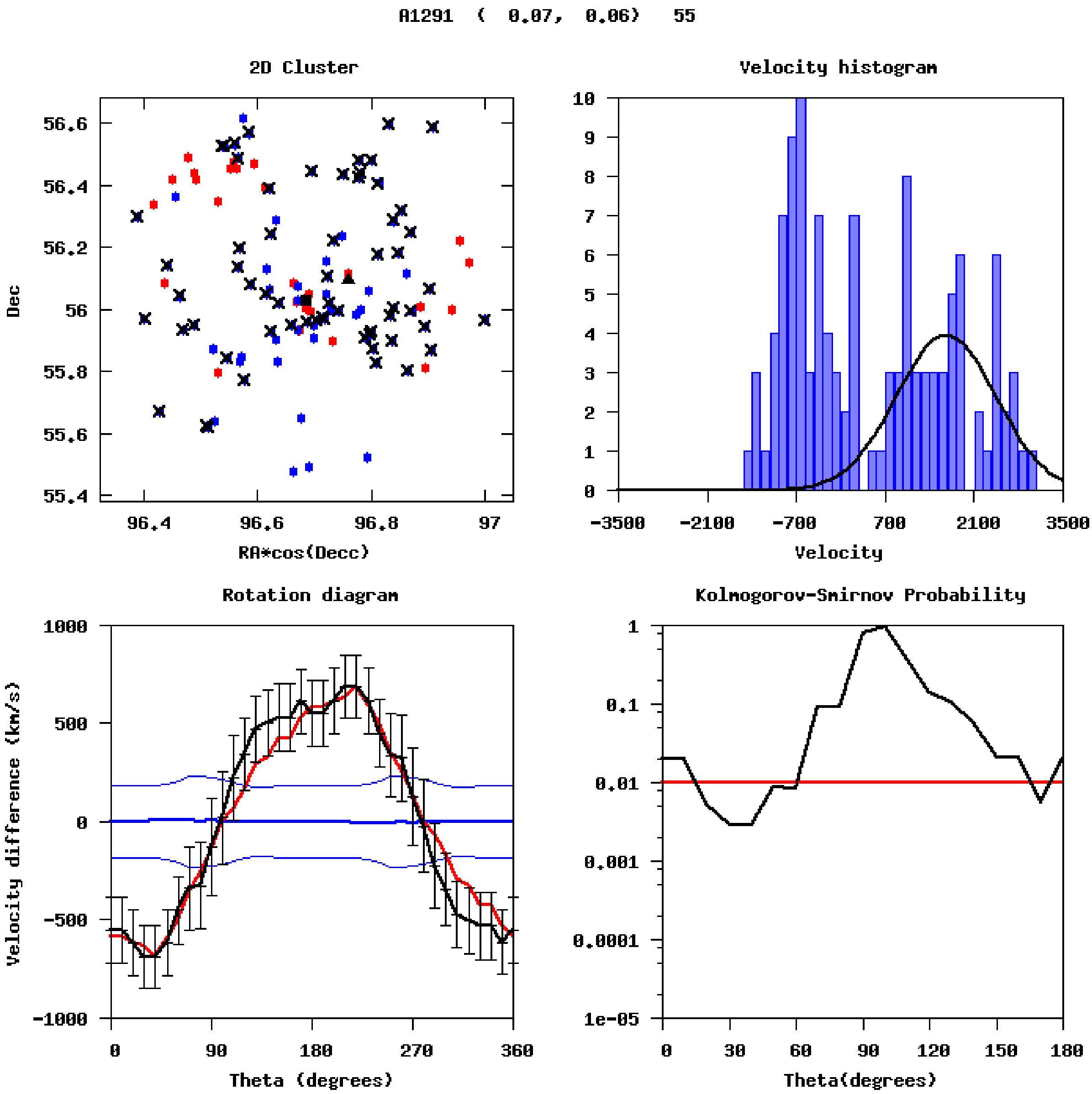

Figure 91: Substructure b of Abell 1291 with radius of 2.5 Mpc. The title of the figure indicates the coordinates of the final selected rotational center (dy, dx) and the number of galaxies included in the study.

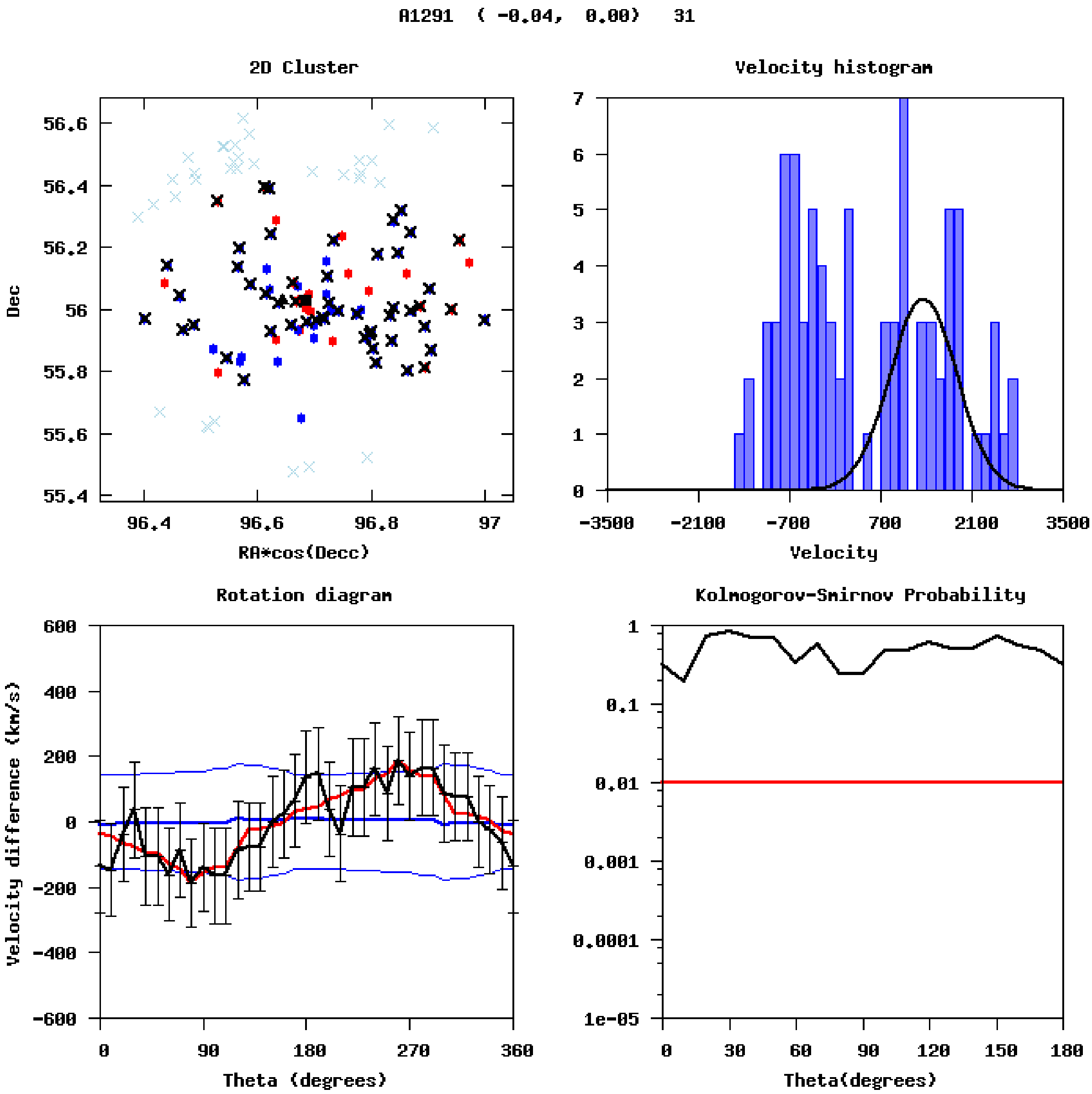

Figure 92: The second substructure of substructure b of Abell 1291 with radius of 2.5 Mpc. The title of the figure indicates the coordinates of the final selected rotational center (dy, dx) and the number of galaxies included in the study.

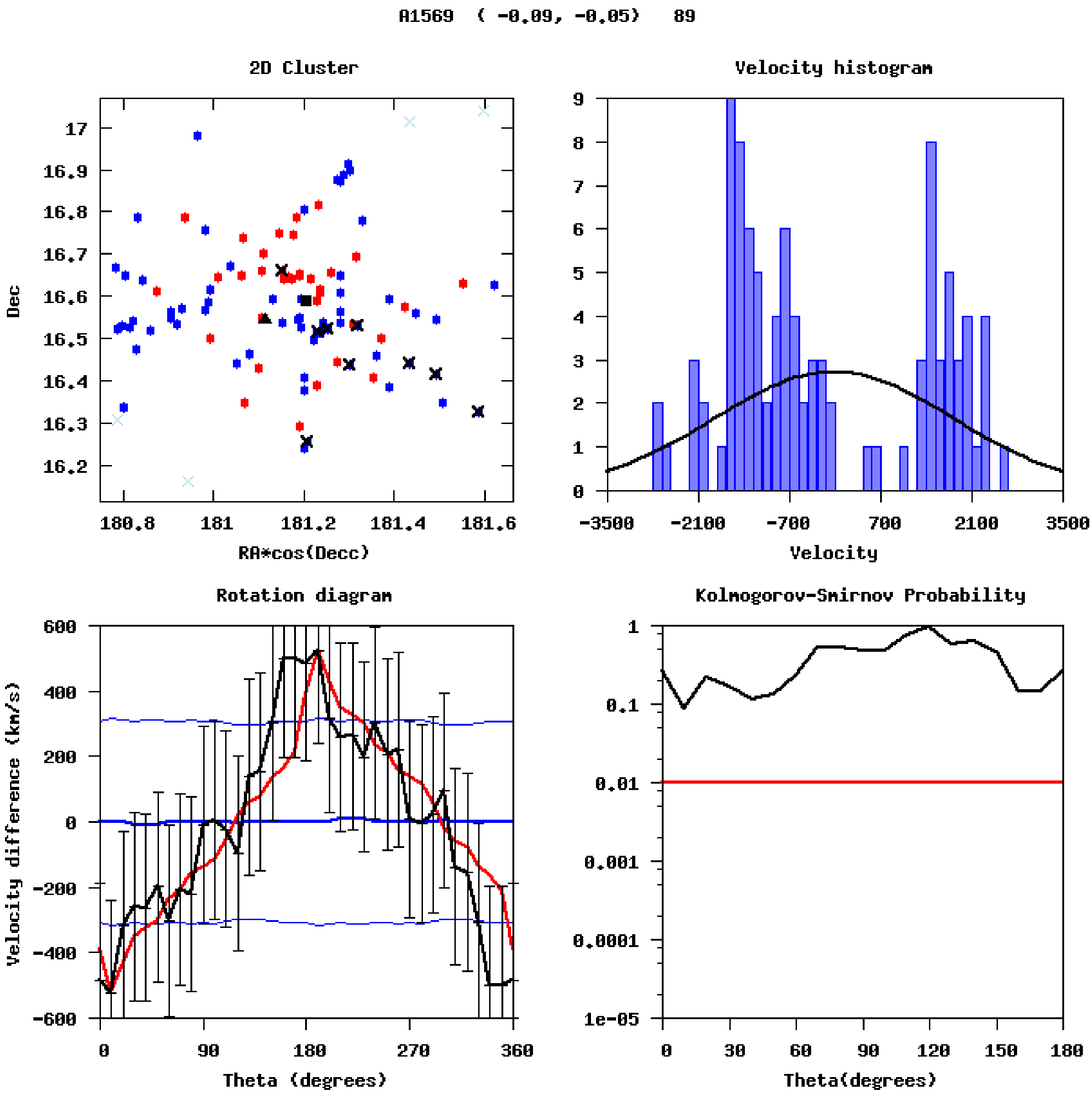

Figure 93: Abell 1569 with radius of 2.5 Mpc. The title of the figure indicates the coordinates of the final selected rotational center (dy, dx) and the number of galaxies included in the study.

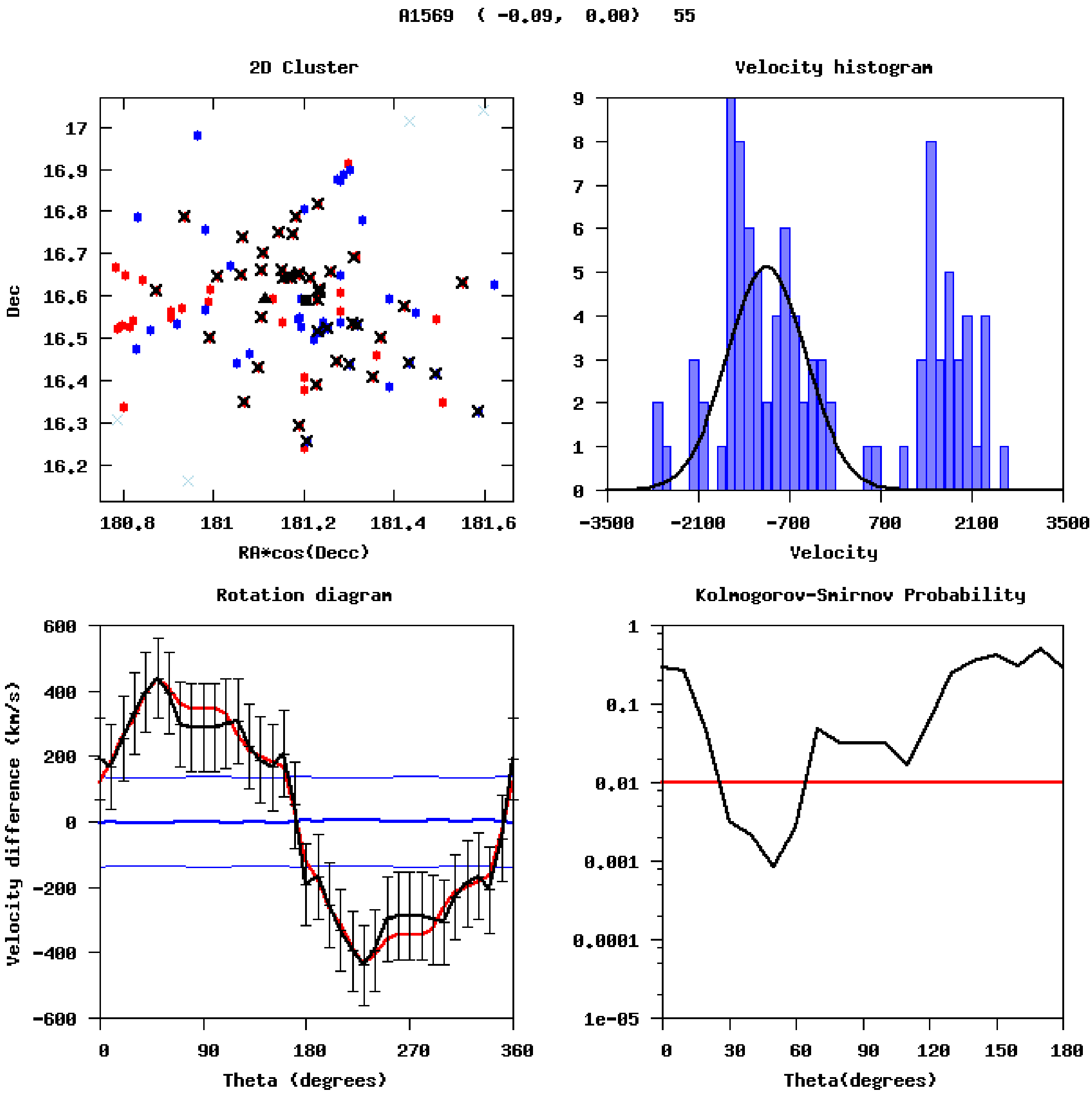

Figure 94: Substructure a of Abell 1569 with radius of 2.5 Mpc. The title of the figure indicates the coordinates of the final selected rotational center (dy, dx) and the number of galaxies included in the study.

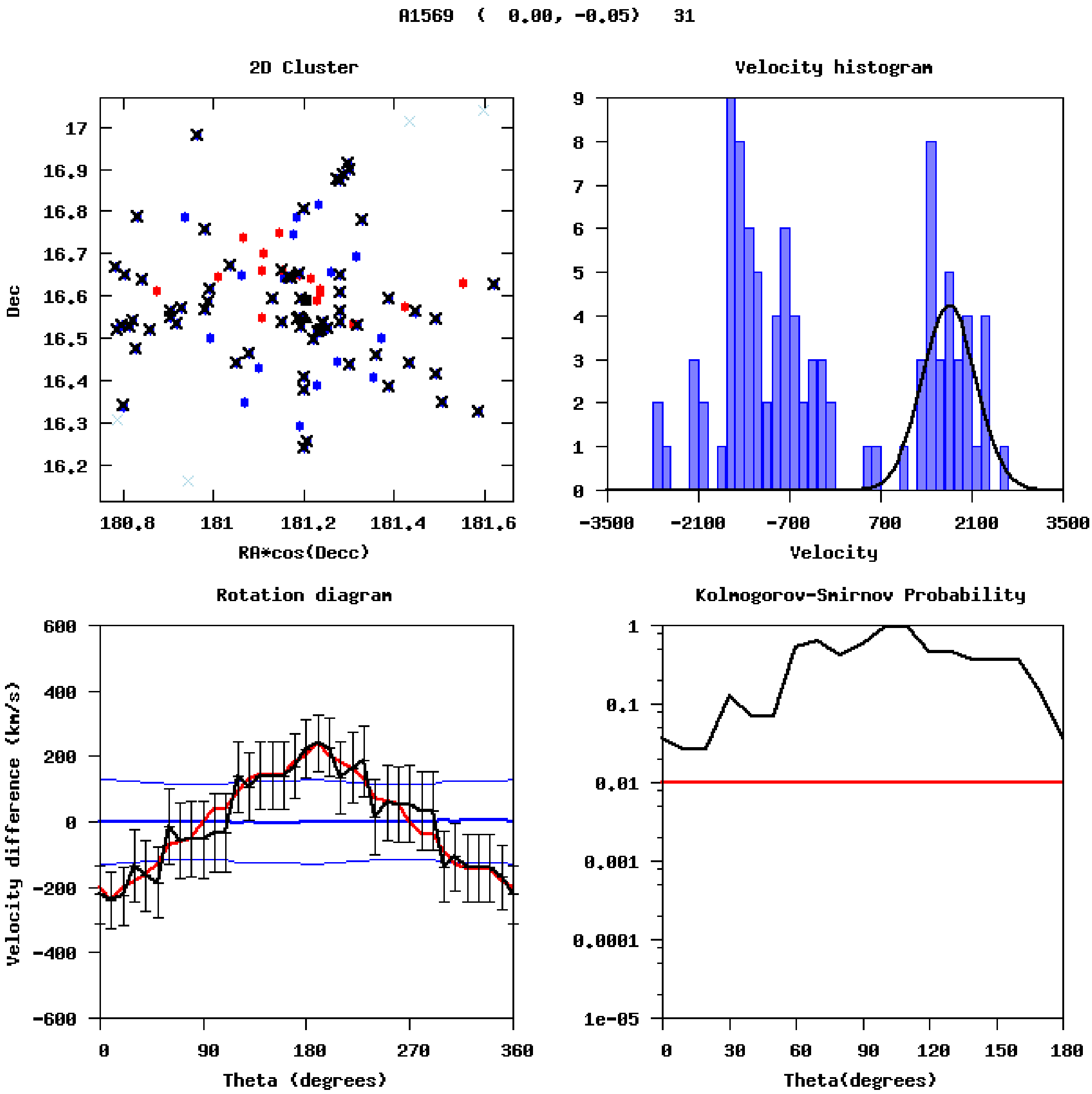

Figure 95: Substructure b of Abell 1569 with radius of 2.5 Mpc. The title of the figure indicates the coordinates of the final selected rotational center (dy, dx) and the number of galaxies included in the study.

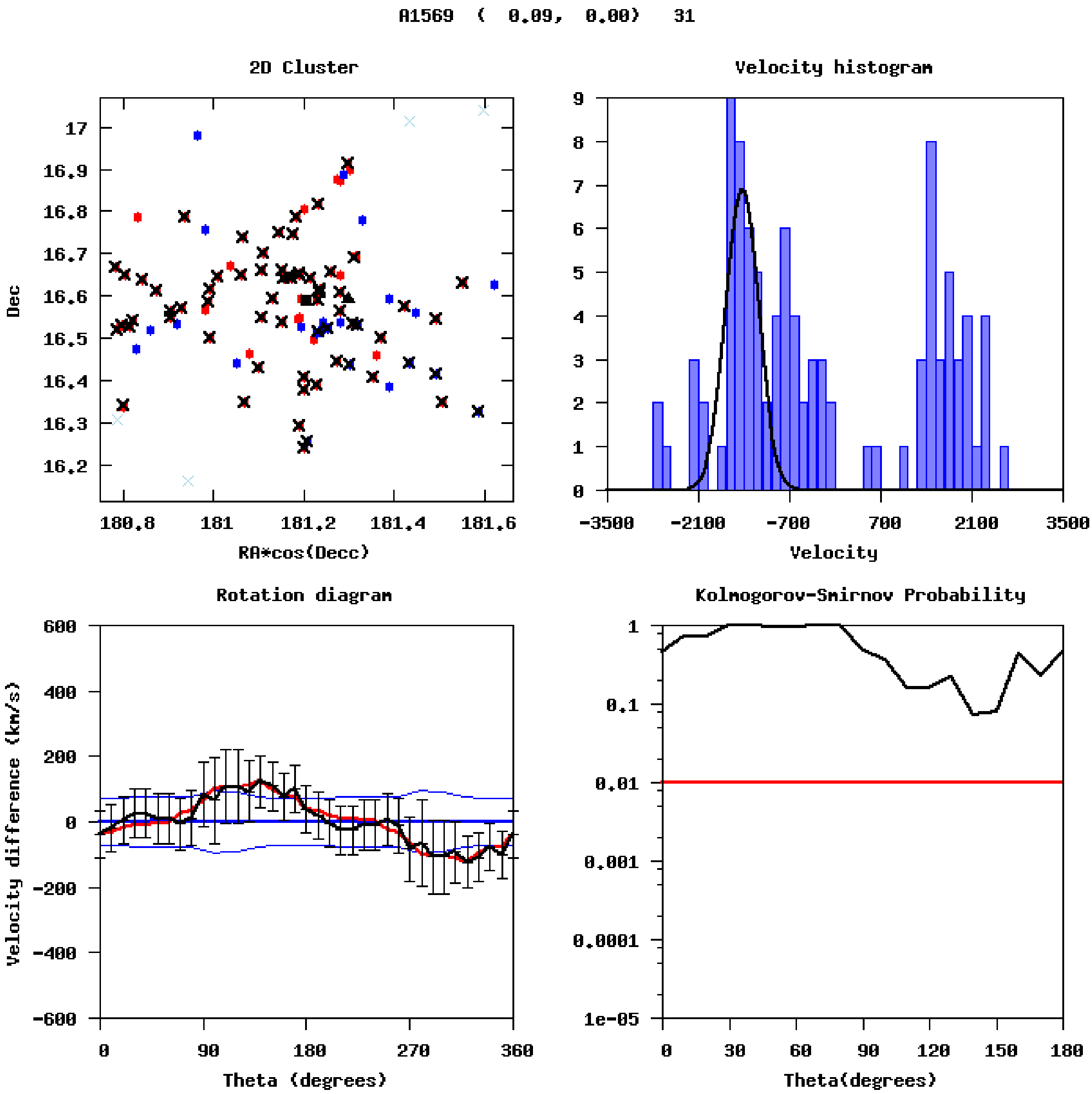

Figure 96: The first substructure of substructure a of Abell 1569 with radius of 2.5 Mpc. The title of the figure indicates the coordinates of the final selected rotational center (dy, dx) and the number of galaxies included in the study.

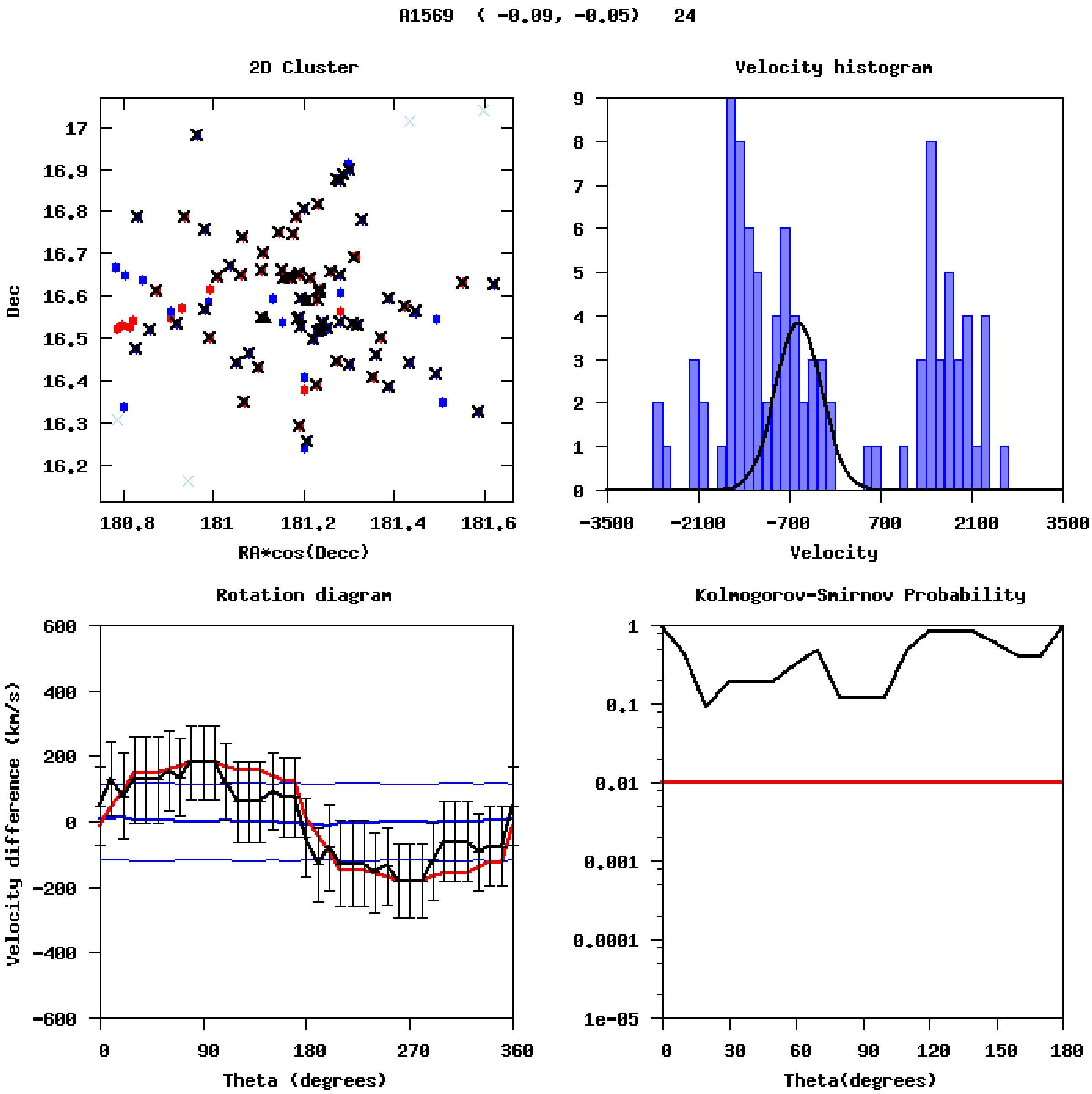

Figure 97: The second substructure of substructure a of Abell 1569 with radius of 2.5 Mpc. The title of the figure indicates the coordinates of the final selected rotational center (dy, dx) and the number of galaxies included in the study.

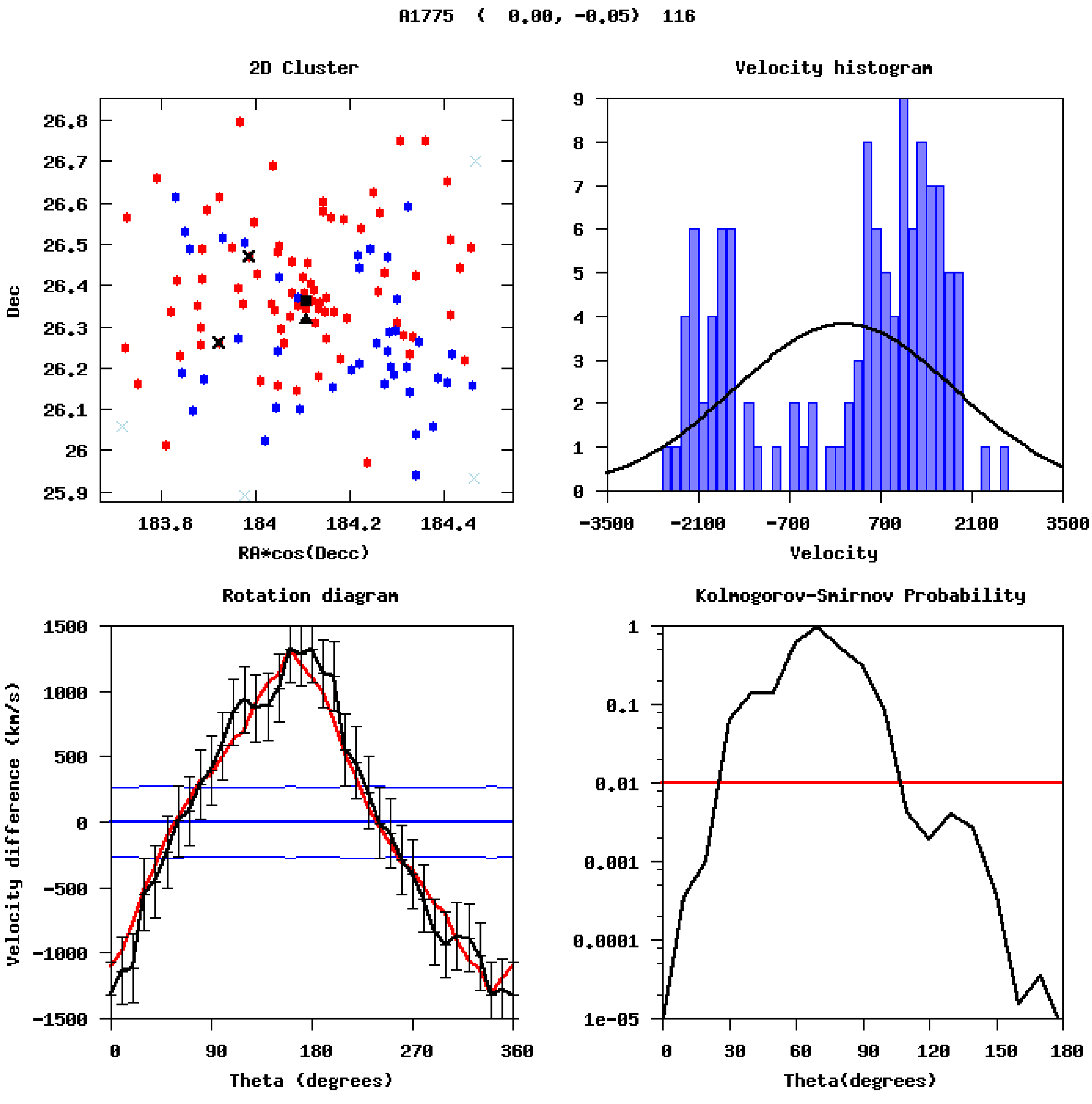

Figure 98: Abell 1775 with radius of 2.5 Mpc. The title of the figure indicates the coordinates of the final selected rotational center (dy, dx) and the number of galaxies included in the study.

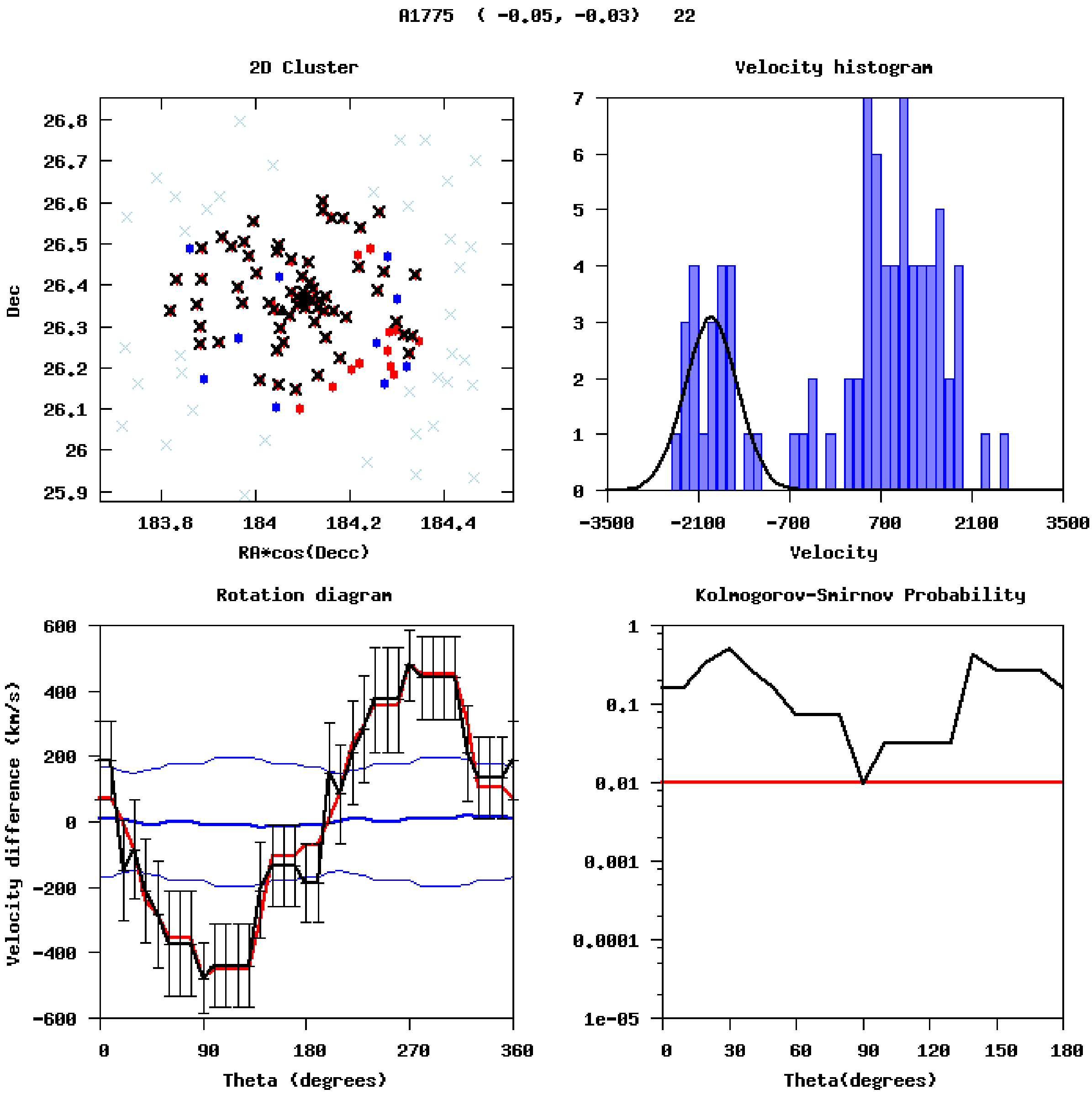

Figure 99: Substructure a of Abell 1775 with radius of 1.5 Mpc. The title of the figure indicates the coordinates of the final selected rotational center (dy, dx) and the number of galaxies included in the study.

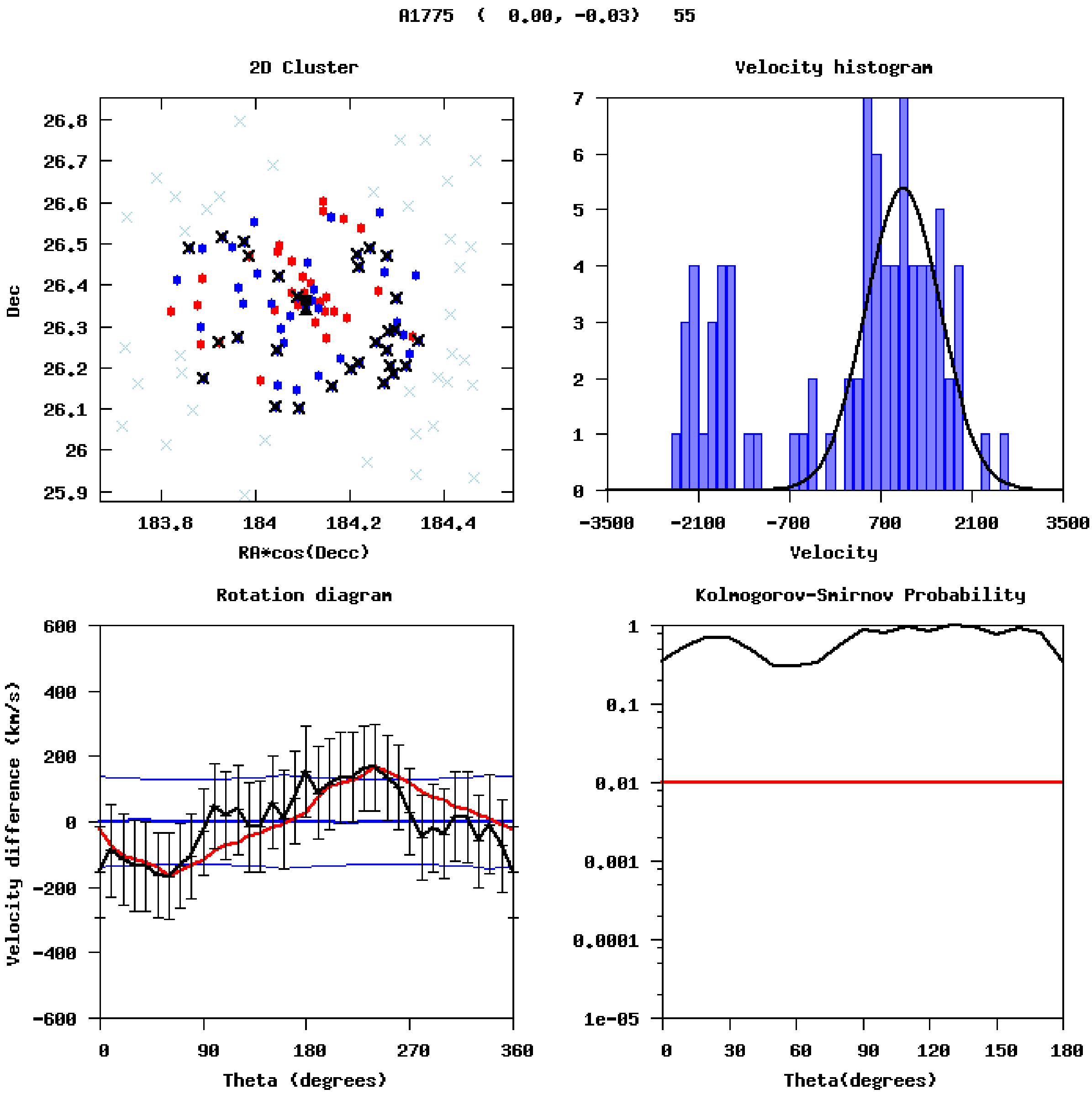

Figure 100: Substructure b of Abell 1775 with radius of 1.5 Mpc. The title of the figure indicates the coordinates of the final selected rotational center (dy, dx) and the number of galaxies included in the study.

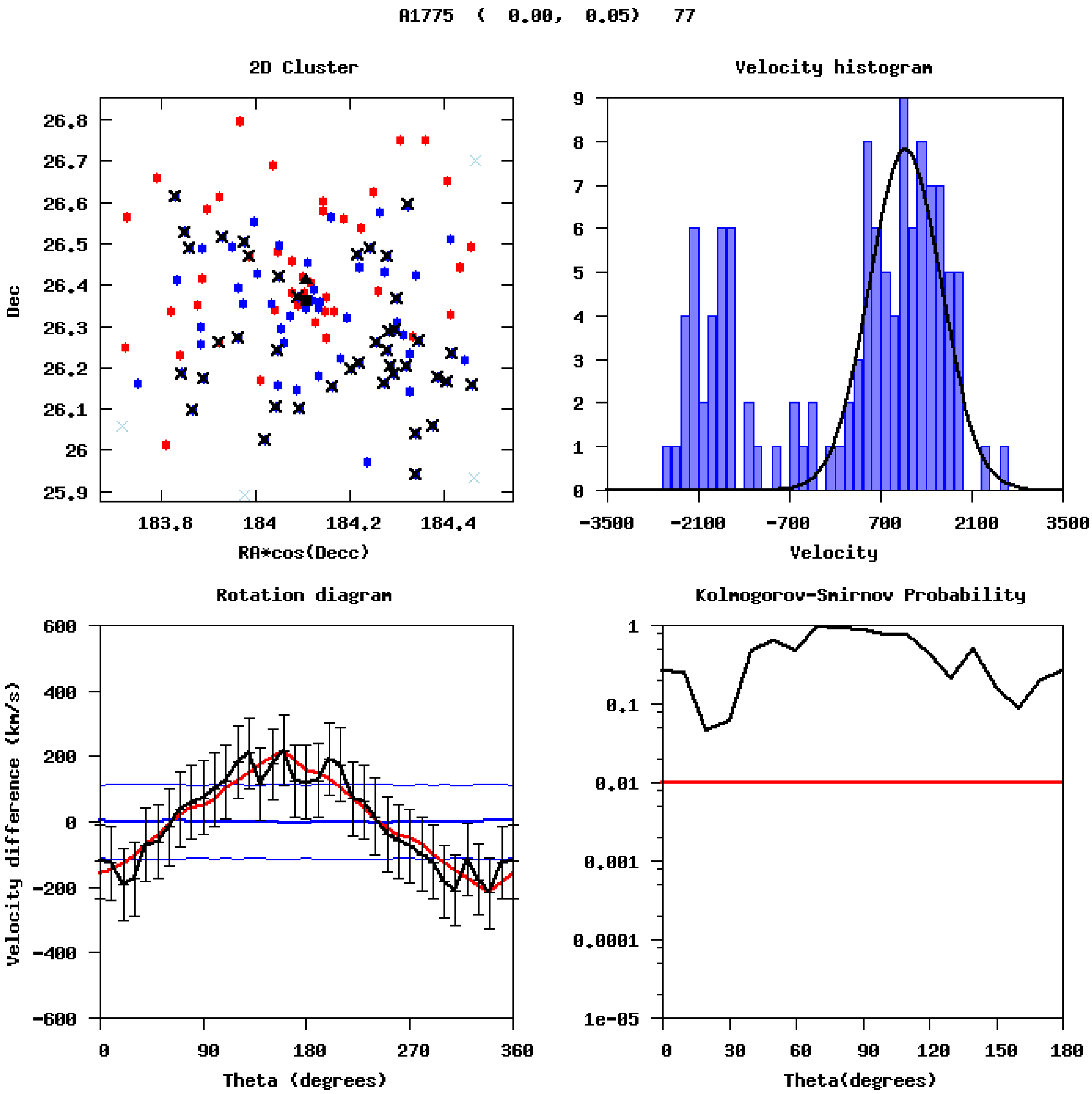

Figure 101: Substructure b of Abell 1775 with radius of 2.5 Mpc. The title of the figure indicates the coordinates of the final selected rotational center (dy, dx) and the number of galaxies included in the study.

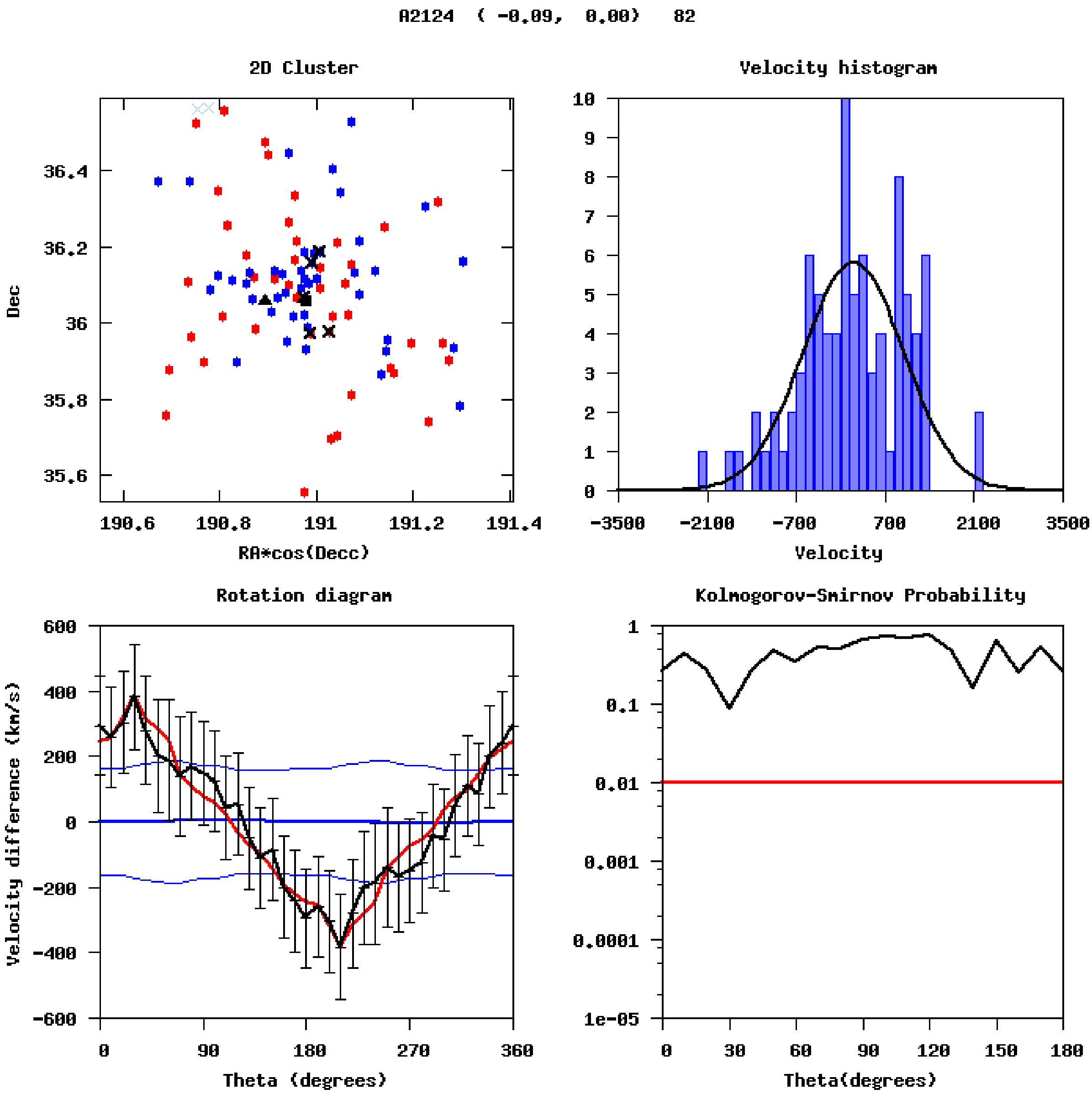

Figure 102: Abell 2124 with radius of 2.5 Mpc. The title of the figure indicates the coordinates of the final selected rotational center (dy, dx) and the number of galaxies included in the study.

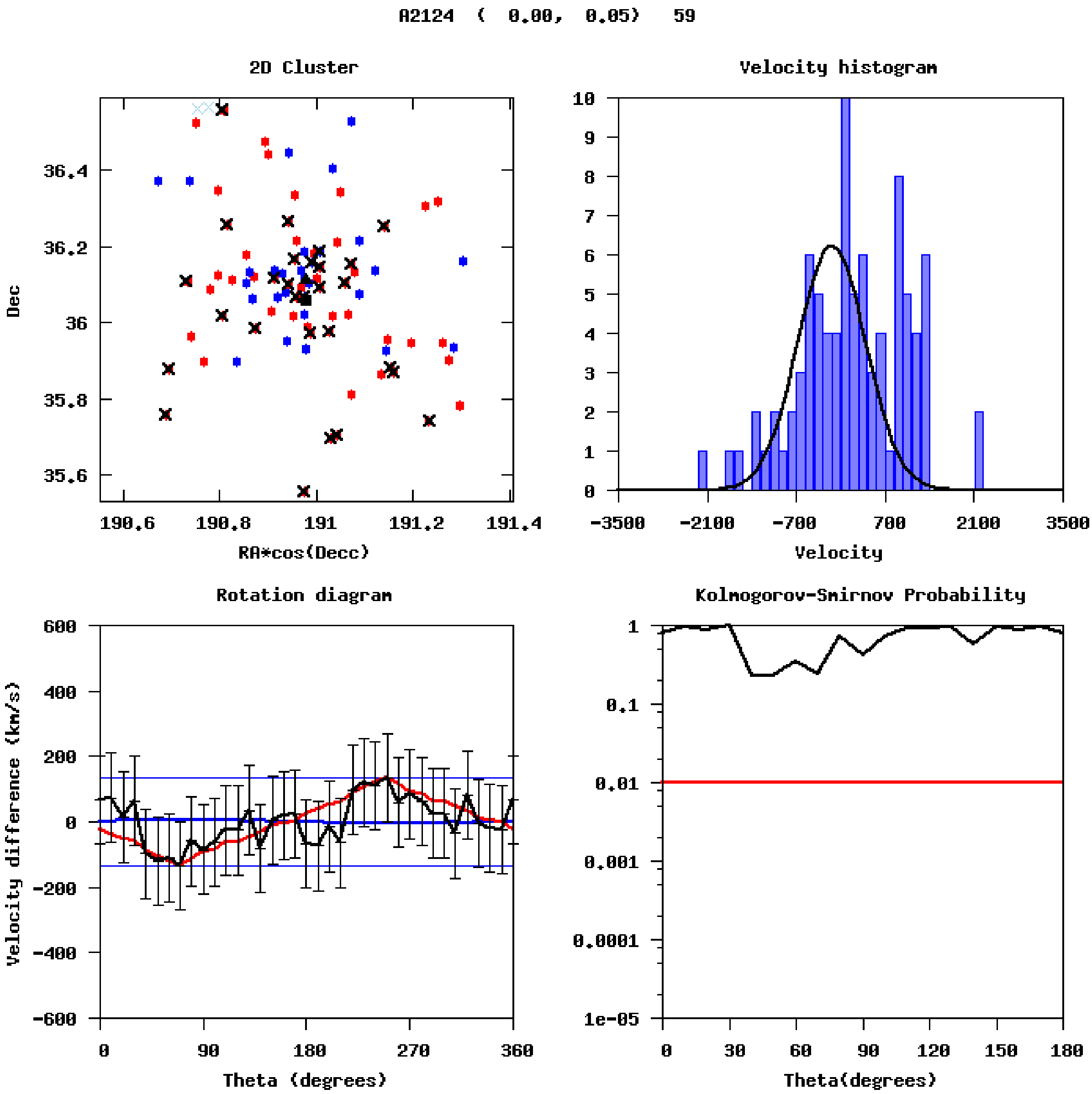

Figure 103: Substructure a of Abell 2124 with radius of 2.5 Mpc. The title of the figure indicates the coordinates of the final selected rotational center (dy, dx) and the number of galaxies included in the study.

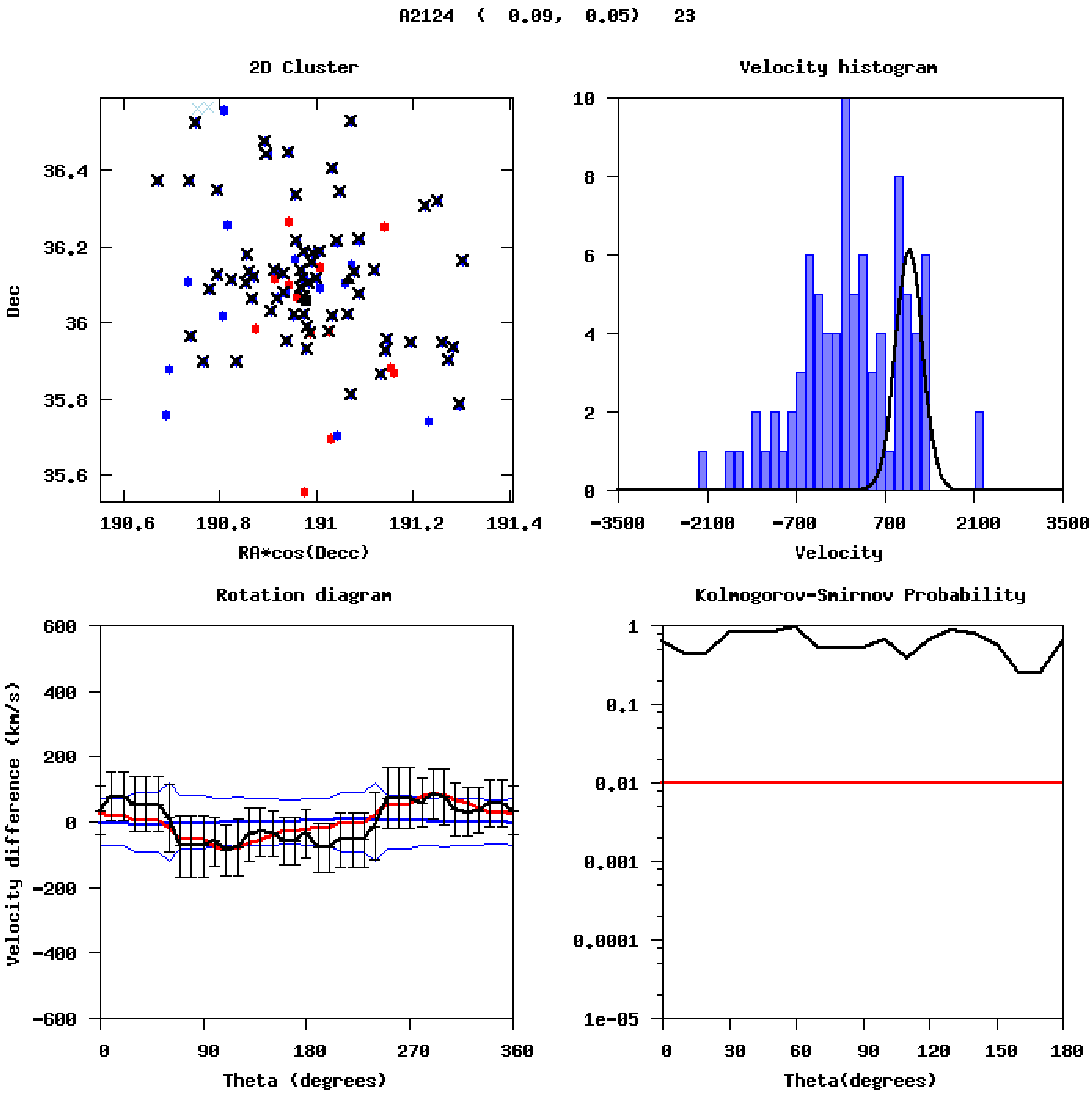

Figure 104: Substructure b of Abell 2124 with radius of 2.5 Mpc. The title of the figure indicates the coordinates of the final selected rotational center (dy, dx) and the number of galaxies included in the study.

References

[1] Abell G.O. (1965), ARA&A, 3, 1

[2] Ade P.A.R., Aghanim N., Armitage-Caplan C. et al. (2013), Planck Collaboration, arXiv:1303.5062

[3] Bahcall N.A., Lubin L.M. & Dorman V. (1995), ApJ, 447, L81

[4] Bahcall N.A. (2000), Physics Reports, 333, 233

[5] Bahcall N.A., Cen R., Dave R., Ostriker J.P. & Yu Q. (2000), ApJ, 541, 1

[6] Bardeen J.M., Bond J.R., Kaiser N. & Szalay A.S. (1986), ApJ , 304, 15

[7] Barkhouse W.A., Yee H.K.C. & Lopez-Cruz O. (2004), *Tracing Cosmic Evolution with Galaxy Clusters*, ASP Conference Series, arXiv:astro-ph/0410173, doi:10.1103/RevModPhys.77.207

[8] Basilakos S., Plionis M. & Maddox S. (2000), MNRAS, 316, 779

[9] Basilakos S., Plionis M., Rowan-Robinson M. (2001), MNRAS, 323, 47

[10] Bautz L.P. & Morgan W.W. (1970), *On the Classification of the Forms of Clusters of Galaxies*, Astrophysical Journal 162: L149, doi:10.1086/180643

[11] Bianconi M, Ettori S. & Nipoti C. (2013), arXiv:1305.5519v1

[12] Binggeli B. (1982), AA, 107, 338

[13] Birkinshaw M. (1999), Phys.Rep., 310, 97

[14] Blakeslee J.P & Tonry J.L. (1992), ApJ, 103, 5

[15] Blanchard A., Sadat R., Bartlett J.G. & Le Dour M. (2000), AA, 362, 809

[16] Borgani S. et al. (2001), ApJ, 561, 13

[17] Borgani S. & Guzzo L. (2001), Nature, 409, 39

[18] Bryan G.L. & Norman M.L. (1998), ApJ, 495, 80

[19] Chluba J. & Mannheim K. (2002), astro-ph/0208392

[20] Coles P. & Lucchin F. (1995), *Cosmology: the origin and evolution of cosmic structure*, John Wiley & Sons

[21] Cooray A. & Chen X. (2002), ApJ, 573, 43-50

[22] de Vaucouleurs G. (1948), Annales d'Astrophysique, 11, 247

[23] Dekel A., Blumenthal G.R., Primack J.R. & Olivier S. (1989), ApJ, 338, 5

[24] Dressler A., Lynden-Bell D., Burstein D., Davies R.L., Faber S.M., Terlevich R.J. & Wegner G. (1987), ApJ, 313, 42

[25] Einasto J. (2001), New Astr.Rev., 45, 355

[26] Eke V.R., Cole S., Frenk C.S. & Patrick H.J. (1998), MNRAS, 298, 1145

[27] Ettori S. & Fabian A.C. (1999), MNRAS, 305, 834

[28] Evrard A.E., Mohr J.J., Fabricant D.G. & Geller M.J. (1993), ApJ, 419, L9

[29] Faber S.M. & Jackson R.E. (1976), ApJ, 204, 668

[30] Fang T., Humphrey Ph. & Buote D. (2008), astro-ph/0808.1106

[31] Ferrari C., Govoni F., Schindler S., Bykov A.M. & Rephaeli Y. (2008), arXiv:0801.0985, doi:10.1007/s11214-008-9311-x

[32] Freedman W.L. et al. (2001), ApJ, 553, 47

[33] Girardi, M. & Mezzetti M. (2001), ApJ, 548, 79

[34] Gioia I. (2001), in the proceedings of Chemical Enrichmen of Intracluster and Intergalactic Medium, Vulcano-Sicily, astro-ph/0107452

[35] Hamden E.T., Simpson C.M., Johnston K.V. & Lee D.M. (2010), arXiv:1005.4430v1

[36] Henry J.P. (2000), ApJ, 534, 565

[37] Hubble E.P. (1926), *Extra-galactic nebulae*, contributions from the Mount Wilson Observatory / Carnegie Institution of Washington, 324, 1b•“49

[38] Hubble E.P. (1926), Astrophysical Journal, 64, 321b•“369, doi:10.1086/143018

[39] Hubble E.P. (1927), *The Classification of Spiral Nebulae*, The Observatory, 50, 276

[40] Hubble E.P. (1936), *The Realm of the Nebulae*, New Haven: Yale University Press

[41] Hubble E.P. (1929), in the proceedings of the National Academy of Sciences, 15, (3): 168-73, doi:10.1073/pnas.15.3.168

[42] Hwang H.S. & Lee M.G. (2007), *Searching for rotating galaxy clusters in SDSS and 2dFGRS*, arXiv:astro-ph/0702184, doi:10.1086/514328

[43] Kalinkov M., Valchanov T., Valtchanov I., Kuneva I. & Dissanska M. (2008), astro-ph/0505091

[44] King I. (1962), AJ, 67, 471

[45] Krauss L.M. & Kernan P.J. (1994), arXiv:astro-ph/9408023

[46] Lacey C. & Cole S. (1996), MNRAS, 262, 627

[47] Lahav O., Rees M.J., Lilje P.B. & Primack J. (1991), MNRAS, 251, 128

[48] Large M.I., Mathewson D.S. & Haslam C.G. (1959), Nature, 183, 1663

[49] Lauer T.R. (1988), ApJ, 325, 49-73

[50] Lemaître G. (1931), Nature, 127, 706

[51] Livio M. (2000), *Type Ia Supernovae: Theory and Cosmology*, Cambridge University Press

[52] Lucey J.R. (1983), MNRAS, 204, 33

[53] Materne J. & Hopp U. (1983), Astronomy and Astrophysics, 124, L13-L15

[54] Melott A.L., Chambers S.W. & Miller C.J. (2001), ApJ, 559, L75

[55] Merritt D. (1985), ApJ, 289, 18

[56] Montero-Dorta A.D. & Prada F. (2008), *The SDSS DR6 Luminosity Functions of Galaxies*, arXiv:0806.4930 [astro-ph], doi:10.1111/j.1365-2966.2009.15197.x

[57] Mulchaey J.S. (2000), ARAA, 38, 289

[58] Navarro J.F, Frenk C.S. & White S.D.M. (1995), arXiv:astro-ph/9508025

[59] Oegerle W.R. & Hill J.M. (1992), The Astronomical Journal, 104, 6, 2078-2085

[60] Olive K., Steigman G., Walker T.P. (2000), Phys.Rept., 333, 389

[61] Olivier S., Primack J.R., Blumenthal G.R, Dekel A. & Stanhill D (1990), ApJ, 356, 1

[62] Peacock J.A. (2000), *Cosmological Physics*, Cambridge University Press

[63] Peebles P.J.E. (1993), *Principles of Physical Cosmology*, Princeton University Press

[64] Peebles P.J.E. (2001), ApJ, 557, 495

[65] Peebles P.J.E. & Ratra B. (2003), arXiv:astro-ph/0207347, doi:10.1103/RevModPhys.75.559.

[66] Perlmutter S. et al. (2995), Supernova Cosmology Project, ApJ, 440, L41

[67] Plionis M. & Valdarnini R. (1991) MNRAS, 249, 46

[68] Plionis M. (2002), ApJ, 572, L67-70

[69] Plionis M. & Basilakos S. (2002a), MNRAS, 329, L47

[70] Plionis M. (2012), *Basics of Cosmology and Structure Formation*, Lecture notes

[71] Poggianti B.M. (1996), *K and evolutionary corrections from UV to IR*, arXiv:astro-ph/9608029, doi:10.1051/aas:1997142

[72] Press W.H., Schechter P. (1974), ApJ, 187, 425

[73] Press W.H., Teukolsky S.A, Vetterling W.T. & Flannery B.P. (1997), *Numerical Recipes in Fortran 77*, Cambridge University Press

[74] Ramella M et al. (2007), A&A, 470, 39-51

[75] Reiprich T.H. & Böhringer H. (2002), ApJ, astro-ph/0111285

[76] Richstone D., Loeb, A. & Turner E.L. (1992), ApJ, 393, 477

[77] Ritchie B.W. & Thomas P.A. (2002), MNRAS, 329, 675

[78] Roettiger K., Burns J. & Loken C. (1993), ApJ, 407, L53

[79] Roettiger K., Stone J.M. & Burns J. (1999), ApJ, 518, 594

[80] Rose J.A., Gaba A.E., Christiansen W.A., Davis D.S., Caldwell N., Hunstead R.W. & Johnston-Hollitt M. (2002), AJ, 123, 1216

[81] Rowan-Robinson M. (1985), *The cosmological distance ladder: Distance and time in the Universe*, New York, W. H. Freeman and Co.

[82] Rowan-Robinson M. (1988), Space Science Reviews, 48

[83] Sarazin C.L. (2001), *Merging Processes in clusters of Galaxies*, eds. Feretti L., Gioia M., Giovannini G., (Dordrecht: Kluwer)

[84] Scaramella R., Vettolani G. & Zamorani G. (1991), ApJ, 376, L1

[85] Schechter P. (1976), ApJ, 203, 297

[86] Schindler S. (1999), in proceedings of the Vulcano Workshop 1999, Multifrequency Behaviour of High Energy Cosmic Sources, eds. Giovanelli F., Sabau-Graziati L., astro-ph/9909042

[87] Schmidt B.P. et al. (1998), ApJ, 507, 46

[88] Schuecker P., Böhringer H., Reiprich T.H. & Feretti L. (2001), AA, 378, 408

[89] Smoot G.F. et al (1991), ApJ, 371, L1

[90] Steigman G. (2001), *The Light Elements and Their Evolution*, IAU Symp. 198, eds L. Da Silva, M. Spite, J.R. Medeiros, ASP Conference Series

[91] Sunyaev R.A. & Zeldovich Ya.B. (1970), Ap&SS, 9, 368

[92] Sutherland W.J. & Efstathiou G. (1991), MNRAS, 248, 159

[93] Thuan T.X., Gott J.R. & Schneider S.E. (1987), ApJ, 315, 93

[94] Tsagas C., *Introduction to Relativistic Cosmology*, Lecture notes

[95] Tully B. & Fisher J.R. (1977), ApJ, 54, 661

[96] Tully R.B., Scaramella R., Vettolani G. & Zamorani G. (1992), ApJ, 388, 9

[97] Viana P.T.P. & Liddle A.R. (1999), MNRAS, 303, 535

[98] van den Bergh S. (1998), *Galaxy morphology and classification*, Cambridge University Press

[99] van de Weygaert R. (2002), *2nd Hellenic Cosmology Meeting on Modern Theoretical and Observational Cosmology*, eds. M.Plionis, S.Cotsakis, Kluwer ASSL series

[100] Weinberg S. (1972), *Gravitation & Cosmology*, John Wiley, New York.

[101] West M.J. (1994), MNRAS, 268, 79

[102] White S.D.M., Navarro J.F., Evrard A.E. & Frenk C.S. (1993), Nature, 366, 429

[103] Zabludoff A.I. & Zaritsky D. (1995), ApJ, 447, L21

[104] Zeldovich Ya.B., Einasto J. & Shandarin S.F. (1982), Nature, 300, 407